

NORTHWESTERN UNIVERSITY

Biofunctionalization and Hazard Assessment of Semiconducting Nanoelectronic Materials

A DISSERTATION

SUBMITTED TO THE GRADUATE SCHOOL
IN PARTIAL FULFILLMENT OF THE REQUIREMENTS

for the degree

DOCTOR OF PHILOSOPHY

Field of Materials Science and Engineering

By

Nikhita Mansukhani Kogar

EVANSTON, ILLINOIS

March 2017

ABSTRACT

Biofunctionalization and Hazard Assessment of Semiconducting Nanoelectronic Materials

Nikhita Mansukhani Kogar

Semiconducting nanoelectronic materials, including single-walled carbon nanotubes (SWCNT) and transition metal dichalcogenides (TMDs) possess interesting optoelectronic properties that could enable next-generation electronics, sensing technologies, and biomedicine. In this thesis, biomolecule-assisted dispersion and assembly of these nanomaterials are explored for human toxicity, environmental hazard potential, and applications in supramolecular hydrogels.

Liquid-based exfoliation of hydrophobic nanomaterials requires the presence of a surfactant in aqueous solution. Surfactant-assisted exfoliation of nanomaterials is a highly scalable and applicable processing method, but often results in dispersions of poor quality or yield. Here, we survey a library of nonionic, biocompatible block copolymers, known commercially as Pluronics and Tetronics, that are capable of stabilizing MoS₂ in aqueous solution. We determine that Pluronic F87 results in the highest concentration MoS₂ dispersion. This poloxamer is applied to the dispersion of a range of emerging 2D materials, establishing a facile aqueous exfoliation method for further studies.

Using the same biocompatible block copolymer found in the previous study, we establish a library of MoS₂ nanomaterials with highly refined physicochemical properties. The library of MoS₂ nanomaterials is comprised of Pluronic-dispersed MoS₂, aggregated MoS₂, and lithiated

MoS₂. In a study of their inhalation risk in humans, it is found that aggregated MoS₂ induces an inflammatory response after acute exposure. None of the MoS₂ nanomaterials are found to induce fibrosis of the lung after subchronic exposure. In the natural aquatic environment, Pluronic-dispersed MoS₂ nanomaterials are comparatively more stable and more likely to interact with surface media than lithiated-MoS₂. Furthermore, the hazard potential of SWCNT is investigated. Specifically, we demonstrate that electronic type has little bearing on the lung inflammatory response of SWCNT. These results are essential to the establishment of safe handling practices for nanomaterials and are of interest from a regulatory perspective.

Finally, biomolecule-assisted assembly is studied in the form of an optothermally responsive SWCNT–DNA supramolecular hydrogel (SMH). In this SMH, SWCNT are dispersed in aqueous solution by helical wrapping of single-stranded DNA. DNA base pairing is employed to form a SWCNT network, thereby providing the cross-linking force necessary for gelation. The mechanical strength of this SMH is proportional to the SWCNT concentration, and can be tuned accordingly. The SMH is fully thermo- and NIR- reversible and therefore has potential for applications in sensing and responsive materials.

Acknowledgements

There are so many people that I would like to thank for supporting this work. First and foremost, I would like to thank my advisor Professor Mark Hersam for his guidance and unwavering support during my time here at Northwestern. In addition to being an excellent advisor, Mark has been a role model and inspiration. His leadership, efficiency, and ability to manage many projects are truly unparalleled, and I will surely spend the rest of my career trying to emulate them!

I would also like to thank my committee members, Professor Derk Joester, Professor Ramille Shah, Professor Phillip Messersmith and Professor Wes Burghardt, for their feedback and contributions to my research. I must also thank Professor Karl Putz for his advice and support in the lab.

I am sincerely grateful for the many excellent teachers and mentors I have had that brought me to graduate school. I thank my teachers at the Montessori School of Lake Forest, for instilling in me a love of learning and confidence to teach myself and others. I thank Mr. Bush, my high school physics teacher, for making physics fun and approachable. I would not have found my calling in research had it not been for two wonderful undergraduate research experiences: working for Professor Chandra Shekhar Mayanil, who I can't thank enough for taking a chance on an unexperienced freshman, and Professor Nadya Mason, who continues to inspire me with her work ethic, excellent science, and optimistic outlook. Dr. Shunsuke Ichi, Dr. Yueh-Wei Shen, Dr. Serena Eley, and Scott Scharfenberg mentored me as an undergraduate researcher, and I am grateful to them for all of their help. I also thank my mentors outside the lab

at the University of Illinois, Celia Elliott and Professor S. Lance Cooper, for their “Everything You Need to Know in Science but the Science” education, and their constant support throughout my academic career.

I have many people to thank at Northwestern. I thank my mentors in the Hersam Group, Matt Duch and Dr. Ted Seo, for bringing me up to speed early in my graduate career. Linda Guiney has been an excellent companion in the Hersam Group that I was fortunate to work with for the last five years, and I thank her for her contributions to this work. In addition to being a constant source of ideas and creativity, Linda is a fierce friend that I feel blessed to know. I thank the Northwestern research staff, including the MSE office staff, Katie Kolhoff, Keith MacRenaris, and Carla Shute, for all of their help during my time here. I thank my collaborators in the lab, Dr. Jae-Hyeok Lee, Yichao Zhao, and Peter Kim for their teamwork and ability to support our many projects. I must also thank all of my group mates, past and present, for their companionship and support, especially Dr. Laila Jaber-Ansari, Dr. Heather Arnold, Dr. Kanan Puntambekar, Dr. Prad Prabhumirashi, Dr. Kyle Luck, Dr. Mike Geier, Dr. Julian McMorrow, Dr. Tejas Shastri, Dr. Eric Pozzi, Dr. Chris Ryder, Dr. Yujin Shin, Amanda Walker, Jade Itamar Balla, and Sarah Clark. Finally, I thank my friends outside the lab for making my days at Northwestern brighter and fuller, especially Kavita Chandra, Lam-Kiu Fong and Amelia Plunk.

I have been fortunate to collaborate with many research groups at the University of California Center for Environmental Applications of Nanotechnology, including those of Dr. André Nel, Professor Sharon Walker, Dr. Dermont Bouchard, and Professor Indranil Chowdhury. I thank them and their group members, Dr. Xiang Wang, Dr. Ivy Ji, Dr. Ruibin Li, Dr. Tian Xia, Dr. Jacob Lanphere, Drew Story, and Mehnaz Shams, for their collaboration and

for expanding my research horizons. I thank my collaborators at Northwestern, Professor Eric Luijten and Dr. Harris Perlman, and their group members, Dr. Alexander Misharin, Rana Saber, and Zonghui Wei, as well, for their contributions to this work.

On a more personal note, I would like to thank my girlfriends that have become more like sisters, Priyanka Agrawal, Divya Iyengar, Priyanka Joseph, Palak Doshi, Akta Mehta and Felicia Martinez, for their unfailing encouragement to do things that I considered impossible. Thank you for expecting me to achieve my best and have fun on the way.

I must thank my parents for being my greatest cheerleaders, support system, and easily two of the best people I know. I cannot thank them enough for their unconditional love and everything they have done for me; having them as my parents is the greatest blessing of my life. My in-laws, Varsha, Ricky and Kaushi Kogar, and the Kogar, Sachdev, and Dawar families, have brought so much light into my world these past five years. I thank my siblings, Prarna and Neel, for the healthy competition they've provided from the earliest days, and always giving the best, most honest advice and example to follow. I must also thank the rest of my family, the Advanis, Prasads, Rajini Shahani, Peter Giammamarinaro, Mirchandanis, Jagi Umesh and Umesh Reghuram, for always believing in me. I would especially like to thank my mom and her sisters, Dr. Shakun Advani, Jagi Umesh, Bina Advani, Rajini Shahani, and Reena Doshi, for being the original girl gang and continually inspiring me to be strong, just, and driven.

Finally, I must thank my husband, Anshul, for his love, for always being in my corner, and for reminding me to have a good sense of humor in all situations. I cannot possibly put into words all the ways you've changed my life for the better. Thank you for sharing in this adventure with me, and I look forward to many more!

For my family

Table of Contents

Abstract	3
Acknowledgements	5
Dedication	8
List of Tables	12
List of Figures	13
Chapter 1: Introduction	21
1.1 Broad Challenges	23
1.2 Outline of Thesis.....	24
Chapter 2: Literature Review	26
2.1 Materials Overview.....	27
2.1.1 Graphitic Nanostructures	27
2.1.2 Introduction to Semiconducting Nanoelectronic Materials	30
2.1.3 Single-Walled Carbon Nanotubes.....	34
2.1.4 Two-Dimensional Materials Beyond Graphene	40
2.1.5 Transition Metal Dichalcogenides	41
2.1.6 Hexagonal Boron Nitride.....	45
2.2 Solution Processing of Nanoelectronic Materials.....	46
2.2.1 Overview	46
2.2.2 Chemical Exfoliation	48
2.2.3 Organic Solvent Exfoliation	51
2.2.4 Aqueous Solution Processing	54
2.2.5 Solution-Based Sorting Methods	56
2.3 Toxicity and Human Health Hazard of Nanomaterials.....	57
2.3.1 Toxicity of Single-Walled Carbon Nanotubes.....	57
2.3.2 Toxicity of TMDs and Hexagonal Boron Nitride.....	60
2.4 Environmental Fate of Nanomaterials	63
2.4.1 Environmental Fate and Transport of Carbon Nanotubes	64
2.4.2 Environmental Fate and Transport of TMDs.....	65

2.5 Introduction to Supramolecular Hydrogels.....	66
2.5.1 Synthetic and Supramolecular Hydrogels.....	67
2.5.2 Types of Supramolecular Hydrogels	68
2.5.3 Rheology	70
Chapter 3: High-Concentration Aqueous Dispersions of Nanoscale Two-Dimensional Materials Using Nonionic, Biocompatible Block Copolymers.....	72
3.1 Introduction.....	73
3.2 Experimental Section.....	75
3.2.1 Nanomaterial Dispersion Conditions.....	75
3.2.2 Removal of Pluronic from Dispersion	77
3.2.3 Inductively Coupled Plasma-Mass Spectroscopy	78
3.2.4 Extinction Coefficient and Concentration Measurements	79
3.2.5 Scanning Transmission Electron Microscopy	79
3.2.6 Size Characterization	80
3.2.7 X-Ray Photoelectron Spectroscopy	80
3.3 Results and Discussion	81
3.4 Conclusion	98
Chapter 4: Human and Environmental Hazard Assessment of Two-Dimensional Molybdenum Disulfide and Single-Walled Carbon Nanotubes	99
4.1 Introduction.....	100
4.2 Experimental Section.....	103
4.2.1 Preparation of MoS ₂ Suspensions.....	103
4.2.2 Source and Preparation of Sorted SWCNT	104
4.2.3 Cell Culture and Co-Incubation with Molybdenum Disulfide	106
4.2.4 Preparation of Nanomaterial Suspensions and Cell Culture with Semiconducting and Metallic SWCNT	106
4.2.5 Cytotoxicity Assessment.....	107
4.2.6 Mouse Exposure and Assessment of Exposure Outcomes	107

4.2.7 Sircol Assay to Assess Total Collagen Production.....	108
4.2.8 Statistical Analysis.....	109
4.2.9 Packed Bed Column Transport Experiments.....	109
4.3 Results and Discussion	110
4.4 Conclusion	128
Chapter 5: Optothermally Reversible Carbon Nanotube-DNA Supramolecular Hybrid Hydrogel.....	130
5.1 Introduction.....	131
5.2 Experimental Section	133
5.2.1 Dispersion of CNT in DNA	133
5.2.2 Optical Characterization	134
5.2.3 NIR-Triggered Release of DNA from CNT	135
5.2.4 CNT–DNA Gel/Network Synthesis.....	141
5.2.5 Rheology	142
5.2.6 Cryo-SEM Characterization.....	143
5.2.7 Near Infrared Reversibility	143
5.3 Molecular Dynamics Simulations.....	144
5.3.1 Modeling Details.....	144
5.3.2 Determination of Annealing Rate	148
5.3.3 Hybridization Mismatch in Simulations	149
5.4 Results and Discussion	150
5.5 Conclusion	162
Chapter 6: Summary and Future Opportunities.....	163
6.1 Summary	164
6.2 Future Opportunities	166
References	170
Vita	203

List of Tables

Table 3.1: Centrifugation processing parameters used in this dispersion study	76
Table 3.2: Concentration of molybdenum disulfide dispersed in aqueous block copolymers	87
Table 3.3: Flake height and lateral area characterization of Pluronic F87-dispersed 2D nanomaterials	92
Table 4.1: Zeta potential and hydrodynamic diameter of MoS ₂ materials used in this study, shown in water and cell culture media.....	111
Table 4.2: The elemental composition of heavy metal impurities in SWCNTs was determined by inductively coupled plasma mass spectroscopy (ICP-MS).....	113

List of Figures

- Figure 2.1:** 2D Graphene (far right) is considered the mother of all graphitic forms, including 0D fullerenes (left), 1D carbon nanotubes (middle) and 3D graphite (right).⁸28
- Figure 2.2:** Schematic of direct (left) and indirect (right) bandgap structures. Bandgap is denoted as E_g . Curves representing conduction and valence bands are plotted as a function of k , the wave vector that defines crystal momentum. For indirect band gaps, photon (green) absorption must be assisted by a phonon (red) to excite an electron from the conduction to valence band. Band structure is shown as a function of the wave vector k31
- Figure 2.3:** Schematic of photoluminescence mechanism. Absorption of a photon with energy larger than the bandgap excites an electron to the conduction band. After non-radiative recombination processes, the excited electron relaxes to the ground state, emitting a photon.....33
- Figure 2.4:** The electromagnetic energy spectrum shown in electron volts (left) and wavelength (right). This thesis concerns direct bandgap materials that span a wide range of bandgap energies, including the biologically relevant visible and infrared regions.....34
- Figure 2.5:** Schematic showing the 2D graphene lattice with an overlay of the possible carbon nanotube species. Each possible type of nanotube is denoted by chiral vector indices (n,m) . The number below the chiral vector denotes the number of possible caps of the nanotube, which increases with diameter.⁴³36
- Figure 2.6:** Schematic of the 1D density of states (DOS) of an individual nanotube, showing the Van Hove singularities in the conduction and valence bands. Solid arrows denote the electronic transitions involved in photoluminescence spectroscopy, wherein a photon promotes an electron from $v1$ to $c1$, whereupon an electron-hole pair (exciton) is formed, which undergoes non-radiative relaxation (dashed arrows), and then ultimately the electron emits light and falls back down to the $v1$ band ($E11$ solid arrow).⁴⁵38
- Figure 2.7:** Photoluminescence maps showing normalized fluorescence intensity for specifically defined SWCNT species. The top map shows a CoMoCAT SWCNT sample, and the bottom map shows a HiPco SWCNT sample.⁵²39
- Figure 2.8:** 2D Materials Family. Materials that are air stable at room temperature are shown in blue; probably air stable are shown in green, unstable in air but may be stable in inert environments is shown in pink. Materials shown in grey have been successfully exfoliated into monolayers, but there is little further information regarding properties and applications. Adapted from Geim, et al Nature 2013.⁵⁴40

Figure 2.9: Structures of 2D transition metal dichalcogenides (A) 2H crystal structure and (B) 1T crystal structure. Here transition metal atoms are shown in green, chalcogen atoms shown in yellow. Top views and side views (bottom). Drawn with CrystalMaker9.43

Figure 2.10: Structure of hexagonal boron nitride top and side views. Boron (blue) is bonded to nitrogen (purple) in a hexagonal lattice analogous to graphene. As seen in the side view, it is atomically flat. Drawn with CrystalMaker9.46

Figure 2.11: The production methods of graphene, which cover a wide range of quality, size, and price. These trends hold true for the production of 2D materials beyond graphene (TMDs, hBN).¹⁴²48

Figure 2.12: An example of chemical exfoliation of SWCNT. SWCNT are commonly modified with carboxyl groups using acid treatments (1a). These carboxyl groups can be further modified in a variety of ways. Shown here, an amino group is attached by virtue of ethylenediamine functionalization (1b).¹⁴⁶49

Figure 2.13: Ions, shown as yellow spheres, are intercalated between layers in bulk materials. Upon agitation, usually in the form of shear, sonication, or thermal forces, the layers exfoliate in solution.¹³⁷51

Figure 2.14: MoS₂, WS₂, and hBN were dispersed in a wide range of organic solvents. Their optical absorption (A/l) is plotted as a function of solvent surface tension γ in (A)-(C). Photos, individual optical absorption spectra, and Lambert-Beer plots are shown in (D)-(F). In (D)-(F), MoS₂ and WS₂ are dispersed in NMP, while hBN is dispersed in IPA.¹⁶²53

Figure 2.15: Structure schematic of Pluronic (top) and Tetronic (bottom) biocompatible block copolymers.¹⁷⁴55

Figure 2.16: (a) Centrifuge tube of small diameter-sorted SWCNT dispersed in SC. The smaller diameter tubes settle at higher points, allowing for fractionation by diameter. (b) Optical absorption spectra of the corresponding bands in (a). (c) Shows centrifuge tube of large-diameter sorted SWCNT dispersed in SC and sodium dodecyl sulfate (SDS). (d) Optical absorption spectra of the semiconducting and metallic bands shown in (c).¹⁸⁸57

Figure 2.17: Nanoscale dispersions of SWCNT do not elicit a toxic response, as compared to untreated cells, particulate matter less than 2.5 μ m in diameter (PM_{2.5}), and asbestos dispersed in PBS (white) or Pluronic F108 (black). A) Mitochondrial ROS was measured in A549 cells (alveolar epithelial cells) that stably express an oxidant sensitive GFP probe that is localized to the mitochondrial matrix. After 24 hours cell death was assayed using an ELISA that detects fragmented DNA (B), bronchiolar lavage (BAL) fluid protein level was measured (C) along with BAL fluid cell count (D) and plasma thrombin-antithrombin complex (E).²⁰⁵60

Figure 2.18: Percentage cell viability of human lung epithelial cells (A549) as measured with (A) MTS assay and (B) WST-8 assay following 24 hours of exposure to varying amounts of exfoliated TMDs. The percentages are normalized to control cells that were not exposed to TMDs.²³³62

Figure 2.19: Boron nitride nanotubes (BNNT) are not cytotoxic. (a) BNNT do not inhibit cell proliferation and (b) have no effect on viability in HEK293 cells.²³⁴63

Figure 2.20: Representative chemical structures of commonly used neutral and charged polymers for synthetic hydrogels.²⁷⁹67

Figure 2.21: Types of supramolecular hydrogels. SMH are classified in terms of (a) non-covalent interaction: (i) hydrogen bonding, (ii) metal-ligand coordination, (iii) host-guest recognition, and (iv) electrostatic interaction. (b) Classification based on size of network and components: (i) macrohydrogel, (ii) microhydrogel, and (iii) nanohydrogel. (c) Classes of SMH according to the type of building blocks/gelators: (i) molecular hydrogel, (ii) supramolecular polymeric hydrogel and (iii) supramolecular hybrid hydrogel.²⁶⁹69

Figure 2.22: Typical parallel-plate setup of a rheometry experiment. A sample is placed between two parallel plates and an oscillatory strain is applied to measure deformation/flow.71

Figure 3.1: Schematic depiction of (A) Pluronic and (B) Tetronic block copolymers on the surface of a single-layer MoS₂ flake. The amphiphilic Pluronic/Tetronic block copolymers adsorb non-covalently to the surface of MoS₂ and prevent the agglomeration of the exfoliated flakes by acting as a surfactant and providing steric repulsion.82

Figure 3.2: (A) Optical absorption spectra showing the range of concentrations possible by dispersing MoS₂ in Pluronics under identical dispersion conditions. Photographs of corresponding solutions shown in the inset. (B) Beer's Law plot of Pluronic F87 MoS₂ dispersion optical absorbance as a function of concentration as measured by ICP-MS. (C) Concentration map of MoS₂ in Pluronics and Tetronics. The color map is based on interpolation of the experimental Pluronic data, while the actual experimental values are shown by colored circles, and the actual Tetronic experimental values are represented by colored squares.85

Figure 3.3: Concentration map of MoS₂ in Pluronics and Tetronics using Delaunay triangulation without smoothing. Experimental data points are indicated by black dots.89

Figure 3.4: Concentration plotted as a function of PPO/PEO molecular weight only (top) or number of PPO/PEO molecules only.90

Figure 3.5: Distribution of height (A) and square root area (B) of MoS₂ dispersed in Pluronic F87.92

Figure 3.6: Size characterization of Pluronic F87-dispersed MoS₂. (A) SEM, (B) high-resolution STEM, (C) AFM, and (D) cross-sections derived from the AFM image. Scale bars in (A) and (C) are 500 nm. The scale bar in (B) is 1 nm.93

Figure 3.7: (A) Representative Mo 3d XPS spectrum of Pluronic F87-dispersed MoS₂. (B) Representative S 2p XPS spectrum of Pluronic F87-dispersed MoS₂.95

Figure 3.8: (A) Optical absorbance spectra, (B) photograph, (C) concentration by ICP-MS, and (D) representative AFM of BN dispersed by Pluronic F87 in water. Spectra in (A) are vertically offset for clarity. Dispersions pictured in (B) from left to right are: MoSe₂, WSe₂, WS₂, SnSe, and BN. The scale bar in (D) is 500 nm.96

Figure 3.9: Representative XPS spectra of (A) WSe₂, (B) MoSe₂, (C) WS₂, (D) SnSe, and (E) BN dispersed in Pluronic F87. Bulk spectra are identical, confirming that minimal oxidation or contamination occurs during the dispersion process.97

Figure 4.1: Characterization of Agg-, Lit- and PF87-MoS₂. (A) Scanning electron micrograph of Agg-MoS₂. (B, C) Representative atomic force microscopy (AFM) images of PF87-MoS₂ and Lit-MoS₂. (D) Optical absorbance spectra of PF87-MoS₂ and Lit-MoS₂. (E, F) AFM histograms of flake thickness and lateral flake sizes of the exfoliated materials.111

Figure 4.2: Scheme and characterization of the electronic-sorted SWCNTs. (A) Scheme for the preparation of electronic-sorted SWCNTs. P2 SWCNTs were sorted into metallic and semiconducting species using density gradient ultracentrifugation (DGU) methods. The detailed methodology appears in the Experimental Section. (B) Characterization of the sorted SWCNTs. Photograph of the DGU separation tube (a) and corresponding optical absorption spectra (b). The purity of the final dispersions was >98.8% for M-SWCNT and >98.5% for S-SWCNT, as determined by optical absorbance spectroscopy. (C and D) Characterization of semiconducting (C) and metallic (D) SWCNTs by AFM and optical absorption spectroscopy. Panels (c) and (g) show the AFM images, panels (d) and (h) show the optical absorption spectra, panels (e) and (i) show length distributions, while panels (f) and (j) show the diameter distributions.113

Figure 4.3: Cytotoxicity of MoS₂ (A,B) and SWCNT (C,D) nanomaterials as measured by MTS assay in a dose-dependent manner. Statistical analysis shows that no nanomaterials had a significant impact on cell viability compared to the negative control, ZnO.115

Figure 4.4: Total cellular Mo content in BEAS-2B and THP-1 cells as determined by ICP-OES. Both cell types were exposed to 50 µg/mL MoS₂ for 24 h, following which the cells were recovered, sonicated and used for acid digestion. The concentration in each sample was expressed as µg Mo per mg of cellular protein.116

Figure 4.5: Exposure to 2D MoS₂ (PF87-MoS₂ and Lit-MoS₂) resulted in significantly decreased cytokine and chemokine production when compared to aggregated MoS₂, indicating a decreased inflammatory response.117

Figure 4.6: Comparative pro-fibrogenic effects, as reflected by IL-1 β and TGF- β 1 production in THP-1 and BEAS-2B cells, respectively. Cells were exposed to the indicated concentrations of the sorted SWCNTs for 24 h. IL-1 β (A) and TGF- β 1 (B) levels were determined on the culture supernatants by ELISA. *p < 0.05 compared to control.118

Figure 4.7: DCF fluorescence spectroscopy: 29 μ mol/L DCF was added to CNT suspensions at 12.5–100 μ g/mL for 24 h, and emission spectra were collected at 500–600 nm, with excitation at 490 nm. Both S- and M-SWCNTs showed significant enhancement of DCF fluorescence compared to the nontreated control. ROS production by Co₃O₄ NPs at 100 μ g/mL was used as positive control. (B) Comparative expression of the fluorescence intensity at 528 nm demonstrated a proportionally bigger dose-dependent increase in fluorescence activity with metallic compared to semiconducting SWCNTs.119

Figure 4.8: Acute pulmonary effects of Agg-, Lit-, and PF87-MoS₂ in mice. Anesthetized C57BL/6 mice were exposed to dispersed MoS₂ materials, delivered by one-time oropharyngeal aspiration of a bolus dose of 2.0 mg/kg. There were 6 animals per group. (A) Representative H&E-stained histological images (100 \times) of the lungs of MoS₂ treated mice. Animals were euthanized after 40 h, and BALF was collected to determine LIX, MCP-1, and IL-6 (not shown) levels as well as measuring neutrophil cell counts (B) Quartz (QTZ) was used as a positive control, at 5.0 mg/kg. *p < 0.05 compared to control.121

Figure 4.9: Assessment of the possible fibrotic effects of MoS₂ materials 21 days after oropharyngeal installation. The experiment, described in Figure 4, was repeated with the exception that animal sacrifice was performed 21 days after oropharyngeal inspiration of a similar particle dose. There were 6 animals in each group. (A) Collagen deposition in the lung as determined by Masson's trichrome staining. Lung tissue was embedded, sectioned, stained with the Masson's trichrome and observed at 100 \times magnification. Blue staining represents collagen deposition in the lung. (B) Total collagen content of the lung tissue was determined using the Sircol collagen kit (Biocolor Ltd., Carrickfergus, U.K.). *p < 0.05 compared with control. (C) ICP-OES analysis of MoS₂ retention in the lung, showing considerably reduced lung burden. Animals exposed to Quartz (QTZ) served as positive control.123

Figure 4.10: Assessment of the pro-fibrogenic effects of the electronic-sorted SWCNTs in mice. Anesthetized C57BL/6 mice were exposed to SWCNTs, delivered by one-time oropharyngeal aspiration of a 2.0 mg/kg bolus dose. Animals were euthanized after 21 d, and BALF was collected to determine (A) TGF- β 1 and (B) PDGF-AA levels. (C) Assessment of total collagen content by a Sircol kit (Biocolor Ltd., Carrickfergus, UK). *p < 0.05 compared to control. (D) Visualization of collagen deposition in the lung, using Masson's trichrome staining. Collagen

deposition is shown as blue staining under 100× magnification. Animals exposed to quartz (QTZ, SiO₂) served as positive control.125

Figure 4.11: Effective diameter as a function of pH (A,B) and ionic strength (C,D) for Pluronic-dispersed MoS₂ (A,C) and Lithiated MoS₂ (B,D).127

Figure 4.12: Summary of packed-bed column transport study, wherein it was found that Pluronic-dispersed MoS₂ has a higher affinity for quartz media.128

Figure 5.1: Representative UV-Vis spectra of CNT before gelation.....134

Figure 5.2: A) PLE map of CNT–DNA dispersions, showing predominance of (6,5) chirality CNT. B) Representative PLE spectra of a pristine CNT dispersion and a CNT–DNA network after the addition of linker DNA.....135

Figure 5.3: Schematic of the CNT/ssDNA/siRNA complex before and after thermal separation induced by NIR excitation.137

Figure 5.4: Hybridization process to form double-stranded overhang functionalization. ssDNA is used to disperse CNT in solution, followed by a complementary strand added in excess that hybridizes to the ssDNA already adsorbed to the surface of the CNT.138

Figure 5.5: Optical absorption spectra showing the overhang formation. The shift in the S22 peak from 994 to 996 nm indicates that the overhang hybridization is complete.138

Figure 5.6: Normalized fluorescence increase as a function of temperature. Heat drives the melting of the dsDNA overhang region, releasing the payload strand. A non-complementary payload is compared for control. When the sample is cooled back to room temperature, the normalized fluorescence value returns to 50, indicating that some rehybridization occurs.140

Figure 5.7: Normalized fluorescence as a function of temperature in the case of thermal release (black) and as a function of final measured temperature for NIR-triggered release. NIR irradiation was carried out with a constant power of 0.75 W/cm² (red) or pulsed (blue). Melting temperatures are taken from the inflexion point, marked by a dashed line.141

Figure 5.8: Photos of CNT–DNA dilute networks compared to a sample which was not mixed with linker DNA (rightmost cuvette).142

Figure 5.9: Schematic illustration of possible inter-S1 strand distance. Each wrapped DNA is assumed to occupy a total length of 12 nm along the CNT, where the (AC)₁₂ strand occupies 8 nm and the S1 strand occupies 4 nm. The (AC)₁₂ strand is ignored in the coarse-grained model and the first bead of the S1 strand is directly bonded to one of the CNT beads. Depending on the

relative orientation of the neighboring wrapped DNA, the inter-S1 strand distance can be 9, 12 or 15 nm.145

Figure 5.10: Schematic illustration of the dynamic bonding function used to simulate the formation of cross-links in an example system with 3 linker DNA beads. A) System components before forming the cross-link. Each bead of different color is assigned with a different bead type. B) Cross-link formation. Each linker DNA bead type can only bind with one specific linker DNA bead type at any given time to mimic the DNA hybridization. In this case, each cyan bead can only bind with one other purple bead and the formed bond (bond type 2) has a strength of 46 *kBT*. The same binding rule applies for pink-pink binding. The terminal S1 strand bead (yellow) can only bind with one specific linker DNA bead type (purple) and the formed bond (bond type 1) has a strength of 149 *kBT*.146

Figure 5.11: The effect of annealing rate on the number of cross-links and gel configuration. A) The simulation time (unit: τ) run for each bond strength during the annealing process for different annealing rates. B) The number of cross-links as a function of annealing rate. C) Representative gel configurations at different annealing rates.148

Figure 5.12: Schematic and physical characterization of CNT–DNA gel structure. A) DNA sequence used to disperse CNT, shown in black; Linker DNA shown in green with two regions: one complementary to S1 to form a connection with CNT and one self-complementary (CG) repeat of variable length, separated by a single adenosine base. B) The proposed structure of gel formation, wherein (AC)_{12S1} helically wraps around the CNT and linker DNA forms duplexes with both S1 and other linker strands, thereby providing the cross-linking mechanism. C) Photos of the inverted vial test to demonstrate the sol-gel transition (solution on left and gel on right). D) Cryo-SEM of a CNT–DNA gel, showing a network of CNT amid frozen buffer salts, DNA, and agglomerated CNT.151

Figure 5.13: Control experiments to support the proposed structure of the gel. In the leftmost column, G' and G'' values of a typical SMH with CNT and linker DNA concentration of 1.8mg/mL. The next column is the result of adding buffer instead of linker DNA before the annealing step, which does not result in gel formation. The third column shows a CNT–DNA SMH in which genomic DNA was added instead of linker DNA, to demonstrate that a complementary linker DNA sequence is needed to form a stronger SMH. Finally, the rightmost column depicts the G' and G'' of a 5mg/mL CNT van der Waals gel, which is considerably weaker than the 1.8mg/mL SMH.153

Figure 5.14: Tunable mechanical properties based on the concentration of CNT. A) Strain sweeps of several representative samples. Squares represent G' ; triangles represent G'' . Purple, green, blue, and black spectra represent gels with CNT concentration of 0.72, 1.25, 1.44, and 1.8 mg/mL, respectively. B) Viscosity vs. Shear stress for a typical gel, compared to an ungelled sample. C) Storage (G') and loss (G'') moduli as a function of CNT concentration. Dashed black and red lines indicate moduli for a 5mg/mL van der Waals gel. D) Number of inter- and intra-

CNT cross-links as a function of the number of CNT for gel systems formed at slow and fast annealing rates. E) and F) Representative simulation configuration of gel formed by 100 CNTs at the slow and fast annealing rates. CNTs are shown in pink. S1 strand and linker DNA are both shown in cyan.154

Figure 5.15: Mechanical properties and melting temperature as a function of linker length and pH, explained by MD simulations. A) G' and G'' as a function of linker length, showing a gradual weakening of the mechanical properties. The number of inter- and intra-CNT cross-links as well as the number of free S1 strands as a function of linker length for gel systems formed at fast (B) and slow (C) annealing rates. D) SMH melting temperatures increase with DNA linker length due to enhanced cross-linking stability. SMH melting temperatures are lower than free duplexes in solution due to confinement effects. SMH mechanical properties (E) and melting temperature (F) remain stable in the range of pH 6-10.....158

Figure 5.16: Optothermal reversibility of CNT–DNA SMH. A) Temperature is cycled between 20°C and 60°C while the SMH is constantly measured. The crossover between G' and G'' marks the reversible sol-gel transition. B) NIR light drives the gel-sol transition after 20 minutes of irradiation. 60 minutes after irradiation, the SMH has recovered to its original rheological state. C) NIR reversibility shown by three cycles of irradiation and recovery of the SMH.161

Figure 5.17: CNT–DNA dilute networks NIR reversibility. NIR reversibility measured by PLE quenching and restoration.162

CHAPTER 1

Introduction

Chapter 1 - Introduction

Nanomaterials are defined as having at least one dimension of approximately 1 to 100 nanometers, and are known for their unique optical, mechanical, electrical, and chemical properties due to their structure at the nanoscale. These nanomaterials take many forms, including noble metal nanomaterials, peptide or polymer-based nanoparticles, and carbon nanomaterials.^{1,2} Here we focus on semiconducting, direct bandgap nanoelectronic materials for their unique optoelectronic properties, including highly efficient light absorption and photoluminescence. These properties could be used for solar cells, light emitting diodes, and other next-generation electronics. They are also important to biomedical applications, such as photothermal therapy, imaging, and sensing. Since the bandgap of the material plays a large role in determining these properties, we chose to study nanoelectronic materials that span the biologically-relevant bandgap energy ranges in the infrared and visible regions. The interactions of these nanoelectronic materials with biomolecules, such as DNA and biocompatible polymers, are useful for novel methods of aqueous-phase dispersion and assembly techniques.

Because new classes of nanomaterials and new polytypes within existing classes are discovered every year, it is essential to continue assessing the human and environmental hazard risks to prepare for possible exposure by airborne and aquatic pathways.³ In particular, it is helpful to understand the role of specific physicochemical properties in toxicity and environmental risk in order to develop deeper understanding regarding the interactions of biological media with nanomaterials. These studies provide strategies for the safe handling of nanoelectronic materials and will prove valuable when they enter the market.

1.1 Broad Challenges

The nanoelectronic materials addressed here are largely hydrophobic. Thus, additives are necessary to obtain pristinely dispersed nanomaterial suspensions in aqueous solutions. Liquid-phase exfoliation of semiconducting two-dimensional nanomaterials represents a scalable path towards mass production for optoelectronic applications in solar cells, light-emitting diodes, and biomedicine. Chemical exfoliation, although one of the most scalable methods to date, utilizes harsh chemical conditions, toxic ion intercalants, and triggers a phase change of 2D materials that encumbers their optoelectronic properties. On the other hand, the use of biomolecules, including biocompatible block copolymers, is an especially scalable and cost-effective method that avoids these drawbacks but is hindered by notoriously low yield and high polydispersity of exfoliated nanomaterials. Liquid-phase exfoliation using biocompatible block copolymers has not been optimized for high yield and concentration, thus obstructing potential applications.

Once scalable, optimized methods of dispersion are achieved, it is imperative to consider the hazard potential of nanoelectronic materials and their derivatives as it relates to human toxicity and environmental fate and transport. It is important to consider what types of nanomaterials pose exposure risk to humans and the environment and their probable pathways. Subsequently, the challenges lie in pinpointing the relationships between physicochemical properties of the nanomaterials and their observed toxicity and environmental fate to inform safe handling practices and regulation.

Lastly, from an applications perspective, biomolecule-nanomaterial complexes tend to form based on non-covalent interactions, and therefore often respond to environmental and

engineered stimuli. This trait is useful for drug delivery, imaging, and more, though many applications have not yet been realized. In particular, the interaction between single-walled carbon nanotubes and DNA has not been harnessed in its simplest form to create supramolecular hydrogels, which have potential in responsive, 3D printed bioinks, sensing, and more.

1.2 Outline of Thesis

This thesis explores the broad challenges associated with biofunctionalized nanoelectronic materials, namely single-walled carbon nanotubes (SWCNT), transition metal dichalcogenides (TMDs), and hexagonal boron nitride (hBN). These materials were chosen for their direct bandgaps, which makes them efficient light absorbers and emitters in the biologically-relevant visible and infrared regions. Herein, progress in three research areas is reported: (i) the optimization of dispersion techniques using nonionic, biocompatible block copolymers, (ii) the hazard potential of these materials in terms of human toxicity and environmental fate and transport, and (iii) potential applications in responsive materials.

In Chapter 3, high-concentration MoS₂ dispersions are explored using biocompatible, nonionic block copolymers. A survey of 19 different poloxamers reveals that MoS₂ concentration is highest using one particular poloxamer, Pluronic F87, which has an intermediate PEO molecular weight and a large PPO molecular weight. These results provide researchers with an optimized dispersion method for MoS₂ and a deeper understanding of its interactions with poloxamers. This method is extended to several more emerging 2D nanomaterials, namely molybdenum diselenide (MoSe₂), tungsten diselenide (WSe₂), tungsten disulfide (WS₂), tin

selenide (SnSe), and hexagonal boron nitride (hBN), thus providing a diverse palette of aqueous 2D nanomaterial dispersions for further studies.

Next, we assess the hazard potential of nanoscale MoS₂ and SWCNT in terms of human toxicity and environmental fate and transport. In Chapter 4, we evaluate the most probable exposure pathway for nanomaterials, inhalation, by studying the toxic potential of these nanomaterials in the lung. This is accomplished by both *in vitro* and *in vivo* studies that elucidate relationships between nanomaterial physicochemical properties and hazard potential. We find that three forms of MoS₂ do not induce inflammation or fibrosis after sub chronic exposure and that the electronic type of SWCNT is not related to toxicity. Regarding their environmental fate and transport, surfactant-stabilized and chemically exfoliated MoS₂ exhibit different behaviors that will be of importance for regulatory purposes.

Finally, in Chapter 5, one possible application of semiconducting nanoelectronic materials is explored. A novel supramolecular hydrogel (SMH) is constructed using SWCNT and DNA. The cross-linking force of this SMH arises from DNA base-pairing, which is a highly tailorable and responsive interaction. Moreover, the mechanical properties of the SMH are tunable by modulating the SWCNT concentration. The SMH are thermally and optically responsive to near infrared light. Their optothermal reversibility is demonstrated by rheological measurements. Thus, these SMH present opportunities in stimuli-responsive materials, sensing, and 3D printing.

CHAPTER 2

Literature Review

This chapter is based, in part, on the research described in the following publication:

*Shams, M.; *Mansukhani, N.; Henderson, M.C.; Zepp, R.; Bouchard, D.; Hersam, M.C.; Chowdhury, I. Environmental Implications of Two-Dimensional Materials. *Environmental Science: Nano* **2017**, *Invited Review, In Preparation*. *Equal Contributions

Chapter 2 - Literature Review

2.1 Materials Overview

An overview of the materials used in this thesis will be provided in this section. A brief description of structure, properties, synthesis methods, and proposed applications will be given for each material/nanomaterial. Emphasis will be placed on proposed applications involving biofunctionalized semiconducting nanomaterials.

2.1.1 Graphitic Nanostructures

Graphene oxide (GO), formerly known as graphite oxide or graphitic acid, was the first graphitic nanostructure synthesized in 1859 by exposing graphite to potassium chloride and fuming nitric acid.⁴ Although nanoscale thickness could not be quantified by the technology at the time, researchers were intrigued by its unusual physicochemical properties. Many years later in the late 20th century, related graphitic nanostructures such as the carbon nanotube and fullerene were discovered and began to be widely explored for their interesting electrical, mechanical, and optical properties.^{5,6} However, a new movement in graphitic nanostructures and two-dimensional (2D) materials began with the isolation of graphene by Geim and Novoselov in 2004, earning them the Nobel Prize in Physics in 2010.⁷ Graphene has since been recognized as the “mother of all graphitic forms,” i.e. the 2D building block of fullerenes, carbon nanotubes, and graphite, and has given rise to an entire family of graphene nanomaterials that are widely studied today, such as halogenated graphene compounds (fluorographene, chlorographene) and other elemental graphene analogues (borophene, silicene, germanene, stanene, and phosphorene).

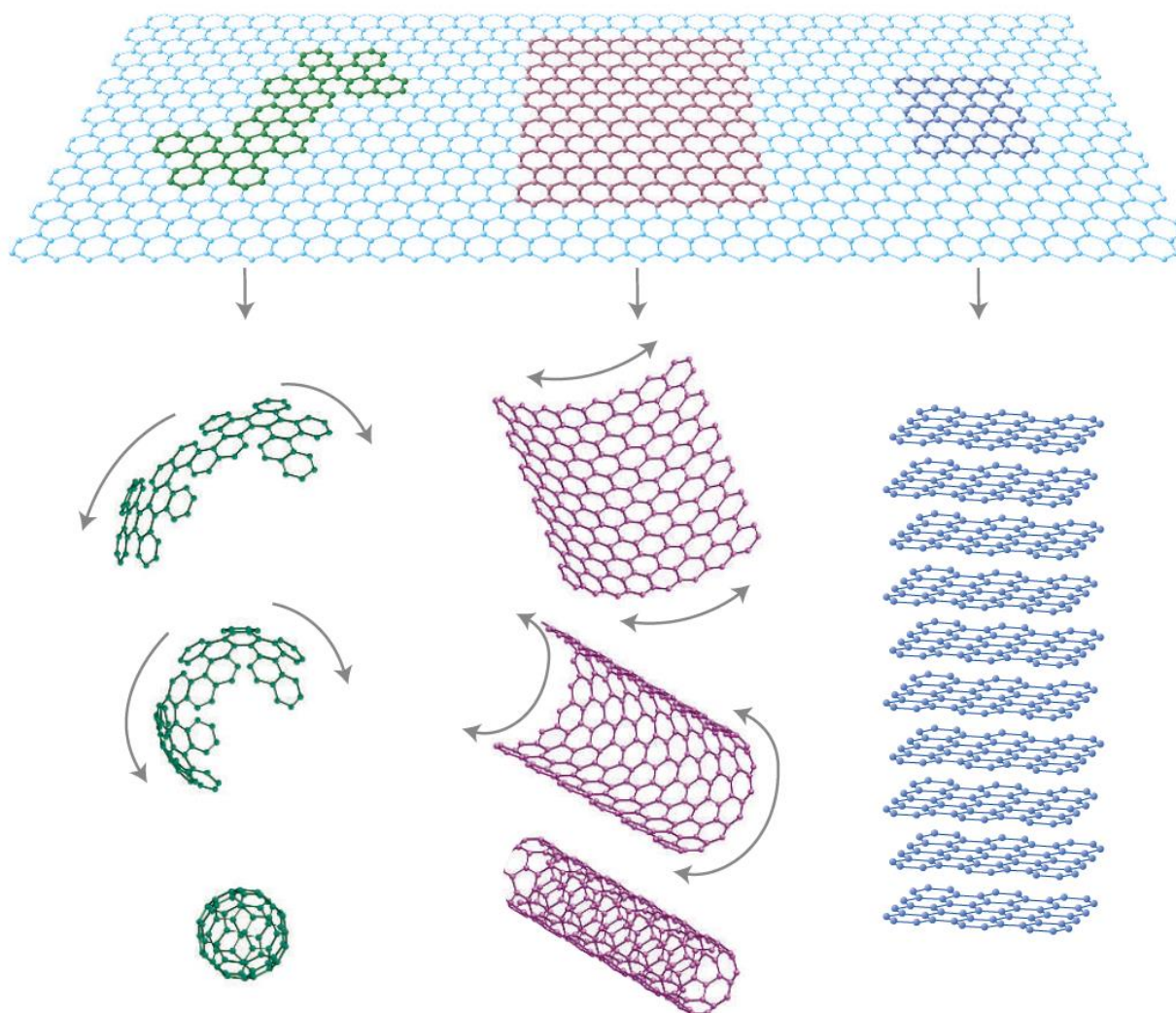


Figure 2.1: 2D Graphene (far right) is considered the mother of all graphitic forms, including 0D fullerenes (left), 1D carbon nanotubes (middle) and 3D graphite (right).⁸

Graphene is a single-atom thick monolayer of sp^2 bonded carbon atoms in a honeycomb lattice (Figure 2.1). Many individual graphene layers of only 0.4nm in thickness stack on top of one another and employ van der Waals interactions to form graphite, though the properties of graphene and graphite have stark differences. First, from a physical standpoint, graphene has enormous theoretical specific surface area ($2620 \text{ m}^2 \text{ g}^{-1}$) and excellent mechanical properties

with a Young's modulus of 1 TPa.^{9,10} Moreover, graphene has a highly unusual electronic band structure wherein the conduction and valence bands touch, making it a zero-gap semiconductor. As a result, graphene has very high electric conductivity; its low-temperature electron mobility of $2 \times 10^5 \text{ cm}^2 \text{ V}^{-1} \text{ s}^{-1}$ at a carrier density of 10^{11} cm^{-2} is more than 1 million times that of copper.¹¹ Graphene also has exceptionally high thermal conductivity, in the range of 4800-5300 $\text{W m}^{-1} \text{ K}^{-1}$, which far exceeds that of the best bulk crystalline semiconducting thermal conductor, diamond, at 1000-2200 $\text{W m}^{-1} \text{ K}^{-1}$.¹²

These superlative properties have made graphene a highly attractive material for many applications. In the realm of electronics, graphene has been incorporated into high frequency transistors with operating frequencies in excess of 100GHz, fueling the possibility of integration into mainstream, next-generation electronics.^{13,14} Graphene is also an exceptional thermal management material, which is important for increasingly smaller devices with higher power densities.¹⁵ Beyond electronics, it has been incorporated into composite materials, paints, and coatings where it can serve as a barrier, reinforcement, or transparent conductor material.¹⁶⁻¹⁸ Many graphene hybrid materials, including graphene-metal nanoparticle systems, graphene-polymer composites, and hydrogels have been created in the interest of highly tailorable properties and wide applicability.¹⁹⁻²⁴ It has also been used as a photocatalyst, sensing material, and bioimaging agent.²⁵⁻²⁸

However, despite all the unique attributes of graphene, it lacks one important electronic property: an electronic bandgap. Roughly speaking, this energy gap between the top of the valence band and bottom of the conduction band, present in semiconductors and insulators but not in conductors, is essential for many applications in electronics and optoelectronics, imaging,

biomedicine, catalysis, and beyond. Most notably, the presence of a bandgap is essential to the modern field-effect transistor as it enables switching of current. In electronics, the lack of a bandgap in graphene has led to low on-off ratios and in some cases, an inability to effectively switch off a device. As such, this work focuses on semiconducting nanoelectronic materials as will be further outlined in the next sections.

2.1.2 Introduction to Semiconducting Nanoelectronic Materials

Energy bands form when atoms, ions, or molecules interact in solids. The highest occupied energy band is called the valence band, and the lowest unoccupied band is called the conduction band. If the valence or conduction band is partially filled, the material is necessarily a metal. On the other hand, if the valence band is full, the material is a semiconductor or insulator.²⁹ The bandgap (E_g) is the energy difference between the top of the valence band and bottom of the conduction band and is characterized by an energy value usually measured in electron volts (eV). The somewhat arbitrary distinction between semiconductors and insulators lies in the value of the bandgap. While there are no established thresholds, semiconductors tend to have smaller bandgaps (0-3.5 eV) compared to insulators (>3.5 eV). Still, pure crystalline semiconductors will not conduct electricity without thermal excitation of some electrons to the conduction band in the case of intrinsic semiconductors, or free electrons or holes provided by a dopant in extrinsic (doped) semiconductors.³⁰

The value and nature of the bandgap are critical components in determining the thermal, electrical, and optical properties of semiconductors and insulators. For example, the energy of the bandgap dictates the longest wavelength (or lowest energy) photon that the material can absorb. However, the nature of the bandgap has a role to play as well. A bandgap can be direct or

indirect in reciprocal or “k-space,” meaning that the valence band and conduction band extrema either have the same momentum or are shifted with respect to one another in the Brillouin zone. When a bandgap is direct, as shown on the left in Figure 2.2, electrons can be excited to the conduction band by absorption of a photon, among other processes, leaving behind a hole (i.e. a positive charge carrier) in the valence band. However, when the bandgap is indirect, absorption of a photon must be aided by absorption or emission of a phonon, a collective vibrational mode of the atoms forming the solid (analogous to the vibrational modes of molecules) to complete the transition.³⁰ Thus, light absorption in indirect bandgap materials is far less efficient and more dependent on temperature than in direct band-gap materials, since there are fewer phonons at low temperature. This consequence of an indirect bandgap has far-reaching consequences where the optical properties of materials are concerned, namely that photon absorption and emission processes are affected.

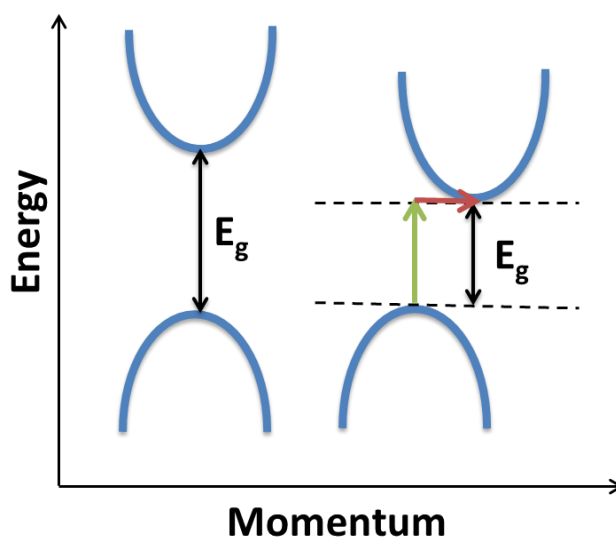


Figure 2.2: Schematic of direct (left) and indirect (right) bandgap structures. Bandgap is denoted as E_g . Curves representing conduction and valence bands are plotted as a function

of k , the wave vector that defines crystal momentum. For indirect band gaps, photon (green) absorption must be assisted by a phonon (red) to excite an electron from the conduction to valence band. Band structure is shown as a function of the wave vector k .

The direct opposite of light absorption is recombination, which encompasses radiative recombination, Shockley-Read-Hall recombination, and Auger recombination, and describes the processes by which electrons excited to the conduction band eventually lose energy and stabilize back to the valence band. We will focus on radiative recombination, wherein a photon is emitted when an electron relaxes from the conduction band to the valence band. Radiative recombination is a highly applicable process, but is only significant in direct bandgap semiconductors due to the low probability of phonon absorption to complete recombination in indirect bandgap semiconductors. Radiative recombination can be stimulated by applied voltage at a p-n junction, which forms the basis of light-emitting diodes. It can also occur in response to an absorbed photon, giving rise to photoluminescence in the form of fluorescence or phosphorescence.²⁹ Photoluminescence by fluorescence is the process by which an electron absorbs a photon of higher energy than the bandgap, thereby exciting an electron to the conduction band. The excited electron then undergoes non-radiative relaxation towards the bottom of the conduction band and eventually recombines with the hole in the conduction band, emitting a photon. The photon emitted has similar energy to the bandgap, and is necessarily lower energy (higher wavelength) than the incident photon. This process is roughly outlined in Figure 2.3. Fluorescence occurs on a short timescale ($<0.1\mu\text{s}$), while phosphorescence occurs on a longer timescale due to a slightly more complicated mechanism. Here we will focus on the fluorescence mechanism of photoluminescence only.

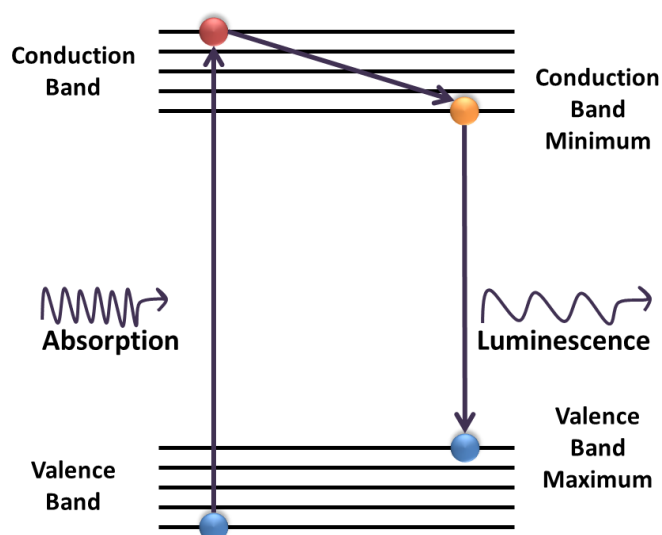


Figure 2.3: Schematic of photoluminescence mechanism. Absorption of a photon with energy larger than the bandgap excites an electron to the conduction band. After non-radiative recombination processes, the excited electron relaxes to the ground state, emitting a photon.

Thus, the presence of a direct band gap is essential for efficient absorption of light and photoluminescence, optical properties that enable solar cells, light emitting diodes, and biomedical applications such as photothermal therapy, wherein absorbed light translates to localized heating of a region to kill malignant cells. It can also be used for simultaneous imaging and light-triggered targeted release: absorbed light prompts the release of a therapeutic and triggers fluorescence that can be translated into an image. For biomedical applications, it is especially important to consider the wavelength of absorbed light to avoid damage to a living system or biomolecules. In particular, there are “biologically transparent” windows in the near-infrared and infrared, prompting studies on materials that absorb and emit in those regions.^{31,32} Materials that absorb efficiently and emit in the visible region are also useful for these purposes, along with the potential to be powerful imaging agents.^{33,34} Thus, in this work, we study direct

bandgap nanomaterials that span the biologically-relevant bandgap energy range, the infrared and visible, as shown in Figure 2.4.

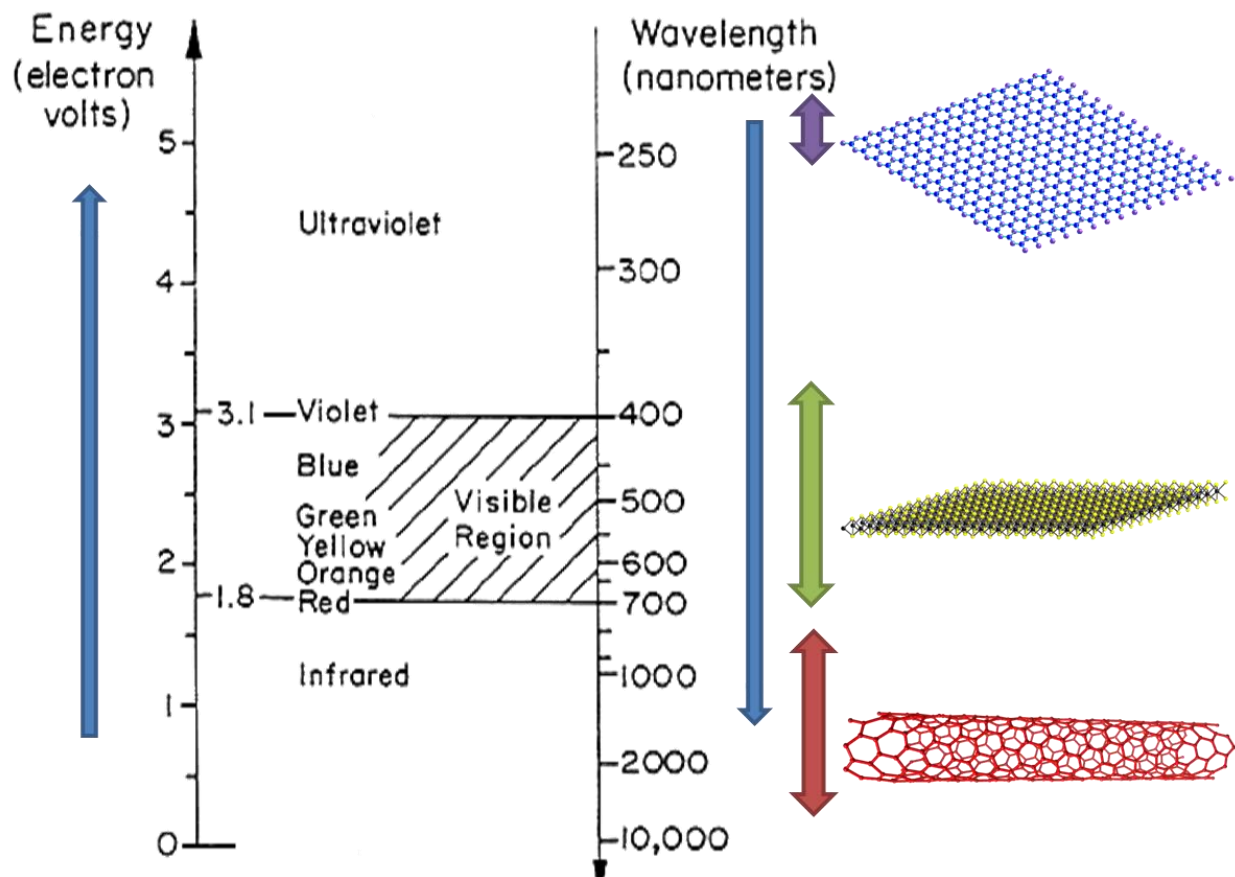


Figure 2.4: The electromagnetic energy spectrum shown in electron volts (left) and wavelength (right). This thesis concerns direct bandgap materials that span a wide range of bandgap energies, including the biologically relevant visible and infrared regions.

2.1.3 Single-Walled Carbon Nanotubes

Carbon nanotubes are a seamless roll of the sp^2 hybridized carbon atoms of graphene. They may be one or more layers thick, which will classify them as single-walled carbon nanotubes (SWCNT) or multi-walled carbon nanotubes (MWCNT). Since their isolation,

graphene and carbon nanotubes have captured the interest of both theorists and experimentalists because of their extraordinary electronic, mechanical, optical, and chemical properties. Among these interesting properties are extremely high charge carrier mobility, inherent strength, and transparent conduction.³⁵⁻⁴⁰ These properties among others have made them an attractive material for use in many technological industries, including medical diagnostics and therapeutics.

Each SWCNT structure has a well-defined diameter on the order of 1-2nm, and can exhibit either semiconducting or metallic behavior depending on its structure.⁴¹ The simplest way to describe the complete structure of the nanotube is through its chiral vector (C_h). The chiral vector is determined based on the integers (n, m) and the basis vectors a_1 and a_2 of the honeycomb lattice of graphene, as shown in Figure 2.5.⁴² The chiral vector is therefore defined as:

$$C_h = na_1 + ma_2$$

It is commonly referred to simply as a pair of indices (n, m) for convenience. These indices uniquely determine the apparent structure of the nanotube; tubes are designated “armchair” if $n=m$ or “zigzag” if $m=0$ based on the appearance of the lattice. They also determine whether the resulting nanotube structure is metallic or semiconducting. If $|m - n| = 3k$, where k is an integer, the nanotube is metallic, while if $|m - n| = 3k \pm 1$, the nanotube is semiconducting.^{43,44} Finally, the diameter of the nanotube is defined as: $d = \frac{a}{\pi} \sqrt{n^2 + nm + m^2}$, where a is the magnitude of the basis vectors a_1 and a_2 and is equal to 0.246nm. As such, SWCNT diameters

fall in the range of 0.67-12 nm. The length of a SWCNT, however, can reach up to several microns, making for an astronomically high aspect ratio.

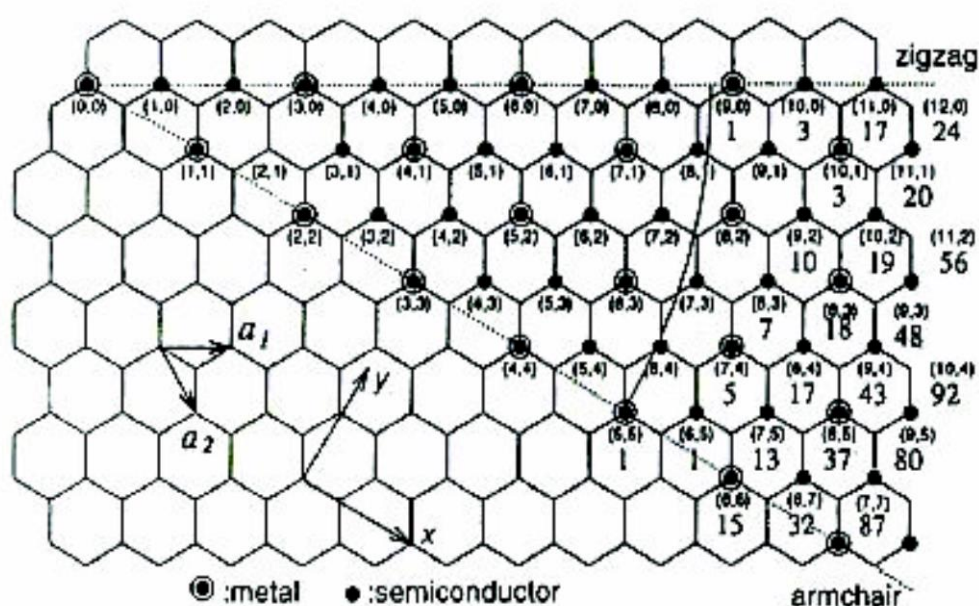


Figure 2.5: Schematic showing the 2D graphene lattice with an overlay of the possible carbon nanotube species. Each possible type of nanotube is denoted by chiral vector indices (n,m) . The number below the chiral vector denotes the number of possible caps of the nanotube, which increases with diameter.⁴³

The structure of the nanotube is also the key to determining its optical properties. It has been shown that for semiconducting nanotubes, the bandgap energy is roughly inversely proportional to the diameter. Thus, SWCNT have bandgaps in the range of 0-1.2eV, which falls in the infrared region.⁴¹ Since individual nanotubes exhibit one-dimensional behavior, their density of states (DOS) is significantly different from conventional three dimensional materials. In particular, instead of a continuous DOS, the DOS of a single SWCNT has “spikes” that arise from their one-dimensional nature.⁴⁵ These irregularities are called Van Hove singularities, the

positions of which are determined by the nanotube structure, and can be slightly altered based on surface functionalization.⁴⁶ The electronic transitions between the Van Hove singularities, such as $|c_1-v_1|$ and $|c_2-v_2|$ (where c and v represent energy levels in the conduction and valence bands, respectively), are otherwise known as E_{11} and E_{22} . The “ E ” is replaced with “ S ” or “ M ” for semiconducting or metallic, respectively, if the conductivity of the SWCNT is of particular concern. A brief schematic of the one-dimensional DOS of an individual SWCNT is shown in Figure 2.6. The Van Hove singularities in the conduction and valence bands give rise to electronic transitions E_{11} and E_{22} . In this figure, the E_{11} absorption creates an electron-hole pair, or exciton, which then non-radiatively relaxes to the c_1 and v_1 state (signified by the dashed arrows). The electron then emits light and falls back down to the v_1 band, reuniting with the hole, thereby giving rise to the photoluminescence in SWCNT. It should be noted that this mechanism is only possible in semiconducting SWCNT, as the hole formed in the valence band would be quickly filled by another electron in metallic SWCNT.

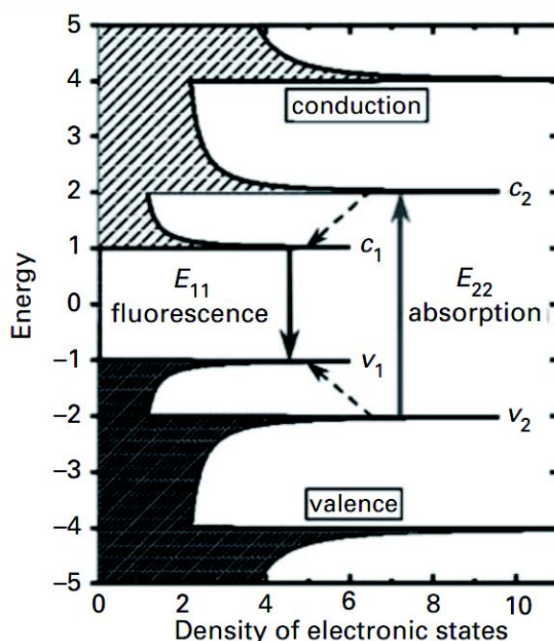


Figure 2.6: Schematic of the 1D density of states (DOS) of an individual nanotube, showing the Van Hove singularities in the conduction and valence bands. Solid arrows denote the electronic transitions involved in photoluminescence spectroscopy, wherein a photon promotes an electron from v_1 to c_1 , whereupon an electron-hole pair (exciton) is formed, which undergoes non-radiative relaxation (dashed arrows), and then ultimately the electron emits light and falls back down to the v_1 band (E_{11} solid arrow).⁴⁵

These electronic transitions can be observed using optical absorption and fluorescence spectroscopy, and used to determine the type and purity of the nanotube.⁴⁷ Optical absorption spectra of SWCNT are marked by sharp peaks that arise from electronic transitions over a broad background, which can be attributed to the π plasmon. The optical absorption peaks are therefore useful in determining the type, purity, and dispersion state of the SWCNT. In addition, since only well-dispersed SWCNT in solution contribute to the optical absorption peak, bundling can be observed in the spectra when the peak broadens or lowers in intensity.⁴⁸⁻⁵⁰ Since some overlap between electronic transitions may occur in absorption spectroscopy, depending on the polydispersity of the sample in question, assignment of chiral indices to peaks is not completely

reliable. However, photoluminescence spectroscopy eliminates any potential for overlap, paving the way for optical absorbance-based structural assignments of SWCNT. By creating a photoluminescence map such as that shown in Figure 2.7, the presence of all SWCNT that do not fall under the categories of $n=m$ or $m=0$ can be quantitatively determined from the peaks.⁵¹⁻⁵³

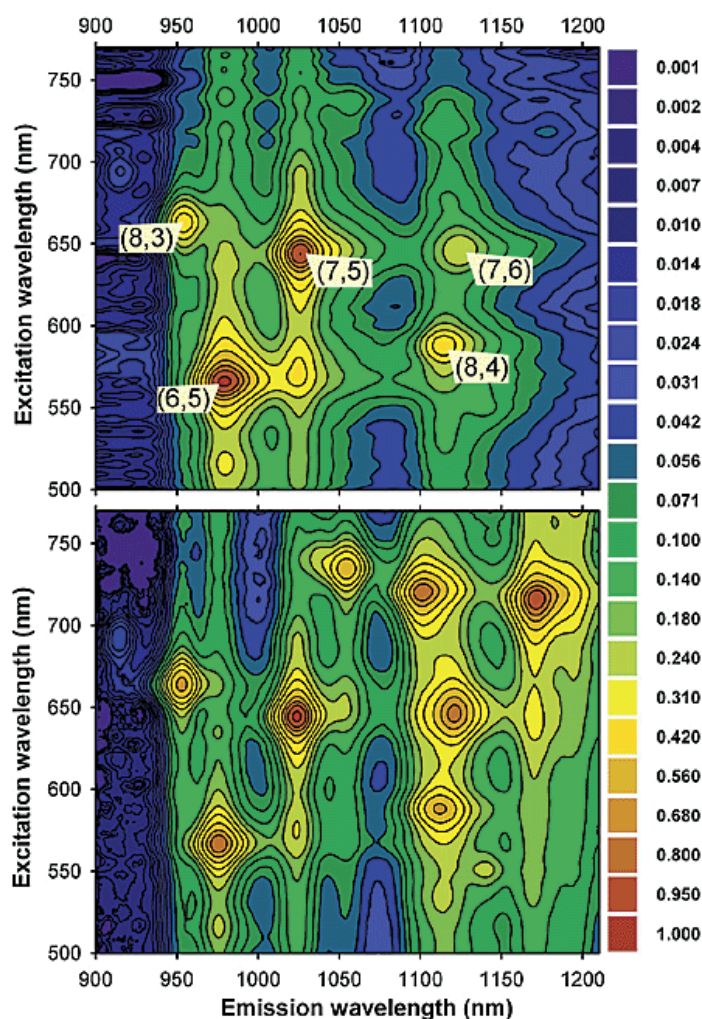


Figure 2.7: Photoluminescence maps showing normalized fluorescence intensity for specifically defined SWCNT species. The top map shows a CoMoCAT SWCNT sample, and the bottom map shows a HiPco SWCNT sample.⁵²

2.1.4 Two-Dimensional Materials Beyond Graphene

Encouraged by the success and widespread applications of graphene family nanomaterials, researchers began to explore all possible 2D structures beyond graphene and its derivatives to find 2D materials that possess non-zero bandgaps. Existing classes of 2D materials such as transition metal dichalcogenides, layered oxides, and layered hydroxides garnered renewed interest. Even more classes of 2D materials were established, such as MXenes and ultra-thin metal structures. These studies have led to a vast library of 2D materials that is briefly summarized in Figure 2.8.⁵⁴

Graphene Family	Graphene	GO/rGO	hBN	BCN	Fluorographene, graphane	Graphdiyne	Germanene, silicene, borophene, BP
2D Chalcogenides	MoS ₂ , WS ₂ , MoSe ₂ , WSe ₂		Semiconducting dichalcogenides: MoTe ₂ , WTe ₂ , ZrS ₂ , ZrSe ₂ , etc.			Metallic dichalcogenides: NbSe ₂ , NbS ₂ , TaS ₂ , TiS ₂ , NiSe ₂ , etc.	
						Layered semiconductors: GaSe, GaTe, InSe, Bi ₂ Se ₃ , etc.	
2D Oxides	Micas, BSCCO	Transition Metal Oxides: TiO ₂ , MoO ₃ , WO ₃			Perovskite-type: LaNb ₂ O ₇ , (Ca,Sr) ₂ Nb ₃ O ₁₀ , Bi ₄ Ti ₃ O ₁₂ , Ca ₂ Ta ₂ TiO ₁₀ , etc.		Hydroxides: Ni(OH) ₂ , Eu(OH) ₂ , etc.
	Layered Cu oxides	MnO ₂ , V ₂ O ₅ , TaO ₃ , RuO ₂ , etc.					Others

Figure 2.8: 2D Materials Family. Materials that are air stable at room temperature are shown in blue; probably air stable are shown in green, unstable in air but may be stable in inert environments is shown in pink. Materials shown in grey have been successfully exfoliated into monolayers, but there is little further information regarding properties and applications. Adapted from Geim, et al Nature 2013.⁵⁴

Besides the graphene family of materials touched upon in Section 2.1.1, 2D chalcogenides and 2D oxides are large classes of 2D materials that present countless opportunities in semiconducting nanoelectronic materials. In this work, we focus on the air-stable 2D transition metal dichalcogenides and hexagonal boron nitride (hBN) for the following reasons. First, these materials provide a range of bandgaps that span the ultraviolet, visible, and

infrared spectrum. They are also very chemically stable, exhibiting no degradation upon contact to water or air. Finally, the bulk forms of these materials are similar to graphene in two ways: they are made up of weakly bonded 2D layers, and are generally hydrophobic. Strong covalent bonds are present in plane, and many layers are held together by van der Waals interactions to form a bulk solid. Because of their hydrophobicity, these materials require encapsulation or the presence of surfactant to remain stable in aqueous solution. These characteristics allow for facile solution processing in the same ways as graphene and CNT. In the coming sections, an overview of these materials and their solution processing techniques will be provided.

2.1.5 Transition Metal Dichalcogenides

Transition metal dichalcogenides (TMDs) are a large group of materials with the generalized formula MX_2 , where M is a transition metal in Groups IV-X, and X is a chalcogen atom (typically S, Se, or Te). Since many TMDs are composed of multilayers bonded by van der Waals forces, they are easily cleaved along the basal planes into 2D structures. Although there have been over 40 reported, TMDs are just a subset of the wider chalcogenide family, including many monochalcogenides and trichalcogenides that can also exist as 2D structures.⁵⁵ The numerous compounds in the chalcogenide family exhibit a diverse range of crystal structures and subsequently material properties, and have been reviewed several times in recent years.⁵⁶⁻⁵⁹ In general, 2D TMDs consist of a single plane of metal atoms between two separate layers of chalcogen atoms in an X-M-X format and adopt one of two possible crystal structures: trigonal prismatic coordination with hexagonal closed packing (2H) or octahedral coordination with trigonal symmetry (1T). Although one phase may be thermodynamically preferred for each TMD, in many cases both are stable but exhibit different physicochemical properties.

Herein, we focus on four of the most stable and consequently most widely studied TMDs: MoS₂, WS₂, MoSe₂, and WSe₂. These materials exhibit bandgaps in the visible to near-infrared region and a host of interesting physicochemical properties that will be outlined below.⁶⁰

Molybdenum Disulfide (MoS₂)

The bulk multilayer form of MoS₂, known as the natural mineral molybdenite, has a long history of use as a solid lubricant that is nearly unparalleled in its lubricity, temperature resistance, and stability. Recently, much focus has landed on 2D MoS₂, which naturally adopts a hexagonal structure with similarities to graphene (Figure 2.9A) though it is comprised of three atomic layers. Both the 2H and 1T phases (Figure 2.9B) are stable in 2D form, though the former is a semiconductor and the latter metallic. One of the most scalable methods of MoS₂ exfoliation, chemical exfoliation by ion intercalation, causes a phase change from 2H to 1T that can be reversed by thermal treatments.⁶¹ In 2D form, MoS₂ is notable for its mechanical strength, stability, and layer-dependent optoelectronic properties.^{62,63} In particular, 2H MoS₂ monolayers are direct band-gap semiconductors with an E_g of 1.2eV that exhibit strong photoluminescence.^{61,64,65} The photoluminescence in bilayers and trilayers is significantly weakened, and the band gap eventually widens and shifts to indirect in bulk form (E_g, bulk=1.9eV). As such, 2D MoS₂ is a promising candidate for optoelectronic applications, such as transistors, photodetectors, photovoltaics, and batteries.⁶⁶⁻⁷¹ MoS₂ heterojunctions with carbon nanotubes, WSe₂, and pentacene have been used to enable unprecedented advances in semiconductor devices such as p-n junction diodes.^{54,72,73} It has also been used as a fluorophore, imaging agent, and photothermal ablation agent in the visible region.^{34,74,75} Moreover, atomic-

scale studies of 2D MoS₂ have allowed chemists to further understand its role in established hydrodesulfurization reaction pathways and water purification treatments.^{76,77}

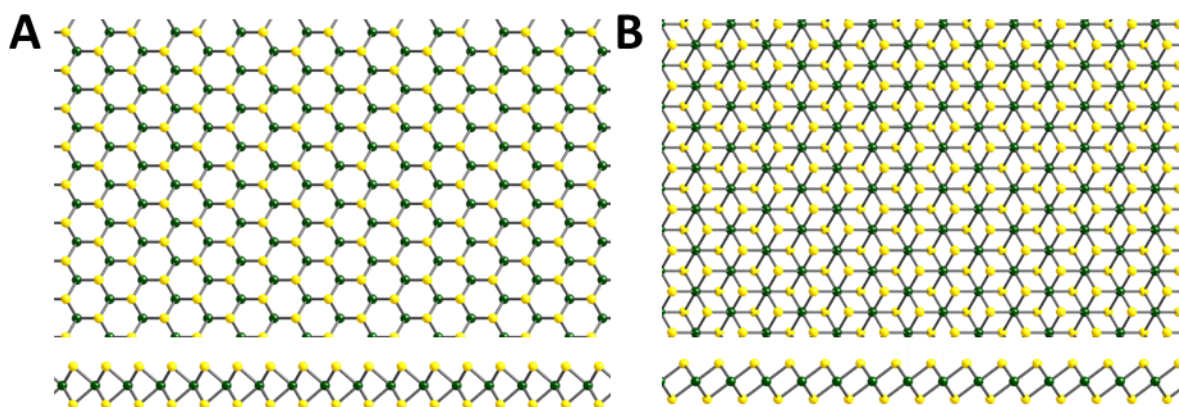


Figure 2.9: Structures of 2D transition metal dichalcogenides (A) 2H crystal structure and (B) 1T crystal structure. Here transition metal atoms are shown in green, chalcogen atoms shown in yellow. Top views and side views (bottom). Drawn with CrystalMaker9.

Tungsten Disulfide (WS₂)

Tungsten disulfide (WS₂) occurs as the natural mineral tungstenite, which has a layered structure and is known for its superlubricity similar to MoS₂. Also like MoS₂, it adopts the 2H structure and is a direct-gap semiconductor in monolayer form that exhibits strong photoluminescence.⁷⁸ Importantly, it exhibits ambipolar behavior and electronic properties that are well suited to photocatalysis.⁷⁹ WS₂ has been shown to be an extremely efficient catalyst for hydrogen evolution reactions with the potential to replace conventional, expensive platinum catalysts.^{80–83} Besides clean energy applications, WS₂ has been used in bone tissue engineering, nanoelectronic devices, water purification, and lithium-ion batteries. It has also been used as a multi-functional theranostic agent for dual-mode CT and photoacoustic imaging-guided photothermal therapy^{77,79,81,84–87}

Tungsten Diselenide (WSe₂)

Tungsten diselenide is a layered semiconductor that shares its hexagonal crystal structure with MoS₂ and WS₂. It is also a direct band-gap semiconductor in monolayer form with E_g or 2.02eV, but distinguishes itself from MoS₂ and WS₂ in its charge carrier properties.⁸⁸ Interestingly, it can be doped to be either n-type or p-type (i.e. have electron or hole charge carriers), while MoS₂ can only be made n-type.⁸⁹ This unique characteristic of WSe₂ is important for optoelectronic applications, where both p- and n-type materials are necessary.⁹⁰ In fact, the first high hole mobility monolayer field-effect transistors were constructed with 2D WSe₂.⁹¹ Furthermore, the p- and n-type behavior can be dynamically tuned by electrostatic means, giving rise to monolayer p-n junctions that could enable next-generation flexible photovoltaics and light-emitting diodes.^{92–95} WSe₂ is also useful in heterostructure archetypes, such as MoS₂-WSe₂ alloys and WSe₂ gold-plasmonic hybrid structures that exhibit greatly enhanced photoluminescence.^{96,97}

Molybdenum Diselenide (MoSe₂)

Molybdenum diselenide (MoSe₂), like WSe₂, is known for its electrically tunable ambipolar behavior in mono and few layer form that is highly applicable to optoelectronic applications.⁹⁸ Remarkably, unlike other 2D TMDs, 2H-MoSe₂ (the most abundant phase) undergoes metallization at high pressure without undergoing a structural change.⁹⁹ It has also been applied to laser technologies, used as a catalyst for the hydrogen evolution reaction, and shown remarkable electrochemical biosensing of mycotoxins, a potent toxin commonly found in many agricultural products.^{100–103}

2.1.6 Hexagonal Boron Nitride (hBN)

The most stable crystalline form of boron nitride, hexagonal boron nitride (hBN), is analogous to graphene and thus for the purposes of this review considered a GFN. Bulk hBN has a long history of use in industry as a thermal management material and lubricant in cosmetics, steels, paints, and sealants, among others.¹⁰⁴ Each layer is composed of alternating B and N atoms in a honeycomb lattice (Figure 2.10), possessing a lattice constant of ≈ 0.25 nm and a bandgap of 5.9 eV, and is arguably the most studied 2D material after graphene.¹⁰⁵ hBN is a white solid that is sometimes known as “white graphene,” though it is electrically insulating. However, hBN possesses excellent thermal conductivity, mechanical properties, lubrication properties, proton mobility, and chemical stability.^{106–110} hBN is also a natural hyperbolic material, in which the dielectric constants are the same in the basal plane but have opposite signs in the normal plane.^{111–114} This makes h-BN a promising substrate material for graphene-based nanoelectronics.¹¹⁵ In addition, many fascinating properties were predicted theoretically for such in-plane heterostructures, such as minimum thermal conductance and robust half-metallic behavior.^{116–119}

Besides graphene nanoelectronics, 2D hBN is suited to several applications. It has been used as a lubricant, a strengthening material in composites, and thermal management material for high-temperature applications.^{107,120–123} It may also prove useful for hydrogen technologies such as fuel cells and water electrolysis due to its excellent proton transport rates.¹¹⁰

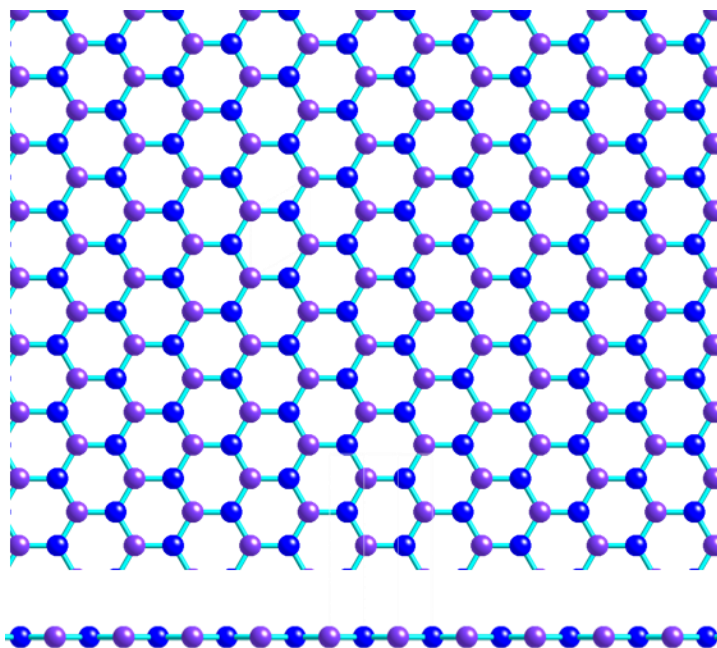


Figure 2.10: Structure of hexagonal boron nitride top and side views. Boron (blue) is bonded to nitrogen (purple) in a hexagonal lattice analogous to graphene. As seen in the side view, it is atomically flat. Drawn with CrystalMaker9.

2.2 Solution Processing of Nanoelectronic Materials

2.2.1 Overview of Synthesis Techniques

The most widespread synthesis methods of SWCNT are growth processes that produce highly polydisperse populations, i.e. the final SWCNT product contains tubes with a wide variety of chiralities and diameters. The majority of commercially available SWCNT are synthesized using the following methods: laser ablation, arc discharge, or, most commonly, high-pressure carbon monoxide disproportionation (HiPco) and chemical vapor deposition (CVD).¹²⁴ HiPco relies on the pyrolysis of metal carbonyls in the presence of other hydrocarbons, optimized for high yield of SWCNT in a high pressure carbon monoxide environment. CVD processes are ultimately dependent on the catalyst that encourages the decomposition of and subsequent

formation of SWCNT from a carbon-containing gas, typically methane. The most commonly used CVD process is CoMoCAT, in which solid supported catalysts of cobalt and molybdenum nanoparticles are used to separate hydrogen from carbon and seed the growth of SWCNT.¹²⁵ As such, it should be noted that these processes inevitably contain some residual metal catalysts and non-SWCNT carbonaceous material impurities in their final forms. These processes result in powdered SWCNT, which require exfoliation and purification for solution-phase handling of SWCNT.

On the other hand, many 2D materials can be produced by both bottom-up and top-down methods, due to the natural occurrence of their bulk forms. Graphene was first isolated by the micromechanical cleavage of graphite, or “scotch-tape” method, which has been extended to many 2D TMDs.^{7,126} This method of isolating 2D materials is known for producing high-quality materials at very low yield. However, more recent methods have improved yield and scalability. Bottom-up production methods include epitaxial growth on silicon carbide (SiC), chemical vapor deposition (CVD), and molecular assembly, among others, which yield high-quality graphene but at a high price.^{90,127–129} These bottom-up production methods require a substrate to produce 2D materials in the solid state and therefore will generally serve electronics applications, such as the production of transistors, conductive layers, and other nanoelectronics. Despite the drawbacks, CVD has resulted in a realistic route for the commercialization of graphene, with reported 30-inch graphene films grown on flexible copper substrates in a roll-to-roll process.¹³⁰ Liquid-phase exfoliation, on the other hand, is suitable for many more of the applications mentioned previously but produces 2D materials of lower size and quality.^{131–133} However, liquid-phase exfoliation is inexpensive and highly scalable, and therefore represents another

realistic route for the commercialization and mass-production of 2D materials. In addition, 2D TMDs can be isolated from their bulk forms by laser ablation, electrochemical cleavage, and ion intercalation.^{64,80,134–141} These synthesis and isolation processes are summarized as a function of quality and price of final material in Figure 2.11.¹⁴² In this work we focus on liquid exfoliation for its superb scalability, facile processing techniques, and compatibility with aqueous systems.

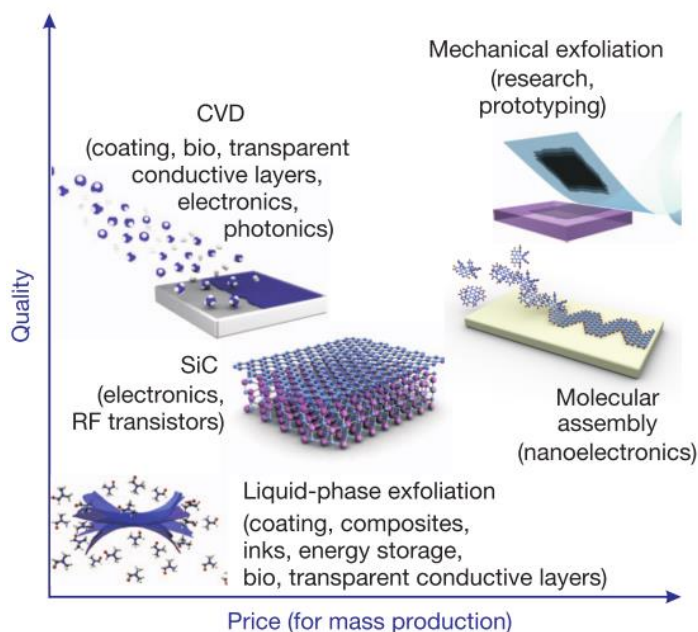


Figure 2.11: The production methods of graphene, which cover a wide range of quality, size, and price. These trends hold true for the production of 2D materials beyond graphene (TMDs, hBN).¹⁴²

2.2.2 Chemical Exfoliation

Chemical exfoliation of nanomaterials encompasses any process that changes the chemical structure during the exfoliation process or exfoliates by ion intercalation. For SWCNT, a common chemical exfoliation procedure is the addition of oxygen-containing functional groups to the surface, such as carboxylic acid.^{143–145} This procedure requires exposure to harsh

conditions, such as incubation with concentrated nitric or sulfuric acid followed by ultrasonication. These carboxyl groups are more reactive than pristine SWCNT and therefore bring the possibility of further covalent functionalization with many different moieties. For example, the carboxyl groups can be further modified to amino groups by exposure to ethylenediamine.¹⁴⁶ In the cases described above, polar oxygen or nitrogen groups provide pH-dependent negative surface charge and colloidal stability in aqueous solutions. Since SWCNT are relatively inert, oxidation is one of only three chemical reactions reported that use the surface chemistry of SWCNT for covalent functionalization.¹⁴⁷

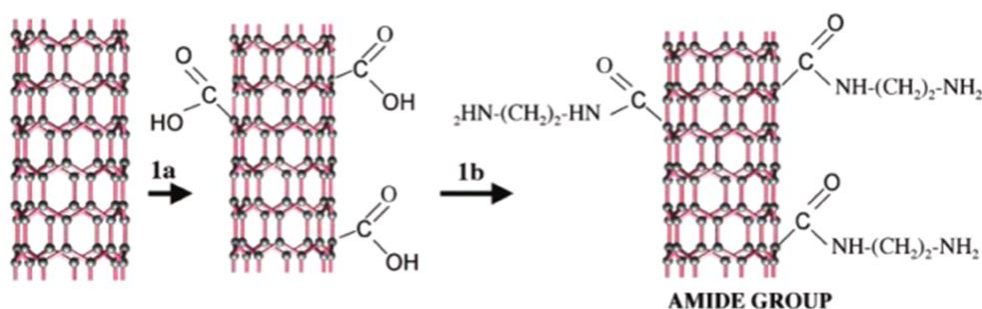


Figure 2.12: An example of chemical exfoliation of SWCNT. SWCNT are commonly modified with carboxyl groups using acid treatments (1a). These carboxyl groups can be further modified in a variety of ways. Shown here, an amino group is attached by virtue of ethylenediamine functionalization (1b).¹⁴⁶

The first and still widely used method of chemical exfoliation in 2D nanomaterials is the Hummers' method to oxidize graphite into graphite oxide, as mentioned in Section 2.1.^{4,148} It is generally accepted that this method introduces oxygen-containing functional groups to the surface of graphite: hydroxyl (-OH) and epoxy (-O-) functional groups decorate the basal plane while the edges become rich with carboxylate (-COOH) groups. The addition of these functional groups disrupts the π - π stacking between the sheets of graphite and allows for easy exfoliation of

the graphite oxide into graphene oxide (GO). Furthermore, the presence of these groups can be tuned by oxidation/reduction processes.^{149–151} Like oxidized SWCNT, GO does not require a surfactant to remain stable in aqueous solutions.¹⁵² It can also be converted back to graphene-like materials through reduction processes, including exposure to hydrazine and its derivatives, Vitamin C, highly alkaline environments, and solvothermal methods.^{10,153–156} However, the distinction between this reduced graphene oxide (rGO) and pristine graphene is necessitated by the few remaining oxygen-containing functional groups and structural defects, as well as the fact that some properties are never fully recovered.¹⁵⁷

For 2D materials beyond graphene, ion intercalation is an alternative chemical exfoliation method that is widely used. In this method, a small metal cation (e.g. Li^+ , Na^+ , K^+) intercalates between layers and drives the exfoliation by interfering with van der Waals interactions. This process is shown in Figure 2.13.¹³⁷ Pre-treatment with hydrazine results in larger flake size 2D materials.¹⁵⁸ Chemical exfoliation of TMDs can also be achieved by electrochemical methods, using an electrochemical bias to introduce ionic intercalants into bulk layered materials.^{135,159}

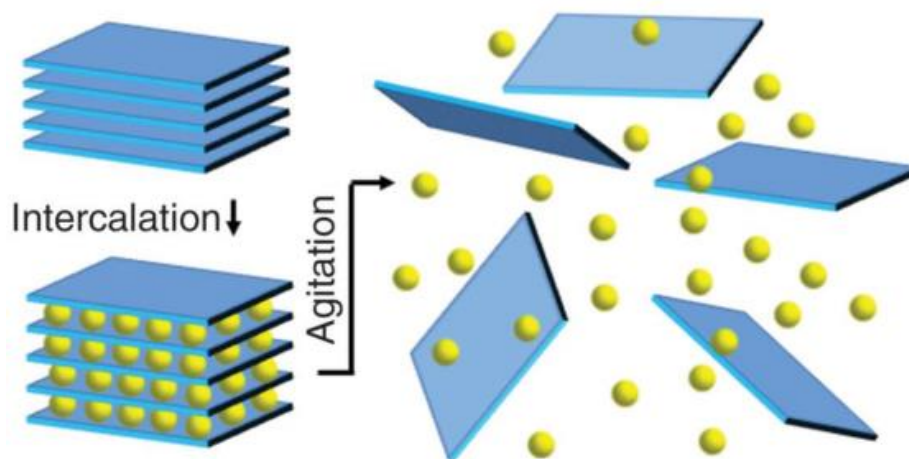


Figure 2.13: Ions, shown as yellow spheres, are intercalated between layers in bulk materials. Upon agitation, usually in the form of shear, sonication, or thermal forces, the layers exfoliate in solution.¹³⁷

The main drawback of chemical exfoliation is that it tends to change the physicochemical properties of the nanomaterial. For instance, carboxylation of SWCNT affects the NIR-absorption and photoluminescence properties. Ion intercalation of TMDs introduces defects and triggers a transformation from the semiconducting 2H to metallic 1T polytype.⁵⁵ This change in crystal structure can be partially reversed by thermal treatment, though complete reversal has not yet been demonstrated.^{160,161}

2.2.3 Organic Solvent Exfoliation

Organic solvent exfoliation offers another surfactant-free process of exfoliation due to the hydrophobic nature of SWCNT and TMDs.¹⁶² Using non-polar solvents allows for the interlayer van der Waals bonding to be disturbed by the energy provided by ultrasonication alone. However, the choices of solvent and sonication method greatly affect the dispersion quality, flake size, and yield. These trends can be explained by matching solvent and solute solubility

parameters such as solvent boiling point, surface tension, and Hansen parameters.¹⁶³ Figure 2.14 shows optical characterization of MoS₂, WS₂ and hBN exfoliated in a wide range of organic solvents. The more promising solvents were n-methyl-2-pyrrolidone (NMP) for MoS₂ and WS₂ and isopropyl alcohol (IPA) for hBN. Photographs of the dispersions, their optical absorption spectra, and Lambert-Beer plots are shown in Figure 2.14E-F.¹⁶² Although graphene, SWCNT, and other 2D materials can also be exfoliated in a wide range of organic solvents, organic solvent exfoliation produces a low yield of finely dispersed nanomaterials compared to aqueous solution processing.^{131,164–168} Furthermore, organic solvents are often incompatible with biomedical applications and some post-synthetic separation methods, such as density gradient ultracentrifugation (DGU).

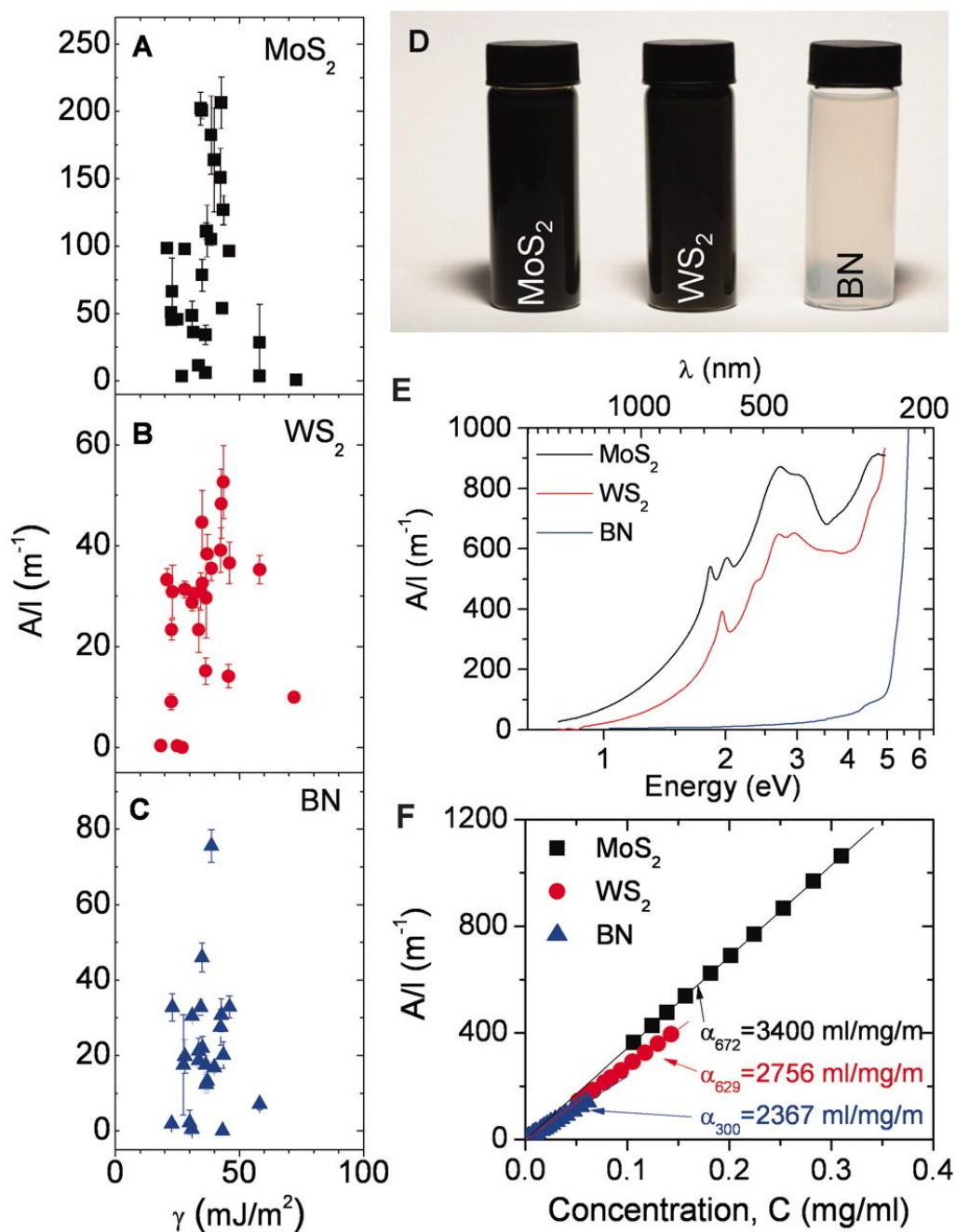


Figure 2.14: MoS₂, WS₂, and hBN were dispersed in a wide range of organic solvents. Their optical absorption (A/I) is plotted as a function of solvent surface tension γ in (A)-(C). Photos, individual optical absorption spectra, and Lambert-Beer plots are shown in (D)-(F). In (D)-(F), MoS₂ and WS₂ are dispersed in NMP, while hBN is dispersed in IPA.¹⁶²

2.2.4 Aqueous Solution Processing

In the absence of chemical exfoliation, the nanomaterials addressed here require amphiphilic additives to remain finely dispersed in water. The hydrophobic regions of the amphiphiles adsorb to the surface of the nanomaterial, while the hydrophilic regions extend into solution, thus providing steric hindrance or electrostatic repulsion to prevent re-aggregation. The nanomaterials under consideration here can be dispersed by a wide range of ionic surfactants, including sodium dodecyl sulfate (SDS) and sodium cholate, and non-ionic surfactants, such as Pluronics/Tetronics, Tween20, and more.¹⁶⁹ They can also be effectively dispersed by many biomolecules, such as DNA, bovine serum albumin (BSA), polysaccharides, lignin, nanofibrillate cellulose, and others, all of which provide the opportunities for biomedical interactions and applications.^{62,170–173} The dispersion efficiency, yield, and quality are highly dependent on the type of surfactant and its interaction with the nanomaterial surface. Processing parameters, namely ultrasonication power and duration, and centrifugation speed and duration, also greatly affect the dispersion outcomes.

In this work we focus on non-ionic surfactants, Pluronics and Tetronics in particular, for their biocompatibility and efficacy in dispersing nanomaterials. Pluronics and Tetronics consist of one central hydrophobic polypropylene oxide block and two or four hydrophilic polyethylene oxide chains, as shown in Figure 2.15. There are many types of Pluronics and Tetronics, owing to the different PPO and PEO chain lengths. Pluronics have been shown to effectively disperse graphene and carbon nanotubes.^{46,133,174}

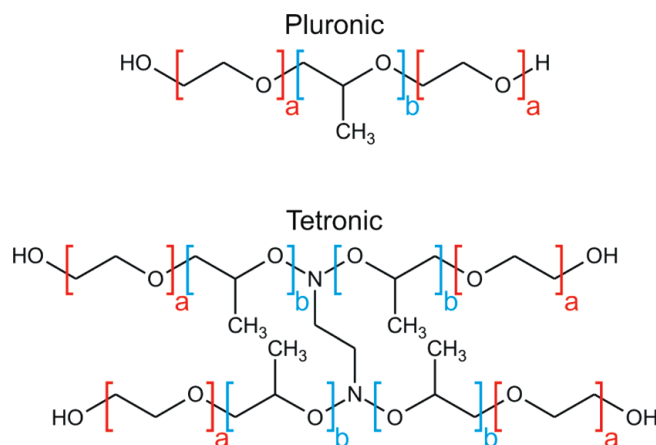


Figure 2.15: Structure schematic of Pluronic (top) and Tetronic (bottom) biocompatible block copolymers.¹⁷⁴

For 2D nanomaterials, drawbacks of aqueous surfactant-assisted exfoliation by ultrasonication include relatively small lateral flake size, polydispersity in size, and poor scalability. However, shear mixing and ball milling have provided alternatives. These techniques are significantly more scalable than ultrasonication, with working volumes on the order of liters to hundreds of liters. Shear mixing is carried out by introducing high shear forces instead of ultrasonication, followed by centrifugation to remove unexfoliated material. It was shown to be an effective method to disperse graphene, MoS₂, WS₂ and hBN in NMP and in aqueous solution containing sodium cholate by Paton, *et al.* and Varrla, *et al.*^{131,141} Ball milling, on the other hand, is a process by which dry powders or liquid mixtures are ground and blended together by blending media such as steel or ceramic balls. The exfoliation of 2D nanomaterials takes place as a result of shear forces and mechanical collisions. Ball milling has been used as a pre-treatment to ultrasonication as well as a stand-alone exfoliation method for hBN, graphene, and MoS₂.¹⁷⁵⁻

2.2.5 Solution-Based Sorting Methods

Density Gradient Ultracentrifugation (DGU) was originally pioneered to, and is still commonly used to, non-destructively separate bio-macromolecules by density. Its first application to the polydispersity problem in SWCNT represented a major breakthrough in nanomaterial science.^{179,180} Using DGU, SWCNT were first separated by diameter and electronic type.¹⁸¹ Since then, the method has been expanded to isolate single chiralities, narrow length distributions, and enantiomers of SWCNT, and sort double-walled carbon nanotubes (DWCNT) by the electronic type of the outer nanotube.^{182–186} It should also be noted that DGU has been successfully used to sort nanotubes dispersed in DNA, ionic surfactants, and non-ionic biocompatible block copolymers (Pluronic).^{180,181,183,187}

In fact, these surfactants make separation by DGU of SWCNT possible. In DGU, small differences in buoyant density caused by physical structure and interaction with a surfactant allow for the separation of different species of carbon nanotubes after sedimentation to their respective isopycnic points in an aqueous density gradient. As an example, Figure 2.16 shows centrifuge tubes following DGU-assisted diameter sorting and DGU-assisted electronic type sorting of SWCNT and their respective optical absorption spectra, indicating successful sorting.¹⁸⁸ This technique of isopycnic DGU has also been extended to 2D materials, namely graphene, MoS₂, hBN, and rhenium disulfide, where DGU was used to successfully sort these materials by thickness.^{189–192} In addition, sedimentation-based DGU, where nanosheets are separated by sedimentation rate, has proven useful to isolate single- and few-layer black phosphorus.^{193,194}

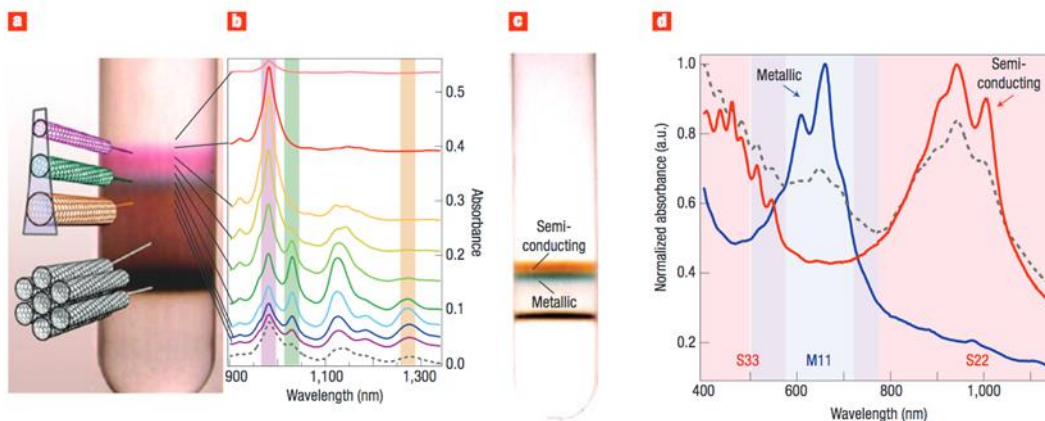


Figure 2.16: (a) Centrifuge tube of small diameter-sorted SWCNT dispersed in SC. The smaller diameter tubes settle at higher points, allowing for fractionation by diameter. (b) Optical absorption spectra of the corresponding bands in (a). (c) Shows centrifuge tube of large-diameter sorted SWCNT dispersed in SC and sodium dodecyl sulfate (SDS). (d) Optical absorption spectra of the semiconducting and metallic bands shown in (c).¹⁸⁸

2.3 Toxicity and Human Health Hazard of Nanomaterials

2.3.1 Toxicity of Single-Walled Carbon Nanotubes

While SWCNT have great potential for future commercialized applications in many arenas, including electronics, composites, and biotechnology, their toxicity must be thoroughly addressed before such advancements can take full form. Carbon nanomaterials are hydrophobic by nature, and thus have a strong tendency to aggregate in air or aqueous solution.^{188,195} This makes the issue of toxicity complicated, as many different parameters of SWCNT must be considered, including covalent functionalization, non-covalent functionalization, dispersion state, size, etc. Shortly after the isolation of SWCNT, many researchers found that intratracheally administered SWCNT elicited fibrosis and respiratory distress in animals.¹⁹⁶ These results raised suspicion that SWCNT were emulating toxic asbestos, because they share a similar aspect ratio, and reduced SWCNT length resulted in reduced toxicity, furthering the comparison.^{197,198}

Toxicological studies have focused on polydisperse SWCNT formulations, which exhibit pulmonary hazard potential based on material attributes such as the method of production, metal and carbon impurities, tube length, reactive carbon surfaces, surface defects and functionalities.^{188,196,199–215} Experimental studies on SWCNTs in rodents have also shown that bolus installation as well as aerosolized inhalation exposures can induce acute lung injury as well as subchronic granulomatous inflammation and fibrosis in the lung.^{196,200–212,214–217} This includes a demonstration that crude, as-purchased (AP) and purified (*e.g.*, eliminating metal contamination) SWCNTs can trigger pro-fibrogenic effects in the lung, regardless of the synthesis method.^{208,210}

However, nanoscale-dispersed SWCNT and graphene elicit a minimal toxic response.^{205,207,218} The key to these nanoscale dispersions is the choice of surfactant. In these studies, biocompatible block copolymers, known commercially as Pluronics and Tetronics, were used to disperse SWCNT and graphene.¹³³ Figure 2.17 shows that SWCNT dispersed in Pluronic F108 does not induce inflammation in the lungs of mice or elicit mitochondrial reactive oxygen species (ROS) *in vivo*. Additionally, cell death was not increased in alveolar epithelial cells when compared to untreated cells, while cells treated with asbestos or particulate matter less than 2.5 μ m in diameter (PM_{2.5}) showed clear signs of distress.²⁰⁵ This study and others have found that SWCNT are taken up and cleared by tissue macrophages. These results have been confirmed, although there are conflicting reports on SWCNT biodistribution and clearance mechanisms.²¹⁹ C¹³ labeled SWCNT in an aqueous solution of 1% w/v Tween 20 were found to distribute throughout the entire body, with major accumulation in the liver, lungs, and spleen, with relatively long circulation times on the order of a day.²²⁰ Other reports found that SWCNT

were circulated *in vivo* for up to five months, excreted through the kidney when shortened past a certain threshold, and do not translocate into organism body compartments in large quantities.^{221,222} On the other hand, when functionalized with certain lengths of polyethylene glycol (PEG), SWCNT are circulated in the blood for about a day, minimally retained in the liver and kidney, and cleared from the main organs in approximately two months by the fecal and renal pathways.^{223,224} When functionalized with a chelating molecule and dispersed in aqueous solution with Tween 20, SWCNT are rapidly cleared from systemic blood circulation through the kidneys with an approximate half-life of three hours.²²⁵ These widely varying reports suggest that surface functionalization, dispersion, size, and administration route are all important aspects to consider in SWCNT toxicity, and that further studies are needed to determine the mechanisms of SWCNT toxicity.^{221,223–226}

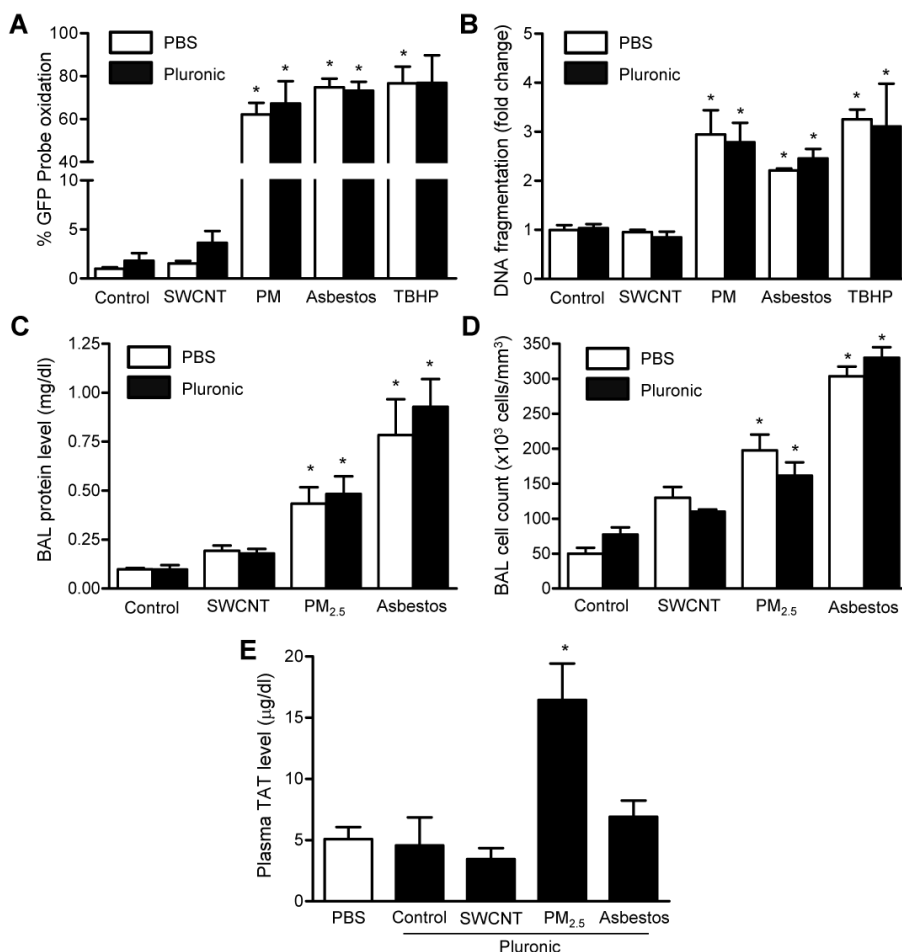


Figure 2.17: Nanoscale dispersions of SWCNT do not elicit a toxic response, as compared to untreated cells, particulate matter less than 2.5 μm in diameter (PM_{2.5}), and asbestos dispersed in PBS (white) or Pluronic F108 (black). A) Mitochondrial ROS was measured in A549 cells (alveolar epithelial cells) that stably express an oxidant sensitive GFP probe that is localized to the mitochondrial matrix. After 24 hours cell death was assayed using an ELISA that detects fragmented DNA (B), bronchiolar lavage (BAL) fluid protein level was measured (C) along with BAL fluid cell count (D) and plasma thrombin-antithrombin complex (E).²⁰⁵

2.3.2 Toxicity of Transition Metal Dichalcogenides and Hexagonal Boron Nitride

Since hBN and many TMDs are used in their bulk form for lubrication products in the market place, most toxicity reports to date focus on bulk forms of these materials. hBN and the TMDs discussed here demonstrated good *in vivo* biocompatibility by the U.S. Public Health

Service.²²⁷ No fatalities or adverse health effects were observed in rats and guinea pigs following inhalation exposure to the bulk materials.²²⁷ The low toxicity of these materials is attributed to low chemical reactivity and low solubility in body fluids. The available data on the toxicity of 2D materials beyond graphene is comparatively limited, though the literature is constantly growing.²²⁸

In one of the most comprehensive toxicity studies of 2D TMDs to date, Teo *et al.* investigated the toxicity of three TMDs that were chemically exfoliated by n-butyllithium ion intercalation. The TMDs investigated—MoS₂, WS₂, and WSe₂—were exposed to human lung epithelial cells (A549) in a dose-dependent manner for 24 hours. They were then compared to control cultures that were not exposed to TMDs and assessed for viability using MTS and WST-8 assays. All three materials showed low cytotoxicity up to 100µg/mL. In higher doses than 100µg/mL, WSe₂ began to affect viability while MoS₂ and WS₂ did not (Figure 2.18). Another study of chemically exfoliated MoS₂ nanosheets found that the specific lithium intercalating agent had an effect on *in vitro* cytotoxicity, namely that tert-butyllithium and n-butyllithium exfoliated MoS₂ were more toxic than methylithium intercalated MoS₂.²²⁹ Lastly, Narayan *et al.* conducted a study on organic-solvent exfoliated MoS₂. MoS₂ was exfoliated in DMF, then filtered, rinsed, and redispersed in DI. Exfoliated MoS₂ were not toxic to rat pheochromocytoma cells (PC12) and rat adrenal medulla endothelial cells (RAMEC) based on sulforhodamine B (SRB) cytotoxic assays and electrical impedance spectroscopy.²³⁰ In fact, these encouraging results have led researchers to use WS₂ and MoS₂ as combined photothermal and therapeutic agents for the treatment of cancer.^{231,232}

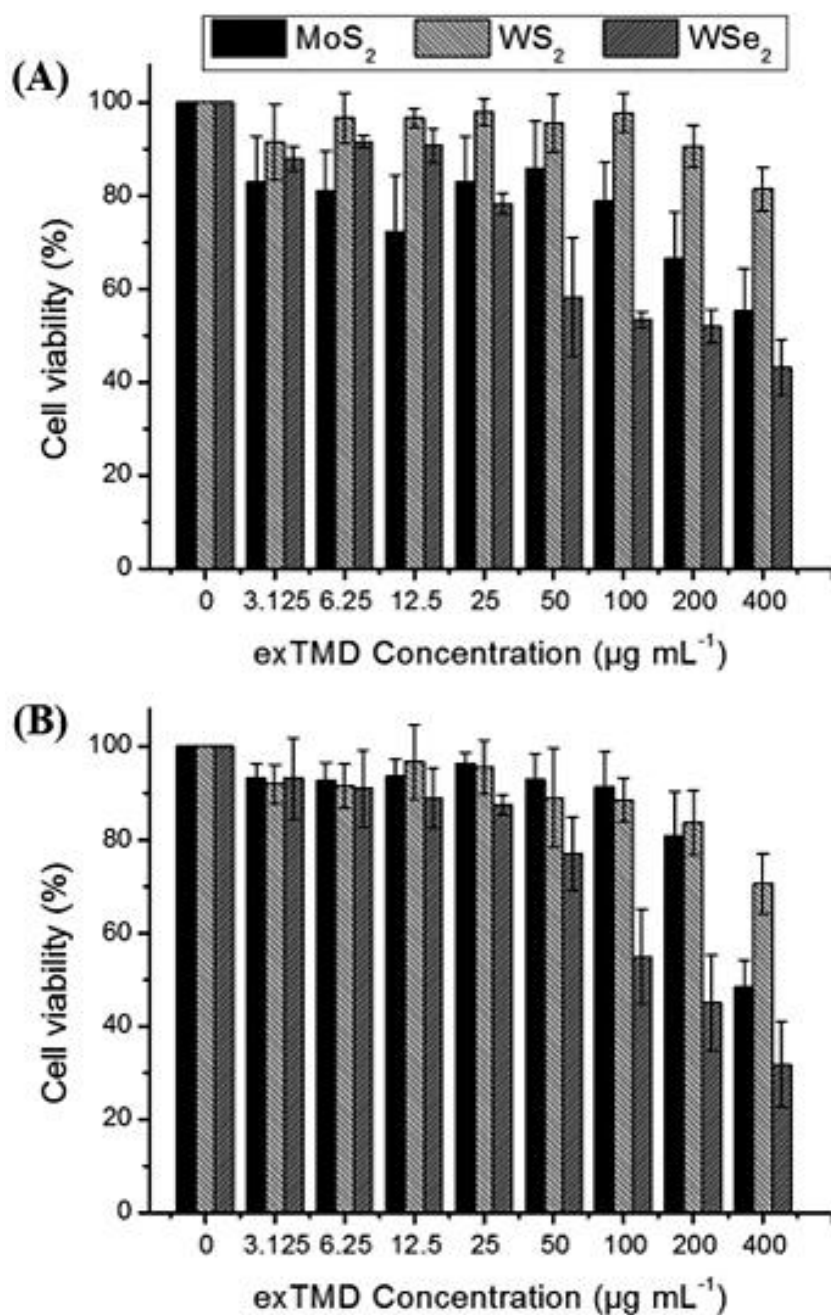


Figure 2.18: Percentage cell viability of human lung epithelial cells (A549) as measured with (A) MTS assay and (B) WST-8 assay following 24 hours of exposure to varying amounts of exfoliated TMDs. The percentages are normalized to control cells that were not exposed to TMDs.²³³

Similar to TMDs, hBN nanomaterials show considerably benign cytotoxic effects compared to carbon nanomaterials. However, this is based on literature concerning boron nitride nanotubes, not 2D hBN, as 2D hBN has not yet been investigated for cytotoxicity. As shown in Figure 2.19, boron nitride nanotubes (BNNT) are not toxic to human embryonic kidney cells (HEK293) as measured by Annexin V-FITC/propidium iodide assay, in stark comparison to multi-walled carbon nanotubes.²³⁴ Though this study halted hBN exposure at 3 days, others have shown low levels of toxicity and high rates of proliferation in cells exposed to BNNT for up to 9 days.^{235–237}

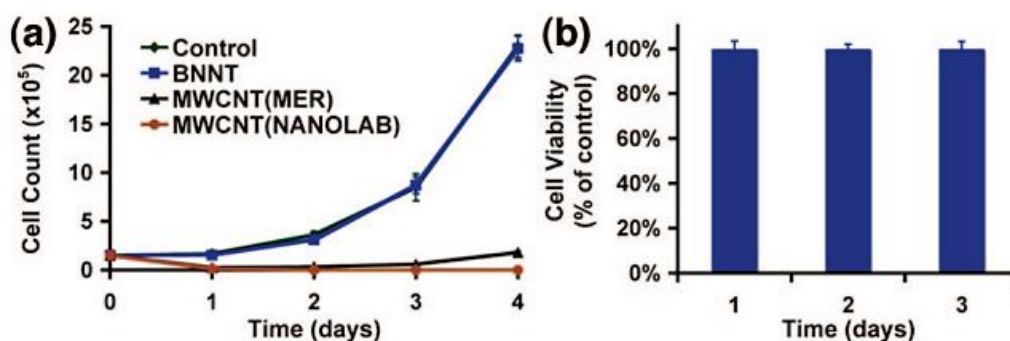


Figure 2.19: Boron nitride nanotubes (BNNT) are not cytotoxic. (a) BNNT do not inhibit cell proliferation and (b) have no effect on viability in HEK293 cells.²³⁴

2.4 Environmental Fate of Nanomaterials

In addition to human exposure, it is highly likely that some portion of engineered nanomaterials that reach a landfill will make their way into the surrounding environment.²³⁸ A broad and detailed insight of the environmental implications of nanomaterials will require knowledge of their release and transport through environmental media, partitioning, chemical and physical transformations, bioaccumulation, and effects on environmental organisms and ecosystems.^{229,239–244} This can be accomplished with detailed research on the environmental

chemistry of bulk materials and of particulate materials to predict the behavior of their 2D and 1D counterparts.^{238,245–252} In the following sections, we touch on what is known about the environmental implications of the semiconducting nanoelectronic materials under consideration in this work.

2.4.1 Environmental Fate and Transport of Carbon Nanotubes

Once CNT are released into the environment, their impact on the environment and ecosystem can be predicted by their mobility, colloidal stability, and degradation pathways. Transport studies in packed-bed columns indicate that the transport of CNT through aqueous systems is highly dependent on the surface functionalization and aggregation state of the CNT as well as the attributes of the porous media being studied.^{253,254} Notably, however, it has been reported that dodecylbenzene sulfonic acid, sodium salt (SDBS) stabilized SWCNT were quite mobile in porous media systems, suggesting that hydrophilic encapsulation escalates aqueous transport.²⁵⁵

Carbon nanomaterials pose the risk of transformation and degradation into other materials, such as carcinogenic polycyclic aromatic hydrocarbons (PAH) or comparatively benign carbon dioxide (CO₂). This risk particularly increases during their transportation and transformation.²⁵⁶ Though the oxidation of CNT requires harsh conditions and is therefore unlikely in the natural environment, photooxidation is possible. Photooxidation is particularly notable in carboxylated SWCNT, where SWCNT can produce reactive oxygen species (ROS) that further modify their surfaces. However, CNT are also readily degraded by naturally occurring enzymes and organelles, thereby diminishing their environmental risk when such enzymes are present.²⁵⁷ SWCNT were degraded and further oxidized by two enzymes,

horseradish peroxidase and neutrophil myeloperoxidase, and one type of organelle that forms when a phagosome fuses with a lysosome.^{258–261}

2.4.2 Environmental Fate and Transport of Transition Metal Dichalcogenides

There is limited data on the environmental fate and transport on the wider TMD family. Most studies to date focus on nanoscale or bulk MoS₂. In terms of dissolution processes, 2D MoS₂ will dissolve based on its participation in oxidative and reductive pathways. The products of these dissolution pathways are generally non-biopersistent and do not elicit pathogenic responses in the lung or pleura.²⁶² Similarly, recent work on few-layer MoS₂ shows dissolution over time due to the usage of environmental and biological simulant fluids.²²⁸ These soluble products are formed due to the photo-induced corrosion process, where the edge sites and defect sites are the primary degradation targets.⁶³

In addition, TMDs can undergo “bacterial leaching”, where biooxidation to soluble metal and sulfur species (e.g. sulfate) by bacterial specialists such as *Thiobacillus ferrooxidans*, *Leptospirillum ferrooxidans* and *Thiobacillus thiooxidans* occurs in the natural environment.²⁶³ Leaching can be direct, wherein physical contact between bacteria and a mineral surface is required, or indirect, which is facilitated by ferric ion generated by bacteria. Though nanoscale studies of bacterial leaching have not been conducted, the leaching products of bulk MoS₂ oxidation are mainly sulfuric acid and molybdic acid (H₂MoO₄).²⁶⁴ Smaller particle size MoS₂ samples undergo faster oxidation leaching.²⁶⁴ The indirect biooxidation of molybdenite can occur through a mechanism where thiosulfate is first produced and then oxidized by ferric iron in a series of reactions, generating tetrathionate (S₄O₆²⁻), disulfane-monosulfonic acid (HSSSO₃⁻) and

finally sulfate (SO_4^{2-}).²⁶⁵ Environmental stability and biooxidation of WS_2 is also similar to MoS_2 .²⁶⁶

Though not much is known about the ecotoxicity of bulk or 2D TMDs, we can look to the relevant literature concerning ecotoxicity of other engineered 2D nanomaterials. In 2014, Conway *et al.* reported that phytoplankton absorbed engineered nanomaterials (CeO_2) in less than 1 hour and had negative impacts on marine mussels in seawater environments.²⁶⁷ It has also been reported in the past that elevated levels of molybdenum (Mo) can result in a physiological copper (Cu) deficiency, which may have negative consequences.²⁶⁸ All this suggests that without careful application of these nanomaterials, they could eventually accumulate in the environment and have long-lasting effects on the aquatic life. However, no comprehensive risk assessment work has been conducted for nanoscale MoS_2 materials to date.

2.5 Introduction to Supramolecular Hydrogels

One promising avenue of research concerning semiconducting nanoelectronic materials is their incorporation into hydrogels and supramolecular hydrogels (SMH) for a variety of applications, including responsive materials, biomedicine, and mechanical reinforcement.^{269,270} Many nanomaterials, including graphene, graphene oxide, CNT, metal nanoparticles and TMDs have been incorporated into hydrogels and supramolecular hydrogels to impart functionality or strength.²⁷¹⁻²⁷⁵ In this section, we provide a brief background on supramolecular hydrogels, particularly those that are stimuli-responsive and/or comprised of CNT and biomolecules, such as DNA, polypeptides, and polysaccharides.

2.5.1 Synthetic and Supramolecular Hydrogels

Hydrogels are three-dimensional networks of hydrophilic cross-linked polymers with soft solid characteristics similar to biological tissues.^{276–278} They are capable of retaining large amounts of water, which typically occupies more volume than the gelators in a hydrogel construct. Hydrogels can be divided into two major categories: synthetic hydrogels and supramolecular hydrogels (SMH). The distinction between the two lies not in the types of materials used, but in the nature of the cross-linking. In general, synthetic hydrogels are cross-linked by non-reversible covalent bonds between repeating units of polymers. Many types of polymers can form synthetic hydrogels, including natural polymers, neutral polymers, and ionic polymers, among others. Some examples of polymers commonly used to form synthetic hydrogels are shown in Figure 2.20.²⁷⁹ While synthetic hydrogels have been investigated for several applications, the permanent, covalent cross-linking often leads to brittle structures that do not allow for self-healing, reversibility, or stimuli-responsive behavior.^{269,280}

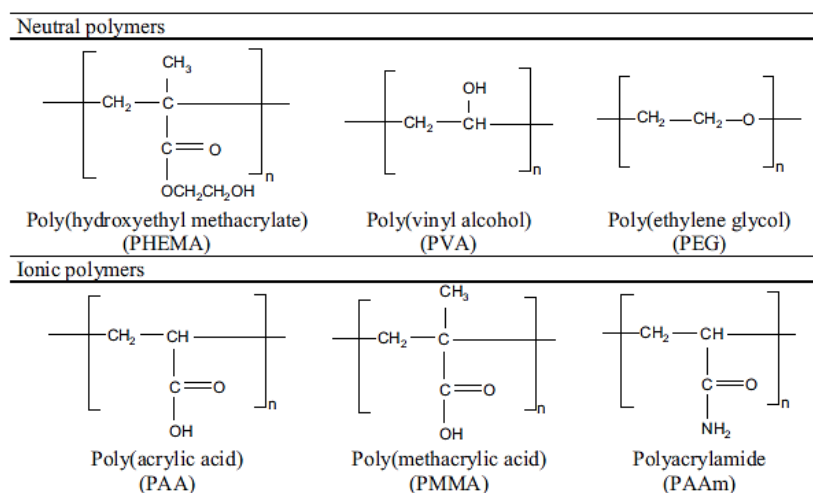


Figure 2.20: Representative chemical structures of commonly used neutral and charged polymers for synthetic hydrogels.²⁷⁹

On the other hand, SMH combine the desirable characteristics of synthetic hydrogels with reversible cross-linking. In contrast to synthetic hydrogels, the cross-linking forces in SMH are necessarily non-covalent and thus modifiable by environmental and engineered stimuli. As such, SMH have been widely studied for their applications in disease diagnostics and therapy in the form of bioimaging, sensing, drug delivery, and tissue engineering.^{273,281,282} In the coming sections, the large number of available SMH will be categorized according to pertinent characteristics. A brief description of rheometry experiments to measure the mechanical properties of SMH will also be presented.

2.5.2 Types of Supramolecular Hydrogels

SMH are categorized according to the non-covalent interaction taking place, the type of building block or gelator, the size of the gelators involved and their largest possible network, as outlined in Figure 2.21. The non-covalent interactions employed for cross-linking in SMH are hydrogen bonding, metal-ligand coordination, host-guest interactions, and electrostatic interactions (Figure 2.21a). There are many gelators that can engage in each of these mechanisms, each with their own strengths and drawbacks. For example, hydrogen bonding is especially amenable to constructing biological supramolecular hydrogels with pH-responsiveness. Biomolecules such as DNA readily engage in hydrogen bonding, and indeed have formed pH-responsive SMH.^{283,284} However, the major disadvantage of hydrogen bonding is its ease of dissociation upon contact with polar solvents including water.

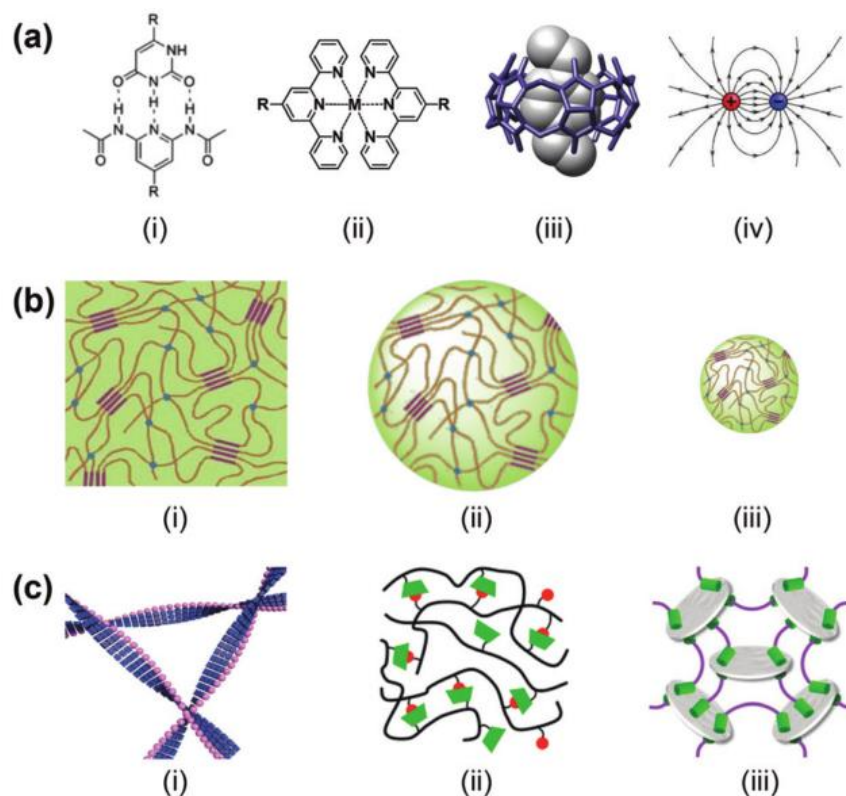


Figure 2.21: Types of supramolecular hydrogels. SMH are classified in terms of (a) non-covalent interaction: (i) hydrogen bonding, (ii) metal-ligand coordination, (iii) host-guest recognition, and (iv) electrostatic interaction. (b) Classification based on size of network and components: (i) macrohydrogel, (ii) microhydrogel, and (iii) nanohydrogel. (c) Classes of SMH according to the type of building blocks/gelators: (i) molecular hydrogel, (ii) supramolecular polymeric hydrogel and (iii) supramolecular hybrid hydrogel.²⁶⁹

Besides non-covalent interaction and size, SMH are also categorized by the type of building block or gelator involved (Figure 2.21c). SMH may be comprised of molecules such as peptide amphiphiles or synthetic molecules functionalized with supramolecular motifs. In a similar manner, SMH can be formed by covalent functionalization of polymers with supramolecular motifs, forming the basis for supramolecular polymeric hydrogels. Lastly, supramolecular hybrid hydrogels are those that contain an inorganic component in the gelation mechanism, such as metal nanoparticles, carbon nanomaterials, quantum dots, and others. This

classification does not include nanomaterial containing composite hydrogels where the nanomaterial is not actively engaged in the hydrogel network, though there are many instances of this type of hydrogel in the literature.

2.5.3 Rheology

Since SMH tend to be weaker than typical solids, their mechanical properties cannot be tested in conventional ways, namely tensile and compressive testing to failure. As such, rheometry is an obvious choice to measure the resistance to flow, thereby potentially characterizing much more than the mechanical properties. Roughly speaking, rheology is the study of flow of matter, and is generally applied to liquids and soft solids. Hydrogels in general have solid-like rheology and do not flow, despite being predominantly comprised of water.²⁸⁵

In a typical rheometry experiment, a sample is held between two parallel plates and an oscillatory strain (or stress) is applied by one of the plates, as shown in Figure 2.22. The deformation (strain) is measured at the same time by the force exerted on the other parallel plate. The elastic storage modulus (G' , or the elastic component) and elastic loss modulus (G'' , or the viscous component) can be measured as a function of applied stress or oscillation frequency. G' and G'' are the real and imaginary components of the complex modulus. For a material to be considered solid, G' must exceed G'' until the yield strain when the network starts to fall apart. In measurements of G' and G'' as a function of frequency, G' generally exceeds G'' over the entire range of frequencies. Other geometries of rheometry experiments, such as cone-plate, and concentric cylinders, are also used for various purposes depending on the nature of the sample in question.²⁸⁶

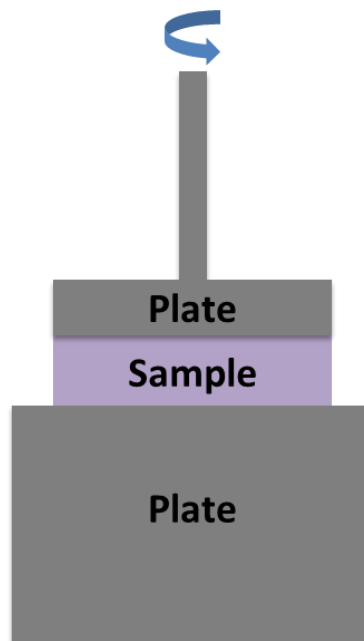


Figure 2.22: Typical parallel-plate setup of a rheometry experiment. A sample is placed between two parallel plates and an oscillatory strain is applied to measure deformation/flow.

CHAPTER 3

High-Concentration Aqueous Dispersions of Nanoscale Two-Dimensional Materials Using Nonionic, Biocompatible Block Copolymers

This chapter is based, in part, on the research described in the following publication:
Mansukhani, N.; Guiney, L.; Kim, P.; Alducin, D.; Ponce, A.; Larios, E.; Jose-Yacaman, M.; Hersam, M.C. Aqueous High Concentration Dispersions of Nanoscale Two-Dimensional Materials Using Nonionic, Biocompatible Block Copolymers. *Small* **2016**, *12*, 294-300.

Chapter 3 - High-Concentration Aqueous Dispersions of Nanoscale Two-Dimensional Materials Using Nonionic, Biocompatible Block Copolymers

3.1 Introduction

Layered two-dimensional (2D) nanomaterials have attracted significant attention due to their large surface areas, nanometer-scale thicknesses, and superlative properties.^{70,287,288} Since the isolation of graphene in 2004, many classes of 2D nanomaterials have been isolated and studied, including chalcogenides, nitrides, oxides, and other elemental analogues of graphene such as 2D silicon and black phosphorus.^{289,290} These nanomaterials display a wide range of interesting mechanical, optical, electrical, and chemical properties, enabling their use in electronics, catalysis, spintronics, and related applications.^{291,292} Of particular interest is the transition metal dichalcogenide (TMD) molybdenum disulfide (MoS_2) because of its widespread commercial availability and semiconducting direct band gap in monolayer form.^{293,294} In addition, nanoscale MoS_2 possesses other attributes including high charge carrier mobility, visible photoluminescence, optical transparency, piezoelectricity, and superlubricity.^{126,160,295–300} Moreover, the semiconducting electronic structure of MoS_2 makes it a favorable candidate in the fields of sensing and electronics over graphene, which is intrinsically a zero band-gap material.^{295,301–304} MoS_2 also holds promise in solution-based applications, although its potential in this area has not yet been fully realized. For example, aqueous dispersions of MoS_2 have been proposed as biological imaging agents, drug delivery vehicles, and photothermal agents, as well as the basis for electronic and electrocatalytic applications.^{305,306}

In order to realize this myriad of applications, scalable methods of exfoliation are needed that will maintain the 2H semiconducting structure and desirable electronic properties of MoS₂ while simultaneously limiting any deleterious biological or environmental effects. Historically, atomically-thin layers of 2D nanomaterials have been isolated by mechanical exfoliation using adhesive tape, which produces high quality flakes but with limited throughput.^{126,294,295} In addition, some 2D nanomaterials can be grown using chemical vapor deposition (CVD), wherein monolayers are produced with high purity and with a greater potential for scalability than mechanical exfoliation or colloidal chemical synthesis.^{90,129,307–310} However, CVD-synthesized monolayers often need to be transferred from their growth substrate using harsh etchants and polymer coatings. These chemical treatments and polymer-based transfer techniques can result in structural damage and/or surface contamination to the resulting films.³¹¹

Solution processing offers a path forward to scalable production of 2D nanomaterials. Current methods, however, present a number of limitations with respect to their potential use in both electronics and biomedical applications. For example, chemical exfoliation can be achieved *via* ion intercalation most commonly lithium ion intercalation.^{312,313} However, for MoS₂, this ion intercalation process involves harsh, toxic chemicals and significantly changes the electronic properties of the final nanomaterial due to a phase change from the semiconducting 2H-MoS₂ to the metallic 1T-MoS₂ polytype.^{90,129,160,307–315} Exfoliation by ultrasonication in aqueous and organic solution has been demonstrated in a manner that preserves the original semiconducting 2H-MoS₂ phase, but to prevent agglomeration, ionic surfactants (*e.g.*, sodium cholate) in aqueous solution or nonionic polymers in organic solvents have been used.^{83,162–164,316} The charged residues from ionic surfactants compromise electronic, electrochemical, and biological

applications, while previously studied nonionic polymer dispersions have not been optimized for high yield and concentration, thereby also hindering applications in the biomedical field.

In this study, we demonstrate the exfoliation and stable dispersion of a suite of 2D nanomaterials in aqueous solution using biocompatible, nonionic poloxamers as a surfactant. A survey of 19 different poloxamers (*i.e.*, Pluronics and Tetronics) reveals the effect of varying composition of block copolymer on the dispersion efficiency of MoS₂. Size characterization analysis by scanning electron microscopy (SEM) and atomic force microscopy (AFM) shows that the resulting dispersions contain flakes that are primarily less than 10 layers in thickness. Furthermore, X-ray photoelectron spectroscopy (XPS) and high-resolution scanning transmission electron microscopy (STEM) confirm the unchanged stoichiometry and high crystalline quality of the resulting solution-processed MoS₂. These exfoliation and dispersion conditions are found to be generally applicable to a wide range of 2D nanomaterials including molybdenum diselenide (MoSe₂), tungsten diselenide (WSe₂), tungsten disulfide (WS₂), tin selenide (SnSe), and boron nitride (BN), thus providing a diverse palate of aqueous 2D nanomaterial dispersions for fundamental studies and emerging applications.

3.2 Experimental Section

3.2.1 Nanomaterial Dispersion Conditions

For nanomaterials dispersed in Pluronics and Tetronics, 300 mg \pm 5 mg bulk powder was added to 8 mL 2% w/v block copolymer solution in deionized water inside a 15 mL conical polypropylene tube. This mixture was then ultrasonicated using a horn ultrasonicator with a 3 mm diameter probe (Fisher Scientific Model 500 Sonic Dismembrator) while being chilled in an

ice water bath. For all samples, excluding those used for X-ray photoelectron spectroscopy, the sonication power was maintained at 16-18 W (25%).

For MoS₂ dispersions, the resulting slurry was then centrifuged under a variety of conditions (see Table 3.1) to eliminate poorly dispersed MoS₂. For all other 2D materials, only centrifugation condition D was used (60 minutes at 5,000 rpm). Centrifugation was carried out in an Eppendorf Model 5424 Microcentrifuge using a 45° fixed-angle rotor (FA-45-24-11). The slurry was centrifuged in 1.5 mL aliquots in conical Eppendorf tubes, of which the top 1 mL was carefully decanted using a 20-gauge needle and syringe for further studies. Seven different centrifugation conditions were tested as shown in Table 3.1. All data shown in the results and discussion section correspond to dispersions that were centrifuged for 60 minutes at 5,000 rpm (centrifugation condition D).

	Centrifugation Time (min)	Centrifugation Speed (rpm)	Relative Centrifugal Force (g)	Relative (speed) ² (time)
A	10	500	23	1
B	10	1000	94	4
C	10	5000	2348	100
D	60	5000	2348	600
E	10	15000	21130	900
F	75	5000	2348	750
G	60	10000	9391	2400

Table 3.1: Centrifugation processing parameters used in this dispersion study.

For the preparation of lithiated MoS₂, 3.0 g of MoS₂ bulk powder was mixed with 3 mL of n-butyllithium solution (Sigma-Aldrich) in an inert argon atmosphere glove box. This mixture was stirred continuously for 48 hr, then filtered and rinsed with 60 mL hexane to remove residual

n-butyllithium. The filter containing pre-exfoliated Li_xMoS_2 was then removed from the glove box and immersed in 750 mL deionized water and exfoliated using 1 hr of bath sonication. This step was followed by a brief centrifugation to remove any unexfoliated MoS_2 flakes and aggregates. In order to remove any remaining hexane and lithium, the solution was dialyzed against deionized water for 7 days in a 20,000 Da molecular weight cut off (MWCO) membrane.

3.2.2 Removal of Pluronic from Dispersion

Polymers such as Pluronic and Tetronic can compromise electrical performance of materials and hinder size characterization. As such, we have used two methods to overcome this issue. The first method was tested in relation to a MoS_2 Pluronic F87 dispersion on a surface rather than in solution. Following deposition of the MoS_2 Pluronic F87 dispersions onto SiO_2 wafers by drop casting, the substrate was annealed for 60 min at 275°C in air to remove the Pluronic.

The second method involved flocculation by the addition of isopropyl alcohol (IPA) in a 4:1 volume ratio. When the mixture was left overnight, the MoS_2 flakes visibly settled out of solution. This destabilization illustrates the reversibility of the interaction between MoS_2 and the surfactants and the ability to remove the surfactant from the surface. Although it is difficult to verify that flocculation by IPA completely removes Pluronic from the MoS_2 surface, the aggregation of the flakes suggests that the interaction between Pluronic and MoS_2 is reversible.

Furthermore, imaging by AFM and STEM before and after these procedures strongly suggests that Pluronic is effectively removed by these procedures. As described in the following sections, AFM was performed on annealed SiO_2 substrates; STEM was performed on aggregated

samples of MoS₂ deposited onto holey grids. The annealing and aggregation steps improved the resolution of AFM and STEM, respectively, presumably due to the removal of Pluronic.

3.2.3 Inductively Coupled Plasma-Mass Spectroscopy

Small aliquots (5 to 100 μ L) of each Pluronic- and Tetronic-dispersed MoS₂ solution and Pluronic F87-dispersed BN, WS₂, SnSe, MoSe₂, and WSe₂ using centrifugation condition D were added to 300 or 450 μ L concentrated trace-grade nitric acid (Sigma-Aldrich) in lightly-capped 15 mL conical polypropylene tubes and heated for at least 12 hr at 65 $^{\circ}$ C. 50 μ L or 75 μ L of ICP-MS multi-element internal standard was then added to the solution for a final concentration of 10 ppb. The solution was diluted to a final concentration of 2% nitric acid using deionized water (10 or 15 mL total). External standards were prepared to span 0.488 ppb to 1000 ppb of the elements of interest by mixing varying quantities of Mo, W, Sn, and B standards (Inorganic Solutions), 150 μ L nitric acid, and 25 μ L internal standard. Each external standard was diluted to a final volume of 5 mL with deionized water. All samples were measured under the same conditions on a ThermoFisher X Series II ICP-MS. The accuracy of the external standard concentration was checked by linear regression of the ICP-MS signal ($R^2 > 99.999$).

The concentration of the undiluted specimens was then determined by using the appropriate dilution factor and the formula weight ratios. Repeated experiments revealed a ~10% uncertainty in the concentration measurements as a result of small differences in sonicator probe placement, contamination of the supernatant by poorly exfoliated material, and digestion conditions for ICP-MS.

3.2.4 Extinction Coefficient and Concentration Measurements

For the extinction coefficient measurement, PF87-dispersed MoS₂ was concentrated using a centrifugal evaporator (GeneVac HT-4X) to a final concentration of 0.47 mg/mL, measured by ICP-MS as described in the previous section. The optical absorbance spectra of the concentrated solution and several dilutions of the solution were taken using a Cary 5000 spectrophotometer (Varian, Inc.) operating in dual-beam mode with a reference sample of 2% w/v Pluronic F87. The spectra were corrected for scattering using a linear background subtraction. Subsequently, the wavelength at which the best correlation was found between the optical absorbance and concentration following Beer's Law was chosen for the mass extinction coefficient. Simple linear regression modeling was used to find the mass extinction coefficient of Pluronic F87-dispersed MoS₂ according to Beer's Law ($R^2 > 99.9999$). These data are represented in Figure 3.2B, wherein the mass extinction coefficient for Pluronic F87-dispersed MoS₂ was measured as $\alpha_{600}=2104$ ml/mg/m.

For all remaining centrifugation conditions, concentration was estimated using the mass extinction coefficient of Pluronic F87-dispersed MoS₂. Optical absorbance spectra were taken as described above with a dilution factor 10-100 into 2% w/v aqueous solutions of the block copolymer as necessary to remain in the linear response region of the spectrophotometer. A reference sample of 2% w/v of the aqueous block copolymer used in the dispersion was subtracted from the spectra to correct for any contribution to the absorbance.

3.2.5 Scanning Transmission Electron Microscopy (STEM)

Pluronic F87-dispersed MoS₂ was flocculated by mixing with isopropanol in a 1:4 volume ratio. The mixture was then vacuum filtered and rinsed with an equal amount of

deionized water to remove residual Pluronic F87 and isopropanol, and finally redispersed in water. This aggregated sample was then deposited by drop casting onto holey grids. STEM images were collected using the High Angle Annular Dark Field (HAADF) detector in a probe Cs-corrected JEOL JEM-ARM operated at 80 kV. HAADF-STEM images were obtained with a convergence angle of 26 mrad and the collection semi-angles from 50 to 180 mrad. The probe size used was about 0.09 nm with a probe current of 22 pA. The HAADF-STEM images were filtered using DeConvHAADF filter by using the Maximum Entropy Method.

3.2.6 Size Characterization

Various Pluronic and Tetronic dispersions were dialyzed against 2% w/v sodium cholate (SC) for 48 hours to prepare for atomic force microscopy (AFM). Silicon wafers with a 300 nm oxide layer were then functionalized with (3-aminopropyl)triethoxysilane (APTES) after which individual flakes were deposited as described previously.¹⁹⁰ This same process can be modified to produce continuous films of MoS₂ on silicon by increasing the incubation time or concentration of MoS₂ during deposition. To remove residual Pluronic, samples were annealed in air for 60 min at 275°C. AFM images were taken using a Bruker Dimension FastScan AFM in tapping mode.

MoS₂ samples for SEM were prepared by drop-casting onto SiO₂ wafers. The resulting samples were imaged using a Hitachi 4800 SEM.

3.2.7 X-Ray Photoelectron Spectroscopy (XPS)

Thin films were formed using vacuum filtration on nitrocellulose membranes (Whatman) and were measured immediately after drying in air. Bulk samples were deposited directly onto copper tape for measurement. XPS spectra were taken using a Thermo Scientific ESCALAB

250Xi. Spectra of MoS₂ samples were then corrected for background and fitted for the following peaks between 220 and 245 eV: Mo 3d satellite (233 eV), Mo 3d_{3/2} (230 eV), Mo 3d_{5/2} (227 eV), and S 2s (224 eV), and the following peaks between 160 and 170 eV: S 2p_{3/2} (162.2 eV) and S 2p_{1/2} (163.4 eV). Additionally, XPS measurements were taken on BN, WS₂, SnSe, MoSe₂, and WSe₂ bulk samples and 2D nanomaterial dispersions to verify that sonication in Pluronic does not alter the chemical structure by way of oxidation, covalent interaction, or contamination.

3.3 Results and Discussion

Pluronics and Tetronics are biocompatible nonionic block copolymers that can be used as surfactants in aqueous solution due to their amphiphilic nature. They are comprised of hydrophobic polypropylene oxide (PPO) chains and hydrophilic polyethylene oxide (PEO) chains in different lengths and ratios. As shown in Figure 3.1, Tetronics consist of two PPO chains covalently linked in a cross shape by ethylenediamine, with four identical PEO chains attached to the end of each PPO chain. On the other hand, Pluronics are based on a single PPO chain with two PEO chains attached on either end. These surfactants disperse well in aqueous solutions and are available with a wide range of PPO and PEO chain lengths. They have been previously employed to disperse and mitigate the toxicity of carbon nanomaterials including graphene and carbon nanotubes.^{133,205,317} Pluronics have also been used to sort carbon nanotubes and molybdenum disulfide by physical structure and electronic type using density gradient ultracentrifugation.^{174,191,318} Thus, in addition to presenting a scalable method of producing two-dimensional nanomaterials, biocompatible surfactants facilitate the deployment of these materials in biomedical applications.

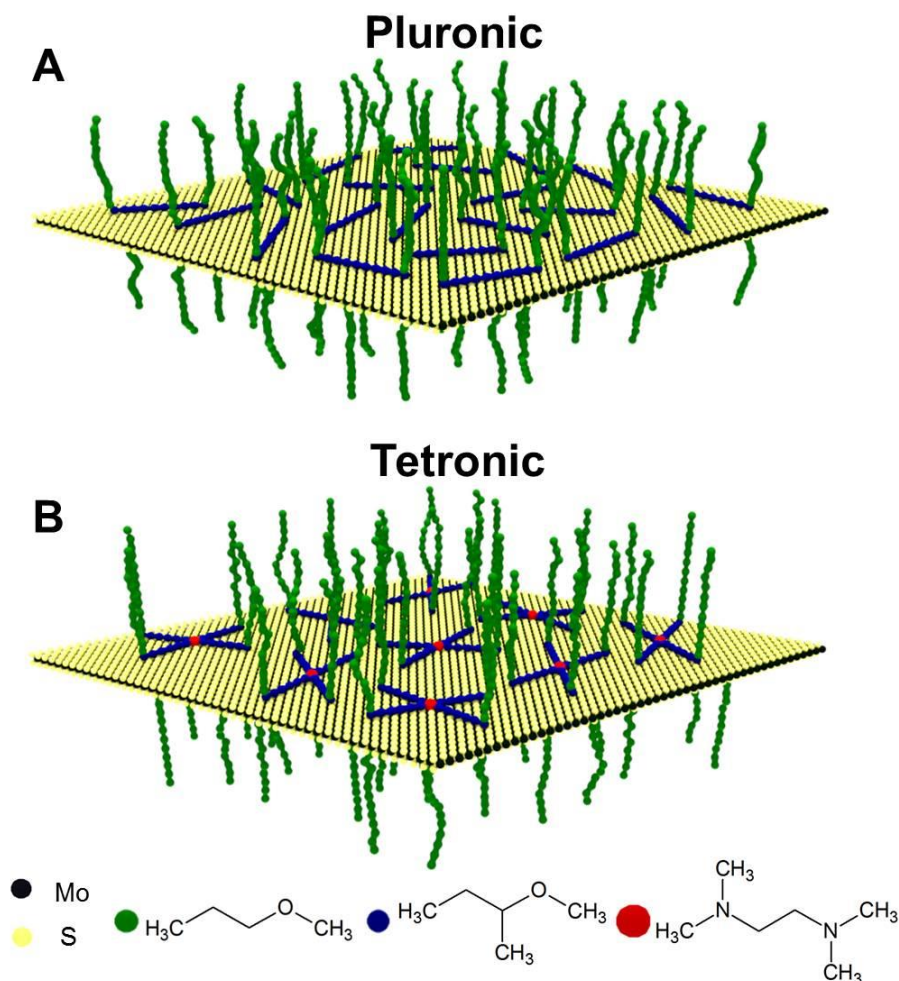


Figure 3.1: Schematic depiction of (A) Pluronic and (B) Tetronic block copolymers on the surface of a single-layer MoS₂ flake. The amphiphilic Pluronic/Tetronic block copolymers adsorb non-covalently to the surface of MoS₂ and prevent the agglomeration of the exfoliated flakes by acting as a surfactant and providing steric repulsion.

Figure 3.1 illustrates the hypothesized interaction between MoS₂ and Pluronic/Tetronic where the PPO chains non-covalently adsorb to the surface of MoS₂ through hydrophobic interactions. The hydrophilic PEO chains extend into solution thereby stabilizing the dispersion by lowering the surface tension and providing steric repulsion. The relative lengths of the PPO

and PEO chains will influence these amphiphilic interactions and thus lead to variations in exfoliation and dispersion efficiency as will be quantified below.

The naming convention for each Pluronic and Tetronic identifies its state at room temperature and the molecular weight of its PPO and PEO chains. Specifically, Pluronics are labelled with a letter that represents their physical state at room temperature (*i.e.*, flake, paste, or liquid), followed by a set of two or three digits. The last digit of each Pluronic number corresponds to the relative percent of PEO in the product. Additionally, the first one or two numbers multiplied by 300 is the approximate molecular weight of the PPO chain. Similarly, the last digit of each Tetronic name multiplied by 10 represents the percentage of PEO weight, while the earlier digits multiplied by 45 provides the molecular weight of the hydrophobic central block. Therefore, the molecular weights of the PEO and PPO components of Pluronics and Tetratics are determined using the total molecular weights provided by the source company (BASF) and the aforementioned naming convention. Overall, a total of 14 Pluronic solutions and 5 Tetronic solutions were tested to elucidate the effect of varying PEO *versus* PPO length on the exfoliation and dispersion efficiency of MoS₂.

Initially, 300 mg of MoS₂ powder (Sigma-Aldrich) was weighed in a 15 mL conical tube, followed by the addition of 8 mL of 2% w/v Pluronic or Tetronic solution. The mixture was then ultrasonicated for 1 hr at 25% amplitude (~16 W) while cooled in an ice water bath. Following ultrasonication, a series of centrifugation conditions were tested for the highest stable concentration of MoS₂. Through a series of early trials, it was determined that centrifugation affected the final dispersion concentration significantly more than the initial mass of Pluronic or Tetronic block copolymer. As such, centrifugation was carried out in a tabletop centrifuge using

a variety of conditions with speeds ranging from 500 rpm to 15,000 rpm, and spin times of 10 min to 75 min (see Section 3.2 for more details). All data depicted here correspond to solutions centrifuged at 5,000 rpm for 60 min, as this centrifugation condition effectively removes aggregates without significantly decreasing overall yield. Solutions were then carefully decanted using a 20-gauge needle and syringe. Optical absorbance measurements were taken immediately following centrifugation, and corrected using a linear background subtraction. A subset of these measurements and their corresponding solutions are shown in Figure 3.2A and B. For BN, WS₂, SnSe, MoSe₂, and WSe₂ dispersions in Pluronic F87, the same ultrasonication procedure was followed, and centrifugation was carried out at 5,000 rpm for 60 min. Lithiated molybdenum disulfide (Li_xMoS₂) was also prepared by ion intercalation and dialysis for a comparison of concentration (see Section 3.2 for experimental details).

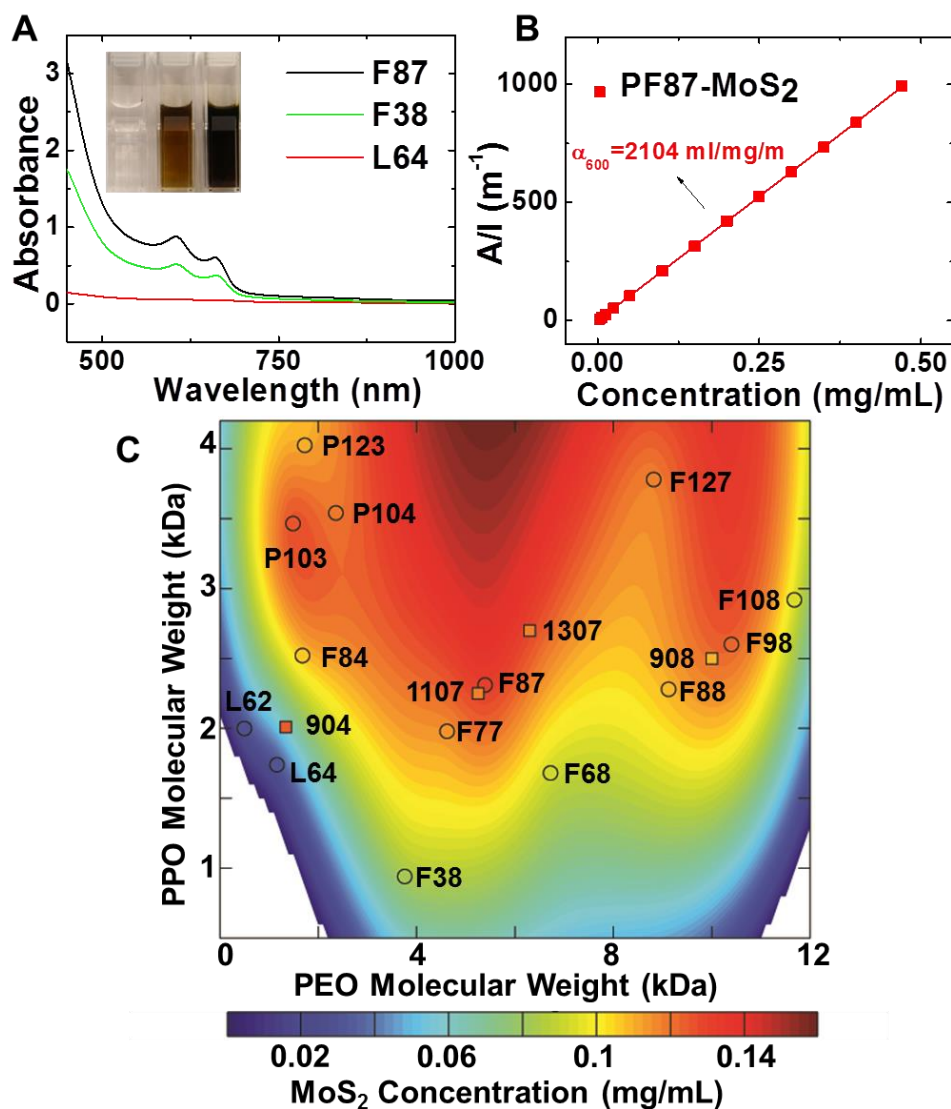


Figure 3.2: (A) Optical absorption spectra showing the range of concentrations possible by dispersing MoS₂ in Pluronic under identical dispersion conditions. Photographs of corresponding solutions shown in the inset. (B) Beer's Law plot of Pluronic F87 MoS₂ dispersion optical absorbance as a function of concentration as measured by ICP-MS. (C) Concentration map of MoS₂ in Pluronic and Tetronics. The color map is based on interpolation of the experimental Pluronic data, while the actual experimental values are shown by colored circles, and the actual Tetronic experimental values are represented by colored squares.

Concentration was inferred from optical absorbance spectroscopy and inductively coupled plasma mass spectrometry (ICP-MS), which allows part-per-billion sensitivity. Samples were digested in >69% nitric acid at 65°C overnight, diluted with deionized water and internal standard to appropriate concentrations, and measured by ICP-MS promptly. The presence of the metal or metalloid was measured in several samples, averaged to eliminate experimental error, and then used to determine the total concentration stoichiometrically. For MoS₂, these results were largely consistent with the excitonic peak heights of background subtracted optical absorbance spectra. As such, both optical absorbance and ICP-MS were correlated to produce the final concentration values as shown in Table 3.2. The same method was applied to determine the mass extinction coefficient as shown in the Beer's Law plot in Figure 3.2B. As seen in the optical absorbance spectra (Figure 3.2A), two sharp absorption peaks are present in the range of 620 nm to 675 nm. According to the photoluminescence spectra, MoS₂ absorbs and emits visible wavelengths, namely photoluminescence emission peaks correspond to the excitonic transitions A1 at 670 nm and B1 at 627 nm.¹²⁶ The direct band gap is responsible for photoluminescence in MoS₂, which grows stronger with reduced flake thickness. Therefore, since the MoS₂ dispersions obtained here are polydisperse in thickness, photoluminescence will only occur after post-processing by density gradient ultracentrifugation, wherein single-layer flakes of Pluronic-dispersed MoS₂ can be isolated.¹⁹¹ The survey of Pluronic and Tetronic block copolymers resulted in a wide range of final concentrations, as shown in Figure 3.2C. In this plot, the actual experimental concentration values of the Pluronic and Tetronic solutions are represented by the colored circles and squares, respectively, while the underlying color map is based on an interpolation of the Pluronic data set. Additionally, Tetronics are plotted at half of their actual

PEO and PPO values since their structure is similar to two Pluronic chains connected at their midpoint. The two-dimensional color map shown in Figure 3.2C was obtained using Matlab.

Polymer	Molecular Weight (Da)	% Weight of Total		MoS ₂ Concentration (mg/mL)							
	Total	PEO	PPO	A	B	C	D	E	F	G	
Pluronics	F108	14600	80%	20%	0.905586	1.07246	1.049697	0.094802	0.029104	0.038404	0.021209
	F127	12600	70%	30%	0.960633	1.13599	1.11838	0.118488	0.052211	0.037079	0.044098
	F38	4700	80%	20%	0.990135	1.055862	1.004323	0.082299	0.067463	0.035069	0.041912
	F68	8400	80%	20%	1.006469	1.20003	1.150438	0.092431	0.024289	0.037232	0.020885
	F77	6600	70%	30%	1.237479	1.344519	1.286472	0.115185	0.042462	0.037119	0.036249
	F87	7700	70%	30%	1.452986	1.545518	1.510053	0.132203	0.056106	0.042002	0.038602
	F88	11400	80%	20%	0.881903	1.044469	0.975908	0.10926	0.038961	0.034716	0.032851
	F98	13000	80%	20%	0.786295	0.9074	0.91603	0.123528	0.042032	0.032581	0.033508
	L62	2500	20%	80%	0.887935	0.92998	0.822836	0.028008	0.000586	0.024145	6.96E-05
	L64	2900	40%	60%	1.162612	1.483893	1.353759	0.030333	0.003461	0.025849	0.001197
	P103	4950	30%	70%	1.078127	1.549958	1.391158	0.126893	0.055794	0.035954	0.038348
	P104	5900	40%	60%	1.403682	1.407833	1.291485	0.120032	0.053083	0.0358	0.034953
	P123	5750	30%	70%	1.168744	1.26763	1.462092	0.110966	0.057351	0.030681	0.028938
P84	4200	40%	60%	1.338088	1.402606	1.340568	0.10709	0.03449	0.038927	0.01723	
Tetronics	T304	1650	40%	60%	1.765	1.841833	1.730883	0.123055	0.00599	0.047758	0.042967
	T904	6700	40%	60%	1.285377	1.423092	1.391896	0.118388	0.075885	0.039561	0.055299
	T908	25000	80%	20%	0.805743	0.999247	0.964132	0.125291	0.036897	0.032214	0.032113
	T1107	15000	70%	30%	1.024512	0.77877	1.137384	0.109634	0.051441	0.034427	0.043384
	T1307	18000	70%	30%	1.227529	1.198875	1.167544	0.118769	0.04812	0.036619	0.033619

Table 3.2: Concentration of molybdenum disulfide dispersed in aqueous block copolymers.

Centrifugation condition D experimental concentration values were interpolated over a two-dimensional grid using the function “griddata” and plotted without any negative interpolated values of concentration. The function “griddata” was used with the Matlab “v4” method, which is based on a biharmonic spline interpolation method. This method was originally used to interpolate irregularly spaced satellite altimeter data in order to produce detailed and accurate sea surface topography maps.³¹⁹ Briefly, the interpolating surface is comprised of a linear combination of Green functions centered at each data point. The amplitudes of the Green functions were found by solving a linear system of equations. In three dimensions, this technique

equates to multiquadric interpolation. Overall, the biharmonic spline interpolation method is well-suited to interpolating irregularly-spaced, sparse data because both values and slopes can be used to find the surface. This also makes it a highly flexible method. However, numerical instabilities can arise when the ratio of the greatest distance between any two points to the least distance between any two points is large.

Though numerical instabilities did not arise in the interpolation of Figure 3.2C, the interpolation method resulted in a local maximum that was outside the range of the data. However, a similar trend is observed in a simple contour plot within the data boundary using Delaunay triangulation without smoothing (Figure 3.3). These data were also plotted as a function of PEO/PPO molecular weight or number of molecules, as shown in Figure 3.4. No discernable trends are observed in these plots, indicating that the relative presence of both PEO and PPO play a role in determining the exfoliation efficiency. Therefore, three-dimensional plotting methods are essential to observe trends in the concentration with respect to polymer characteristics.

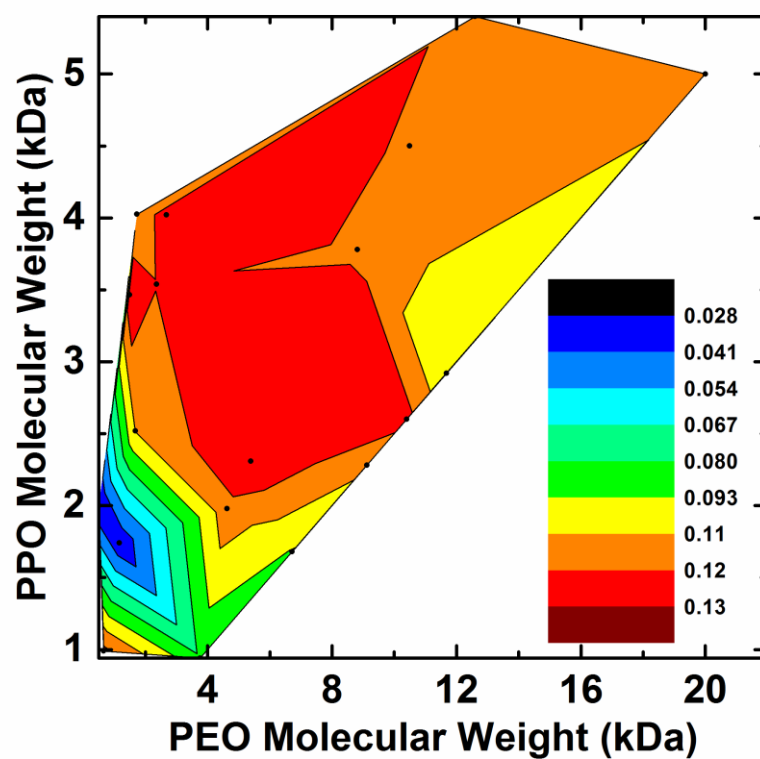


Figure 3.3: Concentration map of MoS₂ in Pluronics and Tetronics using Delaunay triangulation without smoothing. Experimental data points are indicated by black dots.

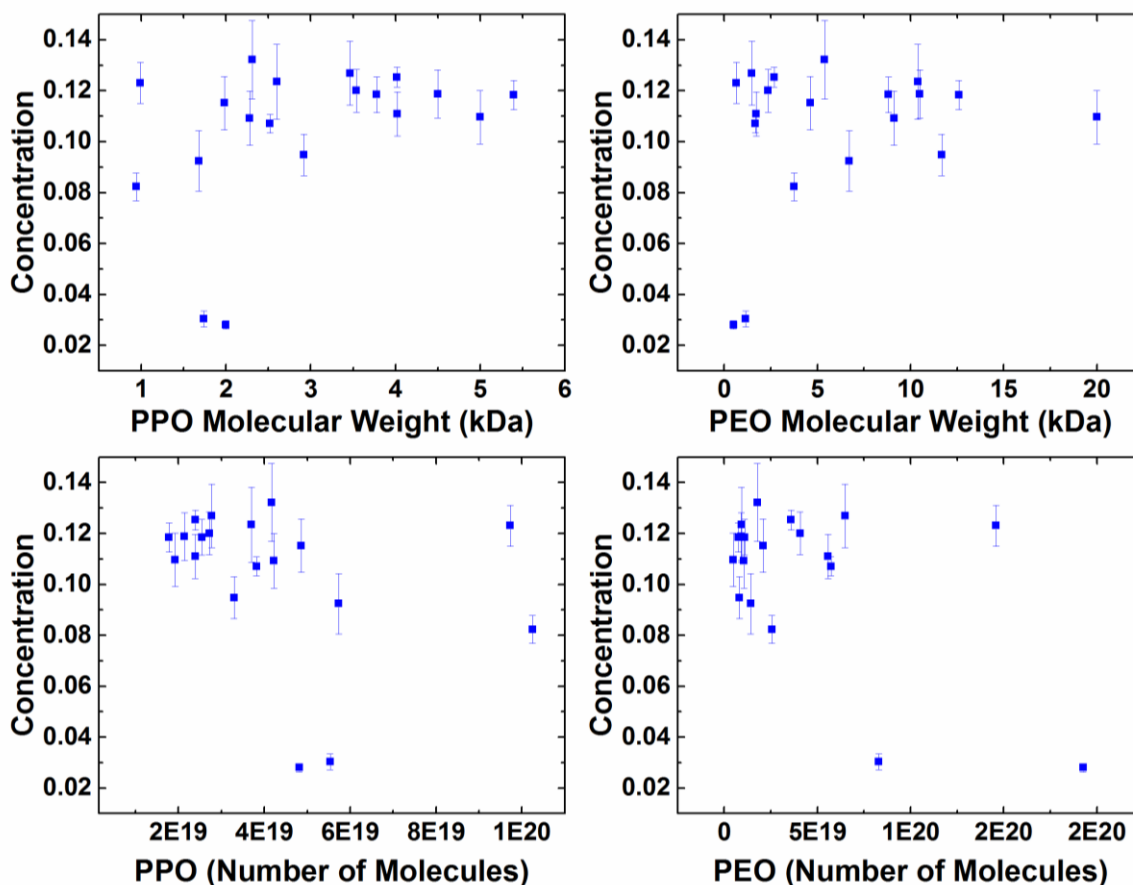


Figure 3.4: Concentration plotted as a function of PPO/PEO molecular weight only (top) or number of PPO/PEO molecules only.

Dispersing MoS₂ in different Pluronics and Tetronics under identical ultrasonication and centrifugation conditions results in a wide range of concentrations, signifying that the various Pluronics and Tetronics have varying exfoliation and dispersion efficiencies. The data in Figure 3.2C show that the concentration of Pluronic-dispersed MoS₂ is highest with an intermediate PEO molecular weight and a large PPO molecular weight. Pluronics with an intermediate PEO molecular weight are well-suited for stable 2D nanomaterial dispersions since they are long enough to provide adequate steric hindrance between flakes, thus suppressing aggregation. The

improved exfoliation and dispersion efficiency with increasing PPO molecular weight can likely be attributed to the hydrophobicity of MoS₂, which has been reported to exceed that of graphene.³²⁰ In contrast to the Pluronics, Tetronics show fewer systematic trends as a function of PEO and PPO molecular weights with Tetronic 904 appearing as a clear outlier in Figure 3.2C. The more complicated behavior of Tetronics may be attributed to the presence of the ethylenediamine linker group in the center of the PPO chains and/or its cross-shaped structure. Overall, Pluronic F87 provided the best combination of exfoliation efficiency and dispersion stability, and consequently it was chosen as the focus for more thorough characterization. For example, the mass extinction coefficient was determined for F87-MoS₂ dispersions by correlating the concentration data from ICP-MS and optical absorbance spectroscopy as shown in Figure 3.2B.

F87-MoS₂ samples were further characterized using AFM and SEM for flake size and thickness (see Section 3.2 for details). As shown in the AFM image (Figure 3.6C) and cross-sections (Figure 3.6D), the thickness of F87-MoS₂ flakes ranges from 2 nm to 15 nm, with an average of 5.2 ± 1.1 nm, indicating that this exfoliation technique results in samples that are primarily less than 10 monolayers in thickness. These thickness values are largely consistent with those that have been reported using other surfactants, such as sodium cholate, in aqueous solution. MoS₂ dispersions in organic solvents using a wide range of polymer stabilizers have also been reported to have a similar range of thicknesses.^{163,316} The lateral size of the F87-MoS₂ flakes has a mean square root area of 27.5 ± 15.5 nm. For each 2D nanomaterial, over 150 individual flakes were measured for height and area, the results of which are shown in Table 3.3.

Histograms depicting the distribution of height and square root area of MoS₂ in Pluronic F87 are shown in Figure 3.5.

Material	Height (nm)			Square Root Area (nm)		
	Median	Mean	St Dev	Median	Mean	St Dev
MoS ₂	4.8	5.2	1.1	22.4	27.6	15.6
MoSe ₂	3.6	3.8	1.0	38.3	44.6	20.8
WS ₂	4.5	4.8	1.4	53.9	59.4	20.6
WSe ₂	4.0	4.3	0.9	35.0	39.8	15.1
SnSe	5.5	6.4	2.9	53.1	70.4	47.1
BN	3.9	4.5	2.1	64.3	77.0	37.9

Table 3.3: Flake height and lateral area characterization of Pluronic F87-dispersed 2D nanomaterials.

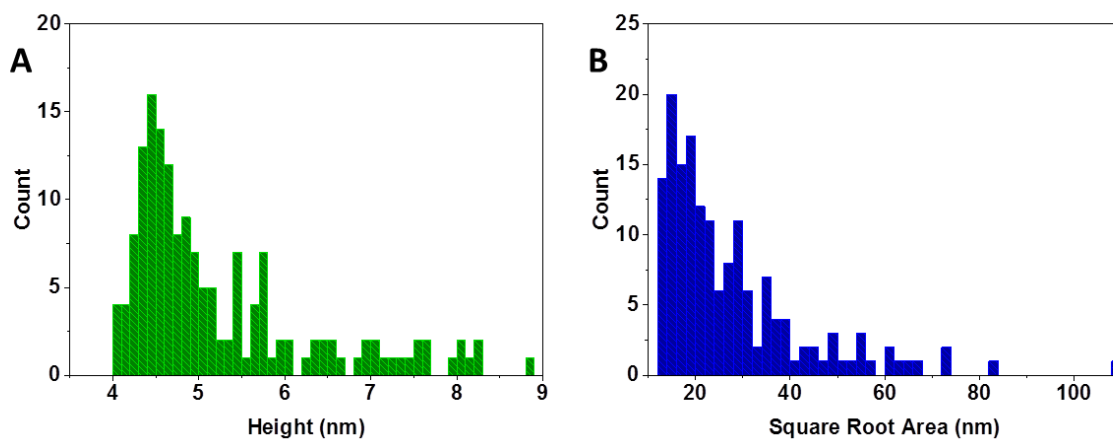


Figure 3.5: Distribution of height (A) and square root area (B) of MoS₂ dispersed in Pluronic F87.

Furthermore, high-resolution scanning transmission electron microscopy (STEM) images were collected using a high angle annular dark field (HAADF) detector (Figure 3.6B). Although the pictured flake in Figure 3.6B is multilayer overall, our analysis suggests that the edge attenuates to a monolayer thickness, thereby allowing us to examine the crystal structure of

the MoS₂. The STEM analysis confirms that the 2H semiconducting crystal structure of MoS₂ is conserved following Pluronic F87 dispersion as compared with literature reports.^{129,312}

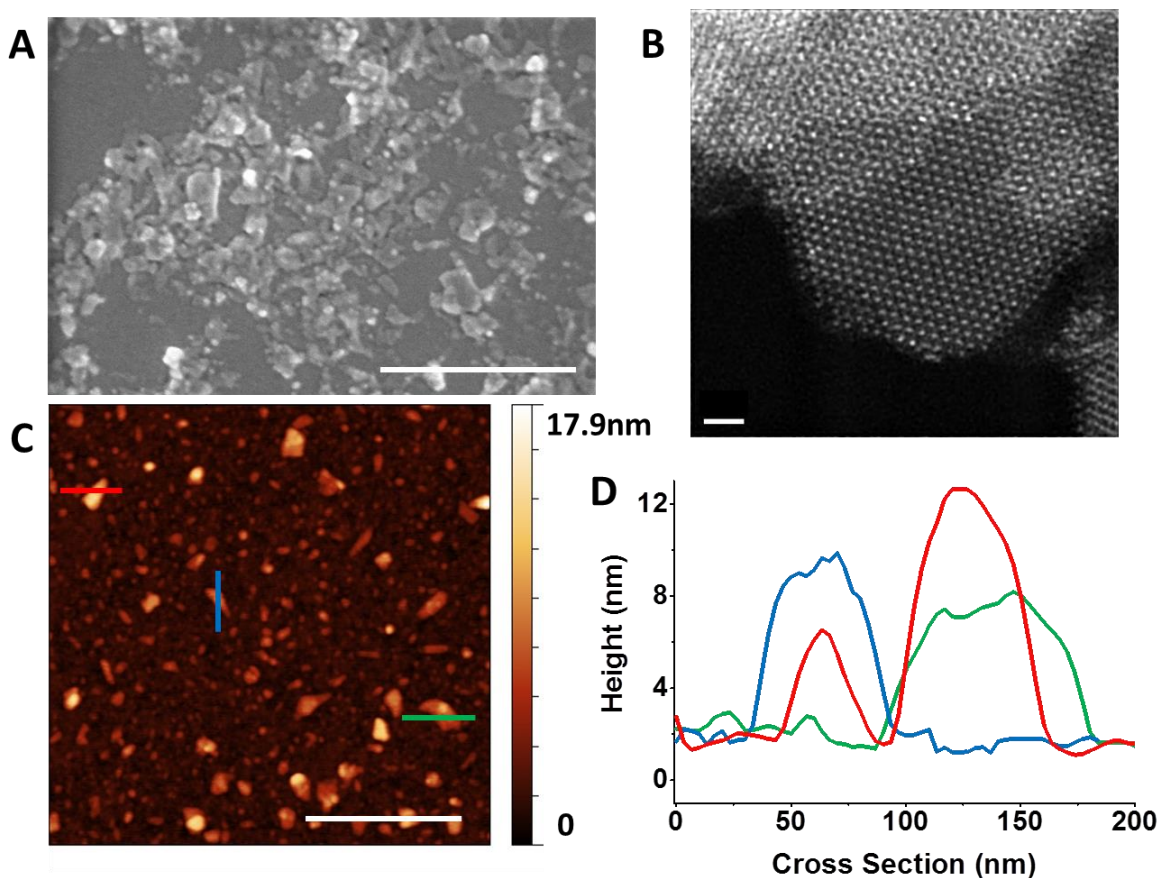


Figure 3.6: Size characterization of Pluronic F87-dispersed MoS₂. (A) SEM, (B) high-resolution STEM, (C) AFM, and (D) cross-sections derived from the AFM image. Scale bars in (A) and (C) are 500 nm. The scale bar in (B) is 1 nm.

Although block copolymers are compatible with a wide range of processes, they are known to hinder the electrical performance of 2D nanomaterials in device applications by acting as electronic insulators or charge trap carriers and may be unwanted in other fabrication procedures.²⁹⁴ As such, we describe two methods to destabilize and remove Pluronic F87 in Section 3.2. In short, when depositing on a surface such as SiO₂, as is necessary for many device

applications, annealing was effective for Pluronic removal. Alternatively, in solution phase, Pluronic F87 dispersion was effectively flocculated by the addition of isopropyl alcohol. Although this approach results in aggregation of the MoS₂ flakes, the destabilization of the Pluronic F87 dispersion is easily achieved. Moreover, imaging by AFM or STEM before and after these processes strongly suggests the removal of the majority of Pluronic F87.

XPS was used to determine the stoichiometry of MoS₂ before and after Pluronic F87 dispersion. In particular, XPS was performed on several Pluronic F87 dispersions of MoS₂ using a wide range of ultrasonication energy, which was calculated using the ultrasonication power and duration of exposure. These samples were compared to raw MoS₂ in its bulk powder form. The XPS analysis revealed that ultrasonication did not oxidize the MoS₂ beyond its original bulk form and that the Pluronic/Tetronic did not covalently interact with the 2D nanomaterials. As shown in Figure 3.7, representative Mo 3d and S 2p spectra have been fitted for the following peaks between 220 and 245 eV: Mo3d satellite (233 eV), Mo 3d^{3/2} (230 eV), Mo 3d^{5/2} (227 eV), and S 2s (224 eV), and the following peaks between 160 and 170 eV: S 2p_{3/2} (162.2 eV) and S 2p_{1/2} (163.4 eV). The peaks present in the XPS spectra of bulk and exfoliated material remain constant regardless of the sonication energy, indicating a consistent level of oxidation for all samples produced in this study.

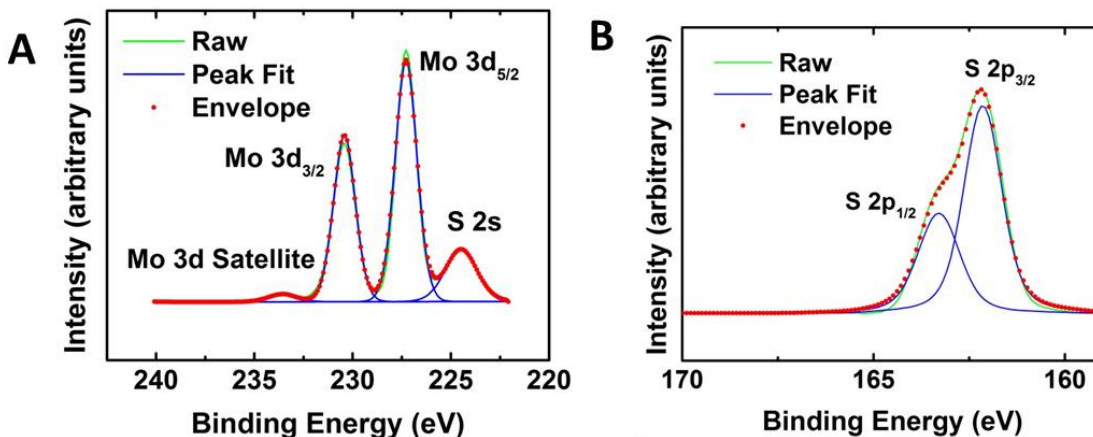


Figure 3.7: (A) Representative Mo 3d XPS spectrum of Pluronic F87-dispersed MoS₂. (B) Representative S 2p XPS spectrum of Pluronic F87-dispersed MoS₂.

The generality of Pluronic F87 as an aqueous dispersant of 2D nanomaterials was explored for BN, WS₂, SnSe, MoSe₂, and WSe₂, all of which showed relatively high concentrations as delineated in Figure 3.8B and C. Overall, the exfoliation yield of the materials studied here falls between 0.2-0.9% given the final concentration with respect to the mass of bulk powder introduced to the mixture before sonication and centrifugation. These values are in line with other ultrasonication-based aqueous and organic exfoliation methods. Unexfoliated material may be recovered from the sediment for re-use.

These 2D nanomaterial dispersions were also characterized by optical absorbance spectroscopy (Figure 3.8A), AFM (Figure 3.8D), ICP-MS, and XPS (Figure 3.9). AFM reveals that the resulting flakes are comparable in dimensions to MoS₂ dispersions, and XPS analysis confirms that the overall chemical composition of these 2D nanomaterials is not altered by the dispersion process. The wide range of 2D nanomaterials that can be effectively dispersed in aqueous solution with Pluronic F87 provides a diverse set of properties for subsequent studies

including thermoelectrics (*i.e.*, SnSe), semiconductors (*i.e.*, MoS₂, WS₂, MoSe₂, and WSe₂), and insulators (*i.e.*, BN).

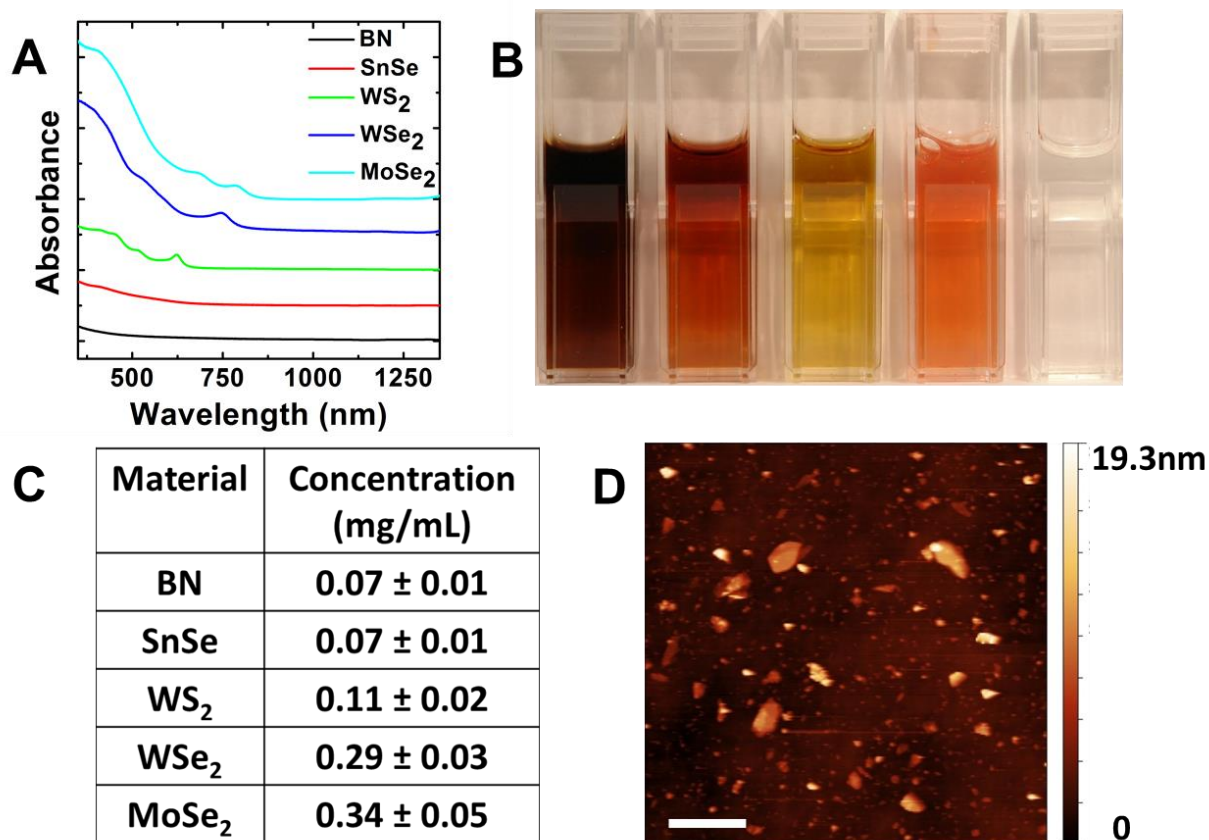


Figure 3.8: (A) Optical absorbance spectra, (B) photograph, (C) concentration by ICP-MS, and (D) representative AFM of BN dispersed by Pluronic F87 in water. Spectra in (A) are vertically offset for clarity. Dispersions pictured in (B) from left to right are: MoSe₂, WSe₂, WS₂, SnSe, and BN. The scale bar in (D) is 500 nm.

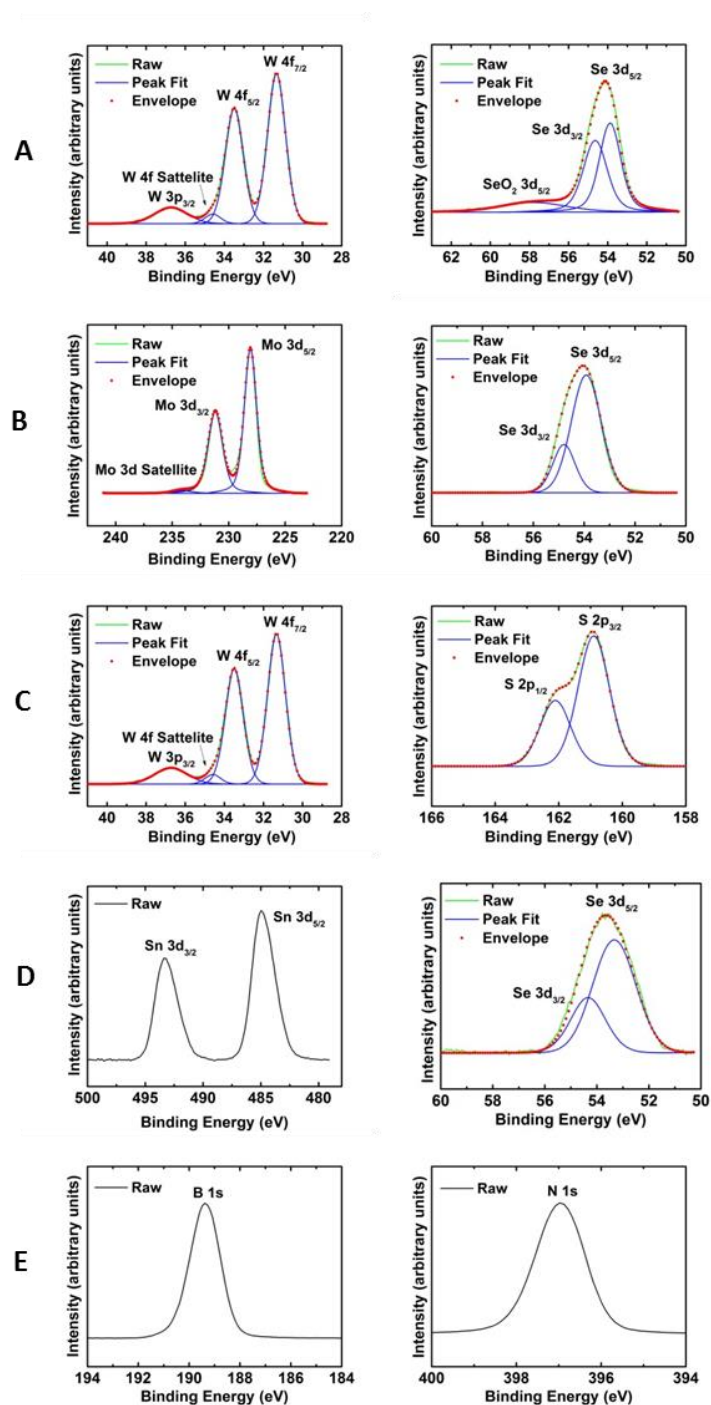


Figure 3.9: Representative XPS spectra of (A) WSe₂, (B) MoSe₂, (C) WS₂, (D) SnSe, and (E) BN dispersed in Pluronic F87. Bulk spectra are identical, confirming that minimal oxidation or contamination occurs during the dispersion process.

3.4 Conclusion

In conclusion, we have demonstrated high-concentration aqueous dispersions of 2D nanomaterials using biocompatible, nonionic block copolymers. A survey of a wide range of Pluronics and Tetronics for MoS₂ optimized the dispersion conditions and yielded maximum concentrations of 0.12 mg/mL for Pluronic F87. Similar results were obtained for Pluronic F87 on multiple other 2D nanomaterials, thus demonstrating the generality of this approach. Since Pluronics and Tetronics are nonionic and widely accepted as biocompatible surfactants, these 2D nanomaterial dispersions may be used for biomedical applications including photoablation therapy and medical device coatings, as well as other applications that harness the superlubricity and catalytic activity of these 2D nanomaterials.^{298,305,321} Furthermore, the use of nonionic Pluronics and Tetronics may facilitate the use of solution-processed 2D nanomaterials in electronic and electrochemical applications since these dispersants lack the charged impurities that are ubiquitous in ionic surfactant dispersions.^{14,322}

CHAPTER 4

Human and Environmental Hazard Assessment of Two-Dimensional Molybdenum Disulfide and Single-Walled Carbon Nanotubes

This chapter is based, in part, on the research described in the following publications:

- 1) Wang, X.; Mansukhani, N.; Guiney, L.; Ji, Z.; Chang, C.H.; Wang, M.; Liao, Y.; Song, T.; Sun, B.; Li, R.; Xia, T.; Hersam, M.C.; Nel, A.E. Toxicological Profiling of Highly Purified Metallic and Semiconducting Single-Walled Carbon Nanotubes in the Rodent Lung and E. Coli. *ACS Nano* **2016**, *10*, 6008-6019.
- 2) Lanphere, J.D.; Luth, C.J.; Guiney, L.; Mansukhani, N.; Hersam, M.C.; Walker, S.L. Fate and Transport of Molybdenum Disulfide Nanomaterials in Sand Columns. *Environ. Eng. Sci.* **2015**, *32*, 163-173.
- 3) Wang, X.; Mansukhani, N.; Guiney, L.; Ji, Z.; Chang, C.H.; Wang, M.; Liao, Y.; Song, T.; Sun, B.; Li, R.; Xia, T.; Hersam, M.C.; Nel, A.E. Differences in the Toxicological Potential of Two-Dimensional vs Aggregated Molybdenum Disulfide in the Lung. *Small* **2015**, *11*, 5079-5087.

***Contribution made by N. Mansukhani in all papers: production and characterization of nanomaterials with refined physicochemical properties.**

Chapter 4 - Human and Environmental Hazard Assessment of Two-Dimensional Molybdenum Disulfide and Single-Walled Carbon Nanotubes

4.1 Introduction

Among different production methods of two-dimensional MoS₂ (2D-MoS₂) and single-walled carbon nanotubes (SWCNT), solution-based processing promises exceptional scalability and low cost, and thus represents the most probable path for incidental exposure including pulmonary exposure.^{191,313} As solution-based nanoscale MoS₂ and SWCNT are poised to enter the market, it is essential to identify their toxic potential and develop safe methods for handling. Furthermore, if the careful implementation of nanomaterials is not employed, then their accidental release into the environment may occur and have long-lasting effects on aquatic life. Therefore, it is crucial that the science community and policy makers have a comprehensive set of research data to help predict the human toxicity, and environmental fate and transport of nanomaterials. Herein, we describe a series of studies completed as collaborations within the University of California Center for Environmental Implications of Nanotechnology that begin to explore the hazard potential of MoS₂ and SWCNT.

In order to assess the potential toxicity and environmental effects of solution-based nanoscale MoS₂ materials, we established a representative test library that includes three aqueous forms of nanoscale MoS₂: chemically exfoliated MoS₂ by lithium ion intercalation (Lit-MoS₂), ultrasonication-assisted exfoliated MoS₂ in the presence of a biocompatible block copolymer, Pluronic F87 (PF87-MoS₂), and aggregated MoS₂ (Agg-MoS₂). These three samples are representative of the possible aqueous nanoscale dispersions of MoS₂ that may enter the market

for the aforementioned applications, spanning chemically and ultrasonically exfoliated, as well as non-surfactant and surfactant stabilization, respectively.

Against this background, we set out to determine whether nanoscale MoS₂ materials pose a biological or environmental hazard. We demonstrate that while Agg-MoS₂ is capable of inducing strong pro-inflammatory and pro-fibrogenic responses *in vitro*, Lit- and PF87-MoS₂ had little or no effects. In an acute oropharyngeal exposure study in mice, Agg-MoS₂ induced acute lung inflammation, while Lit- and PF87-MoS₂ had decreased inflammation or no effects. In a sub-chronic study, all forms of MoS₂ did not induce lung fibrosis. Our data suggest that the exfoliation process attenuates the hazard potential of nanoscale 2D-MoS₂ compared to Agg-MoS₂. Overall, these results suggest strategies for the safe use of nanoscale 2D-MoS₂ materials in industrial and biomedical applications.

We also report the effects of two important environmentally relevant parameters, ionic strength and pH, on MoS₂ nanomaterials stability. Transport studies in a packed bed column and provide critical information regarding how interactions with quartz surfaces influence the transport of MoS₂-PL and MoS₂-Li. The results from this report help to explain the behavior of MoS₂ in engineered or natural systems where they may settle or deposit on sediments in the subsurface water and sheds light on the chemical and physical mechanisms responsible for this behavior.

Finally, we describe hazard profiling for semiconducting (S-SWCNT) and metallic (M-SWCNT) single-walled carbon nanotubes. From a biological perspective, the hazard profiling of purified metallic *versus* semiconducting SWCNTs has only been pursued in bacteria, with the conclusion that aggregated M-SWCNTs are more damaging to bacterial membranes than S-

SWCNTs.³²³ However, no comparative studies have been performed in a mammalian system, where most toxicity studies have been undertaken using relatively crude SWCNTs that include a M:S mix at a 1:2 ratio. In order to compare the toxicological impact of metallic and semiconducting SWCNTs on pulmonary cells and the intact lung, we used density gradient ultracentrifugation (DGU) and extensive rinsing to enrich the population of the SWCNTs with specific chiralities in order to prepare S- and M-SWCNTs at a purity of >98%. DGU allows fractionation of polydisperse SWCNTs into highly purified M- and S-SWCNTs.^{2,5,26} This method has allowed us to gather a representative library of SWCNTs, including S-SWCNTs, M-SWCNTs, unsorted (P2) SWCNTs or a remixed sample containing purified S-SWCNTs and M-SWCNTs in a 2:1 ratio. These materials are unique for the high purity levels (98.5 % S-SWCNT and 98.8 % M-SWCNT) as well as state of dispersion in aqueous biological media.

In vitro screening showed that both tube variants trigger similar amounts of interleukin 1 β (IL-1 β) and transforming growth factor (TGF- β 1) production in THP-1 and BEAS-2B cells, without cytotoxicity. Oropharyngeal aspiration confirmed that both SWCNT variants induce comparable fibrotic effects in the lung and abundance of IL-1 β and TGF- β 1 release in the bronchoalveolar lavage fluid. There was also no change in the morphology, membrane integrity, and viability of *E. coli*, in contradistinction to the previously published effects of aggregated tubes on the bacterial membrane. Collectively, these data indicate that the electronic properties and chirality do not independently impact SWCNT toxicological impact in the lung, which is of significance to the safety assessment and incremental use of purified tubes in the industry.

4.2 Experimental Section

4.2.1 Preparation of MoS₂ Suspensions

The molybdenum disulfide (MoS₂) dispersions were prepared as follows: For lithiated MoS₂ (Lit-MoS₂), lithium ion intercalation was achieved by exposing 300 mg of MoS₂ powder (Sigma Aldrich) to 3 mL of 1.6 M butyllithium solution in hexane while gently stirring for 48 h in an Argon-filled glovebox. The slurry was subsequently transferred to a filter and rinsed with 60 mL hexane. Upon removal from the glovebox, the powder was immersed in 500 mL DI water and bath sonicated immediately to prevent de-intercalation and promote full exfoliation of the MoS₂. The exfoliated solution was briefly centrifuged to remove non-exfoliated MoS₂ and then dialyzed for 7 days to remove excess lithium and hexane. Finally, the solution was removed from dialysis and concentrated using vacuum filtration. Pluronic F87 dispersed MoS₂ (PF87-MoS₂) was prepared by immersing 300 mg of MoS₂ powder in 8 mL 2 % w/v PF87 (BASF) solution in DI water, and then ultrasonicated for 1 hour at an amplitude of approximately 16 Watts. The slurry was centrifuged to remove any non-exfoliated material and aggregates by retaining only the top 80 % of the supernatant. The solution was dialyzed for three days and concentrated using vacuum evaporation. The aggregated MoS₂ (Agg-MoS₂) was prepared from the PF87 dispersion by inducing flocculation through the addition of four parts isopropyl alcohol to one part PF87-MoS₂. The aggregates were filtered from the solution and rinsed thoroughly with DI water, and then resuspended by bath sonication in DI water. The concentrations of the MoS₂ solutions were measured using ICP-MS as described in Section 3.2.3. Briefly, MoS₂ solutions were digested

overnight at 65 °C in nitric acid and subsequently diluted with water and internal standard. Using the ICP-MS measurements, concentration was inferred stoichiometrically.

4.2.2 Source and Preparation of Sorted SWCNTs

P2 SWCNTs (Carbon Solutions, Inc.) were sorted into metallic and semiconducting species using density gradient ultracentrifugation, using a modification of the previously described methods.^{181,206} P2 SWCNTs were dispersed via ultrasonication in an aqueous solution containing 1% w/v surfactant at an initial concentration of 4 mg mL⁻¹ using a Fisher Scientific Sonic Dismembrator 500 for 1 hour at 40% maximum power (~40 Watts). An ice bath was used to prevent heating during sonication. Following sonication, large aggregates were removed via centrifugation at 7500 rpm for 10 minutes using a Beckman-Coulter J-26 XPI Centrifuge. For sorting of metallic SWCNTs, a 3:2 ratio (w/w) of sodium dodecyl sulfate (SDS) and sodium cholate (SC) was used. For sorting of semiconducting tubes, the surfactant was comprised of a 1:4 ratio SDS:SC. Similar ratios were maintained for all aqueous solutions used during DGU sorting.

Linear density gradients were created using aqueous solutions of 60% w/v iodixanol (Optiprep ® purchased from Sigma Aldrich). The gradients were created using a linear gradient maker directly into Beckman-Coulter Ultra Clear ® centrifuge tubes (38.5 mL). An underlayer of 4 mL of 60% iodixanol was pipetted into each tube prior to the linear gradient. For the metallic sort, the linear gradient varied from 20% iodixanol at the top to 35% iodixanol at the bottom, over a volume of 15 mL. For sorting semiconducting tubes, the linear gradient varied from 15% iodixanol at the top to 30% iodixanol at the bottom over a volume of 15 mL. Iodixanol was

added to the P2 SWCNT dispersions to adjust the density of the dispersions. For the metallic sort, the final dispersion was 36% w/v iodixanol; for the semiconducting sort, the final dispersion was 32.5% w/v iodixanol. These SWCNT dispersions were then injected into the centrifuge tubes below the linear density gradient and above the underlayer. An aqueous over-layer containing only the surfactant was pipetted onto the top of the gradient to fill the centrifuge tubes. The tubes were immediately centrifuged for 18 hours at 32,000 rpm using a SW 32 Ti rotor in a Beckman-Coulter Optima L-80 XP centrifuge.

Each centrifuge tube was fractionated using a Piston Gradient Fractionator (Biocomp Instruments, Inc.). 0.25 mm fractions were collected and analyzed optically for purity, using a Cary 500 spectrophotometer. All fractions with metallic or semiconducting purity levels greater than 98% were combined. These combined “pure” metallic or semiconducting dispersions were flocculated by adding ethanol at 1:4 ratio to remove the iodixanol and surfactants. The solutions were then vacuum filtered using a 0.05 μm alumina membrane (Whatman $\text{\textcircled{R}}$ Anodisc) and rinsed with deionized water. Following vacuum filtration, the nanotubes were weighed and then redispersed in deionized water using bath sonication at a concentration of 1 mg mL^{-1} .

Atomic force microscopy (AFM) was used to determine the size distribution of the dispersed SWCNTs in tapping mode in an Asylum Cypher S AFM with Si cantilevers (~290 kHz resonant frequency). To prepare the samples for AFM characterization, silicon wafers were treated with 2.5% (3-aminopropyl) triethoxysilane in isopropyl alcohol for thirty minutes and then rinsed with isopropyl alcohol. The SWCNT dispersion was then drop-casted onto the functionalized silicon wafer and allowed to sit for 10 minutes and then rinsed with deionized water.

4.2.3 Cell culture and Co-incubation with Molybdenum Disulfide

BEAS-2B and THP-1 cells were obtained from ATCC (Manassas, VA). 1×10^4 BEAS-2B cells were cultured in 0.1 mL BEGM in 96-well plates at 37 °C. THP-1 cells were pretreated with 1 µg/mL phorbol 12-myristate acetate (PMA) overnight and primed with 10 ng/mL lipopolysaccharide (LPS) to provide transcriptional activation of the IL-1β precursor.²⁰⁸ Both types of cells were subsequently cultured in 96-well plates (Costar, Corning, NY, USA) at 37 °C for 24 h. MoS₂ suspensions were added to these cultures at 6.25-50 µg/mL. After 24 h of culture, the supernatants were collected for the measurement of IL-8, TNF-α, and IL-1β levels (BD Biosciences, San Diego, CA), using ELISA kits. Cytokine levels were expressed as pg/mL.

4.2.4 Preparation of Nanomaterial Suspensions and Cell Culture with Semiconducting and Metallic SWCNTs

Semiconducting and metallic SWCNT stock solutions were first prepared in DI water at 1 mg/mL. BEAS-2B and THP-1 cells were obtained from ATCC (Manassas, VA). 1×10^4 BEAS-2B cells were cultured in 0.1 mL BEGM in 96-well plates at 37 °C. THP-1 cells were pretreated with 1 µg/mL phorbol 12-myristate acetate (PMA) overnight and primed with 10 ng/mL lipopolysaccharide (LPS). Aliquots of 3×10^4 primed cells were cultured in 0.1 mL medium with carbon nanotubes in 96-well plates (Costar, Corning, NY, USA) at 37 °C for 24 h. In order to provide less aggregated tubes that can be suspended in biological aqueous media, all the SWCNT suspensions were freshly prepared by adding the stock solutions to BEGM or RPMI 1640 media at 12.5-100 µg/mL in the presence of BSA (0.6 mg/mL) and DPPC (0.01 mg/mL). After 24 h of culture, the supernatants were collected for the measurement of IL-1β (BD

Biosciences, San Diego, CA) and TGF- β 1 (Promega, Madison, WI) using ELISA kits according to manufacturer's instructions. Concentrations are expressed as pg/mL.

4.2.5 Cytotoxicity Assessment

Cytotoxicity was determined by an MTS assay, which was carried out with CellTiter 96 Aqueous (Promega Corp.) kit. 1×10^4 BEAS-2B or 3×10^4 THP-1 cells in 100 μ L of culture medium were plated in each well of a 96 multiwell plate (Costar, Corning, NY) for overnight growth. The medium was removed, and cells were treated for 24 h with 100 μ L of 6.25-50 μ g/mL MoS₂ suspensions or 100 μ L of 12.5-100 μ g/mL SWCNT suspensions. After the treatment, the cell culture medium was removed and followed by washing of the plates three times with PBS. Each well received 120 μ L of culture medium containing 16.7 % of MTS stock solution for 1 h at 37 °C in a humidified 5 % CO₂ incubator. The plate was centrifuged at 2000 g for 10 min in NI Eppendorf 5430 with a microplate rotor to spin down the cell debris. An 85 μ L amount of the supernatant was removed from each well and transferred into a new 96 multiwell plate. The absorbance of formazan was read at 490 nm on a SpectraMax M5 microplate reader (Molecular Devices Corp., Sunnyvale, CA, USA).

4.2.6 Mouse Exposure and Assessment of Exposure Outcomes

Eight-week-old male C57Bl/6 mice were purchased from Charles River Laboratories (Hollister, CA). All animals were housed under standard laboratory conditions according to UCLA guidelines for care and treatment as well as the NIH Guide for the Care and Use of Laboratory Animals in Research (DHEW78-23). The animal experiments were approved by the Chancellor's Animal Research Committee at UCLA and include standard operating procedures for animal housing (filter-topped cages; room temperature at 23 ± 2 °C; 60 % relative humidity;

12 h light, 12 h dark cycle) and hygiene status (autoclaved food and acidified water). Animal exposures to nanoparticles were carried out by an oropharyngeal aspiration method developed at NIOSH. Briefly, the animals were anesthetized by intraperitoneal injection of ketamine (100 mg/kg)/xylazine (10 mg/kg) in a total volume of 100 μ L. With the anesthetized animals held in a vertical position, a 50 μ L PBS suspension containing 50 μ g nanoparticles was instilled at the back of the tongue to allow pulmonary aspiration. The experiment included control animals receiving the same volume of PBS with BSA (0.6 mg/mL) and DPPC (0.01 mg/mL). The positive control group in each experiment received 5 mg/kg crystalline silica in the form of quartz (Min-U-Sil or QTZ). The animals in experiment groups received oropharyngeal aspiration of nanomaterial suspensions at 2 mg/Kg at the back of the tongue. The mice were sacrificed after 40 hours to assess acute effects and 21 days to assess sub-chronic effects. The bronchoalveolar lavage fluid (BALF) and lung tissue were collected for measurement of TGF- β 1 and PDGF-AA levels and performance of Hematoxylin and Eosin (H&E) or Masson's trichrome staining.

4.2.7 Sircol Assay to Assess Total Collagen Production

The right upper lobe of each lung was suspended in PBS at ~ 50 mg tissue per ml and homogenized with a tissue homogenizer (Fisher Scientific). Triton X-100 was added at 1% and the samples incubated for 18 h at room temperature. Acetic acid was added to a final of 0.5 M and incubated at room temperature for 90 minutes. Cellular debris was pelleted by centrifugation and the supernatants used to assess total protein, using a BCA Assay kit (Pierce/ThermoFisher Scientific). The Sircol Soluble Collagen Assay kit (Biocolor Ltd., Carrickfergus, UK) was used to extract collagen from duplicate samples, using 200 μ L of supernatant and 800 μ L Sircol Dye Reagent according to the manufacturer's instructions. Similar

prepared collagen standards (10–50 μg) were run in parallel. Collagen pellets were washed twice with alcohol and dried before suspension in an alkaline reagent. Absorbance at 540 nm was read on a plate reader (SpectroMax M5e, Molecular Devices Corp., Sunnyvale, CA). Data were expressed as μg of soluble collagen per mg of total protein.

4.2.8 Statistical Analysis

Mean and standard deviation (SD) were calculated for each parameter. Results were expressed as mean \pm SD of multiple determinations. Comparisons of each group were evaluated by two-sided Student's t tests. A statistically significant difference was assumed when p was <0.05 .

4.2.9 Packed Bed Column Transport Experiments

The effect of ionic strength (1–31.6 mM KCl) on the transport of $\text{MoS}_2\text{-Li}$ and $\text{MoS}_2\text{-PL}$ in saturated porous media was conducted using a packed bed column at pH 5. Transport experiments were conducted using an inverted borosilicate glass column (Omnifit, Boonton, NJ) with an inner diameter of 1.5 cm and a packing depth of 5 cm. Details regarding the packed bed column transport methods, conditions, and sand cleaning procedures can be found in a previous study.³²⁴ Briefly, quartz sand was sieved to obtain an average diameter (d_{50}) of 275 μm and purified before being wet packed at a porosity of 0.47 ± 0.01 in the column prior to transport experiments. MoS_2 suspensions were injected into the column at a flow rate of 2 mL/min to represent similar flow conditions found in the engineered or natural systems using peristaltic pumps and the effluent was collected every minute using a fraction collector (CF 1 Fraction Collector, Spectrum Chromatography, Houston, TX).³²⁵ The effluent was used to determine the concentration at each time interval using a spectrophotometer (DU 800 Beckman Coulter, Fullerton, CA) to correlate the absorbance with concentration. Calibration curves for the $\text{MoS}_2\text{-}$

Li and MoS₂-PL were created by measuring the absorbance as a function of MoS₂ concentration and an R² value of 0.999 was obtained for both types of MoS₂.

Release experiments were also conducted following select transport experiment at each IS for MoS₂-PL and MoS₂-Li to investigate the release of particles as a function of the decrease in IS. To facilitate the release experiments, an additional 12 pore volumes (PV) of DI water was injected into the column after the background absorbance dropped to ~0 and the effluent was collected and the absorbance measured as mentioned earlier.

4.3 Results and Discussion

Agg-, Lit- and PF87-MoS₂ were comprehensively characterized. While Agg-MoS₂ is beyond the size range for AFM measurements, scanning electron microscopy (SEM) analysis shows that these particles span several microns in width and thickness (Figure 4.1A). AFM assessment of PF87-MoS₂ show that these particles have a mean square root surface area of 27.6 ± 15.6 nm and an average height of 5.2 ± 1.1 nm (Figure 4.1B, E and F). Similar measurements show that the Lit-MoS₂ particles are larger than PF87-MoS₂, which have a mean square root surface area of 187.5 ± 126.9 nm and a mean height of 3.9 ± 0.6 nm (Figure 4.1C, E and F). The hydrodynamic sizes of Agg- and Lit-MoS₂ suspended in RPMI 1640 are smaller than BEGM due to the presence of fetal bovine serum (FBS). PF87-MoS₂ is better dispersed than Agg- and Lit-MoS₂ in both media (Table 4.1). The zeta potentials of the three material types were in the range of -4.3 to -8.8 mV in cell culture media, and -12.9 to -34.3 mV in water (Table 4.1).

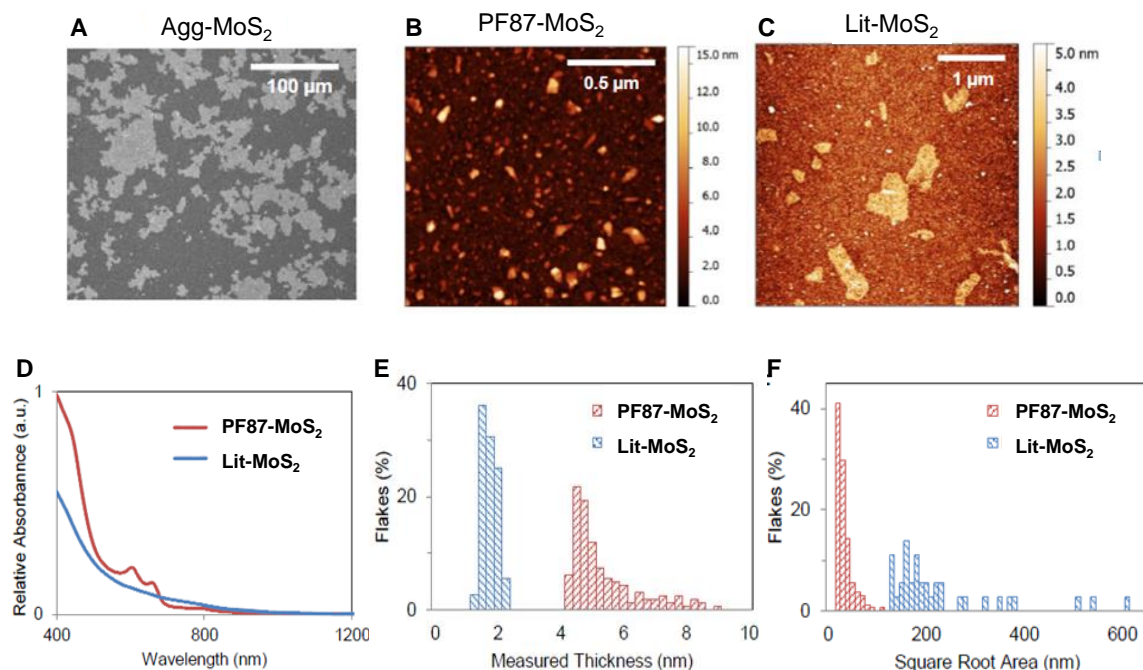


Figure 4.1: Characterization of Agg-, Lit- and PF87-MoS₂. (A) Scanning electron micrograph of Agg-MoS₂. (B, C) Representative atomic force microscopy (AFM) images of PF87-MoS₂ and Lit-MoS₂. (D) Optical absorbance spectra of PF87-MoS₂ and Lit-MoS₂. (E, F) AFM histograms of flake thickness and lateral flake sizes of the exfoliated materials.

	In H ₂ O		In cRPMI1640		In BEGM	
	ζ [mV]	d _H [nm]	ζ [mV]	d _H [nm]	ζ [mV]	d _H [nm]
Agg-MoS ₂	-23.6 ± 0.4	1334.8±47.8	-5.4±1.9	540.8±18.1	-8.8±1.6	1144.7±152.5
Lit-MoS ₂	-34.3 ± 0.1	506.3±11.8	-7.7±3.0	585.6±17.3	-4.3±0.5	746.4±100.3
PF87-MoS ₂	-12.9 ± 1.2	72±0.8	-7.8±1.3	80.1±0.8	-8.5±1.4	78.4±0.7

Table 4.1: Zeta potential and hydrodynamic diameter of MoS₂ materials used in this study, shown in water and cell culture media.

SWCNTs were sorted into metallic and semiconducting variants using density gradient ultracentrifugation of arc-discharge SWCNTs (designated P2) according to the scheme depicted in Figure 4.2A. Density gradient ultracentrifugation (DGU) allows for the separation of M- and

S-SWCNTs.^{174,181,188} Following the removal of detergent by ethanol precipitation and extensive rinsing in deionized (DI) water, the purified M-SWCNT and S-SWCNT dispersions exhibited purities of >98.8% and >98.5%, respectively (Figure 4.2B). Figure 4.2B also shows the absorbance spectrum of the unsorted tubes by optical absorbance spectroscopy. Because the Arc discharge method employs nickel and yttrium as catalysts, ICP-MS was used to determine the amount of residual catalyst in each sample (Table 4.2). Briefly, all three (P2-, M- and S-) SWCNT preparations show a Ni content of ~ 2.40 wt % and a Yi content of ~ 0.43 wt %. Measurement of the size of the sorted SWCNTs by atomic force microscopy (AFM) demonstrated that the semiconducting tubes had an average length of 633 nm and an average diameter of 1.29 nm; the corresponding values for metallic tubes were 634 nm and 1.24 nm, respectively (Figure 4.2C and D). The AFM images also demonstrate excellent dispersion of individual tubes, including narrow length and diameter distributions (Figure 4.2C and D). The corresponding hydrodynamic diameters of the sorted tubes in DI water, complete RPMI medium (containing 10 % FCS), and BEGM (containing 0.6 mg/mL bovine serum albumin and 0.01 mg/mL DPPC), as determined by high-throughput dynamic light scattering (HT-DLS, Dynapro Plate Reader, Wyatt Technology), are shown in Table 4.1. Following dispersion in DI water, the hydrodynamic sizes of S- and M-SWCNTs were 807 and 1192 nm, respectively. Similar trends were seen in BEGM and RPMI media (Table 4.2). There was slightly better dispersion of the unsorted (P2) arc-discharge SWCNTs in both media (Table 4.2). The zeta potential of the tubes ranged from -4.3 to -8.8 mV in cell culture media and -12.9 to -34.3 mV in water.

	P2-SWCNT	M-SWCNT	S-SWCNT
Nickel (wt %)	1.80	2.40	< 0.05
Yttrium (wt %)	0.43	0.10	< 0.04

Table 4.2: The elemental composition of heavy metal impurities in SWCNTs was determined by inductively coupled plasma mass spectroscopy (ICP-MS).

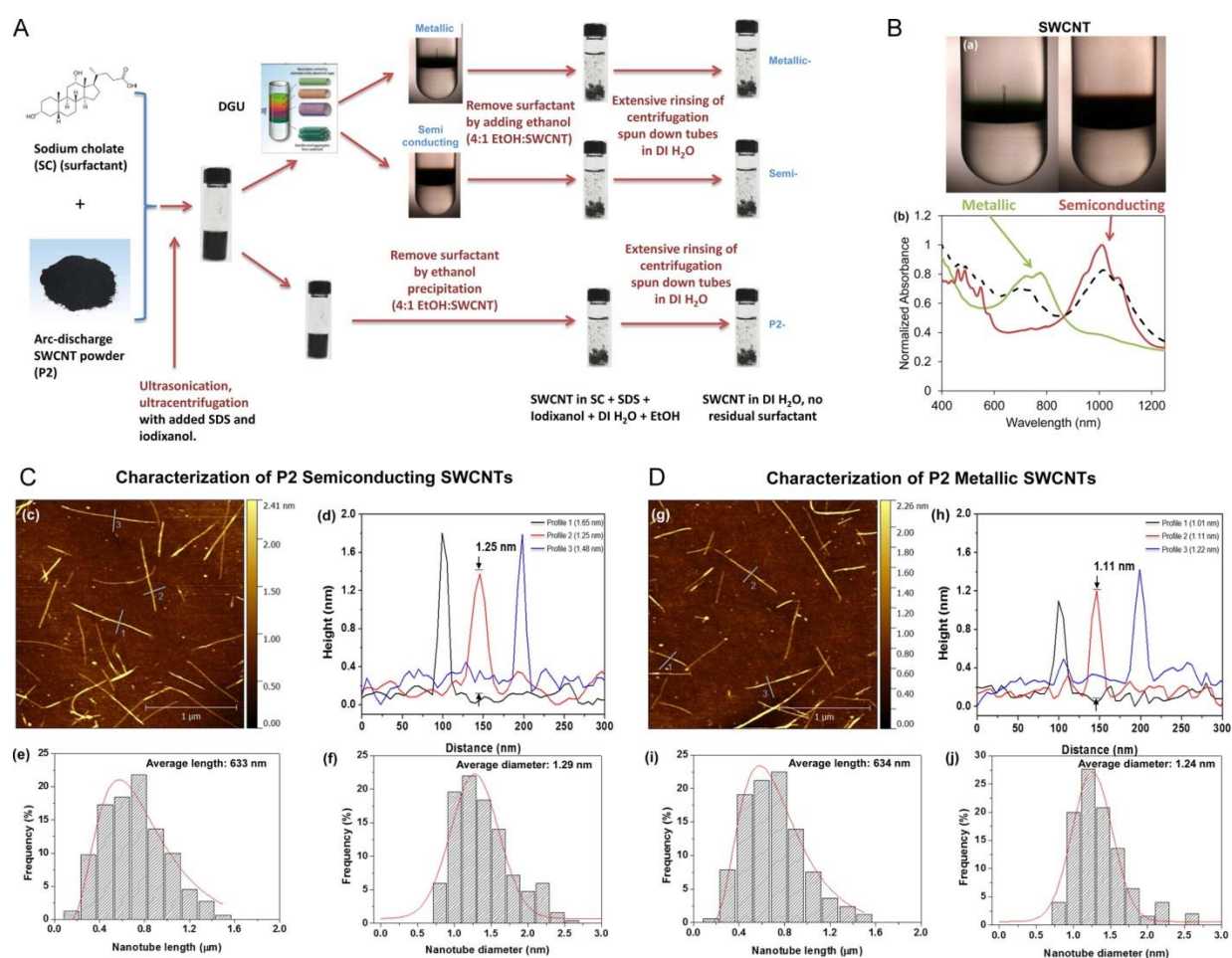


Figure 4.2: Scheme and characterization of the electronic-sorted SWCNTs. (A) Scheme for the preparation of electronic-sorted SWCNTs. P2 SWCNTs were sorted into metallic and semiconducting species using density gradient ultracentrifugation (DGU) methods. The detailed methodology appears in the Experimental Section. (B) Characterization of the sorted SWCNTs. Photograph of the DGU separation tube (a) and corresponding optical absorbance spectra (b). The purity of the final dispersions was >98.8% for M-SWCNT and >98.5% for S-SWCNT, as determined by optical absorbance spectroscopy. (C and D)

Characterization of semiconducting (C) and metallic (D) SWCNTs by AFM and optical absorption spectroscopy. Panels (c) and (g) show the AFM images, panels (d) and (h) show the optical absorption spectra, panels (e) and (i) show length distributions, while panels (f) and (j) show the diameter distributions.

We determined the pro-inflammatory responses of MoS₂ and SWCNT using THP-1 and BEAS-2B cell lines. The myeloid cell line, THP-1, was chosen because it can be differentiated into a lineage with macrophage-like properties, while BEAS-2B cells are derived from human bronchial epithelial cells.^{208,326} These cell types are representative of the cell types that provide the first line of defense at the portal of entry into the lung. While not much is known about the effects of 2D MoS₂ on these cells, it has been documented that BEAS-2B is an immortalized human bronchial epithelial cell line that responds to CNTs with TGF-β1 production and THP-1 differentiates into macrophage-like cells that exhibit NLRP3 inflammasome assembly in response to high aspect ratio (HAR) materials (such as CNTs).^{207,327–329} Use of these cells demonstrated in an MTS assay that none of the MoS₂ form variations or sorted SWCNT had an effect on cell viability (Figure 4.3). In addition, since bioavailability could determine pro-fibrogenic effects, Raman spectroscopy and ICP-OES were used to assess MoS₂ uptake in THP-1 and BEAS-2B cells. This measurement demonstrated that Agg-MoS₂ was present in higher abundance, compared to other materials (Figure 4.4), with PF87-MoS₂ showing the least cellular association. Since these data show good correlation to the lesser pro-inflammatory effects of PF87-MoS₂, it would appear that bioavailability of the materials could indeed determine the effects on cytokine and chemokine production.

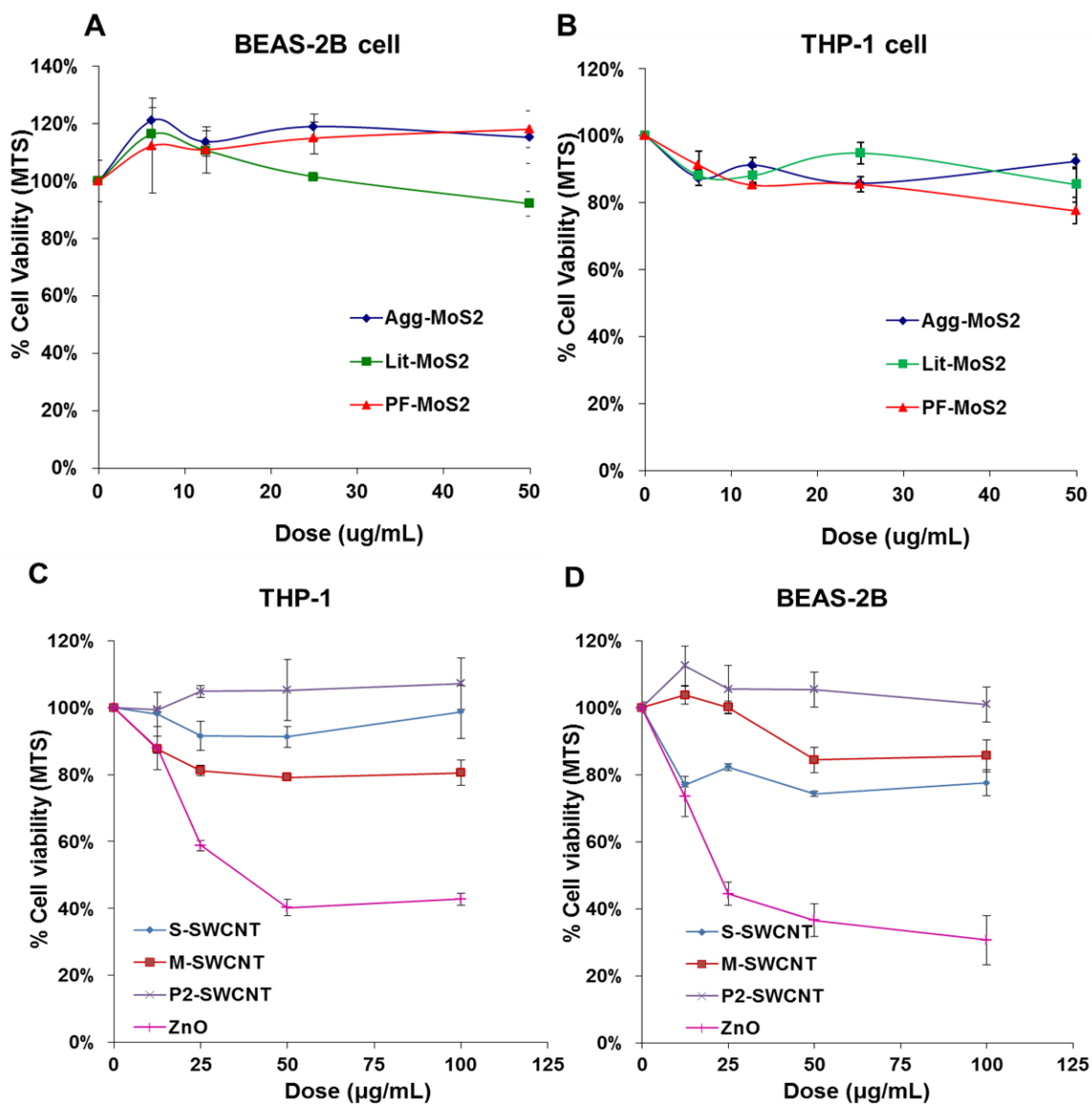


Figure 4.3: Cytotoxicity of MoS₂ (A,B) and SWCNT (C,D) nanomaterials as measured by MTS assay in a dose-dependent manner. Statistical analysis shows that no nanomaterials had a significant impact on cell viability compared to the negative control, ZnO.

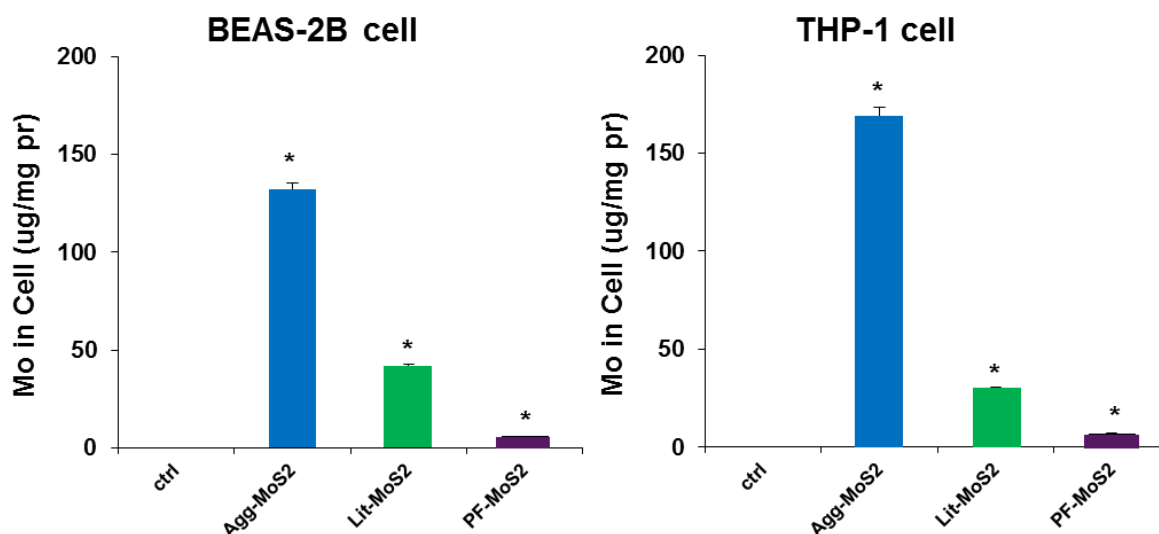


Figure 4.4: Total cellular Mo content in BEAS-2B and THP-1 cells as determined by ICP-OES. Both cell types were exposed to 50 $\mu\text{g/mL}$ MoS₂ for 24 h, following which the cells were recovered, sonicated and used for acid digestion. The concentration in each sample was expressed as μg Mo per mg of cellular protein.

When testing pro-inflammatory cellular effects, we monitored cytokines and chemokines that play important roles in lung inflammation in response to inhaled foreign materials. IL-8, known as a neutrophil chemotactic factor, can induce neutrophil chemotaxis and migration toward sites of particle deposition and inflammation.^{330,331} TNF- α is a member of a group of macrophage-derived cytokines that also play a role in acute inflammation.³³² IL-1 β is an important mediator of acute and sub-chronic inflammatory responses, which can also lead to fibrogenic effects in response to particulate substances and fibers in the lung.^{208,333} TGF- β 1 and PDGF-AA growth factors could be significant from the perspective of pro-fibrogenic pulmonary responses since synergy with IL-1 β during epithelial-mesenchymal transition in the lung in response to carbon nanotubes, graphene and asbestos fibers plays a key role in pulmonary fibrosis.^{202,210,333} Whether growth factor production will result in pulmonary fibrosis is dependent

on the magnitude and duration of the pulmonary response, which is shaped by the dose, lung burden, removal and persistence of the material.^{210,333,334}

When testing pro-inflammatory cellular effects of MoS₂ nanomaterials, we observed that while Agg-MoS₂ induced significant increases in IL-8, TNF- α and IL-1 β production, there were significantly less effects of Lit- or PF87-MoS₂ on cytokine and chemokine production in BEAS-2B and THP-1 cells (Figure 4.5). In addition, the use of an IL-1 β assay to demonstrate the impact of the SWCNTs on NLRP3 inflammasome assembly showed a dose-dependent increase in cytokine production for all tube variants in THP-1 cells (Figure 4.6A). Monosodium urate (MSU) was used as a positive control that induced the strongest effect. Importantly, there was no significant difference in the pro-inflammatory effects of S- *versus* M-SWCNTs. While the assessment of TGF- β 1 production in BEAS-2B yielded less vigorous stimulation indices, it was confirmed that S-SWCNTs do not differ from M-SWCNTs (Figure 4.6B).

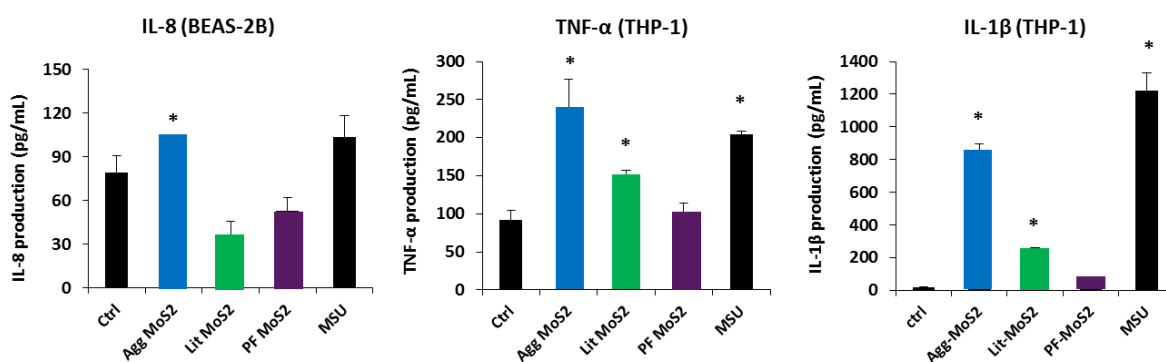


Figure 4.5: Exposure to 2D MoS₂ (PF87-MoS₂ and Lit-MoS₂) resulted in significantly decreased cytokine and chemokine production when compared to aggregated MoS₂, indicating a decreased inflammatory response.

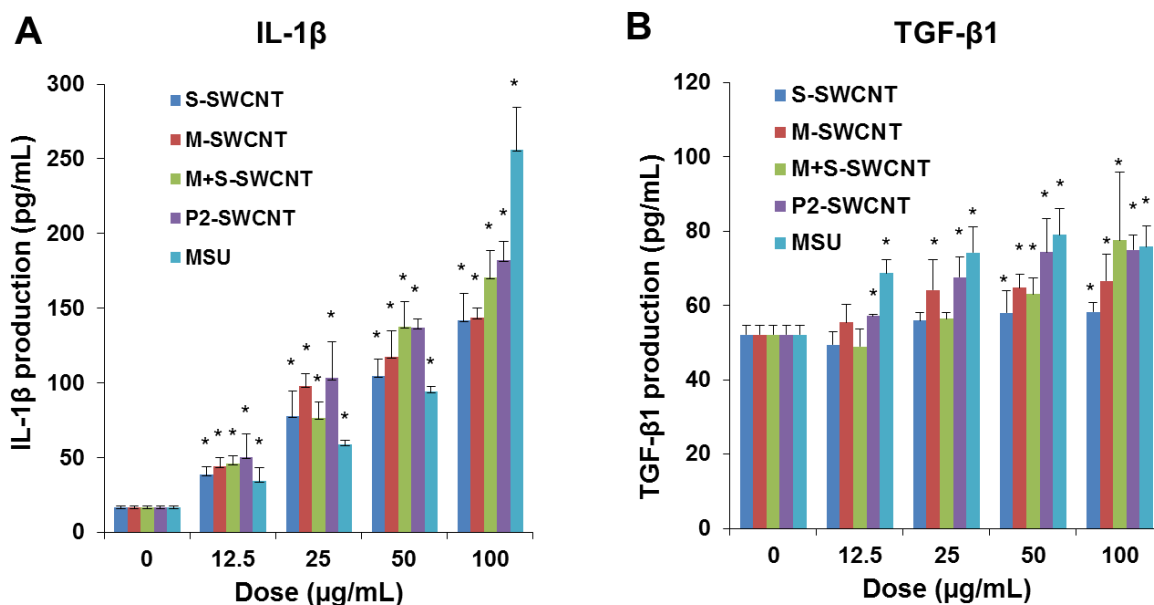


Figure 4.6: Comparative pro-fibrogenic effects, as reflected by IL-1 β and TGF- β 1 production in THP-1 and BEAS-2B cells, respectively. Cells were exposed to the indicated concentrations of the sorted SWCNTs for 24 h. IL-1 β (A) and TGF- β 1 (B) levels were determined on the culture supernatants by ELISA. *p < 0.05 compared to control.

Another important SWCNT characteristic to consider in the cellular response outcome is the electron transfer capabilities of metallic *versus* semiconducting SWCNTs, which could lead to the generation of reactive oxygen species (ROS) and oxidative stress, as shown in bacterial studies.³²³ An abiotic assay to compare ROS production, using the fluorescent dye, 2', 7'-dichlorofluorescein (DCF), was performed. Performance of spectroscopy at 528 nm demonstrated a dose-dependent increase in fluorescence intensity, with M-SWCNTs inducing more ROS generation than S-SWCNTs (Figure 4.7). Co₃O₄, a semiconductor metal oxide, was used as a positive control.³²⁶ Oxidant injury can also be determined by assessing glutathione (GSH) conversion to GSSG, as determined by luminescence-based GSH-Glo assay. Use of this assay under abiotic conditions confirmed that M-SWCNTs lead to more GSH depletion than S-SWCNTs (not shown). No significant differences were observed between M-SWCNTs, P2-

SWCNTs or remixed tubes in this assay. When using the GSH-Glo assay and DCF fluorescence assays to determine the induction of oxidative stress in THP-1 and BEAS-2B cells, which demonstrated slightly increased ROS generation by M- compared to S-SWCNTs (not shown). No differences were observed between M-SWCNTs, P2-SWCNTs, or remixed tubes. All considered, these data demonstrate that in spite of abiotic and cellular differences in the potency of the pro-oxidative SWCNT effects, these dissimilarities do not translate into different levels of IL-1 β and TGF- β 1 production, suggesting that SWCNT characteristics other than chirality play a dominant role in determining the pro-fibrogenic effects of the tubes. This is in keeping with our previous studies demonstrating that a number of SWCNT properties combine in an integrated fashion to generate biological hazard rather than a single property dominating.²¹⁰

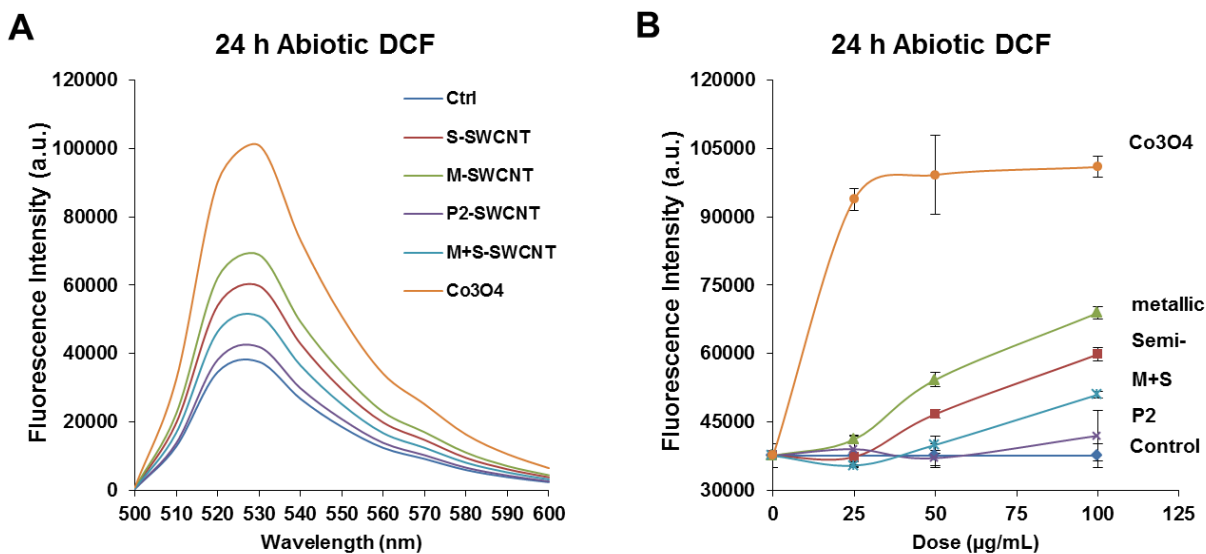


Figure 4.7: DCF fluorescence spectroscopy: 29 $\mu\text{mol/L}$ DCF was added to CNT suspensions at 12.5–100 $\mu\text{g/mL}$ for 24 h, and emission spectra were collected at 500–600 nm, with excitation at 490 nm. Both S- and M-SWCNTs showed significant enhancement of DCF fluorescence compared to the nontreated control. ROS production by Co3O4 NPs at 100 $\mu\text{g/mL}$ was used as positive control. (B) Comparative expression of the fluorescence

intensity at 528 nm demonstrated a proportionally bigger dose-dependent increase in fluorescence activity with metallic compared to semiconducting SWCNTs.

MoS₂ and SWCNT are used in applications with the potential to lead to aerosolized exposure upon inhalation in humans. To determine if they pose pulmonary hazard potential, we used oropharyngeal aspiration to compare our characterized materials in C57Bl/6 mice.

The installation dose was based on the same data for MoS₂ and SWCNT. Due to the absence of MoS₂ exposure data in humans, we used, for comparison, exposure data for MWCNTs in a production laboratory, where the airborne concentration of the tubes can be as high as 400 µg/m³.³³⁵ Assuming a ventilation rate of 20 L/min in healthy human subjects and a particle deposition fraction of 30 %, the estimated exposure (8 h/day, 5 d/week for 16 weeks) of an adult could reach 92.16 mg.³³⁶ Using a human lung alveolar surface area of 102 m², this is equivalent to a deposition level of 903.53 µg/m² in the lung.³³⁷ This equals a dose of 1.81 mg/kg in a 25 g mouse with an alveolar epithelial surface area of 0.05 m².³³⁷ Accordingly, we decided on a 2 mg/kg dose for bolus instillation studies in mice. The positive control included oropharyngeal delivery of 5 mg/kg of Min-U-Sil (α-quartz), a highly inflammogenic material associated with both acute and sub-chronic lung toxicity. Forty hours after oropharyngeal aspiration, Min-U-Sil could be seen to induce significant increases in neutrophil counts in the bronchoalveolar lavage fluid (BALF), along with mild inflammatory changes in the lung (Figure 4.8A). While Agg-MoS₂ induced robust neutrophilic exudation into the BALF, Lit- and PF87-MoS₂ did not trigger the same (Figure 4.8B). Not shown here, the same trends were present for induced increases in LIX (LPS-induced CXC chemokine), MCP-1 (monocyte chemoattractant protein-1) and IL-6 levels. Histopathological changes in animal lungs confirmed these

differential effects (Figure 4.8A), with Agg-MoS₂ inducing focal areas of inflammation around small airways, while Lit- and PF87-MoS₂ had little or no effect. ICP-OES analysis demonstrated less variation in the lung content of the various MoS₂ materials 40 h after initial aspiration (Figure 4.8C). While slightly less for Lit-MoS₂ and PF87-MoS₂ than Agg-MoS₂, the lung content was not statistically significant among the materials and therefore quite different from the variation seen in the cellular studies (Figure 4.4).

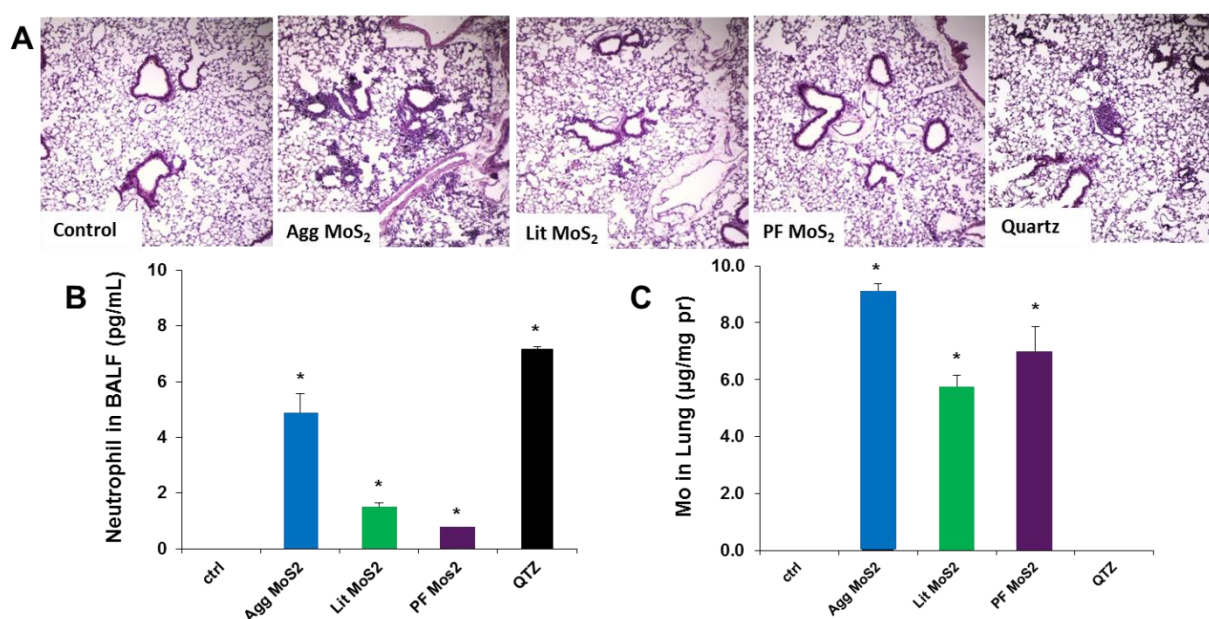


Figure 4.8: Acute pulmonary effects of Agg-, Lit-, and PF87-MoS₂ in mice. Anesthetized C57BL/6 mice were exposed to dispersed MoS₂ materials, delivered by one-time oropharyngeal aspiration of a bolus dose of 2.0 mg/kg. There were 6 animals per group. (A) Representative H&E-stained histological images (100 ×) of the lungs of MoS₂ treated mice. Animals were euthanized after 40 h, and BALF was collected to determine LIX, MCP-1, and IL-6 (not shown) levels as well as measuring neutrophil cell counts (B) Quartz (QTZ) was used as a positive control, at 5.0 mg/kg. *p < 0.05 compared to control.

It is helpful for predictive toxicological modeling to be able to reconcile *in vitro* with *in vivo* dosimetry. We used the lung alveolar epithelium surface area to calculate a surface area dose (SAD) in the mouse. An animal exposed to 2 mg/kg MoS₂ is equivalent to a SAD of 1

mg/m² in a 25 g mouse with an alveolar epithelium surface area of 0.05 m².³³⁷ Assuming that the MoS₂ dose is homogeneously distributed in the tissue culture dish and that the thickness of a cell layer is ~ 15 μm, the *in vitro* exposure dose would be ~ 66 μg/mL. Thus, the *in vitro* dose range (6.25 - 50 μg/mL) that we chose is comparable to the dose in the mouse experiment.

We also determined the sub-chronic effects of MoS₂ in the lung, 21 days post-exposure. Examination of the BALF showed that neutrophil influx had largely disappeared at this point for all of the MoS₂ materials, while quartz still resulted in residual inflammation (not shown). While Min-U-Sil resulted in increased collagen production at 21 days, as determined by a Sircol assay (Figure 4.9B) as well as Masson's trichrome staining (Figure 4.9A), none of the MoS₂ materials resulted in increased collagen production or interstitial collagen deposition in the lungs of exposed animals. Moreover, ICP-OES analysis showed that MoS₂ retention in the lung was considerably reduced (Figure 4.9C). While there was less retention of PF87-MoS₂, the lung contents of Agg- and PF87-MoS₂ were similar. This suggests that the absent or reduced inflammatory effects of the exfoliated materials in the lung have less to do with the total dose than the decreased inflammatory potential of Lit- and PF87-MoS₂ in the lung.

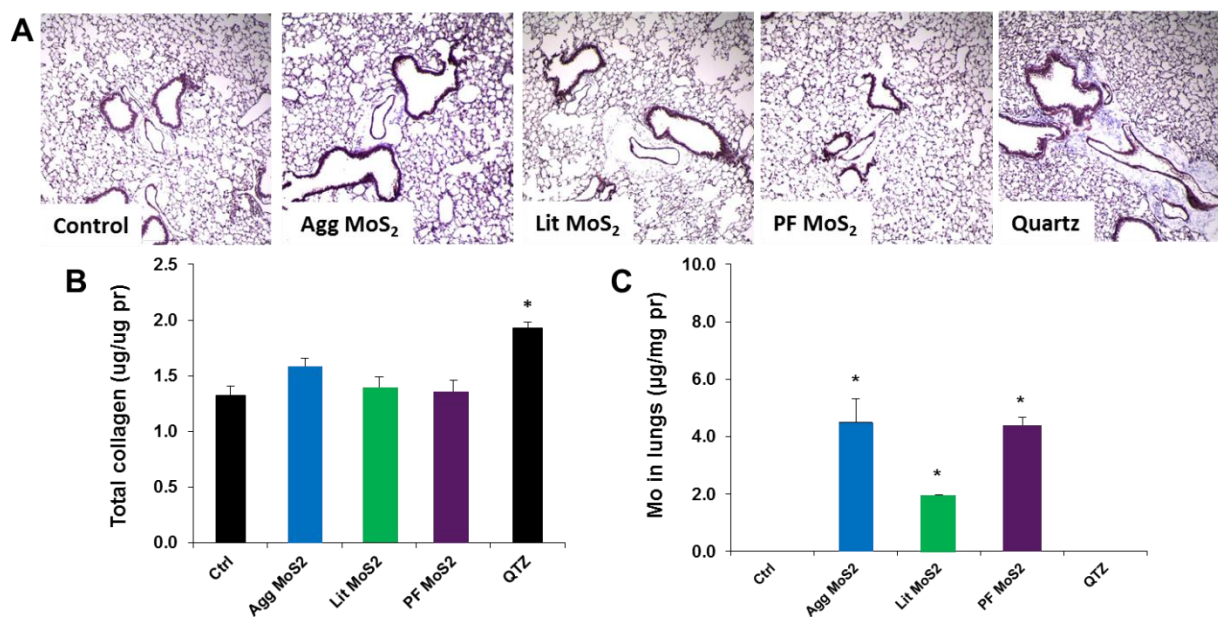


Figure 4.9: Assessment of the possible fibrotic effects of MoS₂ materials 21 days after oropharyngeal installation. The experiment, described in Figure 4, was repeated with the exception that animal sacrifice was performed 21 days after oropharyngeal inspiration of a similar particle dose. There were 6 animals in each group. (A) Collagen deposition in the lung as determined by Masson's trichrome staining. Lung tissue was embedded, sectioned, stained with the Masson's trichrome and observed at 100 × magnification. Blue staining represents collagen deposition in the lung. (B) Total collagen content of the lung tissue was determined using the Sircol collagen kit (Biocolor Ltd., Carrickfergus, U.K.). **p* < 0.05 compared with control. (C) ICP-OES analysis of MoS₂ retention in the lung, showing considerably reduced lung burden. Animals exposed to Quartz (QTZ) served as positive control.

For SWCNT, animal sacrifice was performed 21 days after exposure. Examination of the BALF demonstrated non-significant changes in the total and differential counts in animals exposed to the SWCNTs preparations. Only quartz resulted in a slightly higher neutrophil count after 21 days. Histological examination showed mild pulmonary inflammation in response to quartz and to all of the SWCNT types. These morphological changes were accompanied by a significant increase in TGF-β1 levels in the BALF for quartz and for all SWCNT types (Figure 4.10A). However, there were no differences in the extent of pulmonary inflammation or TGF-β1

levels between metallic and semiconducting SWCNTs. Similar observations were made when measuring PDGF-AA: all the SWCNT types induced an indiscriminate increase in PDGF-AA levels in the BALF (Figure 4.10B). Moreover, while all the tubes and quartz induced increased collagen deposition in the lung as determined by a Sircol assay, we did not observe a significant difference between S- and M-SWCNTs (Figure 4.10C). This was further confirmed by visualization of the collagen deposition with Masson's trichrome staining, which revealed mild but equivalent amounts of lung fibrosis for S-SWCNTs compared to M-SWCNTs (Figure 4.10D). Thus, in spite of the differences in the electron transduction capabilities and the pro-oxidative effects of these materials *in vitro*, we did not observe an independent contribution of chirality to the pro-fibrogenic potential of SWCNTs in the lung.

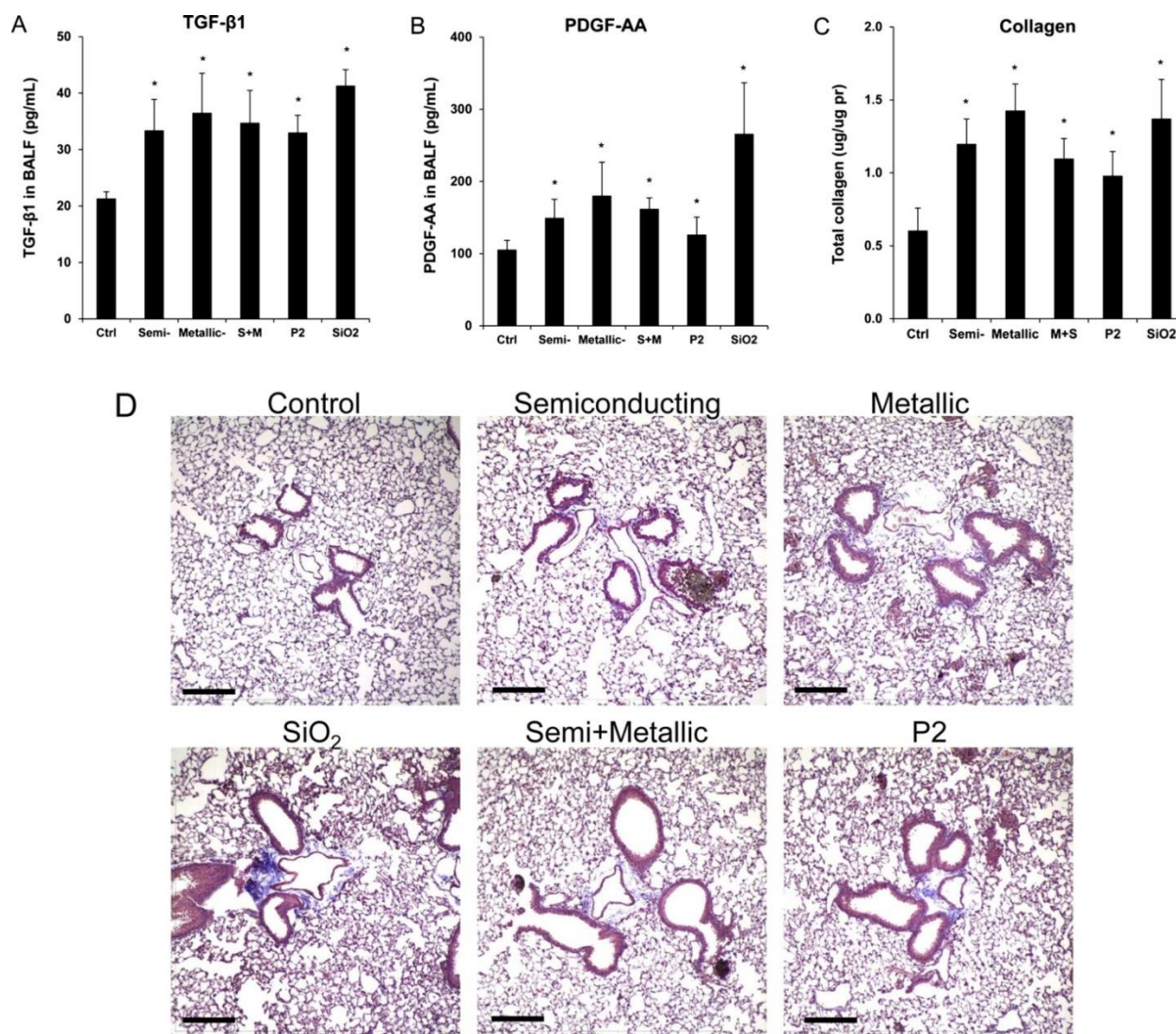


Figure 4.10: Assessment of the pro-fibrogenic effects of the electronic-sorted SWCNTs in mice. Anesthetized C57BL/6 mice were exposed to SWCNTs, delivered by one-time oropharyngeal aspiration of a 2.0 mg/kg bolus dose. Animals were euthanized after 21 d, and BALF was collected to determine (A) TGF- β 1 and (B) PDGF-AA levels. (C) Assessment of total collagen content by a Sircol kit (Biocolor Ltd., Carrickfergus, UK). * $p < 0.05$ compared to control. (D) Visualization of collagen deposition in the lung, using Masson's trichrome staining. Collagen deposition is shown as blue staining under 100 \times magnification. Animals exposed to quartz (QTZ, SiO₂) served as positive control.

Finally, to understand the transport and fate of MoS₂ nanomaterials in the environment, the effective hydrodynamic diameter was measured across an environmentally relevant pH range of 4-10 and an IS range of 0.1-100 mM KCl, respectively. Dynamic light scattering (Brookhaven model BI-9000, Holtsville NY) measurements taken at a wavelength of 661 nm and a scattering angle of 90° were used to determine the effective hydrodynamic diameter of the MoS₂ suspensions. Changes in the pH had no effect on the stability of the PF87-MoS₂ while we saw some slight variations in the effective diameter of the Lit-MoS₂, especially at low pH. This sensitivity to low pH may result in Lit-MoS₂ settling down or removed when moving through sediment beds. In modulating the ionic strength, we saw that the effective diameter does not increase below 10mM KCl. This trend is similar for both forms of 2D MoS₂ but we saw a much more profound effect with the Lit-MoS₂ by almost an order of magnitude. This is most likely due to the loss of the electric double layer repulsion. The effective diameter of PF87-MoS₂ does not increase as profoundly due to the increased stability provided by the pluronic surfactant coating—a result also observed with graphene and carbon nanotubes that had been dispersed using a Pluronic surfactant. Traditional methods used to synthesize Lit-MoS₂ may result in increased transport in sediment beds and aquatic systems under environmentally relevant conditions (1-10 mM KCl). However, at higher IS (≥ 31.6 mM KCl), Lit-MoS₂ becomes less stable and aggregates to sizes greater than 1.5 microns. Under these conditions, Lit-MoS₂ will likely be removed via straining and as a result of secondary minimum interactions in sediment beds and may potentially bio-accumulate in benthic organisms. Conversely, the PF87-MoS₂ will tend to transport farther in aqueous systems due to its stable characteristics at environmental conditions (pH 5-9). However, in packed-bed column experiments, PF-87-MoS₂ had a higher

affinity to be deposited and attach to quartz surfaces, perhaps owing to the presence of the hydrophilic polymer chains. Lit-MoS₂ will be more mobile in sediment beds and aquatic systems under environmentally relevant conditions, which may lead to increased transport through aqueous channels (Figure 4.12).

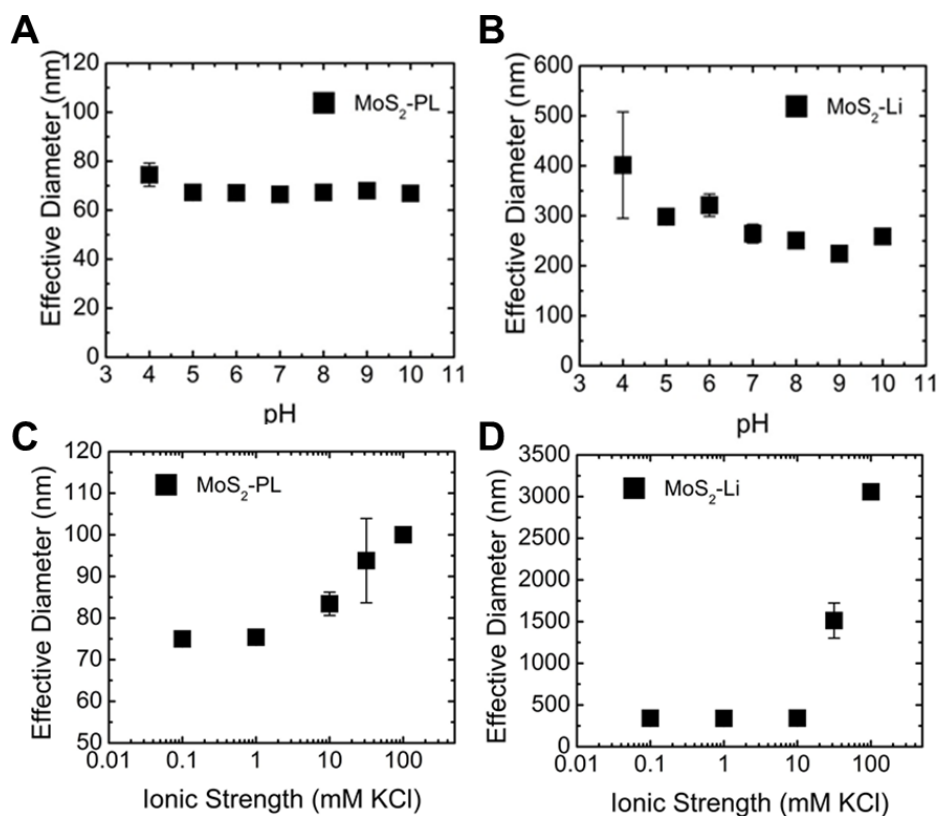


Figure 4.11: Effective diameter as a function of pH (A,B) and ionic strength (C,D) for Pluronic-dispersed MoS₂ (A,C) and Lithiated MoS₂ (B,D).

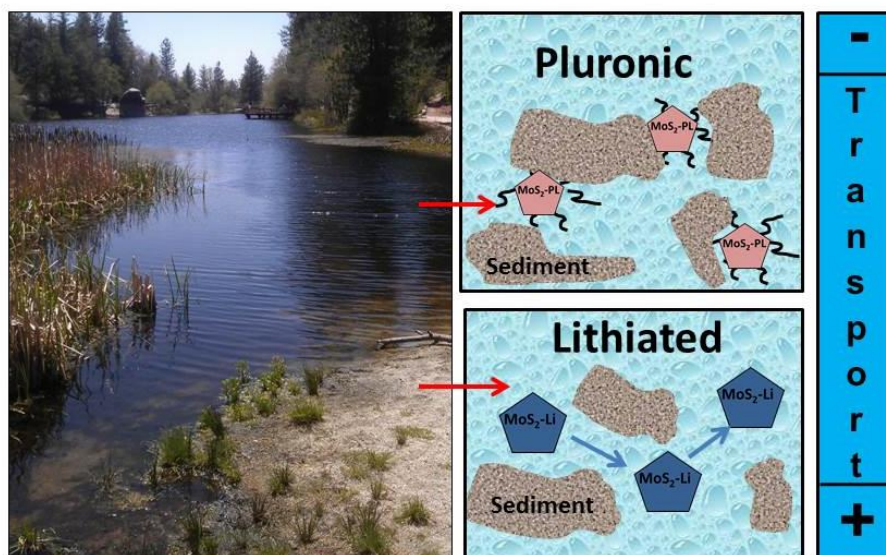


Figure 4.12: Summary of packed-bed column transport study, wherein it was found that Pluronic-dispersed MoS₂ has a higher affinity for quartz media.

4.4 Conclusion

In summary, we have contributed to successful studies on the human and environmental hazard of MoS₂ and SWCNT materials that are of high importance from a regulatory perspective. We addressed the lack of risk assessment for nanoscale MoS₂ by performing comprehensive *in vitro* and *in vivo* toxicological analysis for exfoliated vs. aggregated MoS₂ materials. Our results demonstrate that 2D-MoS₂, including Lit- and PF87-MoS₂, elicit significantly reduced pro-inflammatory effects compared to Agg-MoS₂ at cellular and lung levels. In addition, all MoS₂ formulations did not induce sub-chronic effects in the lung. The reduced hazard of 2D-MoS₂ materials is correlated to improved dispersion and surface coating, which play important roles in determining the bioavailability and surface reactivity of the exfoliated materials. These data suggest that 2D-MoS₂ materials are safer than Agg-MoS₂, which may promote the safe use of 2D-MoS₂ for industrial and biomedical applications. A look at the

environmental fate of MoS₂ nanomaterials showed that while Pluronic-dispersed MoS₂ may be environmentally more stable, it has a higher affinity for quartz surfaces and therefore could deposit more readily than lithiated MoS₂ in aqueous systems. Lithiated MoS₂, on the other hand, has limited stability in environmentally relevant conditions but a lower affinity for quartz surfaces.

We demonstrate that in spite of increased pro-oxidative effects of metallic *versus* semiconducting SWCNTs under abiotic and cellular conditions, there are no differences in the hazard potential of these materials when assessed for their pro-fibrogenic effects in the lung. Our data indicate that highly purified, electronic-sorted SWCNTs do not show significant differences in their hazard potential in the lung. Currently, there appears to be no necessity to use chirality as an independent category for regulatory purposes. These results will also be of significant interest to those interested in using sorted SWCNTs and nanoscale MoS₂ for commercial purposes.

CHAPTER 5

Optothermally Reversible Carbon Nanotube-DNA Supramolecular Hybrid Hydrogel

This chapter is based, in part, on the research described in the following publication:
Mansukhani, N.; Guiney, L.M.; Wei, Z.; Roth, E.W.; Putz, K.; Lijten, E.; Hersam, M.C.
Optothermally Reversible Carbon Nanotube-DNA Supramolecular Hybrid Hydrogel. *In preparation.*

Chapter 5 - Optothermally Reversible Carbon Nanotube-DNA Supramolecular Hydrogel

5.1 Introduction

Hydrogels have attracted wide interest for a variety of mechanical, biomedical, and chemical applications.^{338–344} They are typically based on hydrophilic polymers with covalent cross-linking forces, and have the ability to swell by absorbing and retaining large amounts of water. Supramolecular hydrogels (SMH), on the other hand, consist of a wide range of molecules, biomolecules, and functionalized nanoparticles, and are generally cross-linked by non-covalent forces such as electrostatic interactions, hydrogen bonding, metal–ligand bonding, or host–guest chemistry.^{269,285,345–347} Non-covalent cross-linking forces are relatively weak and dynamic, resulting in constructs that are highly adaptable, tunable, and stimuli-responsive. Consequently, SMH have received wide attention for applications such as self-healing, sensing, and cell encapsulation.^{280,281,348–351}

Single-walled carbon nanotubes (CNT) are well known for their extraordinary physical, optical, and electronic properties.^{35,39,125,147} Among their interesting optical properties are strong absorption peaks due to van Hove singularities that shift depending on the chiral vector of the CNT. Many CNT, for example, absorb light in the near-infrared (NIR) region, which falls in the biological transparency window.^{31,352,353} Since CNT are hydrophobic, functionalization is necessary to form pristine dispersions in aqueous solutions. Covalent functionalization of CNT results in a disruption of the optical properties, while non-covalent functionalization—using

surfactants, synthetic polymers or biomolecules, such as DNA—preserves the molecular structure of the CNT and thus the optical properties.^{173,354,355}

There are many documented examples of the use of CNT in hydrogel and SMH constructs. CNT have been incorporated in traditional hydrogels, where they readily provide mechanical reinforcement and stimuli-responsive properties, most often a mechanical response upon exposure to NIR irradiation.^{356–360} At high concentration, CNT form gels without additives through van der Waals bonding.^{361,362} Finally, since CNT can complex with a variety of macromolecules, they have formed SMH in conjunction with polymers, polysaccharides, DNA, and other biomolecules.^{363,364} Yet, although there have been examples of thermal, chemical, and optical responsiveness in CNT SMH, a NIR-reversible CNT SMH has not been reported.^{365–370}

Here, we present a novel SMH comprised only of CNT, DNA, and buffer, employing DNA base pairing as the cross-linking force. Moreover, we demonstrate the highly tunable mechanical properties of this system as a function of the concentration of CNT, and the stability of the SMH as a function of the DNA sequence length across a biologically relevant range of pH. We posit that the behavior of the gel can be described by molecular dynamics simulations that relate cross-linking density to CNT concentration and DNA sequence length. Finally, we demonstrate the full thermal and optical reversibility of these hydrogels, using heat or a NIR light source to trigger a gel–sol transition. This CNT–DNA SMH has potential in a range of applications, such as substrate-responsive materials, sensing, and 3D printing.^{355,371,372}

5.2 Experimental Section

5.2.1 Dispersion of CNT in DNA

Single-walled CoMoCAT® carbon nanotubes (CNT) enriched in the (6,5) chirality were obtained from SouthWest Nano Technologies, Inc. (Norman, OK) and used in their original form (SG65). DNA strands were purchased from Alpha DNA (Montreal, Quebec), and diluted in buffer made from 4-(2-hydroxyethyl)-1-piperazineethanesulfonic acid (HEPES), potassium acetate, and sodium chloride, all purchased from Sigma-Aldrich. Genomic DNA was purchased from Thermo Fisher Scientific in the form of UltraPure™ Salmon Sperm DNA. Float-a-Lyzer G2 100kDa dialysis tubes were obtained from Spectrum Labs.

In a 4 dram vial, equal amounts (by weight) of SG(6,5) CNT powder and (AC)₁₂S1 DNA were mixed with duplex buffer (30 mM HEPES, 100 mM Potassium Acetate, 1M NaCl, pH 7.5). The mixture was ultrasonicated for 1 hour at a power level of 8–10 W while cooled in an ice bath. Following ultrasonication, the slurry was centrifuged in 1.5 mL conical Eppendorf tubes to remove aggregates, following which the top 80% was carefully removed with a 20-gauge needle. The resulting dispersion was then dialyzed for a minimum of 3 days in a 100 kDa membrane against duplex buffer, during which the buffer was changed daily.

Ultrasonication was performed in a Fisher Scientific Model 500 Sonic Dismembrator with a 0.125 inch diameter tip, followed by centrifugation in an Eppendorf Model 5424 Microcentrifuge using a 45° fixed-angle rotor (FA-45-24-11) for 1 hour at 15,000 rpm. Once decanted, the resultant dispersion was dialyzed for three days against buffer to remove excess DNA.

5.2.2 Optical Characterization

Optical absorbance spectra were used to determine the CNT concentration and quality of CNT–DNA dispersions prior to gel synthesis. Spectra were measured in a Cary 5000 UV-Vis-NIR spectrophotometer with 1cm optical path plastic cuvettes. A representative spectrum is shown in Figure 5.1.

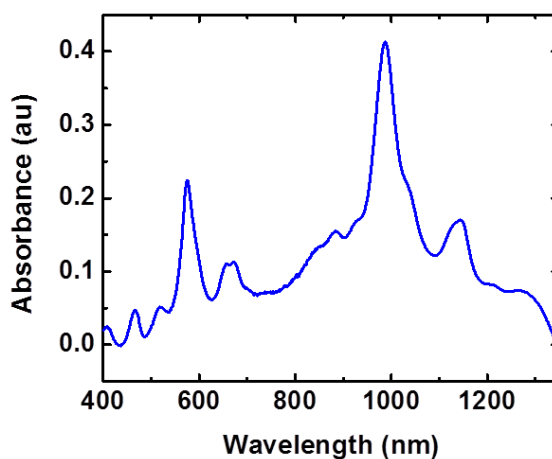


Figure 5.1: Representative UV-Vis spectra of CNT before gelation.

Photoluminescence excitation (PLE) spectra were recorded on a Horiba Fluorolog-3 spectrofluorometer employing a 450W Xe lamp. The CNT samples were measured with an excitation wavelength of 568 nm and emission was measured between 930–1030 nm. For (6,5) CNT, the peak emission is generally near 985 nm. To minimize Rayleigh scattering while concurrently optimizing signal intensity, a 30-second integration time was used, excitation and emission slit widths were set to 10nm, and optical longpass filters of 475 nm and 832 nm were used for excitation and emission, respectively.

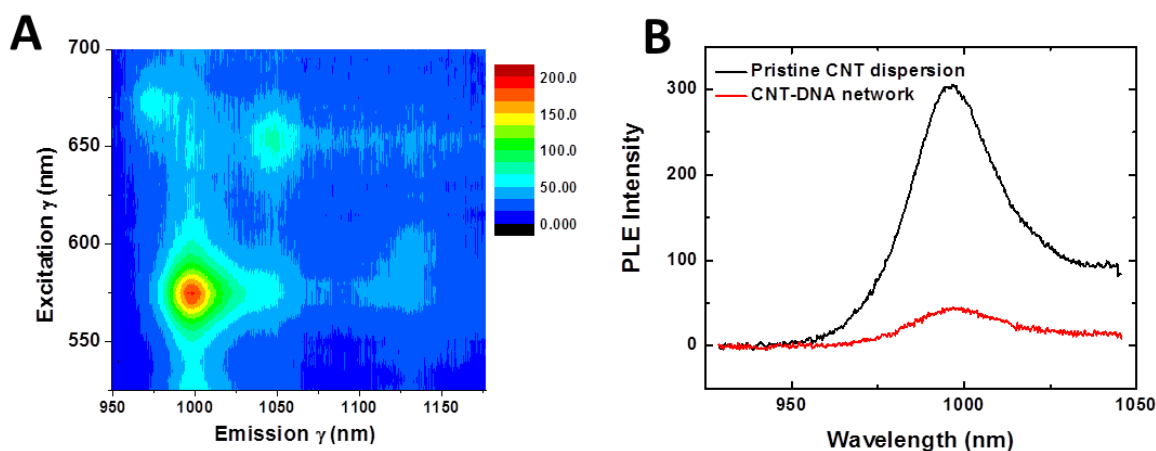


Figure 5.2: A) PLE map of CNT–DNA dispersions, showing predominance of (6,5) chirality CNT. B) Representative PLE spectra of a pristine CNT dispersion and a CNT–DNA network after the addition of linker DNA.

PLE spectra were further used to quantify the formation of CNT–DNA networks under dilute conditions. CNT exhibit PLE only when finely dispersed in solution. Hence, upon addition of linker DNA and subsequent network formation, PLE was quenched. A representative PLE map and spectra before and after network formation are shown in Figure 5.2. To quantify the CNT–DNA network formation, we compare the network PLE intensity to the maximum PLE intensity measured before the addition of linker DNA.

5.2.3 NIR-Triggered Release of DNA from CNT

This research grew out of a previous project in collaboration with Matthew Duch in which CNT were used as DNA delivery vehicles.

CNT are well-suited for targeted, time-resolved, multi-gene delivery due to a combination of unique properties. First, they are biocompatible, as demonstrated in collaboration with the Northwestern University Feinberg School of Medicine.^{205,373} Second, they exhibit strong interactions with DNA, allowing for delivery of nucleic acids and any molecule that binds to

nucleic acids, such as proteins.¹⁷³ Lastly, their optical properties result in strong absorption at specific frequencies in the near-infrared (NIR) region, which fall within the optical transparency window for biological tissue.

For this gene therapy construct, SWCNTs will be dispersed in single-stranded DNA (the carrier strand) that is hybridized to the strand to be released (the payload strand) on an overhang, as shown in Figure 5.3. These SWCNTs will be locally triggered to release the ssDNA or siRNA payload via local heating induced by absorption specific frequencies of NIR light that is converted to thermal energy. Time-resolved multi-gene therapy can be realized by using a series of carbon nanomaterials with distinct functional groups and NIR absorption peaks. In this way, the release of the different nucleic acids and/or proteins can be triggered independently via resonant absorption of different NIR wavelengths. Furthermore, the optical properties of SWCNTs imply that predictable shifts in the NIR absorption spectrum will occur upon release of biological molecules and changes in the local environment.³⁷⁴ These optical properties will allow for NIR imaging before, during, and after gene therapy. Additionally, functionalization with iron oxide nanoparticles or gadolinium also presents a new method to manipulate the nanomaterials with applied magnetic fields and/or gain higher contrast in magnetic resonance imaging (MRI).³⁷⁵ Thus, this method has potential to provide an extraordinarily powerful new method for spatially and temporally resolved multi-gene therapy and real-time imaging utilizing carbon nanomaterials.

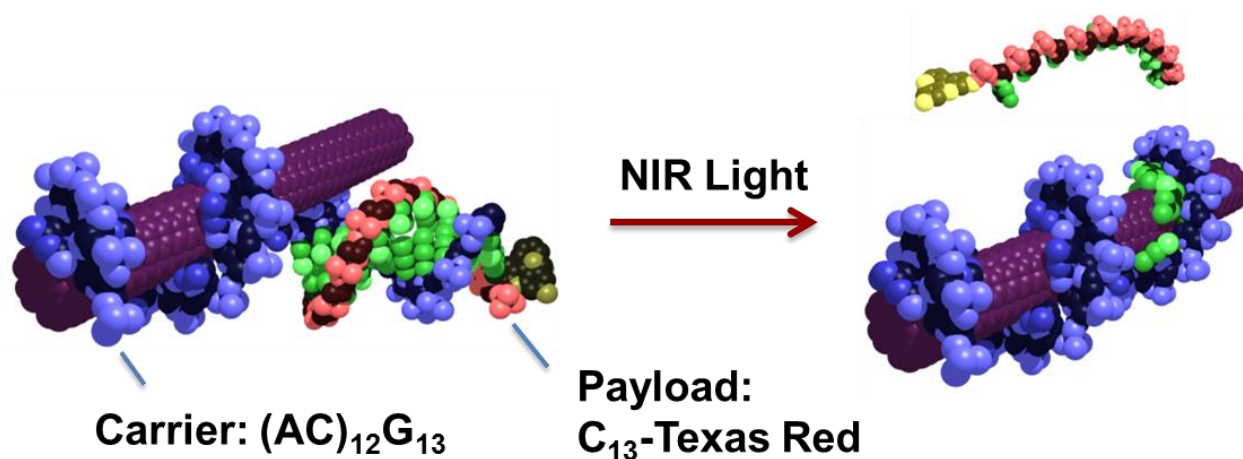


Figure 5.3: Schematic of the CNT/ssDNA/siRNA complex before and after thermal separation induced by NIR excitation.

For DNA release studies, the same procedure described in Section 6.2.1 was used to disperse CNT in carrier DNA, with (AC)₁₂G₁₃ DNA and 0.1M NaCl solution instead of buffer. Following dispersion in carrier DNA and dialysis, an excess of payload DNA (C₁₃ free ssDNA complexed with fluorophore Texas Red) was added to the solution and allowed to hybridize sealed at room temperature for at least 3 days. Trial and error found that a 2:3 ratio of SWCNT: payload DNA by mass was sufficient to enable overhang formation. A salt concentration of 0.1M NaCl is maintained throughout this mixing process. For a series of 3-6 days, the UV-Vis is monitored to observe the shift of the S22 peak from 994 to 996 nm, indicating that hybridization has occurred, as shown in Figure 5.5. Once hybridization has occurred, the solution is dialyzed in 0.1M NaCl using a 100kDa MWCO membrane and stirred continuously for a week to remove any excess reagents or unformed products.

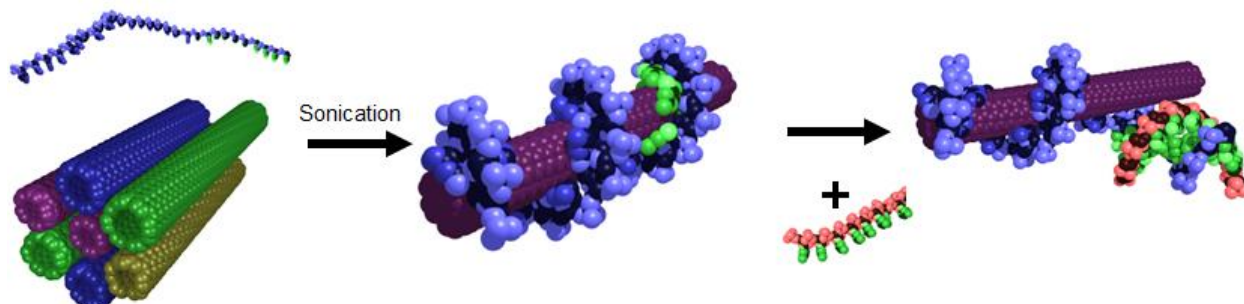


Figure 5.4: Hybridization process to form double-stranded overhang functionalization. ssDNA is used to disperse CNT in solution, followed by a complementary strand added in excess that hybridizes to the ssDNA already adsorbed to the surface of the CNT.

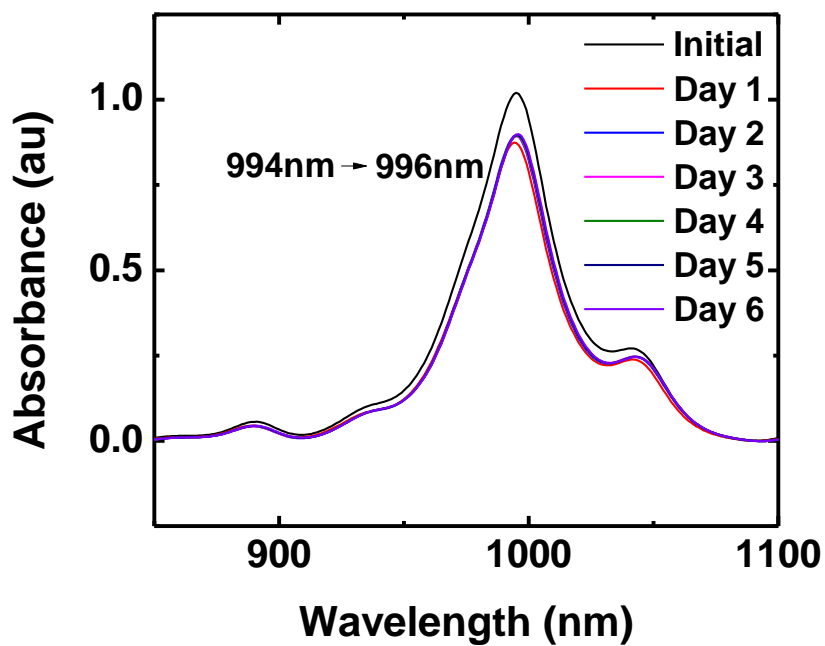


Figure 5.5: Optical absorption spectra showing the overhang formation. The shift in the S22 peak from 994 to 996 nm indicates that the overhang hybridization is complete.

The fluorophore is quenched by interacting with the surface of the nanotube. Therefore, upon triggered release of the payload strand, the fluorescence of the solution increases dramatically. For preliminary payload release studies using heat as the trigger, the final SWCNT solutions were taken out of dialysis and sufficiently diluted so as not to saturate the fluorescence detector. The sample was placed in an ISS PC1 spectrofluorimeter equipped with a temperature-controlled sample chamber. The temperature was raised at a rate of approximately 1°C per minute. At every 1°C increase in temperature, the fluorescence was measured. As shown in Figure 5.6, this process yielded a sharp increase in fluorescence, indicating the successful release of the payload DNA strand. The ratio to room temperature fluorescence is plotted to normalize the data regardless of their original fluorescence, and hence the concentration of SWCNT in solution. The release of the C₁₃ strand is compared to a control sample in which A₁₃ was added in its place. Since A₁₃ is not complementary to the carrier strand, it does not hybridize to the surface of the CNT and therefore is mostly removed by dialysis. The result shown in Figure 5.6 is further evidence that the proposed mechanism of hybridization has occurred.

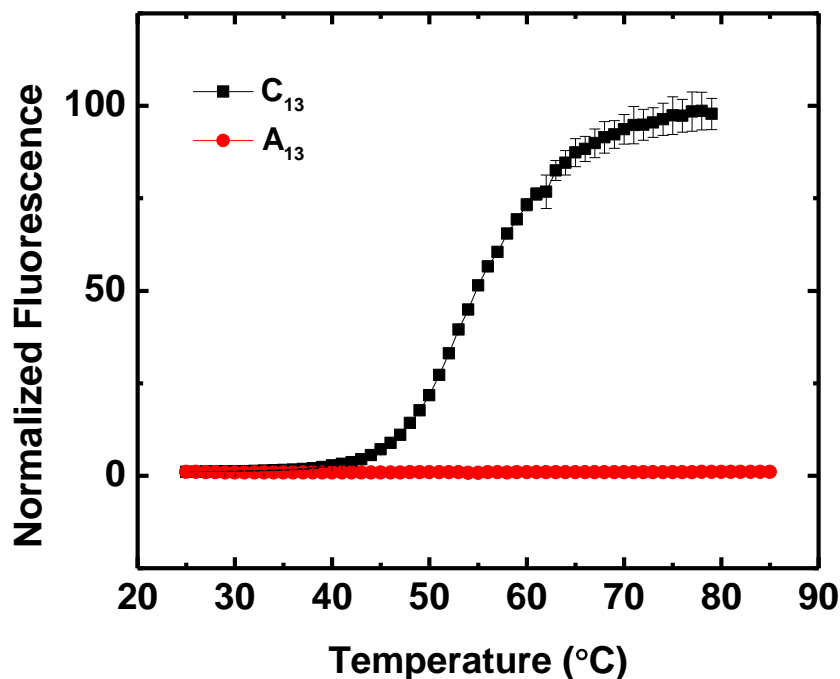


Figure 5.6: Normalized fluorescence increase as a function of temperature. Heat drives the melting of the dsDNA overhang region, releasing the payload strand. A non-complementary payload is compared for control. When the sample is cooled back to room temperature, the normalized fluorescence value returns to 50, indicating that some rehybridization occurs.

Lastly, for preliminary payload release studies using NIR light as the trigger, the final CNT solutions were irradiated by the method described in section 6.2.7 with power densities in the range of 0.25-1.5 W/cm². It was found that irradiation at 0.75 W/cm² (red) caused a lowering of the melting temperature of the dsDNA overhang to 41°C, while pulsing the laser could drop the melting temperature to 31°C, presumably through the localized heating of the surface of the nanotube upon NIR irradiation (Figure 5.7). After the thermally or NIR-induced release of payload, the PLE was measured to ensure that CNT did not aggregate and remained well-dispersed in solution due to the enduring presence of the carrier strand adsorbed to the surface.

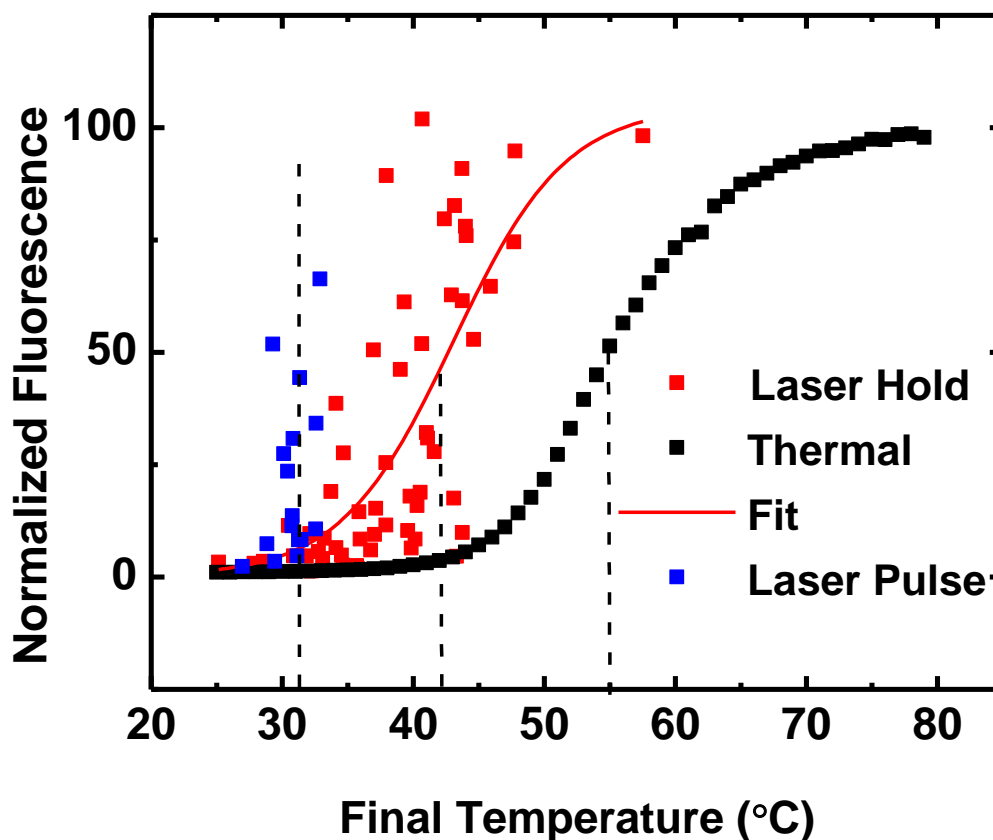


Figure 5.7: Normalized fluorescence as a function of temperature in the case of thermal release (black) and as a function of final measured temperature for NIR-triggered release. NIR irradiation was carried out with a constant power of 0.75 W/cm^2 (red) or pulsed (blue). Melting temperatures are taken from the inflexion point, marked by a dashed line.

This exploratory project laid significant groundwork for the SMH study. Specifically, we realized a better understanding of the prospects of dsDNA hybridization at the CNT surface and the possibility of manipulation by NIR irradiation.

5.2.4 CNT–DNA Gel/Network Synthesis

For the preparation of SMH, CNT dispersed in $(\text{AC})_{12}\text{S1}$ were mixed with linker DNA in a 1:1 concentration ratio. The mixture was slowly heated in a water bath at a rate of $0.5^\circ\text{C}/\text{minute}$

until it reached to 60 °C, and then allowed to cool slowly to room temperature at an approximate rate of 0.25 °C/minute.

For dilute network formation, (AC)₁₂S1 dispersions were diluted to 0.2mg/mL with buffer. The dilute dispersions were then mixed with linker DNA at a 1:1 concentration ratio. After two days, networks formed as depicted in Figure 5.8. In the rightmost cuvette, linker DNA was not added, and the CNT–DNA dispersion remained pristine.

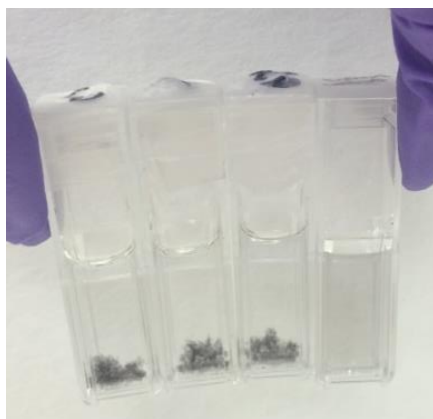


Figure 5.8: Photos of CNT–DNA dilute networks compared to a sample which was not mixed with linker DNA (rightmost cuvette).

Van der Waals gels were prepared as follows: CNT were dispersed in (AC)₁₂S1 DNA at a concentration of 5mg/mL using the same procedure outlined in Section 6.2.1. Following ultrasonication and centrifugation, the dispersion was dialyzed to remove excess DNA and allowed to rest at room temperature. After several days, the van der Waals gel formed unaided.

5.2.5 Rheology

All rheological measurements in this study were taken using an Anton Paar MCR302 rheometer with a 50-mm parallel plate and 0.2–0.5 mm gap. The temperature of the sample was controlled through Peltier heating systems, namely a flat plate Peltier heating system (P-

PTD200) and a Peltier hood (H-PTD150). All measurements were taken at 20°C unless otherwise noted. G' and G'' measurements were recorded as the plateau of strain sweeps (0.001–100%, $f=10$ Hz), generally around $\gamma=1.80\%$. Reversibility and cycling measurements were taken with $f=10$ Hz and $\gamma=0.05\%$.

5.2.6 Cryo-SEM Characterization

2 μL of SMH was pipetted out onto a 6-mm Au planchette and plunge frozen in liquid ethane. The frozen sample was then loaded into a Leica ACE600 cooled down to -125°C and freeze-fractured followed by freeze-etching by raising the temperature from -125°C to -85°C at a rate of $3^\circ\text{C}/\text{minute}$ and holding for 30 minutes at -85°C . Temperature was lowered back to -125°C after freeze-etching and the sample was coated with 8 nm of Pt/C.

The coated sample was finally loaded onto a cryogenic stage cooled down to -125°C inside of a Hitachi S4800-II cold field-emission scanning-electron microscope and imaged at 2 kV.

5.2.7 Near Infrared Reversibility

NIR irradiation was provided by a Frankfurt Laser multimode-cooled high-power laser diode (FBLD-980-5.00-HHL) with a center wavelength of 976 nm, maximum output power of 5.0 W and built-in thermoelectric cooling system. The laser beam was collimated to 1 cm^2 and used at a power of $1\text{ W}/\text{cm}^2$ for all studies reported here.

SMH samples for NIR studies were synthesized in square plastic cuvettes of 1 cm length, and irradiated in their original form. Sample temperature was measured during irradiation with a thermocouple inserted into each SMH. Immediately following irradiation, samples were taken

for rheological testing at the temperature reached by exposure to NIR, which was generally in the range of 37–44 °C.

5.3 Molecular Dynamics Simulations

5.3.1 Modeling Details

We model the coarse-grained CNT through a rigid, linear collection of 280 beads, each with a bead diameter of $\sigma = 1$ nm, where σ is the Lennard-Jones (LJ) unit of length. The inter-bead distance is also 1 nm, so the length of each CNT is 280 nm, which is about 62% of the average length of CNT in experiments (~450 nm). The S1 strand and (CG)_n strand of linker DNA are modeled using the bead–spring polymer model. We assume that the double stranded DNA formed after hybridization with CNT is in B-form, with a pitch distance of 0.332 nm per base pair. Therefore, with a bead size chosen as 1 nm in simulation, the S1 strand with 12 bases is represented by a polymer chain with 4 beads. Similarly, the (CG)_n strand of the linker DNA with n ranging from 2 to 9 correspond to polymer chains with 1 to 6 beads.

The DNA beads are bonded via a harmonic bond potential

$$U_{\text{bond}} = k(r - r_0)^2, k = 200 k_{\text{B}}T/nm^2$$

where r is the center-to-center distance between two beads and $r_0 = 2^{1/6}$ nm. We ignore the (AC)₁₂ strand of the DNA and assume that the S1 strand is directly bonded to one of the CNT beads with the same harmonic bond. An additional harmonic bond-angle potential is applied to the DNA beads to represent the intrinsic stiffness

$$U_{\text{angle}} = k_{\theta}(\theta - \theta_0)^2, k_{\theta} = 20 k_{\text{B}}T$$

where θ is the angle between two adjacent bonds and $\theta_0 = 180^\circ$.

All-atom simulations suggest that there are multiple configurations possible when ssDNA interacts with CNT, depending on the CNT chirality, DNA sequence, salt concentration and so on.³⁷⁶ Within the scope of our focus on the formation of cross-links in the gel system and the coarse-grained model employed, we do not seek to present the detailed wrapping configurations of DNA and CNT hybrids in this simulation. Instead, we assume that each wrapped DNA on CNT is close to B-DNA form, which occupies a total vertical length of 12 nm along the CNT, where the (AC)₁₂ strand occupies 8 nm and the S1 strand occupies 4 nm (Figure 5.9). The (AC)₁₂ strand is ignored in the coarse-grained model and the first bead of the S1 strand is directly bonded to one of the CNT beads. Depending on the relative orientation of the neighboring wrapped DNA along the CNT, the inter-S1 strand distance can be 9, 12 or 15 nm as shown in Figure 5.9. The inter-S1 strand distance is randomly distributed on each CNT in each simulation system and each CNT has 23 S1 strands.

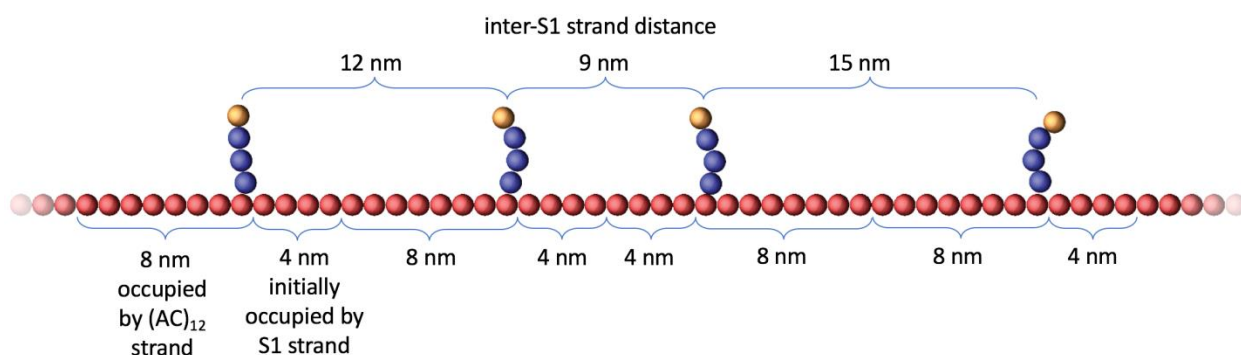


Figure 5.9: Schematic illustration of possible inter-S1 strand distance. Each wrapped DNA is assumed to occupy a total length of 12 nm along the CNT, where the (AC)₁₂ strand occupies 8 nm and the S1 strand occupies 4 nm. The (AC)₁₂ strand is ignored in the coarse-grained model and the first bead of the S1 strand is directly bonded to one of the CNT beads. Depending on the relative orientation of the neighboring wrapped DNA, the inter-S1 strand distance can be 9, 12 or 15 nm.

We employ a dynamic bonding function to simulate the hybridization between the linker DNA beads and the connection between the terminal S1 strand bead and linker DNA bead (Figure 5.10). When separated by a distance equal to or less than $2^{1/6}$ nm, a harmonic bond is formed with $r_0 = 2^{1/6}$ nm and $k = 597$ and $1934 k_B T/\text{nm}^2$ for linker-linker beads and linker-S1 strand beads, respectively. Such bonds will break if subsequently the bond length is equal to or exceeds 1.4 nm with a critical energy of 46 and $149 k_B T$, for linker-linker beads and linker-S1 strand beads, respectively. The former corresponds to the total hybridization enthalpy of the S1 strand with the complementary linker strand (which is not shown in the model); the latter represents the average hybridization enthalpy per bead of the linker (CG)_n strand, both calculated based on the nearest neighbor method.³⁷⁷ The critical energy is defined as bond strength. Each linker DNA bead is assigned with a different bead type and each type can only bind with one specific linker DNA bead type at any given time to mimic the base-pair-specific DNA hybridization. The terminal S1 strand bead can only bind with one specific linker DNA bead type to represent the hybridization of linker DNA with the S1 strand.

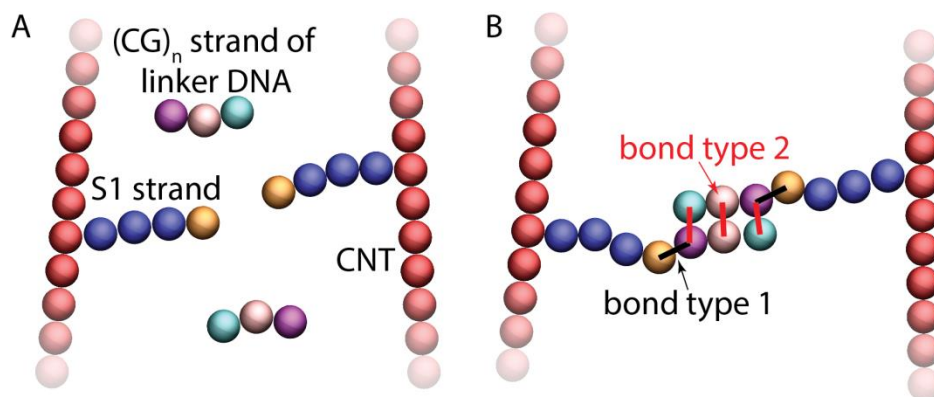


Figure 5.10: Schematic illustration of the dynamic bonding function used to simulate the formation of cross-links in an example system with 3 linker DNA beads. A) System components before forming the cross-link. Each bead of different color is assigned with a

different bead type. B) Cross-link formation. Each linker DNA bead type can only bind with one specific linker DNA bead type at any given time to mimic the DNA hybridization. In this case, each cyan bead can only bind with one other purple bead and the formed bond (bond type 2) has a strength of $46 k_B T$. The same binding rule applies for pink-pink binding. The terminal S1 strand bead (yellow) can only bind with one specific linker DNA bead type (purple) and the formed bond (bond type 1) has a strength of $149 k_B T$.

To investigate the effect of CNT concentration on the cross-linking density, we vary the number of CNT from 80 to 160 with an interval of 20. The linker length is fixed at 1 bead. To study the effect of linker length, we simulate 100 CNT and vary the linker length from 1 to 6 beads. In each system, we put 20% excess linker DNA compared to the number of S1 strands. All components are placed in a periodic cubic box of linear size 380 nm.

The LAMMPS package is used to perform the MD simulations. The equations of motion are integrated using the velocity-Verlet algorithm. A Langevin thermostat is applied with temperature $1.0\varepsilon/k_B$ and damping time 100τ , where ε and τ are the LJ units of energy and time, respectively. The time step is set to 0.01τ . Each simulation first runs for a period of $1 \times 10^5 \tau$ without turning on the dynamic bonding function. Then the dynamic bonding function is turned on with gradually increasing bond strength. At each bond strength, the simulations run for a different amount of time for different annealing rates (Figure 5.11A). Lastly, the simulations run for a period of $8 \times 10^5 \tau$ at the final bond strength (46 and $149 k_B T$ for linker-linker beads and linker-S1 strand beads, respectively). For each parameter choice, 8 independent runs are performed with different S1 strand distributions.

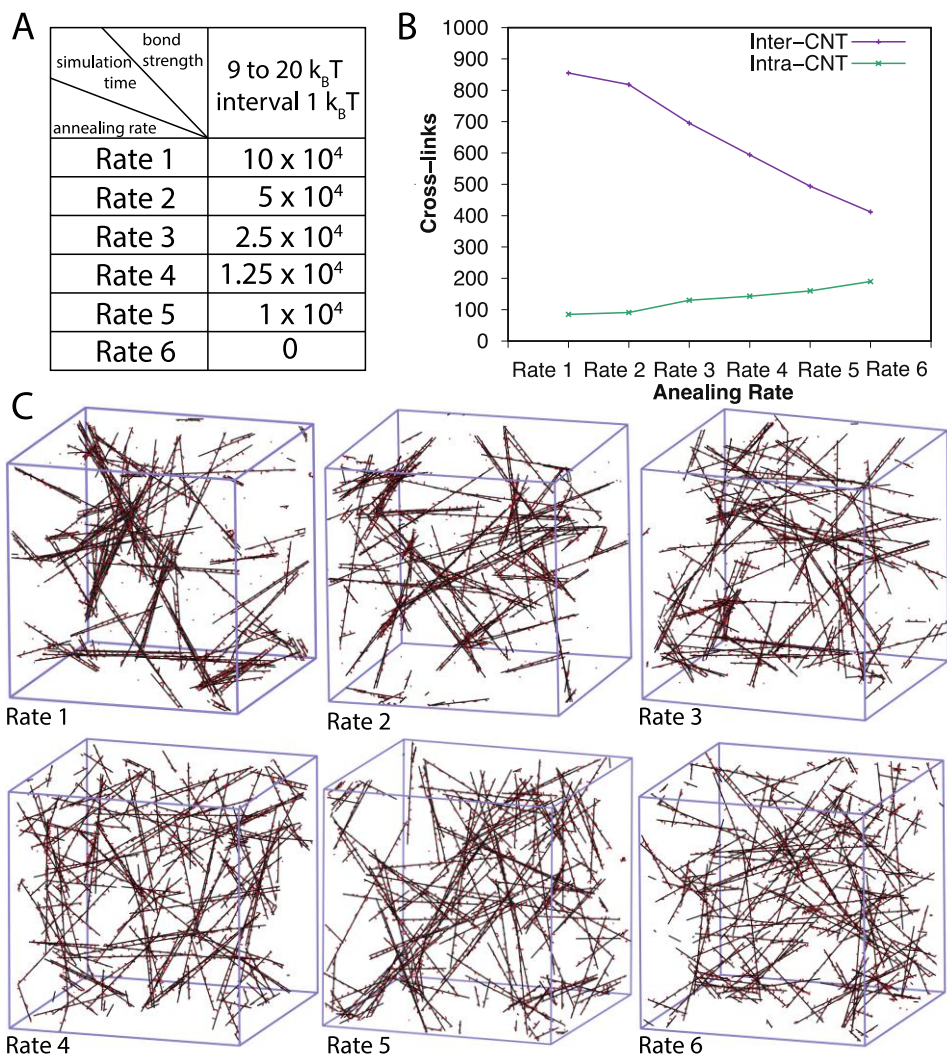


Figure 5.11: The effect of annealing rate on the number of cross-links and gel configuration. A) The simulation time (unit: τ) run for each bond strength during the annealing process for different annealing rates. B) The number of cross-links as a function of annealing rate. C) Representative gel configurations at different annealing rates.

5.3.2 Determination of Annealing Rate

The annealing process is achieved by gradually increasing the strength of the dynamically formed bonds. At the first stage of equilibrium without turning on the dynamic bonding function, the simulation runs for a period of $1 \times 10^5 \tau$ (with a time step of 0.01τ). The bond strength for both

linker-linker beads and linker-S1 strand beads is gradually increased from 9 to 20 $k_B T$ (at which point the formed bond is already non-breakable) at an interval of 1 $k_B T$. At each bond strength, the simulation runs for a certain amount of time as shown in Figure 5.11A. We simulate 6 systems at different annealing rates with a constant 100 CNTs and linker DNA length of 1 bead. Rate 6 corresponds to immediate fast cooling to room temperature, which deviates from the experimental procedure and acts as a reference here. At the final bond strengths, which are 46 and 149 $k_B T$ for linker-linker beads and linker-S1 strand beads, respectively, the simulation runs for a period of $8 \times 10^5 \tau$.

Simulation results show that the number of inter-CNT cross-links decreases as the annealing rate increases from Rate 1 to Rate 6 (Figure 5.11B). The trend is also demonstrated in the gel configurations in Figure 5.11C, wherein slower annealing leads to more alignment and bundling of the CNTs, while faster annealing results in a more isotropic CNT distribution. Given that the synthesized gel is homogeneous, annealing Rate 1 with strong aggregation formation is too slow compared to the experimental annealing rate. Therefore, the appropriate annealing rate in simulation is determined to be in between Rate 1 and Rate 6. In the investigation of the impact of CNT concentration and linker length on the gel cross-linking density, we simulate the gel system with two annealing rates. Slow annealing corresponds to Rate 3 and the fast annealing corresponds to Rate 5.

5.3.3 Hybridization Mismatch in Simulations

When the linker DNA length is larger than one bead, each linker DNA bead is assigned with a different bead type where each type can only bind with one other DNA bead type to mimic the DNA hybridization (Figure 5.10). However, such type-specific dynamic bonding functions

cannot prevent “hybridization mismatch,” where one linker DNA strand is partially bonded with two different linkers simultaneously. We count the number of S1 strands that have mismatched linker DNA connected to them. Out of the total 2300 S1 strands in the system with 100 CNTs, the number of S1 strands that are connected to mismatched linker DNA is around 20, which is negligible.

5.4 Results and Discussion

Looking to the extensive research on DNA-modified gold nanoparticle assembly and DNA hydrogels, we construct a novel hydrogel based on CNT and DNA alone.^{378–381} As shown in Figure 5.12A and B, CNT are dispersed in aqueous solution by a strand of 12 adenosine-cytosine (AC) repeats attached to an 18-mer called “S1,” labeled “(AC)₁₂S1.” This sequence was chosen for its lack of hairpin formation and for the strong affinity of AC bases to CNT.³⁷⁶ The dispersion is formed in aqueous buffer consisting of 4-(2-hydroxyethyl)-1-piperazineethanesulfonic acid (HEPES), potassium acetate, and sodium chloride at pH 7.5. The dispersion is characterized by optical absorbance spectroscopy (Figure 5.1) and then exposed to an excess of linker DNA, shown in Figure 5.12A and B. The linker DNA strands are comprised of two regions: a region that is complementary to the CNT-adsorbed DNA (sequence S1), and another region of (CG) repeats of variable length. Between the two regions is a single adenosine (A) base that enhances the flexibility of the linker.³⁷⁹ The CG region is self-complementary and can form a duplex with other CNT-bound linker DNA strands, thereby providing the basis for a DNA-cross-linked network of CNT.

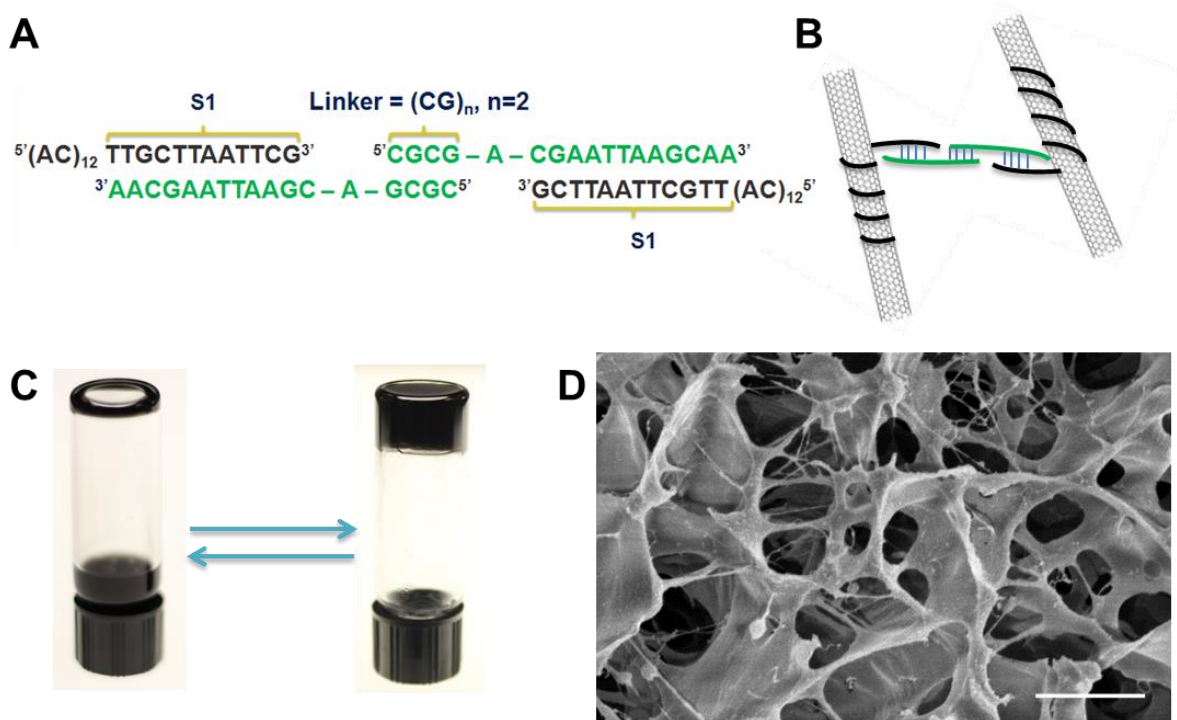


Figure 5.12: Schematic and physical characterization of CNT–DNA gel structure. A) DNA sequence used to disperse CNT, shown in black; Linker DNA shown in green with two regions: one complementary to S1 to form a connection with CNT and one self-complementary (CG) repeat of variable length, separated by a single adenosine base. B) The proposed structure of gel formation, wherein $(AC)_{12}S1$ helically wraps around the CNT and linker DNA forms duplexes with both S1 and other linker strands, thereby providing the cross-linking mechanism. C) Photos of the inverted vial test to demonstrate the sol-gel transition (solution on left and gel on right). D) Cryo-SEM of a CNT–DNA gel, showing a network of CNT amid frozen buffer salts, DNA, and agglomerated CNT.

Upon the addition of excess linker DNA and a slow annealing step, the CNT–DNA SMH is formed. Figure 5.12C demonstrates the sol-gel transition. This transition is fully reversible by both thermal and optical stimuli. The CNT–DNA SMH are also imaged under cryo-SEM (Figure 5.12D) with slow freeze-etching of a lyophilized SMH to visualize the CNT network.

To verify the proposed gelation mechanism, we examine the rheology of the CNT–DNA SMH in both the presence and absence of linker DNA (Figure 5.13). These experiments

determine the necessity of the linker in addition to the base-pair specificity of linker cross-linking. In all rheological studies, strain sweeps are used to determine the storage (G') and loss (G'') moduli (Figure 5.14). A representative shear stress sweep shows the viscosity of a typical 1.8 mg/mL CNT SMH at 900 Pa-s (Figure 5.14). SMH synthesis with a non-complementary linker or a lack of linker does not result in gel formation, supporting our hypothesis that the duplex linker is formed (Figure 5.13). Furthermore, we compare our CNT–DNA SMH to CNT–DNA gels that are known to form through van der Waals interactions at high concentrations. Without linker present, our CNT–DNA dispersions form a van der Waals gel at CNT concentrations above 5 mg/mL. However, in the presence of the linker, gelation occurs at a CNT concentration as low as 1.25 mg/mL. We find that a DNA cross-linked CNT gel at 1.8 mg/mL CNT has a G' of 46 Pa, whereas the 5mg/mL van der Waals gel has a G' of 15 Pa, indicating that DNA base-pairing contributes to the mechanical strength of our SMH.

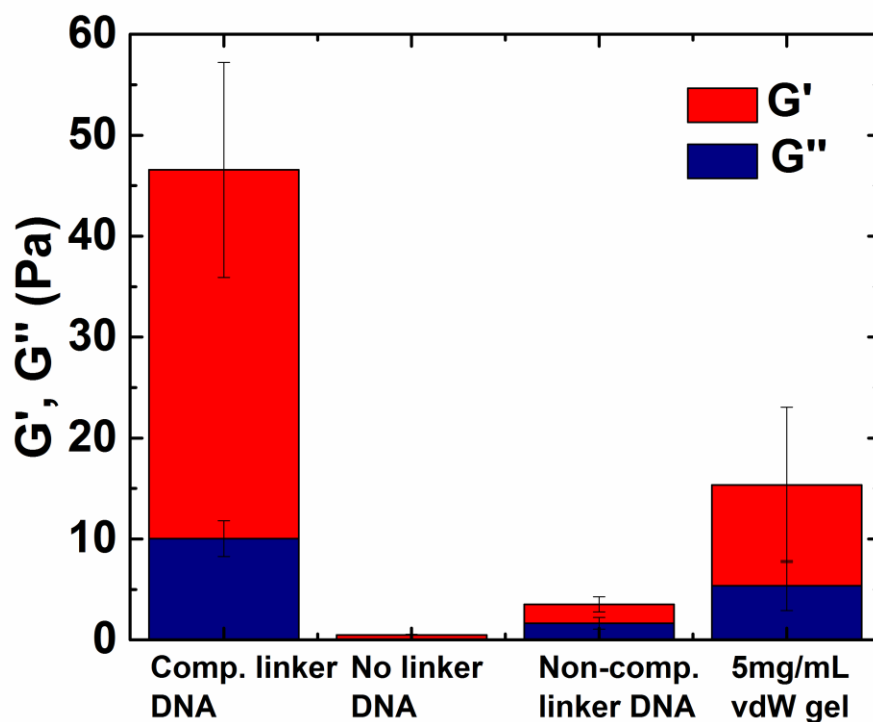


Figure 5.13: Control experiments to support the proposed structure of the gel. In the leftmost column, G' and G'' values of a typical SMH with CNT and linker DNA concentration of 1.8mg/mL. The next column is the result of adding buffer instead of linker DNA before the annealing step, which does not result in gel formation. The third column shows a CNT–DNA SMH in which genomic DNA was added instead of linker DNA, to demonstrate that a complementary linker DNA sequence is needed to form a stronger SMH. Finally, the rightmost column depicts the G' and G'' of a 5mg/mL CNT van der Waals gel, which is considerably weaker than the 1.8mg/mL SMH.

Next we demonstrate tunability of the SMH mechanical properties based on CNT concentration. At concentrations lower than that of the van der Waals gel, the storage modulus of the gels strongly depend on the CNT concentration, with a measured value as large as 200 Pa at 3.2 mg/mL CNT (Figure 5.14C).

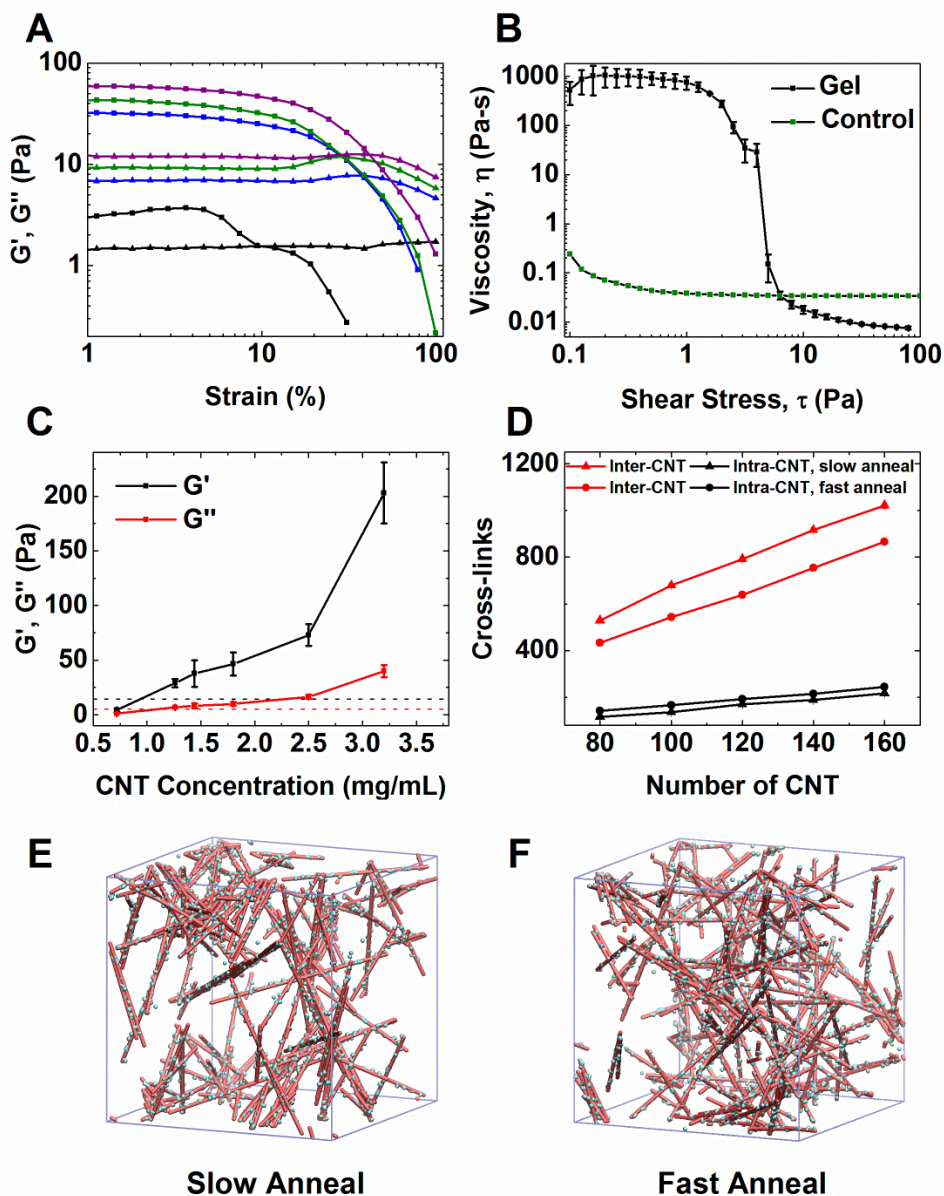


Figure 5.14: Tunable mechanical properties based on the concentration of CNT. A) Strain sweeps of several representative samples. Squares represent G' ; triangles represent G'' . Purple, green, blue, and black spectra represent gels with CNT concentration of 0.72, 1.25, 1.44, and 1.8 mg/mL, respectively. B) Viscosity vs. Shear stress for a typical gel, compared to an ungelled sample. C) Storage (G') and loss (G'') moduli as a function of CNT concentration. Dashed black and red lines indicate moduli for a 5mg/mL van der Waals gel. D) Number of inter- and intra-CNT cross-links as a function of the number of CNT for

gel systems formed at slow and fast annealing rates. E) and F) Representative simulation configuration of gel formed by 100 CNTs at the slow and fast annealing rates. CNTs are shown in pink. S1 strand and linker DNA are both shown in cyan.

As demonstrated previously, cross-linking by DNA base-pairing contributes to the mechanical strength of the gel. To facilitate a deeper understanding of the gel structures realized by the CNT and DNA system and to characterize the dependence of cross-linking density on CNT concentration, molecular dynamics (MD) simulations are carried out using a coarse-grained model. CNT are represented by a rigid linear array of beads, as detailed in Section 6.3. The S1 strand and the $(CG)_n$ strand of linker DNA are modeled using a bead-spring polymer model. For simplicity, this model assumes that the $(AC)_{12}$ strand of the DNA that is wrapped around a CNT has a negligible contribution to the cross-linking and therefore can be represented by a direct bond of the S1 strand to one of the CNT beads (Figure 5.10). Given the small Debye length (~ 0.304 nm) at the experimental salt concentration, we ignore the electrostatic interactions in the simulations. All components interact with each other through excluded-volume interactions, which are modeled via shifted-truncated Lennard-Jones (LJ) potentials. A dynamic bonding function is employed to simulate the formation of cross-links. Modeling details are described in the Section 6.3.

In the simulations, we emulate the heating and subsequent cooling of the mixture of DNA-dispersed CNT and linker DNA that is applied during gel synthesis (see Section 6.3). Since the simulation employs coarse-grained building blocks, we must determine the appropriate annealing rate in simulation. To this end, we first simulate six systems with different annealing rates and compare the configurations and the number of cross-links in the formed gel. Simulation results (Figure 5.11) show that the number of cross-links increases as the annealing rate

decreases, and that the slowest annealing rate (Rate 1) results in strong aggregation of CNT with a large number of inter-CNT cross-links. Given that the synthesized gel is homogeneous, the appropriate annealing rate in simulation thus must be faster than Rate 1. On the other hand, Rate 6 corresponds to immediate fast cooling to room temperature, in contrast with the experimental procedure. Although the reduced units employed in the coarse-grained simulations prevent direct conversion of the experimental annealing rate, we conclude that the appropriate annealing rate must be between Rates 1 and 6. To investigate the impact of CNT concentration on the gel cross-linking density, we simulate the gel system with two representative annealing rates: the slow and fast rates correspond to Rates 3 and 5 shown in Figure 5.11, respectively. Figure 5.14E and F are the representative configurations of the gel formed by 100 CNTs at the slow and fast annealing rates, respectively, where CNT are shown in pink and the DNA strands (S1 and linker) are shown in cyan. Figure 5.14D shows the total number of cross-links as a function of the number of CNT. For both annealing rates, the number of inter-CNT cross-links increases linearly with CNT concentration. Since the inter-CNT cross-links contribute to the mechanical strength of the gel, the modulus of the gel increases (Figure 5.14C). The CNT with the slow annealing rate tend to be more aligned with each other (Figure 5.14E), leading to a larger number of inter-CNT cross-links. Besides the inter-CNT cross-links, the nearby S1 strands can form intra-CNT cross-links in the presence of linker DNA. The number of intra-CNT cross-links also increases linearly with increasing CNT concentration. However, the gel formed at a slower annealing rate has a slightly smaller number of intra-CNT cross-links.

Next, we varied the length of the linker DNA and the pH of the buffer to determine their effect on the mechanical and melting properties of the gel. Specifically, we varied pH from 6 to 10, and the number of repeat units of the $(CG)_n$ region of the linker DNA from $n = 2$ to 9, or 4 to 18 bases. As n increases, the moduli G' and G'' decrease slowly, indicating a weakening but enduring gel structure (Figure 5.15A). Since the inter-CNT cross-linking density is closely related to mechanical strength, we use MD simulations to explore the effect of linker length on cross-linking density. In simulations, the linker length is varied from 1 to 6 beads (with a bead diameter of 1 nm), corresponding to the linker $(CG)_n$ region length changing from 4 to 18 bases in the experimental setup. Figure 5.15B and C show the number of inter- and intra-CNT cross-links as well as free S1 strands (including those that may connect to linker DNA but do not form cross-links otherwise) as a function of linker length for different annealing rates. As linker length increases, the probability of nearby S1 strands forming an intra-CNT cross-link is enhanced. The competing formation of intra-CNT cross-links reduces the overall number of inter-CNT cross-links and free S1 strands, as demonstrated in Figure 5.15B and C for gel systems formed at fast and slow annealing rates. The reduced number of inter-CNT cross-links contributes to the decrease of G' at longer linker length (Figure 5.15A).

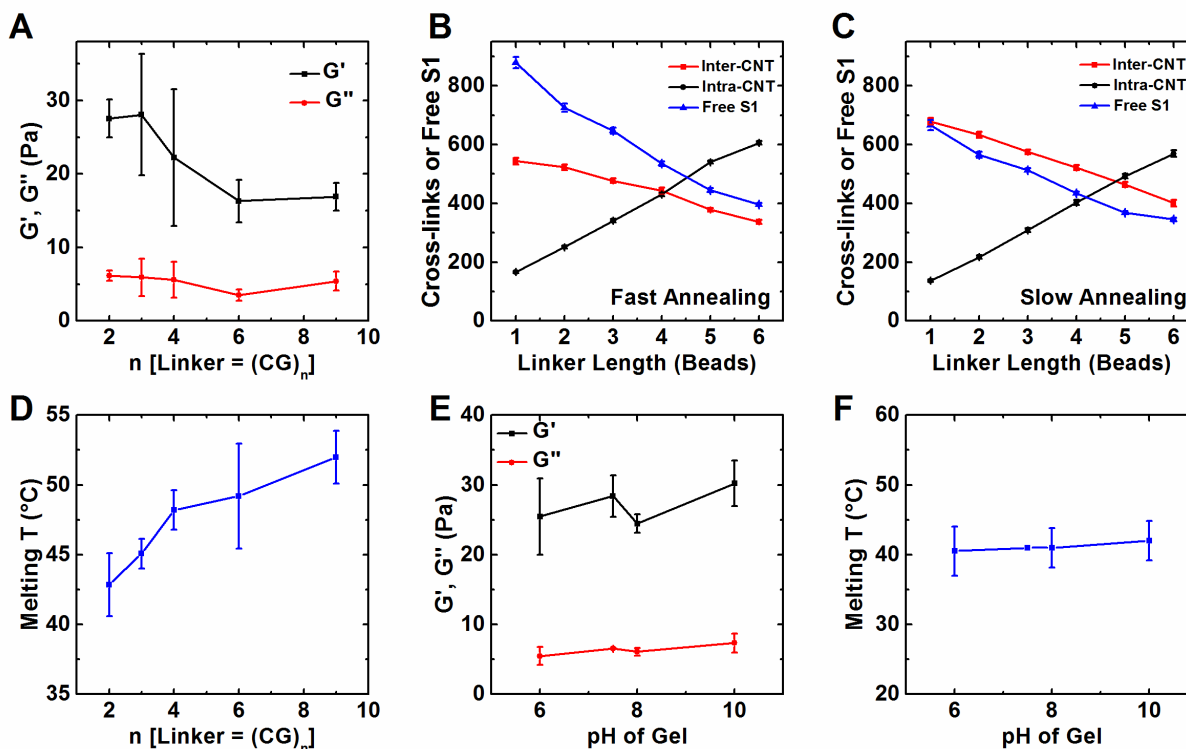


Figure 5.15: Mechanical properties and melting temperature as a function of linker length and pH, explained by MD simulations. A) G' and G'' as a function of linker length, showing a gradual weakening of the mechanical properties. The number of inter- and intra-CNT cross-links as well as the number of free S1 strands as a function of linker length for gel systems formed at fast (B) and slow (C) annealing rates. D) SMH melting temperatures increase with DNA linker length due to enhanced cross-linking stability. SMH melting temperatures are lower than free duplexes in solution due to confinement effects. SMH mechanical properties (E) and melting temperature (F) remain stable in the range of pH 6-10.

In the rheological measurements, the melting temperature in this system, or the gel–sol transition point, is defined as the temperature at which G' drops below G'' , thereby no longer meeting the rheological standard for a solid material. Keeping S1 constant, we expect some increase in the melting temperature of the gel as n is increased from from 4 to 9, and indeed observe a rise in the melting temperature from 42°C to 52°C (Figure 5.15D). DNA duplex

stability can be predicted from the base sequence.^{377,382} The temperature at which complementary strands dissociate increases with the increase of n in the 5'-(CG) $_n$ -3' duplex, consistent with the experimental observation that the gel melting temperature increases with increasing linker length. However, the measured gel melting temperature is well below the dissociation temperatures of free 5'-(CG) $_n$ -3' and free S1 duplex in solution, which are above 86°C. Previous research on DNA-coated colloids suggests that confinement effects may contribute to the lowering of the gel melting temperature.³⁸³ While the free hybridized DNA in solution can explore the same space as single strands, the freedom of motion of hybridized cross-linking DNA that connects the CNT is strongly restricted. This restriction gives rise to an additional configurational entropy penalty upon hybridization, therefore lowering the dissociation temperature of cross-linking DNA. Lastly, since pH is an important factor in applications of hydrogels, we examine its effect on the SMH and find that the mechanical properties and melting temperature of the gel are unaffected in the range of pH 6–10 (Figure 5.15E and F). Below pH 6, the CNT–DNA dispersions are destabilized, most likely due to the disruption of CNT–DNA interaction at low pH. Above pH 10, gels do not form, which it can be assumed is due to the disruption of the DNA-base pairing at high pH.

Finally, we demonstrate the optothermal reversibility of this SMH by rheological means. In measuring the crossover point of G' and G'' , we effectively record repeated gel–sol and sol–gel transitions. Thermoreversibility was demonstrated by cycling the ambient and plate temperature in the rheometer between 20 and 60°C. The gel readily cycles between a sol and gel state dependent on the temperature (Figure 5.16A). Moreover, (6,5) CNT readily absorb NIR light and heat locally upon exposure, thereby providing another means of sol–gel triggering. In

Figure 5.16B, SMH are irradiated with 976 nm light, during which time the crossover between G' and G'' is observed after 20 minutes. After 20 minutes of irradiation, the NIR light source is turned off, and the SMH recover to their original rheological state after 60 minutes. This process is fully reversible, and the SMH do not suffer significant damage or alteration after three cycles of NIR sol–gel reversibility (Figure 5.16C). This process is also reproduced in dilute networks of CNT–DNA that do not gel (Figure 5.8). In dilute networks of CNT–DNA, NIR reversibility was demonstrated using PLE. Once CNT–DNA networks form, PLE intensity is quenched, but can be reversibly restored by irradiation with NIR light (976nm, $1\text{W}/\text{cm}^2$) for 20 minutes (Figure 5.17).

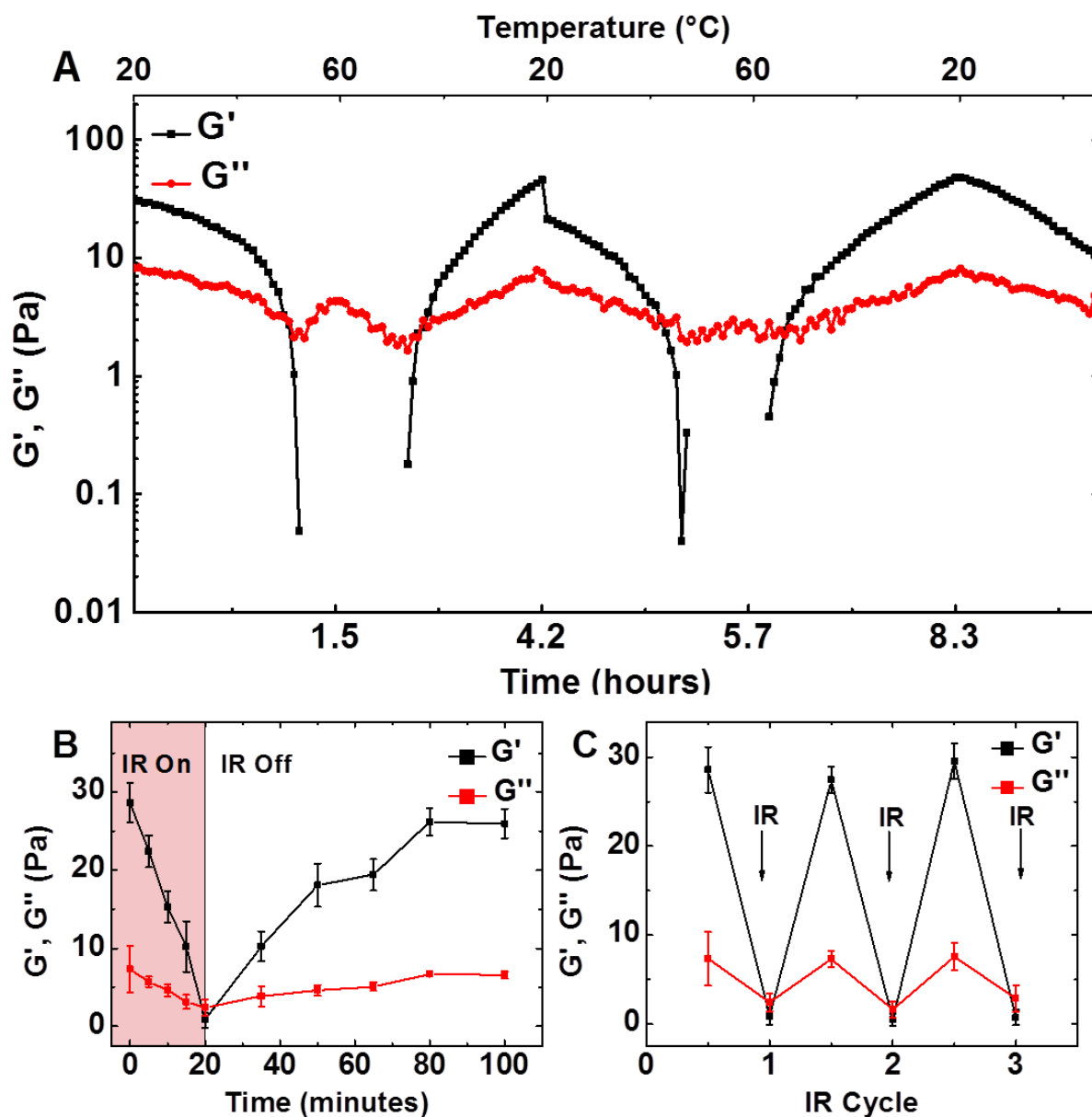


Figure 5.16: Optothermal reversibility of CNT-DNA SMH. A) Temperature is cycled between 20°C and 60°C while the SMH is constantly measured. The crossover between G' and G'' marks the reversible sol-gel transition. B) NIR light drives the gel-sol transition after 20 minutes of irradiation. 60 minutes after irradiation, the SMH has recovered to its original rheological state. C) NIR reversibility shown by three cycles of irradiation and recovery of the SMH.

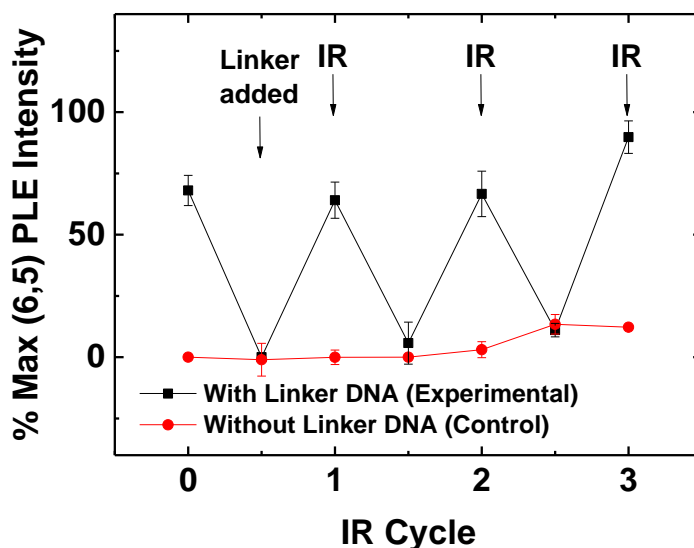


Figure 5.17: CNT–DNA dilute networks NIR reversibility. NIR reversibility measured by PLE quenching and restoration.

5.5 Conclusion

In summary, we have successfully prepared multi-responsive and multi-functional SMH by employing the interactions of CNT, DNA and DNA base pairing. Due to the customizable properties of synthetic DNA, this SMH is highly tailorable to many applications. The SMH is also tailorable on the basis of CNT concentration, allowing for enhancement of the mechanical properties. The CNT–DNA SMH are responsive to heat, NIR irradiation, and pH, and are fully thermo- and NIR-reversible. Therefore, these SMH have great potential in applications such as responsive substrate materials, sensing, and 3D printing.^{355,371,372,384}

CHAPTER 6

Summary and Future Opportunities

Chapter 6 - Summary and Future Opportunities

6.1 Summary

This thesis explores the functionalization, hazard assessment, and potential applications of 1D and 2D semiconducting nanoelectronic materials. Direct band gap materials were chosen for their efficiency of light absorption and luminescence properties. A variety of materials that span the range of infrared, visible and ultraviolet absorption were considered, namely single-walled carbon nanotubes (SWCNT), transition metal dichalcogenides (TMDs) and hexagonal boron nitride (hBN). Visible and infrared absorption and emission are of biological relevance due to the biological transparency window in the infrared region and imaging potential in the visible region.

In Chapter 3, high-concentration MoS₂ dispersions were formed by the adsorption of stabilizing, biocompatible, nonionic block copolymers. A survey of 19 such poloxamers revealed that MoS₂ concentration is highest using Pluronic F87, which has an intermediate PEO molecular weight and a large PPO molecular weight. The improved exfoliation and dispersion efficiency with increasing PPO molecular weight can likely be attributed to the hydrophobicity of MoS₂. These results further the understanding of nanomaterial surface-polymer interaction for aqueous liquid-based exfoliation purposes. Pluronic F87 was also shown to be an effective dispersant for a host of emerging 2D materials, namely molybdenum diselenide (MoSe₂), tungsten diselenide (WSe₂), tungsten disulfide (WS₂), tin selenide (SnSe), and hexagonal boron nitride (hBN), thus providing a diverse collection of aqueous 2D nanomaterial dispersions for further studies.

Next, we assessed the hazard potential of nanoscale MoS₂ and SWCNT in terms of human toxicity and environmental fate and transport. In Chapter 4, we elucidated relationships between the physicochemical properties of these nanomaterials and their hazard potential by providing a library of nanoscale dispersions with highly refined properties. Using density gradient ultracentrifugation, SWCNT were sorted into metallic (M-SWCNT) and semiconducting (S-SWCNT) populations with greater than 98% purity. Three aqueous forms of nanoscale MoS₂ were studied: chemically exfoliated MoS₂ by lithium ion intercalation (Lit-MoS₂), ultrasonication-assisted exfoliated MoS₂ in the presence of a biocompatible block copolymer, Pluronic F87 (PF87-MoS₂), and aggregated MoS₂ (Agg-MoS₂). The results of *in vitro* and *in vivo* studies simulating inhalation exposure show little difference between M-SWCNT and S-SWCNT and suggest that Agg-MoS₂ alone among the MoS₂ dispersions may elicit pro-inflammatory effects after acute exposure. However, no MoS₂ materials induced inflammation in the lung after sub-chronic exposure. Regarding their environmental transport and fate, PF87-MoS₂ may be more stable in the natural aquatic environment, but has a higher affinity for quartz surfaces than Lit-MoS₂. Thus, PF87-MoS₂ could more readily deposit in aqueous systems than Lit-MoS₂. These studies prompt future examination of the safe handling of emerging nanomaterials and are of high importance from a regulatory perspective.

Finally, in Chapter 5, one possible application of semiconducting nanoelectronic materials was explored. A novel supramolecular hybrid hydrogel was constructed out of DNA-dispersed SWCNT and duplex DNA linker strands. The formation of the CNT–DNA network was dependent on DNA base pairing, which made for a highly tailorable and stimuli-responsive system. The mechanical properties of the supramolecular hydrogel were tunable with respect to

CNT concentration, but remained stable across a neutral range of pH. The CNT–DNA hydrogels were responsive to heat and NIR irradiation; full thermo- and NIR-reversibility was demonstrated. Thus, these supramolecular hydrogels can be used in a variety of applications.

6.2 Future Opportunities

The work completed in this thesis presents a number of future research opportunities, including direct continuations of the studies done here and opportunities to extend this work to novel material systems and applications. For example, following from Chapter 3, Pluronics and Tetronics may provide aqueous solubility to a number of emerging hydrophobic 2D materials, such as other semiconducting metal chalcogenides and new analogues of graphene including boron carbon nitrides (BCN).^{385,386} It was recently demonstrated that black phosphorus (BP) is stable in aqueous sparged water in the presence of surfactants such as sodium cholate and Pluronic F68.¹⁹⁴ However, the surface chemistry of BP is different than graphene, TMDs, and hBN, and thus Pluronic F68 may not yield the highest efficiency dispersion of all the Pluronics/Tetronics. The dispersion efficiency and scalability of Pluronic/Tetronic dispersions may be further augmented by exploring the addition of a ball-milling step to pre-exfoliate material before ultrasonication.¹⁷⁷ Furthermore, the dispersions created in Chapter 3 may be of use in 3D printing, tissue engineering, and imaging applications, among others. It was recently shown that graphene materials incorporated into 3D printed structures comprised of biocompatible polymer polylactide-co-glycolide (PLGA) supported human mesenchymal stem cell growth, proliferation, and neurogenic differentiation.³⁸⁷ Replacing graphene with TMDs in this formulation could provide additional functionality, such as NIR and visible light absorption

for photothermal therapy and imaging purposes.³⁰⁵ Additionally, boron nitride nanomaterials have shown cytocompatibility and osteogenic potential in osteoblasts and macrophages *in vitro*, and thus may present an opportunity as an additive in 3D printed scaffolds for bone tissue engineering.^{234,235,388,389} Outside of 3D printed structures for biomedical applications, incorporation of TMDs and hBN into ink formulations may prove useful as thermal management materials.¹⁰⁹ Finally, besides extending Pluronics and Tetronics to other materials and applications, fundamental studies of their interaction with the surface of 2D materials would be useful in designing polymers with even greater dispersion efficiency. For example, density gradient centrifugation studies could provide a measurement of the buoyant density of dispersed nanoflakes which could help determine the conformation of the polymer on the surface. In all likelihood, the polymers have many different possible conformations on the surface, including folded and non-linear shapes that may inform the resulting dispersions in terms of both concentration and overall yield.

Continuation of the research presented in Chapter 4 is essential for the safe handling of emerging nanomaterials. More studies are necessary to determine the structure-property relationships of nanomaterials as they relate to toxicity and environmental fate. Such studies may also prove useful for applications like antibacterial resistance. For example, it was recently found that increased presence of carbon radicals on the surface of GO led to stronger antibacterial activity.³⁹⁰ Furthermore, researchers continue to isolate many new types of ultrathin 2D crystals, such as metal organic frameworks (MOFs), covalent organic frameworks (COFs), ultra-thin metals, and so on.^{391–400} New classes of nanomaterials and new polytypes within existing classes are reported every year, greatly enriching the nanomaterials landscape. It is important that

collaborations between materials scientists, toxicologists, and environmental scientists continue to assess the hazard potential of these novel materials.

Furthermore, structure-property relationships of nanomaterials in the toxicity and environmental space are useful for forming predictive paradigms to ease such investigations in the future. Such frameworks could be constructed using studies like those done here as well as high-throughput screening studies. Such toxicological predictive paradigms could both serve as a hazard assessment tool and reduce the need for rigorous animal testing of emerging nanomaterials.

Finally, the supramolecular hydrogel presented in this thesis holds potential for several applications. First, it meets the rheological criteria for 3D printable materials, the realization of which could lead to NIR-reversible 3D printed structures for tissue engineering, actuators, and more.³⁷² This supramolecular hydrogel is well-suited to sensing applications involving biomolecules, especially DNA.³⁵⁵ It could also be used as an optothermally responsive substrate with the potential to provide accurately defined forces.³⁷¹ Lastly, this supramolecular hydrogel may present an opportunity to probe the lower limit of the efficiency of hydrogen bonding. Previous work has demonstrated that the mechanical properties of hydrogels can be approximated using the theories of rubber elasticity and viscoelasticity. These approximations derive relationships between the network characteristics and mechanical behavior.⁴⁰¹ Since the hydrogel presented here is comprised only of carbon nanotubes and DNA and is relatively dilute compared to most polymer systems, it showcases the efficiency of DNA base pairing through hydrogen bonding. A theoretical or experimental network elasticity study could determine the

number of network-forming units per unit volume, which could lead to details on the kinetics and strength of hydrogen bonding in CNT–DNA systems and beyond.⁴⁰¹

References

- (1) Austin, L. A.; Kang, B.; Yen, C. W.; El-Sayed, M. A. Nuclear Targeted Silver Nanospheres Perturb the Cancer Cell Cycle Differently than Those of Nanogold. *Bioconjug. Chem.* **2011**, *22*, 2324–2331.
- (2) Chen, X.; Liu, Z.; Parker, S. G.; Zhang, X.; Gooding, J. J.; Ru, Y.; Liu, Y.; Zhou, Y. Light-Induced Hydrogel Based on Tumor-Targeting Mesoporous Silica Nanoparticles as a Theranostic Platform for Sustained Cancer Treatment. *ACS Appl. Mater. Inter.* **2016**, *8*, 15857–15863.
- (3) Jastrzębska, A.M., Kurtycz, P. & Olszyna, A. R. Recent Advances in Graphene Family Materials Toxicity Investigations. *J. Nanopart. Res.* **2012**, *14*, 1320–1328.
- (4) Brodie, B. C. On the Atomic Weight of Graphite. *Philos. Trans. R. Soc. London* **1859**, *149*, 249–259.
- (5) Kroto, H. W.; Heath, J. R.; O'Brien, S. C.; Curl, R. F.; Smalley, R. E. C60: Buckminsterfullerene. *Nature* **1985**, *318*, 162–163.
- (6) Iijima, S. Helical Microtubules of Graphitic Carbon. *Nature* **1991**, *354*, 56–58.
- (7) Raimond, J. M.; Brune, M.; Compton, Q.; Martini, F. De; Monroe, C.; Moehring, D. L.; Knight, P. L.; Plenio, M. B.; Vedral, V.; Polzik, E. S.; *et al.* Electric Field Effect in Atomically Thin Carbon Films. *Science* **2004**, *306*, 666–669.
- (8) Geim, A. K.; Novoselov, K. S. The Rise of Graphene. *Nat. Mater.* **2007**, *6*, 183–191.
- (9) Frank, I. W.; Tanenbaum, D. M.; Van Der Zande, A. M.; McEuen, P. L. Mechanical Properties of Suspended Graphene Sheets. *J. Vac. Sci. Technol. B* **2007**, *25*, 2558–2561.
- (10) Wang, C.; Zhang, L.; Guo, Z.; Xu, J.; Wang, H.; Zhai, K.; Zhuo, X. A Novel Hydrazine Electrochemical Sensor Based on the High Specific Surface Area Graphene. *Microchim. Acta* **2010**, *169*, 1–6.
- (11) Bolotin, K. I.; Sikes, K. J.; Jiang, Z.; Klima, M.; Fudenberg, G.; Hone, J.; Kim, P.; Stormer, H. L. Ultrahigh Electron Mobility in Suspended Graphene. *Solid State Commun.* **2008**, *146*, 351–355.
- (12) Balandin, A. A.; Ghosh, S.; Bao, W.; Calizo, I.; Teweldebrhan, D.; Miao, F.; Lau, C. N. Superior Thermal Conductivity of Single-Layer Graphene. *Nano Lett.* **2008**, *8*, 902–907.
- (13) Lin, Y.; Dimitrakopoulos, C.; Jenkins, K. A.; Farmer, D. B.; Chiu, H.; Grill, A.; Avouris, P. 100-GHz Transistors from Wafer-Scale Epitaxial Graphene. *Science* **2010**, *327*, 662.
- (14) Sire, C.; Ardiaca, F.; Lepilliet, S.; Seo, J. W. T.; Hersam, M. C.; Dambrine, G.; Happy,

- H.; Derycke, V. Flexible Gigahertz Transistors Derived from Solution-Based Single-Layer Graphene. *Nano Lett.* **2012**, *12*, 1184–1188.
- (15) Yan, Z.; Liu, G.; Khan, J. M.; Balandin, A. A. Graphene Quilts for Thermal Management of High-Power GaN Transistors. *Nat. Commun.* **2012**, *3*, 827.
- (16) Wassei, J. K.; Kaner, R. B. Graphene, a Promising Transparent Conductor. *Mater. Today* **2010**, *13*, 52–59.
- (17) Chang, C. H.; Huang, T. C.; Peng, C. W.; Yeh, T. C.; Lu, H. I.; Hung, W. I.; Weng, C. J.; Yang, T. I.; Yeh, J. M. Novel Anticorrosion Coatings Prepared from Polyaniline/Graphene Composites. *Carbon* **2012**, *50*, 5044–5051.
- (18) Zhao, X.; Zhang, Q.; Chen, D.; Lu, P. Enhanced Mechanical Properties of Graphene-Based Polyvinyl Alcohol Composites. *Macromolecules* **2010**, *43*, 2357–2363.
- (19) Huang, X.; Qi, X.; Boey, F.; Zhang, H. Graphene-Based Composites. *Chem. Soc. Rev.* **2012**, *41*, 666–686.
- (20) Huang, X.; Yin, Z.; Wu, S.; Qi, X.; He, Q.; Zhang, Q.; Yan, Q.; Boey, F.; Zhang, H. Graphene-Based Materials: Synthesis, Characterization, Properties, and Applications. *Small* **2011**, *7*, 1876–1902.
- (21) Qi, X.; Tan, C.; Wei, J.; Zhang, H. Synthesis of Graphene-Conjugated Polymer Nanocomposites for Electronic Device Applications. *Nanoscale* **2013**, *5*, 1440–1451.
- (22) Stankovich, S.; Dikin, D. A.; Dommett, G. H. B.; Kohlhaas, K. M.; Zimney, E. J.; Stach, E. A.; Piner, R. D.; Nguyen, S. T.; Ruoff, R. S. Graphene-Based Composite Materials. *Nature* **2006**, *442*, 282–286.
- (23) Guo, S.; Wang, E. Noble Metal Nanomaterials: Controllable Synthesis and Application in Fuel Cells and Analytical Sensors. *Nano Today* **2011**, *6*, 240–264.
- (24) Xia, Y.; Xiong, Y.; Lim, B.; Skrabalak, S. E. Shape-Controlled Synthesis of Metal Nanocrystals: Simple Chemistry Meets Complex Physics. *Angew. Chem. Int. Ed.* **2009**, *48*, 60–103.
- (25) Zhang, B.; Tang, D.; Liu, B.; Chen, H.; Cui, Y.; Chen, G. GoldMag Nanocomposite-Functionalized Graphene Sensing Platform for One-Step Electrochemical Immunoassay of Alpha-Fetoprotein. *Biosens. Bioelectron.* **2011**, *28*, 174–180.
- (26) Zhang, H.; Lv, X.; Li, Y.; Wang, Y.; Li, J. P25-Graphene Composite as a High Performance Photocatalyst. *ACS Nano* **2010**, *4*, 380–386.
- (27) Liang, Y. T.; Vijayan, B. K.; Gray, K. A.; Hersam, M. C. Minimizing Graphene Defects Enhances Titania Nanocomposite-Based Photocatalytic Reduction of CO₂ for Improved

- Solar Fuel Production. *Nano Lett.* **2011**, *11*, 2865–2870.
- (28) Zhu, C.; Du, D.; Lin, Y. Graphene and Graphene-like 2D Materials for Optical Biosensing and Bioimaging : A Review. *2D Mater.* **2015**, *2*, 32004.
- (29) Ashcroft, N. W.; Mermin, N. D. *Solid State Physics*; Holt, Rinehart and Winston: New York, 1976.
- (30) Zhang, J. Z. *Optical Properties and Spectroscopy of Nanomaterials*; WSPC: Singapore, 2009.
- (31) Troy, T. L.; Thennadil, S. N. Optical Properties of Human Skin in the near Infrared Wavelength Range of 1000 to 2200 Nm. *J. Biomed. Opt.* **2001**, *6*, 167–176.
- (32) Abdo, A.; Ersen, A.; Sahin, M. Near-Infrared Light Penetration Profile in the Rodent Brain. *J. Biomed. Opt.* **2013**, *18*, 75001.
- (33) Lim, Y. T.; Kim, S.; Nakayama, A.; Stott, N. E.; Bawendi, M. G.; Frangioni, J. V. Selection of Quantum Dot Wavelengths for Biomedical Assays and Imaging. *Mol. Imaging* **2003**, *2*, 50–64.
- (34) Liu, T.; Shi, S.; Liang, C.; Shen, S.; Cheng, L.; Wang, C.; Song, X.; Goel, S.; Barnhart, T. E.; Cai, W.; *et al.* Iron Oxide Decorated MoS₂ Nanosheets with Double PEGylation for Chelator-Free Radiolabeling and Multimodal Imaging Guided Photothermal Therapy. *ACS Nano* **2015**, *9*, 950–960.
- (35) Koechlin, C.; Maine, S.; Haidar, R.; Trétout, B.; Loiseau, A.; Pelouard, J. L. Electrical Characterization of Devices Based on Carbon Nanotube Films. *Appl. Phys. Lett.* **2010**, *96*, 103501.
- (36) Avouris, P.; Chen, Z.; Perebeinos, V. Carbon-Based Electronics. *Nat. Nanotechnol.* **2007**, *2*, 605–615.
- (37) Dürkop, T.; Getty, S. A.; Cobas, E.; Fuhrer, M. S. Extraordinary Mobility in Semiconducting Carbon Nanotubes. *Nano Lett.* **2004**, *4*, 35–39.
- (38) Lau, K.; Hui, D. The Revolutionary Creation of New Advanced Materials-Carbon Nanotube Composites. *Compos. Part B* **2002**, *33*, 263–277.
- (39) Coleman, J. N.; Khan, U.; Blau, W. J.; Gun'ko, Y. K. Small but Strong: A Review of the Mechanical Properties of Carbon Nanotube–Polymer Composites. *Carbon* **2006**, *44*, 1624–1652.
- (40) Ishaq, A.; Sobia, A. R.; Zhou, G.; Yan, L.; Zhou, X. Optically Transparent Carbon Nanowire Thin Film. *J. Exp. Nanosci.* **2012**, *7*, 53–61.

- (41) Odom, T. W.; Huang, J. L.; Kim, P.; Lieber, C. M. Atomic Structure and Electronic Properties of Single-Walled Carbon Nanotubes. *Nature* **1998**, *391*, 62–64.
- (42) Dresselhaus, M. S.; Dresselhaus, G.; Saito, R. Physics of Carbon Nanotubes. *Carbon* **1995**, *33*, 883–891.
- (43) Dresselhaus, M. S. *Science of Fullerenes and Carbon Nanotubes*; Dresselhaus, G.; Eklund, P. C., Eds.; Academic Press: San Diego, 1996.
- (44) Hamada, N.; Sawada, S.; Oshiyama, A. New One-Dimensional Conductors: Graphitic Microtubules. *Phys. Rev. Lett.* **1992**, *68*, 1579–1581.
- (45) Ouyang, M.; Huang, J. L.; Lieber, C. M. Fundamental Electronic Properties and Applications of Single-Walled Carbon Nanotubes. *Acc. Chem. Res.* **2002**, *35*, 1018–1025.
- (46) Arnold, M. S.; Guler, M. O.; Hersam, M. C.; Stupp, S. I. Encapsulation of Carbon Nanotubes by Self-Assembling Peptide Amphiphiles. *Langmuir* **2005**, *21*, 4705–4709.
- (47) Iakoubovskii, K.; Minami, N.; Kim, Y.; Miyashita, K.; Kazaoui, S.; Nalini, B. Midgap Luminescence Centers in Single-Wall Carbon Nanotubes Created by Ultraviolet Illumination. *Appl. Phys. Lett.* **2006**, *89*, 173108.
- (48) Itkis, M. E.; Perea, D. E.; Niyogi, S.; Rickard, S. M.; Hamon, M. A.; Hu, H.; Zhao, B.; Haddon, R. C. Purity Evaluation of As-Prepared Single-Walled Carbon Nanotube Soot by Use of Solution-Phase Near-IR Spectroscopy. *Nano Lett.* **2003**, *3*, 309–314.
- (49) Arepalli, S.; Nikolaev, P.; Gorelik, O.; Hadjiev, V. G.; Holmes, W.; Files, B.; Yowell, L. Protocol for the Characterization of Single-Wall Carbon Nanotube Material Quality. *Carbon* **2004**, *42*, 1783–1791.
- (50) Landi, B. J.; Ruf, H. J.; Evans, C. M.; Cress, C. D.; Raffaele, R. P. Purity Assessment of Single-Wall Carbon Nanotubes, Using Optical Absorption Spectroscopy. *J. Phys. Chem. B* **2005**, *109*, 9952–9965.
- (51) O’Connell, M. J.; Bachilo, S. M.; Huffman, C. B.; Moore, V. C.; Strano, M. S.; Haroz, E. H.; Rialon, K. L.; Boul, P. J.; Noon, W. H.; Kittrell, C.; *et al.* Band Gap Fluorescence from Individual Single-Walled Carbon Nanotubes. *Science* **2002**, *297*, 593–596.
- (52) Bachilo, S. M.; Balzano, L.; Herrera, J. E.; Pompeo, F.; Resasco, D. E.; Weisman, R. B. Narrow (n,m)-Distribution of Single-Walled Carbon Nanotubes Grown Using a Solid Supported Catalyst. *J. Am. Chem. Soc.* **2003**, *125*, 11186–11187.
- (53) Kataura, H. Optical Properties of Single-Wall Carbon Nanotubes. *Synth. Met.* **1999**, *103*, 2555–2558.
- (54) Geim, A. K.; Grigorieva, I. V. Van Der Waals Heterostructures. *Nature* **2013**, *499*, 419–

425.

- (55) Lv, R.; Robinson, J. A.; Schaak, R. E.; Sun, D.; Sun, Y.; Mallouk, T. E.; Terrones, M. Transition Metal Dichalcogenides and beyond: Synthesis, Properties, and Applications of Single- and Few-Layer Nanosheets. *Acc. Chem. Res.* **2015**, *48*, 56–64.
- (56) Chen, X.; McDonald, A. R. Functionalization of Two-Dimensional Transition-Metal Dichalcogenides. *Adv. Mater.* **2016**, 5738–5746.
- (57) Wang, Q. H.; Kalantar-Zadeh, K.; Kis, A.; Coleman, J. N.; Strano, M. S. Electronics and Optoelectronics of Two-Dimensional Transition Metal Dichalcogenides. *Nat. Nanotechnol.* **2012**, *7*, 699–712.
- (58) Chhowalla, M.; Shin, H. S.; Eda, G.; Li, L.J.; Loh, K. P.; Zhang, H. The Chemistry of Two-Dimensional Layered Transition Metal Dichalcogenide Nanosheets. *Nat. Chem.* **2013**, *5*, 263–275.
- (59) Butler, S. Z.; Hollen, S. M.; Cao, L.; Cui, Y.; Gupta, J. A.; Gutiérrez, H. R.; Heinz, T. F.; Hong, S. S.; Huang, J.; Ismach, A. F.; *et al.* Progress, Challenges, and Opportunities in Two-Dimensional Materials beyond Graphene. *ACS Nano* **2013**, *7*, 2898–2926.
- (60) Jariwala, D.; Sangwan, V. K.; Lauhon, L. J.; Marks, T. J.; Hersam, M. C. Emerging Device Applications for Semiconducting Two-Dimensional Transition Metal Dichalcogenides. *ACS Nano* **2014**, *8*, 1102–1120.
- (61) Eda, G.; Yamaguchi, H.; Voiry, D.; Fujita, T.; Chen, M.; Chhowalla, M. Photoluminescence from Chemically Exfoliated MoS₂. *Nano Lett.* **2011**, *11*, 5111–5116.
- (62) Feng, X.; Wang, X.; Xing, W.; Zhou, K.; Song, L.; Hu, Y. Liquid-Exfoliated MoS₂ by Chitosan and Enhanced Mechanical and Thermal Properties of chitosan/MoS₂ Composites. *Compos. Sci. Technol.* **2014**, *93*, 76–82.
- (63) Parzinger, E.; Miller, B.; Blaschke, B.; Garrido, J. A.; Ager, J. W.; Holleitner, A.; Wurstbauer, U. Photocatalytic Stability of Single- and Few-Layer MoS₂. *ACS Nano* **2015**, *9*, 11302–11309.
- (64) Splendiani, A.; Sun, L.; Zhang, Y.; Li, T.; Kim, J.; Chim, C. Y.; Galli, G.; Wang, F. Emerging Photoluminescence in Monolayer MoS₂. *Nano Lett.* **2010**, *10*, 1271–1275.
- (65) Wu, J. Y.; Lin, M. N.; Wang, L. De; Zhang, T. Photoluminescence of MoS₂ Prepared by Effective Grinding-Assisted Sonication Exfoliation. *J. Nanomater.* **2014**, *2014*, 1–7.
- (66) Leong, W. S.; Li, Y.; Luo, X.; Nai, C. T.; Quek, S. Y.; Thong, J. T. L. Tuning the Threshold Voltage of MoS₂ Field-Effect Transistors via Surface Treatment. *Nanoscale* **2015**, *7*, 10823–10831.

- (67) Radisavljevic, B.; Radenovic, A.; Brivio, J.; Giacometti, V.; Kis, A. Single-Layer MoS₂ Transistors. *Nat. Nanotechnol.* **2011**, *6*, 147–150.
- (68) Finn, D. J.; Lotya, M.; Cunningham, G.; Smith, R. J.; McCloskey, D.; Donegan, J. F.; Coleman, J. N. Inkjet Deposition of Liquid-Exfoliated Graphene and MoS₂ Nanosheets for Printed Device Applications. *J. Mater. Chem. C* **2014**, *2*, 925–932.
- (69) Shastry, T. A.; Balla, I.; Bergeron, H.; Amsterdam, S. H.; Marks, T. J.; Hersam, M. C. Mutual Photoluminescence Quenching and Photovoltaic Effect in Large-Area Single-Layer MoS₂-Polymer Heterojunctions. *ACS Nano* **2016**, *10*, 10573–10579.
- (70) Gan, L.; Zhang, Q.; Cheng, Y.; Schwingschlögl, U. Photovoltaic Heterojunctions of Fullerenes with MoS₂ and WS₂ Monolayers. *J. Phys. Chem. Lett.* **2014**, *5*, 1445–1449.
- (71) Bang, G. S.; Nam, K. W.; Kim, J. Y.; Shin, J.; Choi, J. W.; Choi, S. Effective Liquid-Phase Exfoliation and Sodium Ion Battery Application of MoS₂ Nanosheets. *ACS Appl. Mater. Inter.* **2014**, *6*, 7084–7089.
- (72) Jariwala, D.; Sangwan, V. K.; Wu, C. C.; Prabhumirashi, P. L.; Geier, M. L.; Marks, T. J.; Lauhon, L. J.; Hersam, M. C. Gate-Tunable Carbon Nanotube–MoS₂ Heterojunction p-n Diode. *P. Natl. Acad. Sci.* **2013**, *110*, 18076–18080.
- (73) Jariwala, D.; Howell, S. L.; Chen, K. S.; Kang, J.; Sangwan, V. K.; Filippone, S. A.; Turrisi, R.; Marks, T. J.; Lauhon, L. J.; Hersam, M. C. Hybrid, Gate-Tunable, van Der Waals p–n Heterojunctions from Pentacene and MoS₂. *Nano Lett.* **2016**, *16*, 497–503.
- (74) Clark, R. M.; Carey, B. J.; Daeneke, T.; Atkin, P.; Bhaskaran, M.; Latham, K.; Cole, I. S.; Kalantar-zadeh, K. Two-Step Synthesis of Luminescent MoS₂-ZnS Hybrid Quantum Dots. *Nanoscale* **2015**, *7*, 16763–16772.
- (75) Chou, S. S.; Kaehr, B.; Kim, J.; Foley, B. M.; De, M.; Hopkins, P. E.; Huang, J.; Brinker, C. J.; Dravid, V. P. Chemically Exfoliated MoS₂ as Near-Infrared Photothermal Agents. *Angew. Chem. Int. Ed. Engl.* **2013**, *52*, 4160–4164.
- (76) Lauritsen, J. V.; Nyberg, M.; Nørskov, J. K.; Clausen, B. S.; Topsøe, H.; Lægsgaard, E.; Besenbacher, F. Hydrodesulfurization Reaction Pathways on MoS₂ Nanoclusters Revealed by Scanning Tunneling Microscopy. *J. Catal.* **2004**, *224*, 94–106.
- (77) Dervin, S.; Dionysiou, D. D.; Pillai, S. C. 2D Nanostructures for Water Purification: Graphene and beyond. *Nanoscale* **2016**, *8*, 15115–15131.
- (78) Notley, S. M. High Yield Production of Photoluminescent Tungsten Disulphide Nanoparticles. *J. Colloid Interface Sci.* **2013**, *396*, 160–164.
- (79) Feng, C.; Huang, L.; Guo, Z.; Liu, H. Synthesis of Tungsten Disulfide (WS₂) Nanoflakes for Lithium Ion Battery Application. *Electrochem. Commun.* **2007**, *9*, 119–122.

- (80) Voiry, D.; Yamaguchi, H.; Li, J.; Silva, R.; Alves, D. C. B.; Fujita, T.; Chen, M.; Asefa, T.; Shenoy, V. B.; Eda, G.; *et al.* Enhanced Catalytic Activity in Strained Chemically Exfoliated WS₂ Nanosheets for Hydrogen Evolution. *Nat. Mater.* **2013**, *12*, 850–855.
- (81) Cheng, L.; Huang, W.; Gong, Q.; Liu, C.; Liu, Z.; Li, Y.; Dai, H. Ultrathin WS₂ Nanoflakes as a High-Performance Electrocatalyst for the Hydrogen Evolution Reaction. *Angew. Chem. Int. Ed.* **2014**, *53*, 7860–7863.
- (82) Mahler, B.; Hoepfner, V.; Liao, K.; Ozin, G. Colloidal Synthesis of 1T-WS₂ and 2H-WS₂ Nanosheets : Applications for Photocatalytic Hydrogen Evolution. *J. Am. Chem. Soc.* **2014**, *136*, 14121–14127.
- (83) Quinn, M. D. J.; Ho, N. H.; Notley, S. M. Aqueous Dispersions of Exfoliated Molybdenum Disulfide for Use in Visible-Light Photocatalysis. *ACS Appl. Mater. Inter.* **2013**, *5*, 12751–12756.
- (84) Lalwani, G.; Henslee, A. M.; Farshid, B.; Parmar, P.; Lin, L.; Qin, Y. X.; Kasper, F. K.; Mikos, A. G.; Sitharaman, B. Tungsten Disulfide Nanotubes Reinforced Biodegradable Polymers for Bone Tissue Engineering. *Acta Biomater.* **2013**, *9*, 8365–8373.
- (85) Kaul, A. B. Two-Dimensional Layered Materials: Structure, Properties, and Prospects for Device Applications. *J. Mater. Res.* **2014**, *29*, 348–361.
- (86) Liu, X.; Hu, J.; Yue, C.; Della Fera, N. D.; Ling, Y.; Mao, Z.; Wei, J. High Performance Field-Effect Transistor Based on Multilayer Tungsten Disulfide. *ACS Nano* **2014**, 10396–10402.
- (87) Sun, L.; Ying, Y.; Huang, H.; Song, Z.; Mao, Y.; Xu, Z.; Peng, X. Ultrafast Molecule Separation through Layered WS₂ Nanosheet Membranes. *ACS Nano* **2014**, *8*, 6304–6311.
- (88) He, K.; Kumar, N.; Zhao, L.; Wang, Z.; Mak, K. F.; Zhao, H.; Shan, J. Tightly Bound Excitons in Monolayer WSe₂. *Phys. Rev. Lett.* **2014**, *113*, 026803.
- (89) Tributsch, H. Hole Reactions from D – Energy Bands of Layer Type Group VI Transition Metal Dichalcogenides : New Perspectives for Electrochemical Solar Energy Conversion Hole Reactions from D-Energy Bands of Layer Type Group VI Transition Metal Dichalcogenides : New Pe. *J. Electrochem. Soc.* **1978**, *125*, 1086–1093.
- (90) Huang, J. K.; Pu, J.; Hsu, C. L.; Chiu, M. H.; Juang, Z. Y.; Chang, Y. H.; Chang, W. H.; Iwasa, Y.; Takenobu, T.; Li, L. J. Large-Area Synthesis of Highly Crystalline WSe₂ Monolayers and Device Applications. *ACS Nano* **2014**, *8*, 923–930.
- (91) Fang, H.; Chuang, S.; Chang, T. C.; Takei, K.; Takahashi, T.; Javey, A. High-Performance Single Layered WSe₂ P-FETs with Chemically Doped Contacts. *Nano Lett.* **2012**, *12*, 3788–3792.

- (92) Pospischil, A.; Furchi, M. M.; Mueller, T. Solar-Energy Conversion and Light Emission in an Atomic Monolayer p-n Diode. *Nat. Nanotechnol.* **2014**, *9*, 257–261.
- (93) Baugher, B. W. H.; Churchill, H. O. H.; Yang, Y.; Jarillo-Herrero, P. Optoelectronic Devices Based on Electrically Tunable p-n Diodes in a Monolayer Dichalcogenide. *Nat. Nanotechnol.* **2014**, *9*, 262–267.
- (94) Ross, J. S.; Klement, P.; Jones, A. M.; Ghimire, N. J.; Yan, J.; G., M.; Taniguchi, T.; Watanabe, K.; Kitamura, K.; Yao, W.; *et al.* Electrically Tunable Excitonic Light-Emitting Diodes Based on Monolayer WSe₂ p-n Junctions. *Nat. Nanotechnol.* **2014**, *9*, 268–272.
- (95) Gobrecht, J.; Gerischer, H.; Tributsch, H. Electrochemical Solar Cell Based on the D-Band Semiconductor Tungsten-Diselenide. *Berichte der Bunsengesellschaft für Phys. Chemie* **1978**, *82*, 1331–1335.
- (96) Wang, Z.; Dong, Z.; Gu, Y.; Chang, Y. H.; Zhang, L.; Li, L. J.; Zhao, W.; Eda, G.; Zhang, W.; Grinblat, G.; *et al.* Giant Photoluminescence Enhancement in Tungsten-Diselenide–Gold Plasmonic Hybrid Structures. *Nat. Commun.* **2016**, *7*, 11283.
- (97) Zhang, M.; Wu, J.; Zhu, Y.; Dumcenco, D. O.; Hong, J.; Mao, N.; Deng, S.; Chen, Y.; Yang, Y.; Jin, C.; *et al.* Two-Dimensional Molybdenum Tungsten Diselenide Alloys: Photoluminescence, Raman Scattering, and Electrical Transport. *ACS Nano* **2014**, *8*, 7130–7137.
- (98) Pradhan, N. R.; Rhodes, D.; Xin, Y.; Memaran, S.; Bhaskaran, L.; Siddiq, M.; Hill, S.; M. Ajayan, P.; Balicas, L. Ambipolar Molybdenum Diselenide Field-Effect Transistors: Field-Effect and Hall Mobilities. *ACS Nano* **2014**, *8*, 7923–7929.
- (99) Zhao, Z.; Zhang, H.; Yuan, H.; Wang, S.; Lin, Y.; Zeng, Q.; Xu, G.; Liu, Z.; Solanki, G. K.; Patel, K. D.; *et al.* Pressure Induced Metallization with Absence of Structural Transition in Layered Molybdenum Diselenide. *Nat. Commun.* **2015**, *6*, 7312.
- (100) Luo, Z.; Li, Y.; Zhong, M.; Huang, Y.; Wan, X.; Peng, J.; Weng, J. Nonlinear Optical Absorption of Few-Layer Molybdenum Diselenide (MoSe₂) for Passively Mode-Locked Soliton Fiber Laser. *Photonics Res.* **2015**, *3*, A79–A86.
- (101) Saadi, F. H.; Carim, A. I.; Velazquez, J. M.; Baricuatro, J. H.; McCrory, C. C. L.; Soriaga, M. P.; Lewis, N. S. Operando Synthesis of Macroporous Molybdenum Diselenide Films for Electrocatalysis of the Hydrogen-Evolution Reaction. *ACS Catal.* **2014**, *4*, 2866–2873.
- (102) Huang, K. J.; Shuai, H. L.; Chen, Y. X. Layered Molybdenum Selenide Stacking Flower-Like Nanostructure Coupled with Guanine-Rich DNA Sequence for Ultrasensitive Ochratoxin A Aptasensor Application. *Sensors Actuators B Chem.* **2016**, *225*, 391–397.
- (103) Lei, Z.; Xu, S.; Wu, P. Ultra-Thin and Porous MoSe₂ Nanosheets: Facile Preparation and

- Enhanced Electrocatalytic Activity Towards the Hydrogen Evolution Reaction. *Phys. Chem. Chem. Phys.* **2016**, *18*, 70–74.
- (104) Greim, J.; Schwetz, K. A. Boron Carbide, Boron Nitride, and Metal Borides. In *Ullmann's Encyclopedia of Industrial Chemistry*; Wiley-VCH Verlag GmbH & Co. KGaA, 2000.
- (105) Watanabe, K.; Taniguchi, T.; Kanda, H. Direct-Bandgap Properties and Evidence for Ultraviolet Lasing of Hexagonal Boron Nitride Single Crystal. *Nat. Mater.* **2004**, *3*, 404–409.
- (106) Jo, I.; Pettes, M. T.; Kim, J.; Watanabe, K.; Taniguchi, T.; Yao, Z.; Shi, L. Thermal Conductivity and Phonon Transport in Suspended Few-Layer Hexagonal Boron Nitride. *Nano Lett.* **2013**, *13*, 550–554.
- (107) Cho, D. H.; Kim, J. S.; Kwon, S. H.; Lee, C.; Lee, Y. Z. Evaluation of Hexagonal Boron Nitride Nano-Sheets as a Lubricant Additive in Water. *Wear* **2013**, *302*, 981–986.
- (108) Sainsbury, T.; Satti, A.; May, P.; Wang, Z.; McGovern, I.; Gun'ko, Y. K.; Coleman, J. Oxygen Radical Functionalization of Boron Nitride Nanosheets. *J. Am. Chem. Soc.* **2012**, *134*, 18758–18771.
- (109) Zhi, C.; Bando, Y.; Tang, C.; Kuwahara, H.; Golberg, D. Large-Scale Fabrication of Boron Nitride Nanosheets and Their Utilization in Polymeric Composites with Improved Thermal and Mechanical Properties. *Adv. Mater.* **2009**, *21*, 2889–2893.
- (110) Hu, S.; Lozada-Hidalgo, M.; Wang, F. C.; Mishchenko, A.; Schedin, F.; Nair, R. R.; Hill, E. W.; Boukhvalov, D. W.; Katsnelson, M. I.; Dryfe, R. A. W.; *et al.* Proton Transport through One-Atom-Thick Crystals. *Nature* **2014**, *516*, 227–230.
- (111) Guo, Y.; Newman, W.; Cortes, C. L.; Jacob, Z. Applications of Hyperbolic Metamaterial Substrates. *Adv. Optoelectron.* **2012**, *2012*, 9.
- (112) Poddubny, A.; Iorsh, I.; Belov, P.; Kivshar, Y. Hyperbolic Metamaterials. *Nat Phot.* **2013**, *7*, 948–957.
- (113) Caldwell, J. D.; Kretinin, A. V.; Chen, Y.; Giannini, V.; Fogler, M. M.; Francescato, Y.; Ellis, C. T.; Tischler, J. G.; Woods, C. R.; Giles, A. J.; *et al.* Sub-Diffractive Volume-Confinement Polaritons in the Natural Hyperbolic Material Hexagonal Boron Nitride. *Nat. Commun.* **2014**, *5*, 5221.
- (114) Dai, S.; Fei, Z.; Ma, Q.; Rodin, A. S.; Wagner, M.; McLeod, A. S.; Liu, M. K.; Gannett, W.; Regan, W.; Watanabe, K.; *et al.* Tunable Phonon Polaritons in Atomically Thin van Der Waals Crystals of Boron Nitride. *Science* **2014**, *343*, 1125–1129.
- (115) Dean, C. R.; Young, A. F.; Meric, I.; Lee, C.; Wang, L.; Sorgenfrei, S.; Watanabe, K.; Taniguchi, T.; Kim, P.; Shepard, K. L.; *et al.* Boron Nitride Substrates for High-Quality

- Graphene Electronics. *Nat. Nanotechnol.* **2010**, *5*, 722–726.
- (116) Ramasubramaniam, A.; Naveh, D. Carrier-Induced Antiferromagnet of Graphene Islands Embedded in Hexagonal Boron Nitride. *Phys. Rev. B* **2011**, *84*, 75405.
- (117) Jiang, J. W.; Wang, J. S.; Wang, B. S. Minimum Thermal Conductance in Graphene and Boron Nitride Superlattice. *Appl. Phys. Lett.* **2011**, *99*, 43109.
- (118) Pruneda, J. M. Origin of Half-Semimetallicity Induced at Interfaces of C-BN Heterostructures. *Phys. Rev. B* **2010**, *81*, 161409.
- (119) Son, Y. W.; Cohen, M. L.; Louie, S. G. Half-Metallic Graphene Nanoribbons. *Nature* **2006**, *444*, 347–349.
- (120) Khan, U.; May, P.; O'Neill, A.; Bell, A. P.; Boussac, E.; Martin, A.; Semple, J.; Coleman, J. N. Polymer Reinforcement Using Liquid-Exfoliated Boron Nitride Nanosheets. *Nanoscale* **2013**, *5*, 581–587.
- (121) Wang, Y.; Shi, Z.; Yin, J. Boron Nitride Nanosheets: Large-Scale Exfoliation in Methanesulfonic Acid and Their Composites with Polybenzimidazole. *J. Mater. Chem.* **2011**, *21*, 11371–11377.
- (122) Cui, X.; Ding, P.; Zhuang, N.; Shi, L.; Song, N.; Tang, S. Thermal Conductive and Mechanical Properties of Polymeric Composites Based on Solution-Exfoliated Boron Nitride and Graphene Nanosheets: A Morphology-Promoted Synergistic Effect. *ACS Appl. Mater. Inter.* **2015**, *7*, 19068–19075.
- (123) Zhu, J.; Kang, J.; Kang, J.; Jariwala, D.; Wood, J. D.; Seo, J. T.; Chen, K. S.; Marks, T. J.; Hersam, M. C. Solution-Processed Dielectrics Based on Thickness-Sorted Two-Dimensional Hexagonal Boron Nitride Nanosheets. *Nano Lett.* **2015**, *15*, 7029–7036.
- (124) Zhang, Q.; Huang, J. Q.; Qian, W. Z.; Zhang, Y. Y.; Wei, F. The Road for Nanomaterials Industry: A Review of Carbon Nanotube Production, Post-Treatment, and Bulk Applications for Composites and Energy Storage. *Small* **2013**, *9*, 1237–1265.
- (125) Jariwala, D.; Sangwan, V. K.; Lauhon, L. J.; Marks, T. J.; Hersam, M. C. Carbon Nanomaterials for Electronics, Optoelectronics, Photovoltaics, and Sensing. *Chem. Soc. Rev.* **2013**, *42*, 2824–2860.
- (126) Splendiani, A.; Sun, L.; Zhang, Y.; Li, T.; Kim, J.; Chim, C. Y.; Galli, G.; Wang, F. Emerging Photoluminescence in Monolayer MoS₂. *Nano Lett.* **2010**, *10*, 1271–1275.
- (127) Li, X.; Magnuson, C. W.; Venugopal, A.; Tromp, R. M.; Hannon, J. B.; Vogel, E. M.; Colombo, L.; Ruoff, R. S. Large-Area Graphene Single Crystals Grown by Low-Pressure Chemical Vapor Deposition of Methane on Copper. *J. Am. Chem. Soc.* **2011**, *133*, 2816–2819.

- (128) Berger, C.; Song, Z.; Li, T.; Li, X.; Ogbazghi, A. Y.; Feng, R.; Dai, Z.; Marchenkov, A. N.; Conrad, E. H.; First, P. N.; *et al.* Ultrathin Epitaxial Graphite: 2D Electron Gas Properties and a Route toward Graphene-Based Nanoelectronics. *J. Phys. Chem. B* **2004**, *108*, 19912–19916.
- (129) Yu, Y.; Li, C.; Liu, Y.; Su, L.; Zhang, Y.; Cao, L. Controlled Scalable Synthesis of Uniform, High-Quality Monolayer and Few-Layer MoS₂ Films. *Sci. Rep.* **2013**, *3*, 1866.
- (130) Bae, S.; Kim, H.; Lee, Y.; Xu, X.; Park, J. S.; Zheng, Y.; Balakrishnan, J.; Lei, T.; Ri Kim, H.; Song, Y. Il; *et al.* Roll-to-Roll Production of 30-Inch Graphene Films for Transparent Electrodes. *Nat. Nanotechnol.* **2010**, *5*, 574–578.
- (131) Paton, K. R.; Varrla, E.; Backes, C.; Smith, R. J.; Khan, U.; O’Neill, A.; Boland, C.; Lotya, M.; Istrate, O. M.; King, P.; *et al.* Scalable Production of Large Quantities of Defect-Free Few-Layer Graphene by Shear Exfoliation in Liquids. *Nat. Mater.* **2014**, *13*, 624–630.
- (132) Jaber-Ansari, L.; Hersam, M. C. Solution-Processed Graphene Materials and Composites. *MRS Bull.* **2012**, *37*, 1167–1175.
- (133) Seo, J. T.; Green, A. A.; Antaris, A. L.; Hersam, M. C. High-Concentration Aqueous Dispersions of Graphene Using Nonionic, Biocompatible Block Copolymers. *J. Phys. Chem. Lett.* **2011**, *2*, 1004–1008.
- (134) Wu, H.; Yang, R.; Song, B.; Han, Q.; Li, J.; Zhang, Y.; Fang, Y.; Tenne, R.; Wang, C. Biocompatible Inorganic Fullerene-like Molybdenum Disulfide Nanoparticles Produced by Pulsed Laser Ablation in Water. *ACS Nano* **2011**, *5*, 1276–1281.
- (135) Oakes, L.; Zulkifli, D.; Azmi, H.; Share, K.; Hanken, T.; Carter, R.; Pint, C. L. One Batch Exfoliation and Assembly of Two-Dimensional Transition Metal Dichalcogenide Nanosheets Using Electrophoretic Deposition. *J. Electrochem. Soc.* **2015**, *162*, D3063–D3070.
- (136) Liu, N.; Kim, P.; Kim, J. H.; Ye, J. H.; Kim, S.; Lee, C. J. Large-Area Atomically Thin MoS₂ Nanosheets Prepared Using Electrochemical Exfoliation. *ACS Nano* **2014**, *8*, 6902–6910.
- (137) Nicolosi, V.; Chhowalla, M.; Kanatzidis, M. G.; Strano, M. S.; Coleman, J. N. Liquid Exfoliation of Layered Materials. *Science* **2013**, *340*, 1226419.
- (138) Mansukhani, N. D.; Guiney, L. M.; Kim, P. J.; Zhao, Y.; Alducin, D.; Ponce, A.; Larios, E.; Yacaman, M. J.; Hersam, M. C. High-Concentration Aqueous Dispersions of Nanoscale 2D Materials Using Nonionic, Biocompatible Block Copolymers. *Small* **2016**, *12*, 294–300.
- (139) Backes, C.; Szydłowska, B. M.; Harvey, A.; Yuan, S.; Vega-Mayoral, V.; Davies, B. R.;

- Zhao, P.; Hanlon, D.; Santos, E. J. G.; Katsnelson, M. I.; *et al.* Production of Highly Monolayer Enriched Dispersions of Liquid-Exfoliated Nanosheets by Liquid Cascade Centrifugation. *ACS Nano* **2016**, *10*, 1589–1601.
- (140) Smith, R. J.; King, P. J.; Lotya, M.; Wirtz, C.; Khan, U.; De, S.; O'Neill, A.; Duesberg, G. S.; Grunlan, J. C.; Moriarty, G.; *et al.* Large-Scale Exfoliation of Inorganic Layered Compounds in Aqueous Surfactant Solutions. *Adv. Mater.* **2011**, *23*, 3944–3948.
- (141) Varrla, E.; Backes, C.; Paton, K. R.; Harvey, A.; Gholamvand, Z.; McCauley, J.; Coleman, J. N. Large-Scale Production of Size-Controlled MoS₂ Nanosheets by Shear Exfoliation. *Chem. Mater.* **2015**, *27*, 1129–1139.
- (142) Novoselov, K. S.; Fal'ko, V. I.; Colombo, L.; Gellert, P. R.; Schwab, M. G.; Kim, K. A Roadmap for Graphene. *Nature* **2012**, *490*, 192–200.
- (143) Mu, S.; Liang, Y.; Chen, S.; Zhang, L.; Liu, T. MWNT-Hybridized Supramolecular Hydrogel for Hydrophobic Camptothecin Delivery. *Mater. Sci. Eng. C* **2015**, *50*, 294–299.
- (144) Kovtyukhova, N. I.; Mallouk, T. E.; Pan, L.; Dickey, E. C. Individual Single-Walled Nanotubes and Hydrogels Made by Oxidative Exfoliation of Carbon Nanotube Ropes. *J. Am. Chem. Soc.* **2003**, *125*, 9761–9769.
- (145) Mehra, N. K.; Mishra, V.; Jain, N. K. A Review of Ligand Tethered Surface Engineered Carbon Nanotubes. *Biomaterials* **2014**, *35*, 1267–1283.
- (146) Ramanathan, T.; Fisher, F.; Ruoff, R. S.; Brinson, L. C. Amino-Functionalized Carbon Nanotubes for Binding to Polymers and Biological Systems. *Chem. Mater.* **2005**, *17*, 1290–1295.
- (147) Sajid, M. I.; Jamshaid, U.; Jamshaid, T.; Zafar, N.; Fessi, H.; Elaissari, A. Carbon Nanotubes from Synthesis to in Vivo Biomedical Applications. *Int. J. Pharm.* **2016**, *501*, 278–299.
- (148) Hummers, W. S.; Offeman, R. E. Preparation of Graphitic Oxide. *J. Am. Chem. Soc.* **1958**, *80*, 1937.
- (149) Loh, K. P.; Bao, Q.; Eda, G.; Chhowalla, M. Graphene Oxide as a Chemically Tunable Platform for Optical Applications. *Nat. Chem.* **2010**, *2*, 1015–1024.
- (150) Bagri, A.; Mattevi, C.; Acik, M.; Chabal, Y. J.; Chhowalla, M.; Shenoy, V. B. Structural Evolution During the Reduction of Chemically Derived Graphene Oxide. *Nat. Chem.* **2010**, *2*, 581–587.
- (151) Dreyer, D. R.; Park, S.; Bielawski, C. W.; Ruoff, R. S. The Chemistry of Graphene Oxide. *Chem. Soc. Rev.* **2010**, *39*, 228–240.

- (152) Chowdhury, I.; Duch, M. C.; Mansukhani, N. D.; Hersam, M. C.; Bouchard, D. Colloidal Properties and Stability of Graphene Oxide Nanomaterials in the Aquatic Environment. *Environ. Sci. Technol.* **2013**, *47*, 6288–6296.
- (153) Fernández-Merino, M. J.; Guardia, L.; Paredes, J. I.; Villar-Rodil, S.; Solís-Fernández, P.; Martínez-Ionso, A.; Tascón, J. M. D. Vitamin C Is an Ideal Substitute for Hydrazine in the Reduction of Graphene Oxide Suspensions. *J. Phys. Chem. C* **2010**, *114*, 6426–6432.
- (154) Fan, X.; Peng, W.; Li, Y.; Li, X.; Wang, S.; Zhang, G.; Zhang, F. Deoxygenation of Exfoliated Graphite Oxide under Alkaline Conditions: A Green Route to Graphene Preparation. *Adv. Mater.* **2008**, *20*, 4490–4493.
- (155) Shen, Y.; Zhang, H. H. B.; Ren, W.; Dasari, A.; Tang, G. S.; Yu, Z. Z. Structural Evolution of Functionalized Graphene Sheets During Solvothermal Reduction. *Carbon* **2013**, *56*, 132–138.
- (156) Pham, V. H.; Cuong, T. V.; Hur, S. H.; Oh, E.; Kim, E. J.; Shin, E. W.; Chung, J. S. Chemical Functionalization of Graphene Sheets by Solvothermal Reduction of a Graphene Oxide Suspension in N-Methyl-2-Pyrrolidone. *J. Mater. Chem.* **2011**, *21*, 3371–3377.
- (157) Pei, S.; Cheng, H. M. The Reduction of Graphene Oxide. *Carbon* **2012**, *50*, 3210–3228.
- (158) Zheng, J.; Zhang, H.; Dong, S.; Liu, Y.; Nai, C. T.; Shin, H. S.; Jeong, H. Y.; Liu, B.; Loh, K. P. High Yield Exfoliation of Two-Dimensional Chalcogenides Using Sodium Naphthalenide. *Nat. Commun.* **2014**, *5*, 2995.
- (159) Liu, N.; Kim, P.; Kim, J. H.; Ye, J. H.; Kim, S.; Lee, C. J. Large-Area Atomically Thin MoS₂ Nanosheets Prepared Using Electrochemical Exfoliation. *ACS Nano* **2014**, *8*, 6902–6910.
- (160) Eda, G.; Yamaguchi, H.; Voiry, D.; Fujita, T.; Chen, M. W.; Chhowalla, M. Photoluminescence from Chemically Exfoliated MoS₂. *Nano Lett.* **2011**, *11*, 5111–5116.
- (161) Lin, Z.; Carvalho, B. R.; Kahn, E.; Xu, D.; Zhu, Y.; Liu, J.; Li, Y.; Peng, W. Microwave-Assisted 1T to 2H Phase Reversion of MoS₂ in Solution : A Fast Route to Processable Dispersions of 2H-MoS₂ Nanosheets and Nanocomposites. *Nanotechnology* **2016**, *27*, 1–7.
- (162) Coleman, J. N.; Lotya, M.; O'Neill, A.; Bergin, S. D.; King, P. J.; Khan, U.; Young, K.; Gaucher, A.; De, S.; Smith, R. J.; *et al.* Two-Dimensional Nanosheets Produced by Liquid Exfoliation of Layered Materials. *Science* **2011**, *331*, 568–571.
- (163) May, P.; Khan, U.; Hughes, J. M.; Coleman, J. N. Role of Solubility Parameters in Understanding the Steric Stabilization of Exfoliated Two-Dimensional Nanosheets by Adsorbed Polymers. *J. Phys. Chem. C* **2012**, *116*, 11393–11400.

- (164) Zhou, K. G.; Mao, N. N.; Wang, H. X.; Peng, Y.; Zhang, H. L. A Mixed-Solvent Strategy for Efficient Exfoliation of Inorganic Graphene Analogues. *Angew. Chem.* **2011**, *50*, 10839–10842.
- (165) Cunningham, G.; Lotya, M.; Cucinotta, C. S.; Sanvito, S.; Bergin, S. D.; Menzel, R.; Shaffer, M. S. P.; Coleman, J. N. Solvent Exfoliation of Transition Metal Dichalcogenides: Dispersibility of Exfoliated Nanosheets Varies Only Weakly between Compounds. *ACS Nano* **2012**, *6*, 3468–3480.
- (166) Paredes, J. I.; Villar-Rodil, S.; Martínez-Alonso, A.; Tascón, J. M. D. Graphene Oxide Dispersions in Organic Solvents. *Langmuir* **2008**, *24*, 10560–10564.
- (167) Shen, J.; He, Y.; Wu, J.; Gao, C.; Keyshar, K.; Zhang, X.; Yang, Y.; Ye, M.; Vajtai, R.; Lou, J.; *et al.* Liquid Phase Exfoliation of Two-Dimensional Materials by Directly Probing and Matching Surface Tension Components. *Nano Lett.* **2015**, *15*, 5449–5454.
- (168) Lin, Y.; Williams, T. V.; Connell, J. W. Soluble, Exfoliated Hexagonal Boron Nitride Nanosheets. *J. Phys. Chem. Lett.* **2010**, *1*, 277–283.
- (169) Niu, L.; Coleman, J. N.; Zhang, H.; Shin, H.; Chhowalla, M.; Zheng, Z. Production of Two-Dimensional Nanomaterials via Liquid-Based Direct Exfoliation. *Small* **2016**, *12*, 272–293.
- (170) Guan, G.; Zhang, S.; Liu, S.; Cai, Y.; Low, M.; Teng, C. P.; Phang, I. Y.; Cheng, Y.; Duei, K. L.; Srinivasan, B. M.; *et al.* Protein Induces Layer-by-Layer Exfoliation of Transition Metal Dichalcogenides. *J. Am. Chem. Soc.* **2015**, *137*, 6152–6155.
- (171) Liu, W. S.; Zhao, C. Y.; Zhou, R.; Zhou, D.; Liu, Z. L.; Lu, X. H. Lignin-Assisted Exfoliation of Molybdenum Disulfide in Aqueous Media and Its Application in Lithium Ion Batteries. *Nanoscale* **2015**, *7*, 9919–9926.
- (172) Li, Y.; Zhu, H.; Shen, F.; Wan, J.; Lacey, S.; Fang, Z.; Dai, H.; Hu, L. Nanocellulose as Green Dispersant for Two-Dimensional Energy Materials. *Nano Energy* **2015**, *13*, 346–354.
- (173) Zheng, M.; Jagota, A.; Semke, E. D.; Diner, B. A.; McLean, R. S.; Lustig, S. R.; Richardson, R. E.; Tassi, N. G. DNA-Assisted Dispersion and Separation of Carbon Nanotubes. *Nat. Mater.* **2003**, *2*, 338–342.
- (174) Antaris, A. L.; Seo, J.-W. T.; Green, A. A.; Hersam, M. C. Sorting Single-Walled Carbon Nanotubes by Electronic Type Using Nonionic, Biocompatible Block Copolymers. *ACS Nano* **2010**, *4*, 4725–4732.
- (175) Fan, D.; Feng, J.; Liu, J.; Gao, T.; Ye, Z.; Chen, M.; Lv, X. Hexagonal Boron Nitride Nanosheets Exfoliated by Sodium Hypochlorite Ball Mill and Their Potential Application in Catalysis. *Ceram. Int.* **2016**, *42*, 7155–7163.

- (176) Li, L. H.; Chen, Y.; Behan, G.; Zhang, H.; Petracic, M.; Glushenkov, A. M. Large-Scale Mechanical Peeling of Boron Nitride Nanosheets by Low-Energy Ball Milling. *J. Mater. Chem.* **2011**, *21*, 11862–11866.
- (177) León, V.; Quintana, M.; Herrero, M. A.; Fierro, J. L. G.; Hoz, A. D. La; Prato, M.; Vázquez, E. Few-Layer Graphenes from Ball-Milling of Graphite with Melamine. *Chem. Commun.* **2011**, *47*, 10936–10938.
- (178) Yao, Y.; Lin, Z.; Li, Z.; Song, X.; Moon, K. S.; Wong, C. Large-Scale Production of Two-Dimensional Nanosheets. *J. Mater. Chem.* **2012**, *22*, 13494–13499.
- (179) Harman, N. L.; Griffin, B. A.; Davies, I. G. Separation of the Principal HDL Subclasses by Iodixanol Ultracentrifugation. *J. Lipid Res.* **2013**, *54*, 2273–2281.
- (180) Arnold, M. S.; Stupp, S. I.; Hersam, M. C. Enrichment of Single-Walled Carbon Nanotubes by Diameter in Density Gradients. *Nano Lett.* **2005**, *5*, 713–718.
- (181) Arnold, M. S.; Green, A. A.; Hulvat, J. F.; Stupp, S. I.; Hersam, M. C. Sorting Carbon Nanotubes by Electronic Structure Using Density Differentiation. *Nat. Nanotechnol.* **2006**, *1*, 60–65.
- (182) Green, A. A.; Hersam, M. C. Nearly Single-Chirality Single-Walled Carbon Nanotubes Produced via Orthogonal Iterative Density Gradient Ultracentrifugation. *Adv. Mater.* **2011**, *23*, 2185–2190.
- (183) Green, A. A.; Duch, M. C.; Hersam, M. C. Isolation of Single-Walled Carbon Nanotube Enantiomers by Density Differentiation. *Nano Res.* **2009**, *2*, 69–77.
- (184) Green, A. A.; Hersam, M. C. Properties and Application of Double-Walled Carbon Nanotubes Sorted by Outer-Wall Electronic Type. *ACS Nano* **2011**, *5*, 1459–1467.
- (185) Hennrich, F.; Li, W.; Fischer, R.; Lebedkin, S.; Krupke, R.; Kappes, M. M. Length-Sorted, Large-Diameter, Polyfluorene-Wrapped Semiconducting Single-Walled Carbon Nanotubes for High-Density, Short-Channel Transistors. *ACS Nano* **2016**, *10*, 1888–1895.
- (186) Fagan, J. A.; Becker, M. L.; Chun, J.; Hobbie, E. K. Length Fractionation of Carbon Nanotubes Using Centrifugation. *Adv. Mater.* **2008**, *20*, 1609–1613.
- (187) Block, B.; Antaris, A. L.; Seo, J. T.; Green, A. A.; Hersam, M. C. Sorting Single-Walled Carbon. **2010**, *4*, 4725–4732.
- (188) Hersam, M. C. Progress towards Monodisperse Single-Walled Carbon Nanotubes. *Nat. Nanotechnol.* **2008**, *3*, 387–394.
- (189) Zhu, J.; Kang, J. J.; Kang, J. J.; Jariwala, D.; Wood, J. D.; Seo, J. W. T.; Chen, K. S.; Marks, T. J.; Hersam, M. C. Solution-Processed Dielectrics Based on Thickness-Sorted

- Two-Dimensional Hexagonal Boron Nitride Nanosheets. *Nano Lett.* **2015**, *15*, 7029–7036.
- (190) Green, A. A.; Hersam, M. C. Solution Phase Production of Graphene with Controlled Thickness via Density Differentiation. *Nano Lett.* **2009**, *9*, 4031–4036.
- (191) Kang, J.; Seo, J. W. T.; Alducin, D.; Ponce, A.; Yacaman, M. J.; Hersam, M. C. Thickness Sorting of Two-Dimensional Transition Metal Dichalcogenides via Copolymer-Assisted Density Gradient Ultracentrifugation. *Nat. Commun.* **2014**, *5*, 5478.
- (192) Kang, J.; Sangwan, V. K.; Wood, J. D.; Liu, X.; Balla, I.; Lam, D.; Hersam, M. C. Layer-by-Layer Sorting of Rhenium Disulfide via High-Density Isopycnic Density Gradient Ultracentrifugation. *Nano Lett.* **2016**, *16*, 7216–7223.
- (193) Kang, J.; Wood, J. D.; Wells, S. A.; Lee, J.; Liu, X.; Hersam, M. C. Solvent Exfoliation of Electronic-Grade, Two-Dimensional Black Phosphorus. *ACS Nano* **2015**, *9*, 3596–3604.
- (194) Kang, J.; Wells, S. A.; Wood, J. D.; Lee, J.; Liu, X. Stable Aqueous Dispersions of Optically and Electronically Active Phosphorene. *P. Natl. Acad. Sci USA.* **2016**, *113*, 11688–11693.
- (195) Ghosh, S.; Bachilo, S. M.; Simonette, R. A.; Beckingham, K. M.; Weisman, R. B. Oxygen Doping Modifies Near-Infrared Band Gaps in Fluorescent Single-Walled Carbon Nanotubes. *Science* **2010**, *330*, 1656–1659.
- (196) Warheit, D. B.; Laurence, B. R.; Reed, K. L.; Roach, D. H.; Reynolds, G. A. M.; Webb, T. R. Comparative Pulmonary Toxicity Assessment of Single-Wall Carbon Nanotubes in Rats. *Toxicol. Sci.* **2004**, *77*, 117–125.
- (197) Donaldson, K.; Aitken, R.; Tran, L.; Stone, V.; Duffin, R.; Forrest, G.; Alexander, A. Carbon Nanotubes: A Review of Their Properties in Relation to Pulmonary Toxicology and Workplace Safety. *Toxicol. Sci.* **2006**, *92*, 5–22.
- (198) Poland, C. A.; Duffin, R.; Kinloch, I.; Maynard, A.; Wallace, W. A. H.; Seaton, A.; Stone, V.; Brown, S.; Macnee, W.; Donaldson, K. Carbon Nanotubes Introduced into the Abdominal Cavity of Mice Show Asbestos-like Pathogenicity in a Pilot Study. *Nat. Nanotechnol.* **2008**, *3*, 423–428.
- (199) Shvedova, A. A.; Kisin, E.; Murray, A. R.; Johnson, V. J.; Gorelik, O.; Arepalli, S.; Hubbs, A. F.; Mercer, R. R.; Keohavong, P.; Sussman, N.; *et al.* Inhalation vs. Aspiration of Single-Walled Carbon Nanotubes in C57BL/6 Mice: Inflammation, Fibrosis, Oxidative Stress, and Mutagenesis. *Am. J. Physiol. Lung Cell. Mol. Physiol.* **2008**, *295*, L552–L565.
- (200) Jia, G.; Wang, H. F.; Yan, L.; Wang, X.; Pei, R. J.; Yan, T.; Zhao, Y. L.; Guo, X. B. Cytotoxicity of Carbon Nanomaterials: Single-Wall Nanotube, Multi-Wall Nanotube, and Fullerene. *Environ. Sci. Technol.* **2005**, *39*, 1378–1383.

- (201) Kayat, J.; Gajbhiye, V.; Tekade, R. K.; Jain, N. K. Pulmonary Toxicity of Carbon Nanotubes: A Systematic Report. *Nanomedicine* **2011**, *7*, 40–49.
- (202) Li, R. B.; Wang, X.; Ji, Z. X.; Sun, B. B.; Zhang, H. Y.; Chang, C. H.; Lin, S. J.; Meng, H.; Liao, Y. P.; Wang, M. Y.; *et al.* Surface Charge and Cellular Processing of Covalently Functionalized Multiwall Carbon Nanotubes Determine Pulmonary Toxicity. *ACS Nano* **2013**, *7*, 2352–2368.
- (203) Shvedova, A. A.; Kisin, E. R.; Mercer, R.; Murray, A. R.; Johnson, V. J.; Potapovich, A. I.; Tyurina, Y. Y.; Gorelik, O.; Arepalli, S.; Schwegler-Berry, D.; *et al.* Unusual Inflammatory and Fibrogenic Pulmonary Responses to Single-Walled Carbon Nanotubes in Mice. *Am. J. Physiol. Lung Cell. Mol. Physiol.* **2005**, *289*, L698–L708.
- (204) Wang, X.; Jia, G.; Wang, H.; Nie, H.; Yan, L.; Deng, X. Y.; Wang, S. Diameter Effects on Cytotoxicity of Multi-Walled Carbon Nanotubes. *J. Nanosci. Nanotechnol.* **2009**, *9*, 3025–3033.
- (205) Mutlu, G. M.; Budinger, G. R. S.; Green, A. a; Urich, D.; Soberanes, S.; Chiarella, S. E.; Alheid, G. F.; McCrimmon, D. R.; Szeleifer, I.; Hersam, M. C. Biocompatible Nanoscale Dispersion of Single-Walled Carbon Nanotubes Minimizes in Vivo Pulmonary Toxicity. *Nano Lett.* **2010**, *10*, 1664–1670.
- (206) Nagai, H.; Okazaki, Y.; Chew, S. H.; Misawa, N.; Yamashita, Y.; Akatsuka, S.; Ishihara, T.; Yamashita, K.; Yoshikawa, Y.; Yasui, H.; *et al.* Diameter and Rigidity of Multiwalled Carbon Nanotubes Are Critical Factors in Mesothelial Injury and Carcinogenesis. *P. Natl. Acad. Sci. USA* **2011**, *108*, E1330–E1338.
- (207) Wang, X.; Xia, T.; Duch, M. C.; Ji, Z. X.; Zhang, H. Y.; Li, R. B.; Sun, B. B.; Lin, S. J.; Meng, H.; Liao, Y. P.; *et al.* Pluronic F108 Coating Decreases the Lung Fibrosis Potential of Multiwall Carbon Nanotubes by Reducing Lysosomal Injury. *Nano Lett.* **2012**, *12*, 3050–3061.
- (208) Wang, X.; Xia, T.; Ntim, S. A.; Ji, Z.; Lin, S.; Meng, H.; Chung, C.; George, S.; Zhang, H.; Wang, M.; *et al.* Dispersal State of Multi-Walled Carbon Nanotubes Elicits Pro-Fibrogenic Cellular Responses That Correlate with Fibrogenesis Biomarkers and Fibrosis in the Murine Lung. *ACS Nano* **2011**, *5*, 9772–9787.
- (209) Wang, X.; Xia, T.; Ntim, S. A.; Ji, Z. X.; George, S.; Meng, H.; Zhang, H.; Castranova, V.; Mitra, S.; Nel, A. E. Quantitative Techniques for Assessing and Controlling the Dispersion and Biological Effects of Multiwalled Carbon Nanotubes in Mammalian Tissue Culture Cells. *ACS Nano* **2010**, *4*, 7241–7252.
- (210) Wang, X.; Duch, M. C.; Mansukhani, N.; Ji, Z.; Liao, Y. P.; Wang, M.; Zhang, H.; Sun, B.; Chang, C. H.; Li, R.; *et al.* Use of a Pro-Fibrogenic Mechanism-Based Predictive Toxicological Approach for Tiered Testing and Decision Analysis of Carbonaceous

- Nanomaterials. *ACS Nano* **2015**, *9*, 3, 3032–3043.
- (211) Sun, B. B.; Wang, X.; Ji, Z. X.; Li, R. B.; Xia, T. NLRP3 Inflammasome Activation Induced by Engineered Nanomaterials. *Small* **2013**, *9*, 1595–1607.
- (212) Fubini, B.; Ghiazza, M.; Fenoglio, I. Physico-Chemical Features of Engineered Nanoparticles Relevant to Their Toxicity. *Nanotoxicology* **2010**, *4*, 347–363.
- (213) Ge, C. C.; Meng, L.; Xu, L. G.; Bai, R.; Du, J. F.; Zhang, L. L.; Li, Y.; Chang, Y. Z.; Zhao, Y. L.; Chen, C. Y. Acute Pulmonary and Moderate Cardiovascular Responses of Spontaneously Hypertensive Rats after Exposure to Single-Wall Carbon Nanotubes. *Nanotoxicology* **2012**, *6*, 526–542.
- (214) Liu, Y.; Zhao, Y. L.; Sun, B. Y.; Chen, C. Y. Understanding the Toxicity of Carbon Nanotubes. *Acc. Chem. Res.* **2013**, *46*, 702–713.
- (215) Kagan, V.; Potapovich, A.; Osipov, A.; Schwegler-Berry, D.; Kisin, E.; Mercer, R.; Castranova, V.; Shvedova, A. Iron-Rich Single Walled Carbon Nanotubes Are Effective Catalysts of Oxidative Stress in Raw 264.7 Macrophage Cell Culture Model: Interactions with Inflammatory Response and in Vivo Implications. *Free Radic. Biol. Med.* **2004**, *37*, S51–S52.
- (216) Mercer, R. R.; Scabilloni, J.; Wang, L.; Kisin, E.; Murray, A. R.; Schwegler-Berry, D.; Shvedova, A. A.; Castranova, V. Alteration of Deposition Pattern and Pulmonary Response as a Result of Improved Dispersion of Aspirated Single-Walled Carbon Nanotubes in a Mouse Model. *Am. J. Physiol. Lung Cell. Mol. Physiol.* **2008**, *294*, L87–L97.
- (217) Wang, X.; Guo, J.; Chen, T.; Nie, H. Y.; Wang, H. F.; Zang, J. J.; Cui, X. X.; Jia, G. Multi-Walled Carbon Nanotubes Induce Apoptosis via Mitochondrial Pathway and Scavenger Receptor. *Toxicol. Vitro.* **2012**, *26*, 799–806.
- (218) Duch, M. C.; Budinger, G. R. S.; Liang, Y. T.; Soberanes, S.; Urich, D.; Chiarella, S. E.; Campochiaro, L. A.; Gonzalez, A.; Chandel, N. S.; Hersam, M. C. Minimizing Oxidation and Stable Nanoscale Dispersion Improves the Biocompatibility of Graphene in the Lung. *Nano Lett.* **2011**, *11*, 5201–5207.
- (219) Singh, R. P.; Jain, S.; Ramarao, P. Surfactant-Assisted Dispersion of Carbon Nanotubes: Mechanism of Stabilization and Biocompatibility of the Surfactant. *J. Nanopart. Res.* **2013**, *15*, 1985–1987.
- (220) Yang, S.; Guo, W.; Lin, Y.; Deng, X.; Wang, H.; Sun, H.; Liu, Y.; Wang, X.; Wang, W.; Chen, M.; *et al.* Biodistribution of Pristine Single-Walled Carbon Nanotubes In Vivo. *J. Phys. Chem. C* **2007**, *111*, 17761–17764.
- (221) Jackson, P.; Jacobsen, N. R.; Baun, A.; Birkedal, R.; Kühnel, D.; Jensen, K. A.; Vogel, U.;

- Wallin, H. Bioaccumulation and Ecotoxicity of Carbon Nanotubes. *Chem. Cent. J.* **2013**, *7*, 154.
- (222) Kolosnjaj-Tabi, J.; Hartman, K. B.; Boudjemaa, S.; Ananta, J. S.; Morgant, G.; Szwarc, H.; Wilson, L. J.; Moussa, F. In Vivo Behavior of Large Doses of Ultrashort and Full-Length Single-Walled Carbon Nanotubes After Oral and Intraperitoneal Administration to Swiss Mice. *ACS Nano* **2010**, *4*, 1481–1492.
- (223) Liu, Z.; Davis, C.; Cai, W.; He, L.; Chen, X.; Dai, H. Circulation and Long-Term Fate of Functionalized, Biocompatible Single-Walled Carbon Nanotubes in Mice Probed by Raman Spectroscopy. *P. Natl. Acad. Sci. USA* **2008**, *105*, 1410–1415.
- (224) Liu, Z.; Cai, W.; He, L.; Nakayama, N.; Chen, K.; Sun, X.; Chen, X.; Dai, H. In Vivo Biodistribution and Highly Efficient Tumour Targeting of Carbon Nanotubes in Mice. *Nat. Nanotechnol.* **2007**, *2*, 47–52.
- (225) Singh, R.; Pantarotto, D.; Lacerda, L.; Pastorin, G.; Klumpp, C.; Prato, M.; Bianco, A.; Kostarelos, K. Tissue Biodistribution and Blood Clearance Rates of Intravenously Administered Carbon Nanotube Radiotracers. *P. Natl. Acad. Sci. USA* **2006**, *103*, 3357–3362.
- (226) Lin, Y.; Taylor, S.; Li, H.; Fernando, K. A. S.; Qu, L.; Wang, W.; Gu, L.; Zhou, B.; Sun, Y. P. Advances toward Bioapplications of Carbon Nanotubes. *J. Mater. Chem.* **2004**, *14*, 527–541.
- (227) Fairhall Dunn, R. C., Sharpless, N. E. and Pritchard, E. A., The Toxicity of Molybdenum, U. S. Public Health Service, Public Health Bulletin, 1945, 293.
- (228) Wang, Z.; Zhu, W.; Qiu, Y.; Yi, X.; von dem Bussche, A.; Kane, A.; Gao, H.; Koski, K.; Hurt, R. Biological and Environmental Interactions of Emerging Two-Dimensional Nanomaterials. *Chem. Soc. Rev.* **2016**, *45*, 1750–1780.
- (229) Chng, E. L. K.; Sofer, Z.; Pumera, M. MoS₂ Exhibits Stronger Toxicity with Increased Exfoliation. *Nanoscale* **2014**, *6*, 14412–14418.
- (230) Shah, P.; Narayanan, T. N.; Li, C. Z.; Alwarappan, S. Probing the Biocompatibility of MoS₂ Nanosheets by Cytotoxicity Assay and Electrical Impedance Spectroscopy. *Nanotechnology* **2015**, *26*, 315102.
- (231) Liu, T.; Wang, C.; Gu, X.; Gong, H.; Cheng, L.; Shi, X.; Feng, L.; Sun, B.; Liu, Z. Drug Delivery with PEGylated MoS₂ Nano-Sheets for Combined Photothermal and Chemotherapy of Cancer. *Adv. Mater.* **2014**, *26*, 3433–3440.
- (232) Cheng, L.; Liu, J.; Gu, X.; Gong, H.; Shi, X.; Liu, T.; Wang, C. PEGylated WS₂ Nanosheets as a Multifunctional Theranostic Agent for in Vivo Dual-Modal CT/Photoacoustic Imaging Guided Photothermal Therapy. *Adv. Mater.* **2014**, *26*, 1886–1893.

- (233) Teo, W. Z.; Chng, E. L. K.; Sofer, Z.; Pumera, M. Cytotoxicity of Exfoliated Transition-Metal Dichalcogenides (MoS_2 , WS_2 , and WSe_2) Is Lower Than That of Graphene and Its Analogues. *Chem. Eur. J.* **2014**, *20*, 9627–9632.
- (234) Chen, X.; Wu, P.; Rousseas, M.; Okawa, D.; Gartner, Z.; Zettl, A.; Bertozzi, C. R. Boron Nitride Nanotubes Are Noncytotoxic and Can Be Functionalized for Interaction with Proteins and Cells. *J. Am. Chem. Soc.* **2009**, *131*, 890–891.
- (235) Ciofani, G.; Danti, S.; Alessandro, D. D.; Ricotti, L.; Moscato, K. S.; Bertoni, G.; Falqui, A.; Berrettini, S.; Petrini, M.; Mattoli, V.; *et al.* Enhancement of Neurite Outgrowth in Neuronal-Like Cells Following Boron Nitride Nanotube-Mediated Stimulation. *ACS Nano* **2010**, *4*, 6267–6277.
- (236) Ciofani, G.; Danti, S.; D'Alessandro, D.; Moscato, S.; Menciassi, A. Assessing Cytotoxicity of Boron Nitride Nanotubes: Interference with the MTT Assay. *Biochem. Biophys. Res. Commun.* **2010**, *394*, 405–411.
- (237) Ferreira, T. H.; Rocca, A.; Marino, A.; Mattoli, V.; de Sousa, E. M. B.; Ciofani, G. Evaluation of the Effects of Boron Nitride Nanotubes Functionalized with Gum Arabic on the Differentiation of Rat Mesenchymal Stem Cells. *RSC Adv.* **2015**, *5*, 45431–45438.
- (238) Colvin, V. L. The Potential Environmental Impact of Engineered Nanomaterials. *Nat. Biotechnol.* **2003**, *21*, 1166–1170.
- (239) Han, J. H.; Lee, S.; Cheon, J. Synthesis and Structural Transformations of Colloidal 2D Layered Metal Chalcogenide Nanocrystals. *Chem. Soc. Rev.* **2013**, *42*, 2581–2591.
- (240) Wang, X.; Mansukhani, N. D.; Guiney, L. M.; Ji, Z.; Chang, C. H.; Wang, M.; Liao, Y. P.; Song, T. B.; Sun, B.; Li, R.; *et al.* Differences in the Toxicological Potential of 2D versus Aggregated Molybdenum Disulfide in the Lung. *Small* **2015**, *11*, 5079–5087.
- (241) Qian, X.; Shen, S.; Liu, T.; Cheng, L.; Liu, Z. Two-Dimensional TiS_2 Nanosheets for in Vivo Photoacoustic Imaging and Photothermal Cancer Therapy. *Nanoscale* **2015**, *7*, 6380–6387.
- (242) Deng, R.; Xie, X.; Vendrell, M.; Chang, Y.-T.; Liu, X. Intracellular Glutathione Detection Using MnO_2 -Nanosheet-Modified Upconversion Nanoparticles. *J. Am. Chem. Soc.* **2011**, *133*, 20168–20171.
- (243) Song, S. H.; Kim, B. H.; Choe, D. H.; Kim, J. J. M.; Kim, D. C.; Lee, D. J.; Kim, J. J. M.; Chang, K. J.; Jeon, S. Bandgap Widening of Phase Quilted, 2D MoS_2 by Oxidative Intercalation. *Adv. Mater.* **2015**, *27*, 3152–3158.
- (244) Lanphere, J. D.; Luth, C. J.; Guiney, L. M.; Mansukhani, N. D.; Hersam, M. C.; Walker, S. L. Fate and Transport of Molybdenum Disulfide Nanomaterials in Sand Columns. *Environ. Eng. Sci.* **2014**, *32*, 163–172.

- (245) Klaine, S. J.; Alvarez, P. J. J.; Batley, G. E.; Fernandes, T. F.; Handy, R. D.; Lyon, D.; Mahendra, S.; McLaughlin, M. J.; Lead, J. R. Nanomaterials in the Environment: Behavior, Fate, Bioavailability, and Effects. *Environ. Toxicol. Chem.* **2008**, *27*, 1825–1851.
- (246) Bertino, D. J.; Zepp, R. G. Effects of Solar Radiation on Manganese Oxide Reactions with Selected Organic Compounds. *Environ. Sci. Technol.* **1991**, *25*, 1267–1273.
- (247) Catts, J. G.; Langmuir, D. Adsorption of Cu, Pb and Zn by δMnO_2 : Applicability of the Site Binding-Surface Complexation Model. *Appl. Geochemistry* **1986**, *1*, 255–264.
- (248) Cofer, C. G.; Economy, J. Oxidation Protection of Carbon Composites Oxidative and Hydrolytic Stability of Boron Nitride — A New Approach to Improving the Oxidation Resistance of Carbonaceous Structures. *Carbon* **1995**, *33*, 389–395.
- (249) Dong, L.; Zhu, Z.; Ma, H.; Qiu, Y.; Zhao, J. Simultaneous Adsorption of Lead and Cadmium on MnO_2 -Loaded Resin. *J. Environ. Sci.* **2010**, *22*, 225–229.
- (250) Kim, E. J.; Lee, C. S.; Chang, Y. S. Hierarchically Structured Manganese Oxide-Coated Magnetic Nanocomposites for the Efficient Removal of Heavy Metal Ions from Aqueous Systems. *ACS Appl. Mater. Inter.* **2013**, *5*, 9628–9634.
- (251) Remucal, C. K.; Ginder-Vogel, M. A Critical Review of the Reactivity of Manganese Oxides with Organic Contaminants. *Environ. Sci. Process. Impacts* **2014**, *16*, 1247–1266.
- (252) Sunda, W. G.; Huntsman, S. A.; Harvey, G. R. Photoreduction of Manganese Oxides in Seawater and Its Geochemical and Biological Implications. *Nature* **1983**, *301*, 234–236.
- (253) Lecoanet, H. F.; Bottero, J.; Wiesner, M. R. Laboratory Assessment of the Mobility of Nanomaterials in Porous Media Laboratory Assessment of the Mobility of Nanomaterials in Porous Media. *Environ. Sci. Technol.* **2004**, *38*, 5164–5169.
- (254) Tian, Y.; Gao, B.; Silvera-Batista, C.; Ziegler, K. J. Transport of Engineered Nanoparticles in Saturated Porous Media. *J. Nanopart. Res.* **2010**, *12*, 2371–2380.
- (255) Tian, Y.; Gao, B.; Ziegler, K. J. High Mobility of SDBS-Dispersed Single-Walled Carbon Nanotubes in Saturated and Unsaturated Porous Media. *J. Hazard. Mater.* **2011**, *186*, 1766–1772.
- (256) Ray, P. C.; Yu, H.; Fu, P. P. Toxicity and Environmental Risks of Nanomaterials: Challenges and Future Needs. *J. Environ. Sci. Heal. Part C* **2009**, *27*, 1–35.
- (257) Petersen, E. J.; Zhang, L.; Mattison, N. T.; O’Carroll, D. M.; Whelton, A. J.; Uddin, N.; Nguyen, T.; Huang, Q.; Henry, T. B.; Holbrook, R. D.; *et al.* Potential Release Pathways, Environmental Fate, and Ecological Risks of Carbon Nanotubes. *Environ. Sci. Technol.* **2011**, *45*, 9837–9856.

- (258) Kagan, V. E.; Konduru, N. V.; Feng, W.; Allen, B. L.; Conroy, J.; Volkov, Y.; Vlasova, I. I.; Belikova, N. A.; Yanamala, N.; Kapralov, A.; *et al.* Carbon Nanotubes Degraded by Neutrophil Myeloperoxidase Induce Less Pulmonary Inflammation. *Nat. Nanotechnol.* **2010**, *5*, 354–359.
- (259) Allen, B. L.; Kotchey, G. P.; Chen, Y.; Yanamala, N. V. K.; Klein-Seetharaman, J.; Kagan, V. E.; Star, A. Mechanistic Investigations of Horseradish Peroxidase-Catalyzed Degradation of Single-Walled Carbon Nanotubes. *J. Am. Chem. Soc.* **2009**, *131*, 17194–17205.
- (260) Allen, B. L.; Kichambare, P. D.; Gou, P.; Vlasova, I. I.; Kapralov, A. A.; Konduru, N.; Kagan, V. E.; Star, A. Biodegradation of Single-Walled Carbon Nanotubes through Enzymatic Catalysis. *Nano Lett.* **2008**, *8*, 3899–3903.
- (261) Liu, X.; Hurt, R. H.; Kane, A. B. Biodurability of Single-Walled Carbon Nanotubes Depends on Surface Functionalization. *Carbon* **2010**, *48*, 1961–1969.
- (262) Wang, Z.; von dem Bussche, A.; Kabadi, P. K.; Kane, A. B.; Hurt, R. H. Biological and Environmental Transformations of Copper-Based Nanomaterials. *ACS Nano* **2013**, *7*, 8715–8727.
- (263) Bosecker, K. Bioleaching: Metal Solubilization by Microorganisms. *FEMS Microbiol. Rev.* **1997**, *20*, 591–604.
- (264) Bryner, L.; Anderson, R. Microorganisms in Leaching Sulfide Minerals. *Ind. Eng. Chem.* **1957**, *49*, 1721–1724.
- (265) Schippers, A.; Sand, W. Bacterial Leaching of Metal Sulfides Proceeds by Two Indirect Mechanisms via Thiosulfate or via Polysulfides and Sulfur. *Appl. Environ. Microbiol.* **1999**, *65*, 319–321.
- (266) Tributsch, H.; Bennett, J. C. Semiconductor-Electrochemical Aspects of Bacterial Leaching: Part 2. Survey of Rate-Controlling Sulphide Properties. *J. Chem. Technol. Biotechnol.* **1981**, *31*, 627–635.
- (267) Conway, J. R.; Hanna, S. K.; Lenihan, H. S.; Keller, A. A. Effects and Implications of Trophic Transfer and Accumulation of CeO₂ Nanoparticles in a Marine Mussel. *Environ. Sci. Technol.* **2014**, *48*, 1517–1524.
- (268) Ward, G. M. Molybdenum Toxicity and Hypocuprosis in Ruminants: A Review. *J. Anim. Sci.* **1978**, *46*, 1078–1085.
- (269) Dong, R.; Pang, Y.; Su, Y.; Zhu, X. Supramolecular Hydrogels: Synthesis, Properties and Their Biomedical Applications. *Biomater. Sci.* **2015**, *3*, 937–954.
- (270) Tomatsu, I.; Peng, K.; Kros, A. Photoresponsive Hydrogels for Biomedical Applications.

- Adv. Drug Deliv. Rev.* **2011**, *63*, 1257–1266.
- (271) Adhikari, B.; Banerjee, A. Short Peptide Based Hydrogels: Incorporation of Graphene into the Hydrogel. *Soft Matter* **2011**, *7*, 9259–9266.
- (272) Adhikari, B.; Biswas, A.; Banerjee, A. Graphene Oxide-Based Supramolecular Hydrogels for Making Nanohybrid Systems with Au Nanoparticles. *Langmuir* **2012**, *28*, 1460–1469.
- (273) Zo, H. J.; Lee, J. S.; Song, K. W.; Kim, M.; Lee, G.; Park, J. S. Incorporation of Graphene Oxide into Cyclodextrin-Dye Supramolecular Hydrogel. *J. Incl. Phenom. Macrocycl. Chem.* **2013**, *79*, 357–363.
- (274) Das, D.; Kar, T.; Das, P. K. Gel-Nanocomposites: Materials with Promising Applications. *Soft Matter* **2012**, *8*, 2348–2365.
- (275) Bigall, N. C.; Herrmann, A. K.; Vogel, M.; Rose, M.; Simon, P.; Carrillo-Cabrera, W.; Dorfs, D.; Kaskel, S.; Gaponik, N.; Eychmüller, A. Hydrogels and Aerogels from Noble Metal Nanoparticles. *Angew. Chem. Int. Ed.* **2009**, *48*, 9731–9734.
- (276) Mannoor, M. S.; Jiang, Z.; James, T.; Kong, Y. L.; Malatesta, K. a.; Soboyejo, W. O.; Verma, N.; Gracias, D. H.; McAlpine, M. C. 3D Printed Bionic Ears. *Nano Lett.* **2013**, *13*, 2634–2639.
- (277) Gupta, M. K.; Meng, F.; Johnson, B. N.; Kong, Y. L.; Tian, L.; Yeh, Y. W.; Masters, N.; Singamaneni, S.; McAlpine, M. C. 3D Printed Programmable Release Capsules. *Nano Lett.* **2015**, *15*, 5321–5329.
- (278) Jeong, B.; Bae, Y. H.; Lee, D. S.; Kim, S. W. Biodegradable Block Copolymers as Injectable Drug-Delivery Systems. *Nature* **1997**, *388*, 860–862.
- (279) Peppas, N. A.; Hilt, J. Z.; Khademhosseini, A.; Langer, R. Hydrogels in Biology and Medicine: From Molecular Principles to Bionanotechnology. *Adv. Mater.* **2006**, *18*, 1345–1360.
- (280) Ikeda, M.; Tanida, T.; Yoshii, T.; Hamachi, I. Rational Molecular Design of Stimulus-Responsive Supramolecular Hydrogels Based on Dipeptides. *Adv. Mater.* **2011**, *23*, 2819–2822.
- (281) Appel, E. A.; Biedermann, F.; Rauwald, U.; Jones, S. T.; Zayed, J. M.; Scherman, O. A. Supramolecular Cross-Linked Networks via Host-Guest Complexation with Cucurbit[8]uril. *J. Am. Chem. Soc.* **2010**, *132*, 14251–14260.
- (282) Jing, B.; Chen, X.; Wang, X.; Zhao, Y.; Qiu, H. Sol-Gel-Sol Transition of Gold Nanoparticle-Based Supramolecular Hydrogels Induced by Cyclodextrin Inclusion. *Chem. Phys. Chem* **2008**, *9*, 249–252.

- (283) Guo, W.; Lu, C. H.; Orbach, R.; Wang, F.; Qi, X. J.; Cecconello, A.; Seliktar, D.; Willner, I. pH-Stimulated DNA Hydrogels Exhibiting Shape-Memory Properties. *Adv. Mater.* **2015**, *27*, 73–78.
- (284) Lee, J. B.; Peng, S.; Yang, D.; Roh, Y. H.; Funabashi, H.; Park, N.; Rice, E. J.; Chen, L.; Long, R.; Wu, M.; *et al.* A Mechanical Metamaterial Made from a DNA Hydrogel. *Nat. Nanotechnol.* **2012**, *7*, 816–820.
- (285) Steed, J. W. Supramolecular Gel Chemistry: Developments over the Last Decade. *Chem. Commun.* **2011**, *47*, 1379–1383.
- (286) Chen, D. T. N.; Chen, K.; Hough, L. A.; Islam, M. F.; Yodh, A. G. Rheology of Carbon Nanotube Networks during Gelation. *Macromolecules* **2010**, *43*, 2048–2053.
- (287) Plashnitsa, V. V.; Vietmeyer, F.; Petchsang, N.; Tongying, P.; Kosel, T. H.; Kuno, M. Synthetic Strategy and Structural and Optical Characterization of Thin Highly Crystalline Titanium Disulfide Nanosheets. *J. Phys. Chem. Lett.* **2012**, *3*, 1554–1558.
- (288) Faber, M. S.; Park, K.; Caba, M.; Santra, P. K.; Jin, S. Earth-Abundant Cobalt Pyrite (CoS₂) Thin Film on Glass as a Robust, High-Performance Counter Electrode for Quantum Dot-Sensitized Solar Cells. *J. Phys. Chem. Lett.* **2013**, *4*, 1843–1849.
- (289) Koski, K. J.; Cui, Y.; Science, M.; States, U.; Sciences, E.; National, S.; Road, S. H.; Park, M. The New Skinny in Two-Dimensional Materials. **2013**, 3739–3743.
- (290) Butler, S. Z.; Hollen, S. M.; Cao, L.; Cui, Y.; Gupta, J. A.; Gutiérrez, H. R.; Heinz, T. F.; Hong, S. S.; Huang, J.; Ismach, A. F.; *et al.* Progress, Challenges, and Opportunities in Two-Dimensional Materials Beyond Graphene. *ACS Nano* **2013**, *7*, 2898–2926.
- (291) Zhao, L. D.; Lo, S. H.; Zhang, Y.; Sun, H.; Tan, G.; Uher, C.; Wolverton, C.; Dravid, V. P.; Kanatzidis, M. G. Ultralow Thermal Conductivity and High Thermoelectric Figure of Merit in SnSe Crystals. *Nature* **2014**, *508*, 373–377.
- (292) Lin, Y.; Connell, J. W. Advances in 2D Boron Nitride Nanostructures: Nanosheets, Nanoribbons, Nanomeshes, and Hybrids with Graphene. *Nanoscale* **2012**, *4*, 6908–6939.
- (293) Mak, K. F.; Lee, C.; Hone, J.; Shan, J.; Heinz, T. F. Atomically Thin MoS₂: A New Direct-Gap Semiconductor. *Phys. Rev. Lett.* **2010**, *105*, 136805.
- (294) Wang, Q. H.; Kalantar-Zadeh, K.; Kis, A.; Coleman, J. N.; Strano, M. S. Electronics and Optoelectronics of Two-Dimensional Transition Metal Dichalcogenides. *Nat. Nanotechnol.* **2012**, *7*, 699–712.
- (295) Radisavljevic, B.; Radenovic, A.; Brivio, J.; Giacometti, V.; Kis, A. Single-Layer MoS₂ Transistors. *Nat. Nanotechnol.* **2011**, *6*, 147–150.

- (296) Wang, H.; Yu, L.; Lee, Y. H.; Shi, Y.; Hsu, A.; Chin, M. L.; Li, L. J.; Dubey, M.; Kong, J.; Palacios, T. Integrated Circuits Based on Bilayer MoS₂ Transistors. *Nano Lett.* **2012**, *12*, 4674–4680.
- (297) Duerloo, K. N.; Ong, M. T.; Reed, E. J. Intrinsic Piezoelectricity in Two-Dimensional Materials. *J. Phys. Chem. Lett.* **2012**, *3*, 2871–2876.
- (298) Martin, J. M.; Donnet, C.; Le Mogne, T. Superlubricity of Molybdenum Disulphide. *Phys. Rev. B* **1993**, *48*, 10583.
- (299) Blumberg, A.; Keshet, U.; Zaltsman, I.; Hod, O. Interlayer Registry to Determine the Sliding Potential of Layered Metal Dichalcogenides: The Case of 2H-MoS₂. **2012**, 1936–1940.
- (300) Levita, G.; Cavaleiro, A.; Molinari, E.; Polcar, T.; Righi, M. C. Sliding Properties of MoS₂ Layers : Load and Interlayer Orientation Effects. *J. Phys. Chem. C* **2014**, *118*, 13809–13816.
- (301) Wu, C.; Jariwala, D.; Sangwan, V. K.; Marks, T. J.; Hersam, M. C.; Lauhon, L. J. Elucidating the Photoresponse of Ultrathin MoS₂ Field-Effect Transistors by Scanning Photocurrent Microscopy. *J. Phys. Chem. Lett.* **2013**, *4*, 2508–2513.
- (302) Li, Y.; Wu, D.; Zhou, Z.; Cabrera, C. R.; Chen, Z. Enhanced Li Adsorption and Diffusion on MoS₂ Zigzag Nanoribbons by Edge Effects: A Computational Study. *J. Phys. Chem. Lett.* **2012**, *3*, 2221–2227.
- (303) Kou, L.; Tang, C.; Zhang, Y.; Heine, T.; Chen, C.; Frauenheim, T. Tuning Magnetism and Electronic Phase Transitions by Strain and Electric Field in Zigzag MoS₂ Nanoribbons. *J. Phys. Chem. Lett.* **2012**, *3*, 2934–2941.
- (304) Sun, Z.; James, D. K.; Tour, J. M. Graphene Chemistry : Synthesis and Manipulation. **2011**, 2425–2432.
- (305) Chou, S. S.; Kaehr, B.; Kim, J.; Foley, B. M.; De, M.; Hopkins, P. E.; Huang, J.; Brinker, C. J.; Dravid, V. P. Chemically Exfoliated MoS₂ as Near-Infrared Photothermal Agents. *Angew. Chem. Int. Ed. Engl.* **2013**, *52*, 4160–4164.
- (306) Kim, J.; Byun, S.; Smith, A. J.; Yu, J.; Huang, J. Enhanced Electrocatalytic Properties of Transition-Metal Dichalcogenides Sheets by Spontaneous Gold Nanoparticle Decoration. *J. Phys. Chem. Lett.* **2013**, *4*, 1227–1232.
- (307) Komsa, H. P.; Krasheninnikov, A. V. Two-Dimensional Transition Metal Dichalcogenide Alloys: Stability and Electronic Properties. *J. Phys. Chem. Lett.* **2012**, *3*, 3652–3656.
- (308) Wang, X.; Gong, Y.; Shi, G.; Chow, W. L.; Keyshar, K.; Ye, G.; Vajtai, R.; Lou, J.; Liu, Z.; Ringe, E.; *et al.* Chemical Vapor Deposition Growth of Crystalline Monolayer MoSe₂.

- ACS Nano* **2014**, *8*, 5125–5131.
- (309) Shim, G. W.; Yoo, K.; Seo, S. B.; Shin, J.; Jung, D. Y.; Kang, I. S.; Ahn, C. W.; Cho, B. J.; Choi, S. Y. Large-Area Single-Layer MoSe₂ and Its van Der Waals Heterostructures. *ACS Nano* **2014**, *8*, 6655–6662.
- (310) Mahler, B.; Hoepfner, V.; Liao, K.; Ozin, G. Colloidal Synthesis of 1T-WS₂ and 2H-WS₂ Nanosheets : Applications for Photocatalytic Hydrogen Evolution. *J. Am. Chem. Soc.* **2014**, *136*, 14121–14127.
- (311) Najmaei, S.; Liu, Z.; Zhou, W.; Zou, X.; Shi, G.; Lei, S.; Yakobson, B. I.; Idrobo, J. C.; Ajayan, P. M.; Lou, J. Vapour Phase Growth and Grain Boundary Structure of Molybdenum Disulphide Atomic Layers. *Nat. Mater.* **2013**, *12*, 754–759.
- (312) Osada, M.; Sasaki, T. Exfoliated Oxide Nanosheets: New Solution to Nanoelectronics. *J. Mater. Chem.* **2009**, *19*, 2503–2511.
- (313) Gordon, R. A.; Yang, D.; Crozier, E. D.; Jiang, D. T.; Frindt, R. F. Structures of Exfoliated Single Layers of WS₂, MoS₂, MoSe₂ in Aqueous Suspension. *Phys. Rev. B* **2002**, *65*, 125407.
- (314) Kan, M.; Wang, J. Y.; Li, X. W.; Zhang, S. H.; Li, Y. W.; Kawazoe, Y.; Sun, Q.; Jena, P. Structures and Phase Transition of a MoS₂ Monolayer. *J. Phys. Chem. C* **2014**, *118*, 1515–1522.
- (315) Frey, G. L.; Reynolds, K. J.; Friend, R. H.; Cohen, H.; Feldman, Y. Solution-Processed Anodes from Layer-Structure Materials for High-Efficiency Polymer Light-Emitting Diodes. *J. Am. Chem. Soc.* **2003**, *125*, 5998–6007.
- (316) Smith, R. J.; King, P. J.; Lotya, M.; Wirtz, C.; Khan, U.; De, S.; O'Neill, A.; Duesberg, G. S.; Grunlan, J. C.; Moriarty, G.; *et al.* Large-Scale Exfoliation of Inorganic Layered Compounds in Aqueous Surfactant Solutions. *Adv. Mater.* **2011**, *23*, 3944–3948.
- (317) Duch, M. C.; Budinger, G. R. S.; Liang, Y. T.; Soberanes, S.; Urich, D.; Chiarella, S. E.; Campochiaro, L. a; Gonzalez, A.; Chandel, N. S.; Hersam, M. C.; *et al.* Minimizing Oxidation and Stable Nanoscale Dispersion Improves the Biocompatibility of Graphene in the Lung. *Nano Lett.* **2011**, *11*, 5201–5207.
- (318) Bonaccorso, F.; Hasan, T.; Tan, P. H.; Sciascia, C.; Privitera, G.; Di Marco, G.; Gucciardi, P. G.; Ferrari, A. C. Density Gradient Ultracentrifugation of Nanotubes: Interplay of Bundling and Surfactants Encapsulation. *J. Phys. Chem. C* **2010**, *114*, 17267–17285.
- (319) Sandwell, D. T. Biharmonic Spline Interpolation of GEOS-3 and SEASAT Altimeter Data. *Geophys. Res. Lett.* **1987**, *14*, 139–142.
- (320) Li, Z.; Wang, Y.; Kozbial, A.; Shenoy, G.; Zhou, F.; McGinley, R.; Ireland, P.;

- Morganstein, B.; Kunkel, A.; Surwade, S. P.; *et al.* Effect of Airborne Contaminants on the Wettability of Supported Graphene and Graphite. *Nat. Mater.* **2013**, *12*, 925–931.
- (321) Eng, A. Y. S.; Ambrosi, A.; Sofer, Z.; Šimek, P.; Pumera, M.; Simek, P.; Yong, A.; Eng, S.; Ambrosi, A.; Pumera, M. Electrochemistry of Transition Metal Dichalcogenides: Strong Dependence on the Metal-to-Chalcogen Composition and Exfoliation Method. *ACS Nano* **2014**, *8*, 12185–12198.
- (322) Secor, E. B.; Prabhumirashi, P. L.; Puntambekar, K.; Geier, M. L.; Hersam, M. C. Inkjet Printing of High Conductivity, Flexible Graphene Patterns. *J. Phys. Chem. Lett.* **2013**, *4*, 1347–1351.
- (323) Vecitis, C. D.; Zodrow, K. R.; Kang, S.; Elimelech, M. Electronic-Structure-Dependent Bacterial Cytotoxicity of Single-Walled Carbon Nanotubes. *ACS Nano* **2010**, *4*, 5471–5479.
- (324) Lanphere, J. D.; Luth, C. J.; Walker, S. L. Effects of Solution Chemistry on the Transport of Graphene Oxide in Saturated Porous Media. *Environ. Sci. Technol.* **2013**, *47*, 4255–4261.
- (325) Hemond Fechner-Levy, E.J., H. F. *Chemical Fate and Transport in the Environment*; Academic Press: San Diego, 2009.
- (326) Zhang, H. Y.; Pokhrel, S.; Ji, Z. X.; Meng, H.; Wang, X.; Lin, S. J.; Chang, C. H.; Li, L. J.; Li, R. B.; Sun, B. B.; *et al.* PdO Doping Tunes Band-Gap Energy Levels as Well as Oxidative Stress Responses to a Co_3O_4 p-Type Semiconductor in Cells and the Lung. *J. Am. Chem. Soc.* **2014**, *136*, 6406–6420.
- (327) Yazdi, A. S.; Guarda, G.; Riteau, N.; Drexler, S. K.; Tardivel, A.; Couillin, I.; Tschopp, J. Nanoparticles Activate the NLR Pyrin Domain Containing 3 (Nlrp3) Inflammasome and Cause Pulmonary Inflammation through Release of IL-1 Alpha and IL-1 Beta. *P. Natl. Acad. Sci. USA* **2010**, *107*, 19449–19454.
- (328) Ji, Z.; Wang, X.; Zhang, H.; Lin, S.; Meng, H.; Sun, B.; George, S.; Xia, T.; Nel, A. E.; Zink, J. I. Designed Synthesis of CeO_2 Nanorods and Nanowires for Studying Toxicological Effects of High Aspect Ratio Nanomaterials. *ACS Nano* **2012**, *6*, 5366–5380.
- (329) Lin, S. J.; Wang, X.; Ji, Z. X.; Chang, C. H.; Dong, Y.; Meng, H.; Liao, Y. P.; Wang, M. Y.; Song, T. B.; Kohan, S.; *et al.* Aspect Ratio Plays a Role in the Hazard Potential of CeO_2 Nanoparticles in Mouse Lung and Zebrafish Gastrointestinal Tract. *ACS Nano* **2014**, *8*, 4450–4464.
- (330) Kim, Y. M.; Reed, W.; Lenz, A. G.; Jaspers, I.; Silbajoris, R.; Nick, H. S.; Samet, J. M. Ultrafine Carbon Particles Induce Interleukin-8 Gene Transcription and p38 MAPK

- Activation in Normal Human Bronchial Epithelial Cells. *Am. J. Physiol. Lung Cell. Mol. Physiol.* **2005**, 288, L432–L441.
- (331) Singh, S.; Shi, T. M.; Duffin, R.; Albrecht, C.; van Berlo, D.; Hoehr, D.; Fubini, B.; Martra, G.; Fenoglio, I.; Borm, P. J. A.; *et al.* Endocytosis, Oxidative Stress and IL-8 Expression in Human Lung Epithelial Cells upon Treatment with Fine and Ultrafine TiO₂: Role of the Specific Surface Area and of Surface Methylation of the Particles. *Toxicol. Appl. Pharmacol.* **2007**, 222, 141–151.
- (332) Xia, T.; Kovoichich, M.; Liong, M.; Madler, L.; Gilbert, B.; Shi, H. B.; Yeh, J. I.; Zink, J. I.; Nel, A. E. Comparison of the Mechanism of Toxicity of Zinc Oxide and Cerium Oxide Nanoparticles Based on Dissolution and Oxidative Stress Properties. *ACS Nano* **2008**, 2, 2121–2134.
- (333) Bonner, J. C. Mesenchymal Cell Survival in Airway and Interstitial Pulmonary Fibrosis. *Fibrogenes. Tissue Repair* **2010**, 3, 15.
- (334) Palomaki, J.; Valimaki, E.; Sund, J.; Vippola, M.; Clausen, P. A.; Jensen, K. A.; Savolainen, K.; Matikainen, S.; Alenius, H. Long, Needle-like Carbon Nanotubes and Asbestos Activate the NLRP3 Inflammasome through a Similar Mechanism. *ACS Nano* **2011**, 5, 6861–6870.
- (335) Lee, J. H.; Ahn, K.; Kim, S. M.; Jeon, K. S.; Lee, J. S.; Yu, I. J. Continuous 3-Day Exposure Assessment of Workplace Manufacturing Silver Nanoparticles. *J. Nanopart. Res.* **2012**, 14, 1134–1138.
- (336) Galer, D. M.; Leung, H. W.; Sussman, R. G.; Trzos, R. J. Scientific and Practical Considerations for the Development of Occupational Exposure Limits (OELs) for Chemical-Substances. *Regul. Toxicol. Pharmacol.* **1992**, 15, 291–306.
- (337) Stone, K. C.; Mercer, R. R.; Gehr, P.; Stockstill, B.; Crapo, J. D. Allometric Relationships of Cell Numbers and Size in the Mammalian Lung. *Am. J. Respir. Cell Mol. Biol.* **1992**, 6, 235–243.
- (338) Kim, D.; Kim, J.; Ko, Y.; Shim, K.; Kim, J. H.; You, J. A Facile Approach for Constructing Conductive Polymer Patterns for Application in Electrochromic Devices and Flexible Microelectrodes. *ACS Appl. Mater. Inter.* **2016**, 8, 33175–33182.
- (339) Duan, J.; Liang, X.; Guo, J.; Zhu, K.; Zhang, L. Ultra-Stretchable and Force-Sensitive Hydrogels Reinforced with Chitosan Microspheres Embedded in Polymer Networks. *Adv. Mater.* **2016**, 28, 8037–8044.
- (340) Du, R.; Xu, Y.; Luo, Y.; Zhang, X.; Zhang, J. Synthesis of Conducting Polymer Hydrogels with 2D Building Blocks and Their Potential-Dependent Gel-Sol Transitions. *Chem. Commun.* **2011**, 47, 6287–6289.

- (341) Li, C.; Rowland, M. J.; Shao, Y.; Cao, T.; Chen, C.; Jia, H.; Zhou, X.; Yang, Z.; Scherman, O. A.; Liu, D. Responsive Double Network Hydrogels of Interpenetrating DNA and CB[8] Host-Guest Supramolecular Systems. *Adv. Mater.* **2015**, *27*, 3298–3304.
- (342) Lee, B. P.; Konst, S. Novel Hydrogel Actuator Inspired by Reversible Mussel Adhesive Protein Chemistry. *Adv. Mater.* **2014**, *26*, 3415–3419.
- (343) Wang, H.; Heilshorn, S. C. Adaptable Hydrogel Networks with Reversible Linkages for Tissue Engineering. *Adv. Mater.* **2015**, *27*, 3717–3736.
- (344) Kim, C. C.; Lee, H. H.; Oh, K. H.; Sun, J. Y. Highly Stretchable, Transparent Ionic Touch Panel. *Science* **2016**, *353*, 682–687.
- (345) Banerjee, S.; Das, R. K.; Maitra, U. Supramolecular Gels “in Action.” *J. Mater. Chem.* **2009**, *19*, 6649–6687.
- (346) Dankers, P. Y. W.; Hermans, T. M.; Baughman, T. W.; Kamikawa, Y.; Kieltyka, R. E.; Bastings, M. M. C.; Janssen, H. M.; Sommerdijk, N. A. J. M.; Larsen, A.; Van Luyn, M. J. A.; *et al.* Hierarchical Formation of Supramolecular Transient Networks in Water: A Modular Injectable Delivery System. *Adv. Mater.* **2012**, *24*, 2703–2709.
- (347) Yu, G.; Yan, X.; Han, C.; Huang, F. Characterization of Supramolecular Gels. *Chem. Soc. Rev.* **2013**, *42*, 6697–6722.
- (348) Shi, Y.; Wang, M.; Ma, C.; Wang, Y.; Li, X.; Yu, G. A Conductive Self-Healing Hybrid Gel Enabled by Metal–Ligand Supramolecule and Nanostructured Conductive Polymer. *Nano Lett.* **2015**, *15*, 6276–6281.
- (349) Roy, S.; Baral, A.; Banerjee, A. An Amino-Acid-Based Self-Healing Hydrogel: Modulation of the Self-Healing Properties by Incorporating Carbon-Based Nanomaterials. *Chem. Eur. J.* **2013**, *19*, 14950–14957.
- (350) Kahn, J. S.; Trifonov, A.; Ceconello, A.; Guo, W.; Fan, C.; Willner, I. Integration of Switchable DNA-Based Hydrogels with Surfaces by the Hybridization Chain Reaction. *Nano Lett.* **2015**, *15*, 7773–7778.
- (351) Rodell, C. B.; Dusaj, N. N.; Highley, C. B.; Burdick, J. A. Injectable and Cytocompatible Tough Double-Network Hydrogels through Tandem Supramolecular and Covalent Crosslinking. *Adv. Mater.* **2016**, *28*, 8419–8424.
- (352) Berciaud, S.; Cognet, L.; Poulin, P.; Weisman, R. B.; Lounis, B. Absorption Spectroscopy of Individual Single-Walled Carbon Nanotubes. *Nano Lett.* **2007**, *7*, 1203–1207.
- (353) Weisman, R. B.; Bachilo, S. M. Dependence of Optical Transition Energies on Structure for Single-Walled Carbon Nanotubes in Aqueous Suspension: An Empirical Kataura Plot. *Nano Lett.* **2003**, *3*, 1235–1238.

- (354) Seo, J. T.; Yoder, N. L.; Shastry, T. A.; Humes, J. J.; Johns, J. E.; Green, A. A.; Hersam, M. C. Diameter Refinement of Semiconducting Arc Discharge Single-Walled Carbon Nanotubes via Density Gradient Ultracentrifugation. *J. Phys. Chem. Lett.* **2013**, *4*, 2805–2810.
- (355) Yang, R.; Tang, Z.; Yan, J.; Kang, H.; Kim, Y.; Zhu, Z.; Tan, W. Noncovalent Assembly of Carbon Nanotubes and Single-Stranded DNA: An Effective Sensing Platform for Probing Biomolecular Interactions. *Anal. Chem.* **2008**, *80*, 7408–7413.
- (356) Zhang, X.; Pint, C. L.; Lee, M. H.; Schubert, B. E.; Jamshidi, A.; Takei, K.; Ko, H.; Gillies, A.; Bardhan, R.; Urban, J. J.; *et al.* Optically- and Thermally-Responsive Programmable Materials Based on Carbon Nanotube-Hydrogel Polymer Composites. *Nano Lett.* **2011**, *11*, 3239–3244.
- (357) Shin, S. R.; Bae, H.; Cha, J. M.; Mun, J. Y.; Chen, Y. C.; Tekin, H.; Shin, H.; Farshchi, S.; Dokmeci, M. R.; Tang, S.; *et al.* Carbon Nanotube Reinforced Hybrid Microgels as Scaffold Materials for Cell Encapsulation. *ACS Nano* **2012**, *6*, 362–372.
- (358) Fujigaya, T.; Morimoto, T.; Niidome, Y.; Nakashima, N. NIR Laser-Driven Reversible Volume Phase Transition of Single-Walled Carbon Nanotube/Poly(N-Isopropylacrylamide) Composite Gels. *Adv. Mater.* **2008**, *20*, 3610–3614.
- (359) Miyako, E.; Nagata, H.; Hirano, K.; Hirotsu, T. Photodynamic Thermoresponsive Nanocarbon-Polymer Gel Hybrids. *Small* **2008**, *4*, 1711–1715.
- (360) Yan, L. Y.; Chen, H.; Li, P.; Kim, D. H.; Chan-Park, M. B. Finely Dispersed Single-Walled Carbon Nanotubes for Polysaccharide Hydrogels. *ACS Appl. Mater. Inter.* **2012**, *4*, 4610–4615.
- (361) Fukushima, T.; Kosaka, A.; Ishimura, Y.; Yamamoto, T.; Takigawa, T.; Ishii, N.; Aida, T. Molecular Ordering of Organic Molten Salts Triggered by Single-Walled Carbon Nanotubes. *Science* **2003**, *300*, 2072–2074.
- (362) Kim, K. H.; Oh, Y.; Islam, M. F. Graphene Coating Makes Carbon Nanotube Aerogels Superelastic and Resistant to Fatigue. *Nat. Nanotechnol.* **2012**, *7*, 562–566.
- (363) Tan, Z.; Ohara, S.; Naito, M.; Abe, H. Supramolecular Hydrogel of Bile Salts Triggered by Single-Walled Carbon Nanotubes. *Adv. Mater.* **2011**, *23*, 4053–4057.
- (364) Wang, Z.; Chen, Y. Supramolecular Hydrogels Hybridized with Single-Walled Carbon Nanotubes. *Macromolecules* **2007**, *40*, 3402–3407.
- (365) Ogoshi, T.; Takashima, Y.; Yamaguchi, H.; Harada, A. Chemically-Responsive Sol-Gel Transition of Supramolecular Single-Walled Carbon Nanotubes (SWNTs) Hydrogel Made by Hybrids of SWNTs and Cyclodextrins. *J. Am. Chem. Soc.* **2007**, *129*, 4878–4879.

- (366) You, Y. Z.; Yan, J. J.; Yu, Z. Q.; Cui, M. M.; Hong, C. Y.; Qu, B. J. Multi-Responsive Carbon Nanotube Gel Prepared via Ultrasound-Induced Assembly. *J. Mater. Chem.* **2009**, *19*, 7656–7660.
- (367) Cheng, E.; Li, Y.; Yang, Z.; Deng, Z.; Liu, D. DNA-SWNT Hybrid Hydrogel. *Chem. Commun.* **2011**, *47*, 5545–5547.
- (368) Tamesue, S.; Takashima, Y.; Yamaguchi, H.; Shinkai, S.; Harada, A. Photochemically Controlled Supramolecular Curdlan/Single-Walled Carbon Nanotube Composite Gel: Preparation of Molecular Distaff by Cyclodextrin Modified Curdlan and Phase Transition Control. *Eur. J. Org. Chem.* **2011**, *2011*, 2801–2806.
- (369) Ostojic, G. N.; Hersam, M. C. Biomolecule-Directed Assembly of Self-Supported, Nanoporous, Conductive, and Luminescent Single-Walled Carbon Nanotube Scaffolds. *Small* **2012**, *8*, 1840–1845.
- (370) Du, R.; Wu, J.; Chen, L.; Huang, H.; Zhang, X.; Zhang, J. Hierarchical Hydrogen Bonds Directed Multi-Functional Carbon Nanotube-Based Supramolecular Hydrogels. *Small* **2014**, *10*, 1387–1393.
- (371) Zeng, Y.; Lu, J. Q. Optothermally Responsive Nanocomposite Generating Mechanical Forces for Cells Enabled by Few-Walled Carbon Nanotubes. *ACS Nano* **2014**, *8*, 11695–11706.
- (372) Jungst, T.; Smolan, W.; Schacht, K.; Scheibel, T.; Groll, J. Strategies and Molecular Design Criteria for 3D Printable Hydrogels. *Chem. Rev.* **2016**, *116*, 1496–1539.
- (373) Edelstein, M. L. Gene Therapy Clinical Trials Worldwide to 2007 – an Update. *J. Gene Med.* **2007**, *9*, 833–842.
- (374) Jeng, E. S.; Moll, A. E.; Roy, A. C.; Gastala, J. B.; Strano, M. S. Detection of DNA Hybridization Using the Near-Infrared Band-Gap Fluorescence of Single-Walled Carbon Nanotubes. *Nano Lett.* **2006**, *6*, 371–375.
- (375) Sitharaman, B.; Kissell, K. R.; Hartman, K. B.; Tran, L. A.; Baikalov, A.; Rusakova, I.; Sun, Y.; Khant, H. A.; Ludtke, S. J.; Chiu, W.; *et al.* Superparamagnetic Gadonanotubes Are High-Performance MRI Contrast Agents. *Chem. Commun.* **2005**, 3915–3917.
- (376) Shankar, A.; Mittal, J.; Jagota, A. Binding between DNA and Carbon Nanotubes Strongly Depends upon Sequence and Chirality. *Langmuir* **2014**, *30*, 3176–3183.
- (377) SantaLucia, J. A Unified View of Polymer, Dumbbell, and Oligonucleotide DNA Nearest-Neighbor Thermodynamics. *P. Natl. Acad. Sci. USA* **1998**, *95*, 1460–1465.
- (378) Mirkin, C. A.; Letsinger, R. L.; Mucic, R. C.; Storhoff, J. J. A DNA-Based Method for Rationally Assembling Nanoparticles into Macroscopic Materials. *Nature*, **1996**, 382,

607–609.

- (379) Park, S. Y.; Lytton-Jean, A. K. R.; Lee, B.; Weigand, S.; Schatz, G. C.; Mirkin, C. A. DNA-Programmable Nanoparticle Crystallization. *Nature* **2008**, *451*, 553–556.
- (380) Lytton-Jean, A. K. R.; Mirkin, C. A. A Thermodynamic Investigation into the Binding Properties of DNA Functionalized Gold Nanoparticle Probes and Molecular Fluorophore Probes. *J. Am. Chem. Soc.* **2005**, *127*, 12754–12755.
- (381) Lee, J. S.; Lytton-Jean, A. K. R.; Hurst, S. J.; Mirkin, C. A. Silver Nanoparticle-Oligonucleotide Conjugates Based on DNA with Triple Cyclic Disulfide Moieties. *Nano Lett.* **2007**, *7*, 2112–2115.
- (382) Breslauer, K. J.; Frank, R.; Blöcker, H.; Marky, L. A. Predicting DNA Duplex Stability from the Base Sequence. *P. Natl. Acad. Sci. USA* **1986**, *83*, 3746–3750.
- (383) Dreyfus, R.; Leunissen, M. E.; Sha, R.; Tkachenko, A. V.; Seeman, N. C.; Pine, D. J.; Chaikin, P. M. Simple Quantitative Model for the Reversible Association of DNA Coated Colloids. *Phys. Rev. Lett.* **2009**, *102*, 48301.
- (384) Xu, Y.; Pehrsson, P. E.; Chen, L.; Zhang, R.; Zhao, W. Double-Stranded DNA Single-Walled Carbon Nanotube Hybrids for Optical Hydrogen Peroxide and Glucose Sensing. *J. Phys. Chem. C* **2007**, *111*, 8638–8643.
- (385) Raidongia, K.; Nag, A.; Hembram, K. P. S. S.; Waghmare, U. V.; Datta, R.; Rao, C. N. R. BCN: A Graphene Analogue with Remarkable Adsorptive Properties. *Chem. Eur. J.* **2010**, *16*, 149–157.
- (386) Wang, S.; Zhang, L.; Xia, Z.; Roy, A.; Chang, D. W.; Baek, J. BCN Graphene as Efficient Metal-Free Electrocatalyst for the Oxygen Reduction Reaction. *Angew. Chem.* **2012**, *124*, 4285–4288.
- (387) Jakus, A. E.; Secor, E. B.; Rutz, A. L.; Jordan, S. W.; Hersam, M. C. Three-Dimensional Printing of High-Content Graphene Scaffolds for Electronic and Biomedical Applications. *ACS Nano* **2015**, *9*, 4636–4648.
- (388) Lahiri, D.; Rouzaud, F.; Richard, T.; Keshri, A. K.; Bakshi, S. R.; Kos, L.; Agarwal, A. Boron Nitride Nanotube Reinforced Polylactide – Polycaprolactone Copolymer Composite : Mechanical Properties and Cytocompatibility with Osteoblasts and Macrophages in Vitro. *Acta Biomater.* **2010**, *6*, 3524–3533.
- (389) Li, X.; Wang, X.; Jiang, X.; Yamaguchi, M.; Ito, A.; Bando, Y.; Golberg, D. Boron Nitride Nanotube-Enhanced Osteogenic Differentiation of Mesenchymal Stem Cells. *J. Biomed. Mater. Res. B Appl. Biomater.* **2016**, *104*, 323–329.
- (390) Li, R.; Mansukhani, N. D.; Guiney, L. M.; Ji, Z.; Zhao, Y.; Chang, C. H.; French, C. T. C.

- T.; Miller, J. F.; Hersam, M. C.; Nel, A. E.; *et al.* Identification and Optimization of Carbon Radicals on Hydrated Graphene Oxide for Ubiquitous Antibacterial Coatings. *ACS Nano* **2016**, *10*, 10966–10980.
- (391) Peng, Y.; Li, Y.; Ban, Y.; Jin, H.; Jiao, W.; Liu, X.; Yang, W. Metal-Organic Framework Nanosheets as Building Blocks for Molecular Sieving Membranes. *Science* **2014**, *346*, 1356–1359.
- (392) Rodenas, T.; Luz, I.; Prieto, G.; Seoane, B.; Miro, H.; Corma, A.; Kapteijn, F.; Llabrés i Xamena, F. X.; Gascon, J. Metal–Organic Framework Nanosheets in Polymer Composite Materials for Gas Separation. *Nat. Mater.* **2015**, *14*, 48–55.
- (393) Colson, J. W.; Woll, A. R.; Mukherjee, A.; Levendorf, M. P.; Spitler, E. L.; Shields, V. B.; Spencer, M. G.; Park, J.; Dichtel, W. R. Oriented 2D Covalent Organic Framework Thin Films on Single-Layer Graphene. *Science* **2011**, *332*, 228–231.
- (394) Kory, M. J.; Wörle, M.; Weber, T.; Payamyar, P.; van de PollStan, W.; Dshemuchadse, J.; Trapp, N.; Schlüter, A. D. Gram-Scale Synthesis of Two-Dimensional Polymer Crystals and Their Structure Analysis by X-Ray Diffraction. *Nat. Chem.* **2014**, *6*, 779–784.
- (395) Kissel, P.; Murray, D. J.; Wulftange, W. J.; Catalano, V. J.; King, B. T. A Nanoporous Two-Dimensional Polymer by Single-Crystal-to-Single-Crystal Photopolymerization. *Nat. Chem.* **2014**, *6*, 774–778.
- (396) Tan, C.; Qi, X.; Huang, X.; Yang, J.; Zheng, B.; An, Z.; Chen, R.; Wei, J.; Tang, B. Z.; Huang, W.; *et al.* Single-Layer Transition Metal Dichalcogenide Nanosheet-Assisted Assembly of Aggregation-Induced Emission Molecules to Form Organic Nanosheets with Enhanced Fluorescence. *Adv. Mater.* **2014**, *26*, 1735–1739.
- (397) Fan, Z.; Huang, X.; Tan, C.; Zhang, H. Thin Metal Nanostructures: Synthesis, Properties and Applications. *Chem. Sci.* **2015**, *6*, 95–111.
- (398) Huang, X.; Li, S.; Huang, Y.; Wu, S.; Zhou, X.; Li, S.; Gan, C. L.; Boey, F.; Mirkin, C. A.; Zhang, H. Synthesis of Hexagonal Close-Packed Gold Nanostructures. *Nat. Commun.* **2011**, *2*, 292.
- (399) Huang, X.; Tang, S.; Mu, X.; Dai, Y.; Chen, G.; Zhou, Z.; Ruan, F.; Yang, Z.; Zheng, N. Freestanding Palladium Nanosheets with Plasmonic and Catalytic Properties. *Nat. Nanotechnol.* **2011**, *6*, 28–32.
- (400) Duan, H.; Yan, N.; Yu, R.; Chang, C. R.; Zhou, G.; Hu, H. S.; Rong, H.; Niu, Z.; Mao, J.; Asakura, H.; *et al.* Ultrathin Rhodium Nanosheets. *Nat. Commun.* **2014**, *5*, 3093.
- (401) Anseth, K. S.; Bowman, C. N.; Brannon-Peppas, L. Mechanical Properties of Hydrogels and Their Experimental Determination. *Biomaterials* **1996**, *17*, 1647–1657.

NIKHITA MANSUKHANI
 ndm@u.northwestern.edu
 810 Roosevelt Drive, Libertyville, IL 60048
 (847) 571-0442

Education

- Northwestern University (Evanston, IL)** September 2011-March 2017
 Doctor of Philosophy in Materials Science and Engineering
 Advisor: Professor Mark Hersam
- University of Illinois at Urbana-Champaign (Urbana, IL)** August 2007-May 2011
 Bachelor of Science with High Distinction
 Concentration: Physics (Biophysics), Chemistry Minor

Research Experience

- Mark Hersam Research Group (Evanston, IL)** October 2011-March 2017
Graduate Research Assistant
- Built expertise in solution processing and characterization of nanomaterials
 - Managed productive collaborations with interdisciplinary research teams and centers
- Nadya Mason Research Group (Urbana, IL)** May 2010-August 2011
Undergraduate Research Assistant
- Developed a technique that determined the nature of adhesion properties of 2D materials
- Children's Memorial Hospital Research Center (Chicago, IL)** May-August 2008 & 2009
Summer Undergraduate Research Student
- Deepened the understanding of neural tube defect development in fetuses

Certificates and Training

- Kellogg School of Management** June 2014-August 2014
 Management for Scientists and Engineers Certificate Program
- Surveyed topics including economics, finance, leadership, negotiation, and marketing
- Biotechnology Pre-doctoral Training Program** September 2012-August 2013
 National Institutes of Health Training Program
- Awarded competitive research fellowship and membership in a community of trainees
 - Organized day-long practicums with industry experts to enhance biotechnology training

Honors and Awards

- John E. Hilliard Symposium, Second Place** (May 2016)
NSF Graduate Research Fellowship (September 2013-September 2016)
Biotechnology Training Program Fellowship (September 2012-September 2013)
Department of Materials Science First Year Fellowship (September 2011-September 2012)
James Scholar Designee (August 2007-May 2011)
Lorella M. Jones Summer Research Fellowship (2010)
Laura B. Eisenstein Excellence in Physics Award (2011)

Publications

Google Scholar: <https://scholar.google.com/citations?user=0RYvZfcAAAAJ&hl=en&oi=sra>

Mansukhani, N.; Guiney, L.M.; Wei, Z.; Roth, E.W.; Putz, K.; Luijten, E.; Hersam, M.C. Optothermally Reversible Carbon Nanotube-DNA Supramolecular Hybrid Hydrogel. *In preparation.*

*Shams, M.; ***Mansukhani, N.;** Henderson, M.C.; Zepp, R.; Bouchard, D.; Hersam, M.C.; Chowdhury, I. Environmental Implications of Two-Dimensional Materials. *Environmental Science: Nano* **2017**, *Invited Review, In Preparation.* *Equal Contributions

Li, R.; **Mansukhani, N.;** Guiney, L.; Ji, Z.; Zhao, Y.; Chang, C.; French, C.T.; Miller, J.F.; Hersam, M.C.; Nel, A.E.; Xia, T. Identification and Optimization of Carbon Radicals on Hydrated Graphene Oxide for Ubiquitous Antibacterial Coatings. *ACS Nano* **2016**, *10*, 10966-10980.

Wang, X.; **Mansukhani, N.;** Guiney, L.; Lee, J.; Li, R.; Sun, B.; Liao, Y.; Chang, C. H.; Ji, Z.; Hersam, M.C.; Nel, A.E. Toxicological Profiling of Highly Purified Metallic and Semiconducting Single-Walled Carbon Nanotubes in the Rodent Lung and E. Coli. *ACS Nano* **2016**, *10*, 6008-6019.

Mansukhani, N.; Guiney, L.; Kim, P.; Alducin, D.; Ponce, A.; Larios, E.; Jose-Yacaman, M.; Hersam, M.C. Aqueous High Concentration Dispersions of Nanoscale Two-Dimensional Materials Using Nonionic, Biocompatible Block Copolymers. *Small* **2016**, *12*, 294-300.

Wang, X.; **Mansukhani, N.;** Guiney, L.; Ji, Z.; Chang, C.H.; Wang, M.; Liao, Y.; Song, T.; Sun, B.; Li, R.; Xia, T.; Hersam, M.C.; Nel, A.E. Differences in the Toxicological Potential of Two-Dimensional vs Aggregated Molybdenum Disulfide in the Lung. *Small* **2015**, *11*, 5079-5087.

Wang, X.; Duch, M.C.; **Mansukhani, N.;** Ji, Z.; Liao, Y.; Wang, M.; Zhang, H.; Sun, B.; Chang, C.H.; Li, R.; Lin, S.; Meng, H.; Xia, T.; Hersam, M.C.; Nel, A.E. Use of a Pro-Fibrogenic Mechanisms-Based Predictive Toxicological Approach for Tiered Testing and Decision Analysis of Carbonaceous Nanomaterials. *ACS Nano* **2015**, *9*, 3032-3043.

Lanphere, J.D.; Luth, C.J.; Guiney, L.; **Mansukhani, N.;** Hersam, M.C.; Walker, S.L. Fate and Transport of Molybdenum Disulfide Nanomaterials in Sand Columns. *Environ. Eng. Sci.* **2015**, *32*, 163-173.

Chowdhury, I.; **Mansukhani, N.;** Guiney, L.; Hersam, M.C. Aggregation and Stability of Reduced Graphene Oxide: Complex Roles of Divalent Cations, pH, and Natural Organic Matter. *Environ. Sci. Technol.* **2015**, *49*, 10886-10893.

Hung, A.H.; Holbrook, R.J.; Rotz, M.W.; Classcock, C.J.; **Mansukhani, N.;** MacRenaris, K.W.; Manus, L.M.; Duch, M.C.; Dam, K.T.; Hersam, M.C.; Meade, T.J. Graphene Oxide Enhances Cellular Delivery of Hydrophilic Small Molecules by Co-Incubation. *ACS Nano* **2014**, *8*, 10168-10177.

Chowdhury, I.; Duch, M.C.; **Mansukhani, N.**; Hersam, M.C.; Bouchard, D. Interactions of Graphene Oxide Nanomaterials with Natural Organic Matter and Metal Oxide Surfaces. *Environ. Sci. Technol.* **2014**, *48*, 9382-9390.

Chowdhury, I.; Duch, M.C.; **Mansukhani, N.**; Hersam, M.C.; Bouchard, D. Deposition and Release of Graphene Oxide Nanomaterials Using a Quartz Crystal Microbalance. *Environ. Sci. Technol.* **2014**, *48*, 961-969.

Chowdhury, I.; Duch, M.C.; **Mansukhani, N.**; Hersam, M.C.; Bouchard, D. Colloidal Properties and Stability of Graphene Oxide Nanomaterials in the Aquatic Environment. *Environ. Sci. Technol.* **2013**, *47*, 6288-6296.

Scharfenberg, S.; **Mansukhani, N.**; Chialvo, C.; Weaver, R. L.; Mason, N. Observation of a Snap-Through Instability in Graphene. *Appl Phys Lett* **2012**, *100*, 021910.

Ichi, S.; Boshnjaku, V.; Shen, Y.; Mania-Farnell, B.; Ahlgren, S.; Sapru, S.; **Mansukhani, N.**; McLone, D.G.; Tomita, T.; Mayanil, C.S.K. "Role of Pax3 acetylation in the regulation of *Hes1* and *Neurog2*." *Mol. Biol. Cell* **2010**, *22*, 503-512.

Volunteer and Outreach

Mentorship Opportunities for Research Engagement, Northwestern University

Letters to a Pre-Scientist, Northwestern University

Materials Science Students Association, Northwestern University

Women in Physics, University of Illinois

Engineering Student-Alumni Ambassadors, University of Illinois

Operation Smile, University of Illinois